UNIVERSIDAD POLITÉCNICA DE MADRID
Escuela Técnica Superior de Ingenieros de Caminos, Canales y Puertos

Accurate prediction of phase diagrams of binary alloys from first-principles calculations and statistical mechanics

DOCTORAL THESIS

Submitted for the degree of Doctor by:

Wei Shao

Master in Material Science and Engineering

Madrid, 2024

UNIVERSIDAD POLITÉCNICA DE MADRID
Escuela Técnica Superior de Ingenieros de Caminos,
Canales y Puertos

Doctoral Degree in Engineering of Structures, Foundations and Materials

Accurate prediction of phase diagrams of binary alloys from first-principles calculations and statistical mechanics

DOCTORAL THESIS

Submitted for the degree of Doctor by:

Wei Shao
Master in Material Science and Engineering

Under the supervision of:
Dr. Javier LLorca
Dr. Sha Liu

Madrid, 2024

Title: Accurate prediction of phase diagrams of binary alloys from first-principles calculations and statistical mechanics

Author: Wei Shao

Doctoral Programme: Engineering of Structures, Foundations and Materials

Thesis Supervision:

Dr. Javier LLorca, Professor, Universidad Politécnica de Madrid

Dr. Sha Liu, Professor, Yanshan University

External Reviewers:

Thesis Defense Committee:

Thesis Defense Date:

Acknowledgements

In the blink of an eye, I have been in Madrid for three years. These three years have benefited me a lot. Here, I would like to express my sincere thanks and blessings to them.

First and foremost, I would like to thank my supervisors Prof. Javier LLorca and Prof. Sha Liu who adhering to the rigorous scientific spirit, carefully analyzed my calculation results and gave me a lot of guidance. In addition, they also exercised and cultivated my awareness of independent thinking, as well as writing and reporting. They gave me a lot of feasible suggestions and made me achieved rapid growth. By the learning and support from them, I can overcome many difficulties and move on firmly.

Secondly, I am very grateful to all researchers and colleagues for their help and support: José Manuel Guevara-Vela, Dr. Martínez Carmen, Prof. Antonio Fernández-Caballero. I also want to express my gratitude to my friends for their help and companionship, which made me feel the warmth of home in this city: Tian Xie, Biaobiao Yang, Shuanglan Du, Yuyao Liu, Jun Hu, and Xiang Ao.

Most of all, I wish to acknowledge the China Scholarship Council (CSC, No. 202108130137) for supporting me to study in Spain. Without this financial support, this work could also not be possible.

Lastly, I would like to thank my family for their silent support over the years, your understanding, trust, and expectations, which are the driving force for me to move forward.

Wei Shao

Abstract

Lightweight and high-temperature performance are important indicators to promote the development of the aviation industry. Al-Li alloys with low density, high specific strength, excellent low temperature performance and good corrosion resistance are an ideal aerospace structural material. Ni-based and Co-based superalloys with superior high-temperature properties are key materials for aero-engine turbine blades. However, with the continuous development of the aviation industry, higher requirements have been placed on the performance of these materials. Therefore, designing materials with better performance is the focus of current research in the aviation field.

Understanding how the presence and stability of phases in a given material influences its mechanical properties is critical to designing novel materials. Systematic analysis of stable and metastable phases in alloy systems by experiments is expensive and time-consuming because slow kinetics may hinder the convergence towards thermodynamic equilibrium. Thus, in this thesis, the stability of the different phases in Al-Li, Ni-Al and Co-Al alloys were studied by first-principles calculations in combination with statistical mechanics principles. The obtained thermodynamic information can provide theoretical support for the design of novel multi-composition alloy.

Firstly, the whole solid-state region of the Al-Li phase diagram was predicted by first-principles calculations and statistical mechanics, including the effect of configurational disorder and lattice vibrations. The formation enthalpy of different configurations at different temperatures was accurately predicted by means of cluster expansions that were fitted from first-principles calculations. The vibrational contribution was determined from the bond length *vs.* bond stiffness relationships for each type of chemical bond within and the Gibbs free energy of each phase as a function of temperature was obtained from Monte Carlo simulations. The predicted phase diagram was in excellent agreement with the currently accepted experimental one in terms of the stable (AlLi, Al_2Li_3, $AlLi_2$, Al_4Li_9) and metastable (Al_3Li) phases. In addition, it provided accurate information about the gap between Al_3Li and AlLi solvus lines.

The Ni-Al phase diagram was also predicted using the same methodology. The contribution of magnetic enthalpy was also included in the Gibbs free energy of each phase in this case. The computed phase diagram was in excellent agreement with the experimentally accepted phase diagram and provided information about the phase boundary between $AlNi_3$ and Ni below 300 K, which was unknow before.

Finally, the phase diagram of the Co-Al system was predicted. The magnetic entropic contribution was also included through the Heisenberg Hamiltonian. The computed phase diagram was compared with the currently accepted experimental phase diagram and the different contributions to the stability of each phase were analyzed independently. The potential of this strategy to predict phase diagrams of magnetic systems was clearly established. Overall, the methodology developed in this thesis shows that accurate phase diagrams of alloys of technological interest can be predicted from first-principles calculations and statistical mechanics principles.

Resumen

Baja densidad y buen comportamiento a altas temperaturas son indicadores importantes para promover el desarrollo de la industria de la aviación. Las aleaciones de Al-Li con baja densidad, alta resistencia específica, excelentes propiedades mecánicas a bajas temperaturas y buena resistencia a la corrosión son un material estructural aeroespacial ideal. Las superaleaciones a base de Ni y Co con las mejores propiedades a altas temperaturas son materiales clave para los álabes de turbinas de motores aeronáuticos. Sin embargo, con el continuo desarrollo de la industria de la aviación, se han impuesto mayores requisitos al rendimiento de estos materiales. Por tanto, diseñar materiales con mejores prestaciones es uno de los focos de la investigación actual en el campo de la aviación.

Comprender cómo la presencia y estabilidad de las fases en un material determinado afectan sus propiedades mecánicas es fundamental para diseñar nuevos materiales. El análisis sistemático de las fases estables y metaestables en aleaciones mediante experimentos es costoso y requiere mucho tiempo porque la cinética lenta hace difícil la convergencia hacia el equilibrio termodinámico. En esta tesis, la estabilidad de las fases en aleaciones Al-Li, Ni-Al y Co-Al se estudió mediante cálculos de primeros principios combinados con mecánica estadística. La información termodinámica obtenida puede proporcionar apoyo teórico para el diseño nuevas aleaciones con una composición compleja.

En primer lugar, el diagrama de fases de Al-Li se predijo mediante cálculos de primeros principios y mecánica estadística, incluyendo el efecto del desorden configuracional y la vibración de la red. La entalpía de formación de diferentes configuraciones a diferentes temperaturas se calcularon con precisión mediante expansiones en serie que se ajustaron a partir de los cálculos de primeros principios. La contribución vibracional se determinó a partir de las relaciones entre la longitud del enlace y la rigidez del enlace para cada tipo de enlace químico y la energía libre de Gibbs de cada fase en función de la temperatura se obtuvo a partir de simulaciones de Monte Carlo. El diagrama de fases calculado coincidió con el diagrama experimental actualmente aceptado en términos de las fases estables (AlLi, Al_2Li_3, $AlLi_2$, Al_4Li_9) y metaestables (Al_3Li). Además, proporcionó información precisa sobre la brecha de miscibilidad entre las líneas de solvus de Al_3Li y AlLi.

El diagrama de fases de Ni-Al también se calculó siguiendo la misma metodología. La contribución de la entalpía magnética también se incluyó en la energía libre de Gibbs de cada fase. El diagrama de fases calculado concordó perfectamente con el diagrama de fases aceptado experimentalmente y proporcionó información sobre los límites entre $AlNi_3$ y Ni por debajo de 300 K, que se desconocía hasta ahora.

Finalmente, se predijo el diagrama de fases del sistema Co-Al, donde también se incluyó la contribución entrópica magnética a través del hamiltoniano de Heisenberg. El diagrama de fases calculado se comparó con el diagrama de fases experimental actualmente aceptado y las diferentes contribuciones a la estabilidad de cada fase se analizaron de forma independiente. El potencial de esta estrategia para predecir diagramas de fases de sistemas magnéticos está claramente establecido. En general, la metodología desarrollada en esta tesis muestra que se pueden predecir diagramas de fases precisos de aleaciones de interés tecnológico a partir de cálculos de primeros principios en combinación con mecánica estadística.

Table of Contents

List of Figures

List of Tables

Glossary

Acronym	Definition
ATAT	Alloy Theoretic Automated Toolkit
AFM	Anti-ferromagnetic
bcc	Body-Centered Cubic
Calphad	Calculation of Phase Diagrams
CE	Cluster Expansion
CV	Cross Validation
CVM	Cluster Variation Method
DC	Diffusion Couples
DOS	Density Of States
DFT	Density Functional Theory
ECI	Effective Cluster Interaction
FM	Ferromagnetic
fcc	Face-Centered Cubic
GGA	Generalized Gradient Approximation
hcp	Hexagonal-Close Packed
IHJ	Inden-Hillert-Jarl
ICME	Integrated Computational Materials Engineering
LSDA	Local Spin Density Approximation
L-S	Bond Length *vs*. Bond Stiffness

Table 1: Recurrent acronyms used throughout this thesis (A-L).

Acronym	Definition
MC	Monte Carlo
NN	Nearest-Neighbour
PAW	Projector Augmented Wave
PBE	Perdew-Burke-Ernzerhof
PWs	Plane Waves
PPs	Pseudopotentials
SQS	Special Quasirandom Structure
TA	Thermal Analysis
TEM	Transmission Electron Microscopy
TCP	Topologically Close-Packed
XRD	X-Ray Powder Diffraction

Table 2: Recurrent acronyms used throughout this thesis (M-Z).

Symbol	Definition	Reference
T_C	Curie temperature	Sec.1.4
e	electron charge	Eq. 2.1
E_{XC}	exchange correlation energy	Eq. 2.3
m_e	electronic mass	Eq. 2.1
U	Potential energy	Eqs. 2.4, 2.5
u	atomic displacements	Eqs. 2.4, 2.5
$D_{i,j}(\mathrm{q})$	dynamical matrix	Eq. 2.6
F_{vib}	Vibrational free energy	Eq. 2.9
S_{vib}	vibrational entropy	Eqs. 2.9, 2.10
b	bending stiffness	Eq. 2.11
s	stretching stiffness	Eq. 2.11
$N_{nn}^{\uparrow\uparrow}$	Number of the NN atomic pairs with parallel spins	Eq. 2.12, Table 5.2
$N_{nn}^{\uparrow\downarrow}$	Number of the NN atomic pairs with antiparallel spins	Eq. 2.12, Table 5.2
J_{ij}	coupling constant	Eq. 2.12, Table 5.3
F_{mag}	magnetic free energy	Eq. 2.13
S_{mag}	magnetic entropy	Eqs. 2.14
C_{mag}	magnetic specific heat	Eqs. 2.15
$\vec{l}$	unit cell vectors	Table 2.1

$\vec{n}$	Lattice vector	Table 2.1
$\vec{b}$	Basis sites	Table 2.1
H_{mix}	mixing enthalpy	Eq. 2.17
J_{α}	effective cluster interaction	Eq. 2.22
m_{α}	multiplicities	Eq. 2.22
Z	partition function	Eq. 2.28
G	Gibbs free energy	Eq. 2.32

Table 3: Recurrent notations used throughout this thesis — Latin symbols.

Symbol	Definition	Reference
γ'	Ni_3Al, $Co_3(Al,W)$	Sec1.2
γ	Ni matrix, Co matrix	Sec.1.1.2, Sec.1.1.3
ε_i	the ith one-electron energy eigenvalue	Eq. 2.1
$\psi_i(\vec{r})$	ith one-electron wavefunction	Eq. 2.1
$\hbar$	reduced Planck constant	Eq. 2.1
$\rho(\vec{r}')$	electron density	Eqs. 2.1, 2.3
$\Psi(i,j)$	force constant matrices	Eqs. 2.5, 2.6, 2.11
$g(\omega)$	phonon density of states	Eq. 2.10
$\omega(q)$	phonon frequencies	Eq. 2.7
σ_i	occupation variable	Eq. 2.23
$\varphi_\alpha(\vec{\sigma})$	cluster functions	Eq. 2.23
$\emptyset$	grand potential	Eqs. 2.27, 2.29
$\Delta\mu$	chemical potential difference	Eq. 2.27
k_B	Boltzmann’s constant	Eq. 2.27
$\langle H_f \rangle$	average formation enthalpy	Eq. 2.29
δ'	Al_3Li	Sec. 3.1
δ	AlLi	Sec. 3.1

Table 4: Recurrent notations used throughout this thesis — Greek symbols

1. Introduction

1.1. Phase diagram

In the field of Materials Science and Engineering, phase diagrams are the foundation to study the evolution of the material microstructure during solidification, crystal growth, joining, solid-state reactions, phase transformation, oxidation, etc. [1,2]. Moreover, a phase diagram also serves as a roadmap to support the development of materials, from their synthesis to their applications [3,4]. Detailed knowledge of phase equilibria and the underlying thermodynamics enables the establishment of the link between processing and microstructure, which is a crucial step in modern material design.

Phase diagrams were determined primarily through time-consuming and expensive experiments until the last decades of 20 century. Although this approach is both feasible and necessary for determining phase equilibria of binary and ternary species within limited compositional regions, it is nearly impossible to obtain phase diagrams for ternary and higher-order systems over wide composition and temperature ranges. Thus, one of the current challenges in this field is to use alternative methods to obtain multicomponent phase diagrams.

Most recent advances on ICME (Integrated Computational Materials Engineering) have produced new approaches on modelling and simulation in Materials Science and Engineering [5,6]. ICME has played an important role in multi-scale modeling and simulation-based design of materials. Motivated by the ever increasing computing power and the large amount of data repositories, the integration of first-principles calculation based on DFT (Density functional theory) and Calphad (Calculation of Phase Diagrams) [7,8] establish a robust development framework of data-driven ICME, as shown in Figure 1.1. Material design strategies can be established within this framework since the issues/questions related to phase stability, kinetics, phase transformations and control of the mechanical properties - that are important for the development of novel alloys - can be currently addressed. The three approaches of determining the phase diagram including experiment, Calphad and first-principles calculations will be elaborated as follows.

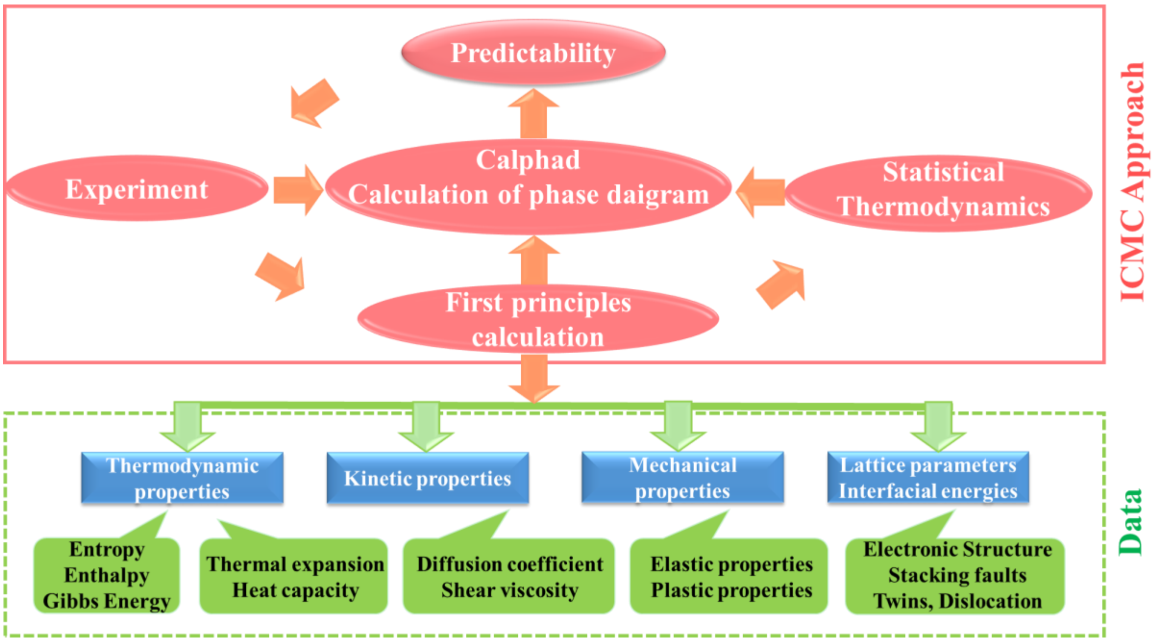

Figure 1.1: Schematic diagram of the ICME roadmap to design new materials for engineering applications.

1.2. **Experimental determination of phase diagrams**

Various experimental techniques are currently utilized to determine phase diagrams based on the principle that the physical and chemical properties, the phase composition and/or the structure varies when a phase transition occurs. These techniques include Differential Scanning Calorimetry (DSC), X-Ray Diffraction (XRD), and diffusion couples (DC).

DSC is a thermal analysis technique that measures the absorbed or released energy of a sample during heating or cooling. When there exists a phase transition, DSC will show a sharp change in the energy absorbed or released at the corresponding transition temperature [9,10]. Although the absorbed or released energy is associated with enthalpy information of the phase transition [11], the actual enthalpy is difficult to obtain from DSC because thermal transfer inside the sample is neglected [12,13]. Moreover, DSC cannot provide crystallographic information about the phases, and the reaction mechanism during phase transition cannot be revealed. DSC is usually combined with XRD techniques to determine the structural characteristics and the loci of phase boundaries [14,15]. However, it is still difficult or impossible to determine complex phase changes, such as magnetic transitions [16].

Another powerful tool to determine phase diagram is the DC technique. It can be used to determine the solubility range of each phase in the phase diagram. However, it is assumed that local equilibrium at the interphase boundary is achieved even though the boundary is still migrating. Therefore, the data evaluated from the DC method are not always valid for the determination of equilibrium compositions [17].

It should be noted that the accuracy of phase diagram highly depends on the sample preparation [18]. For instance, Al-Re phase diagram [19] has not been fully characterized because the difference in the melting temperature of Al (660 °C) and Re (3186 °C) is very large, which leads to experimental difficulties in specimen preparation. Additionally, the convergence towards thermodynamic equilibrium can be hindered by slow kinetics, especially at low temperature, and it is almost impossible to ensure that the actual stable phases have been obtained [20,21]. For this reason, there are low-temperature regions in the phase diagram that can never be analyzed experimentally.

Given the cost and the time necessary to calculate the phase diagram by means of experiments, modeling and simulation in conjunction with experiments can be employed to improve the efficiency of phase diagram determination.

1.3. Phase diagram calculation by Calphad

The thermodynamic modeling based on the Calphad method is a major part of ICME. The essence of the Calphad method is to use thermodynamic data parameters such as heat capacity, mixing energy, etc. obtained from experiments, combined with thermodynamic models (solution model, sublattice solution model and order-disorder model) to express the Gibbs free energy of each phase as a function of composition and temperature [21-23]. The Calphad method has proven its capability to describe multicomponent systems from to the Gibbs free energies obtained from binary and ternary systems in Calphad models [25,26]. However, extrapolation of binaries and ternaries into higher order systems is limited in many situations [27,28]. This is the case when there are new stable quaternary or higher-order phases, or when the descriptions of unstable or hypothetical phases/endmembers are so unphysical that cause undesired over-stabilization or underestimated stability. Since Calphad itself is not a predictive methodology, the thermodynamic descriptions for all phases in the system must be pre-defined. If there exists new quaternary or higher-order compound phase in the system, their Gibbs free energy descriptions should be determined beforehand [29].

In addition, the credibility of Calphad highly depends on the suitability and quality of the thermodynamic database [30,31]. However, many thermodynamic databases available today are designed for conventional single principal element alloys [32], which means that: 1) the thermodynamic descriptions are apparently not adequate for multi-principal element systems, such as high entropy alloys; 2) the thermodynamic descriptions may not be complete for a whole system but limited to only the major component rich corner [33]; and 3) phases irrelevant to the targeted type of alloys are deliberately excluded [31]. At the same time, it is challenging to use the Calphad method to deal with magnetism, and a comprehensive review on the measurement of magnetic properties calls for more efforts than merely evaluating the thermodynamic properties for the system. Finally, the spin and magnetic moment phenomena are dominated by quantum mechanical effects, which are difficult to accurately describe by the classic thermodynamics in the Calphad method [34].

1.4. **Phase diagram calculation by first-principles**

The low-temperature thermodynamics of alloys has remained a challenge in Materials Science, primarily because of the slow diffusion kinetics. It can be regarded as an unknown region in the phase diagrams and cannot be filled by Calphad method [35]. In recent decades, application of first-principles calculations in condensed matter physics has greatly expanded to fill this gap [36,37]. The methodology based on first-principles calculations and statistical mechanics principles supported by the cluster expansion (CE) formalism was developed at the end of the last century [38-40]. It did not only provide physics-based thermo-chemistry data for predicting phase equilibria without experimental input [41], but also can be used as an input for Calphad method.

The CE approach, firstly introduced by Sanchez et al. [42], expresses the energy of a given configuration as a linear combination of atomic clusters multiplied by the corresponding cluster interaction coefficients, that are fitted from the mixing enthalpies at 0 K obtained by DFT for a (sufficiently) large number of configurations. The configurations on the convex hull in the enthalpy-composition space are ground state phases at 0 K. The thermodynamic properties of each phase at high temperature depends on all possible microstates whose properties can be easily and accurately determined by means of the CE formalism according to their configuration [38,40]. Thus, the free energies of different phases (including the entropic contribution due to the configurational disorder) can be obtained as a function of temperature from Monte Carlo (MC) simulations using the principles of statistical mechanics. This method has been widely used in several systems, such as Al-Cu [39], Co-Ni [43], CrMoNbV high entropy alloys [44], refractory binary alloys [45], and many others.

However, some configurations above the convex hull may appear at higher temperatures due to thermal fluctuations [39,46], which results - for instance - in a considerable discrepancy in the predicted miscibility gap [39]. A typical example is the stability of θ and θ' phases in the Al-Cu phase diagram. Both phases have the same stoichiometry (Al_2Cu) but different lattices. θ' is in the convex hull and remains the stable phase up to 550K, but becomes metastable (and θ becomes the stable phase) at higher temperature due to the contribution of the vibrational disorder to the free energy, and the solvus line of θ' also changes accordingly.

The standard strategy to account for the vibrational entropy contribution to the free energy is based in the quasi-harmonic approximation [47,48]. Within this framework, the thermal properties of solid materials are traced back to those of a system of non-interacting phonons whose frequencies are, however, allowed to depend on volume or on other thermodynamic constraints. Thus, phonon calculations have to be carried out to determine the force constant matrix of each atom, which reflects the energy response from lattice vibration at each temperature [49]. The lattice vibration is a degree of freedom under the configurational dimension, which means any change of atomic configuration will make the lattice vibration different. Therefore, it is not feasible to perform phonon calculations for solid solutions or phases with certain solubility, because the phonon calculations should be performed for all possible microstates [50,51]. This effort can be, however, dramatically reduced in systems with simple lattices because the force constant matrix can be transferred among different configurations and the stretching and bending stiffness of the different bonds can be accurately approximated through a bond length *vs*. bond stiffness relationship (thereafter denominated L-S relationship) in the force constant matrix [52-54]. Thus, the L-S relationship is determined from several configurations by comparison with full phonon calculations, and then it is used to predict the force constant matrix of atoms in other configurations with the same lattice structure to minimize the computational effort. The vibrational entropy contribution to the free energy can be obtained through this approach, so that accurate predictions of the phase diagram at high temperature of different systems can be obtained [55-57].

Magnetic enthalpy and entropy also contribute to the stability of phases in the system in which at least one component is magnetic. The magnetic contribution to the free energy can be determined through the Inden-Hillert-Jarl (IHJ) model [58]. This approach assumes that spin orientations are uniformly distributed in the magnetic materials, neglecting the details of the interaction between magnetic elements in the lattice, and this simplification affects the temperature dependence of the magnetic heat capacity [58]. Overall, this model provides an empirical analytical expression for the magnetic entropy above and below the Curie temperature, T_C, based on the experimental results [59,60] but its accuracy is limited when temperature is close to or below the magnetic phase transition temperature because it is based on the framework of classical statistical mechanics [61]. Moreover, the IHJ model neglects the dynamic behavior of magnetic moments (spin fluctuations and spin flips), which may lead to a unrealistic miscibility gap in some magnetic systems, such as Fe-Ni [62] and Ni-Si alloys [63].

A more accurate approach is based on the Heisenberg model and can be used to obtain the magnetic contribution to the free energy [64]. In this approach, the atomic occupation variable is replaced by the magnetic spin [65-67] and a Heisenberg Hamiltonian reflecting the magnetic interactions among atoms is obtained from DFT calculations. Afterwards, the magnetic specific heat of each phase at different temperature is determined by MC simulations based on the Heisenberg Hamiltonian. Then, T_C is obtained from the peak value of the magnetic specific heat [68], while the magnetic entropies of different phases can be obtained by integrating the magnetic specific heat with respect to the temperature [64]. This technique has been applied to predict the T_C in a broad range of materials, such as 3d transition metals [69,70] and rare-earth magnets [71,72].

In summary, methods based on first-principles calculations and statistical mechanical simulations play a key role in the prediction of alloy phase diagrams. It can not only fill the gaps in experimental data but also provide broader thermodynamic information for the development and design of new materials.

1.5. **Binary systems**

Weight reduction and the higher operation temperature of turbine blades and engines are two important factors that drive the development of new materials for aerospace applications [73]. Guiding the design and development of novel alloys through the solid solution information (including solubility and critical temperature) of different phases provided in the phase diagram has become an important approach to improve the performance and reliability of aerospace components.

Currently, Aluminum-Lithium (Al-Li) alloys play a vital role in weight reduction of key aerospace components, which not only improved fuel efficiency but also increased load capacity [74]. Nickel (Ni)-based and Cobalt (Co)-based superalloys are key materials for aerospace engines, in which the addition of Al leads to the apparition of strengthening precipitates that improve the strength at high temperature [75]. The development process and existing problems of Al-Li, Ni-based and Co-based superalloy will be introduced in detail as follow.

1.5.1. **Al-Li system**

Al-Li alloy is one of the most widely used structural materials in the aviation industry due to its high modulus of elasticity, high hardness, high fatigue crack growth resistance, and low density [74,76]. The strength of Al-Li alloy is strongly dependent on Li content. It has been found that addition of 1 wt.% of Li to Al can reduce alloy density up to 3% and increases the elasticity modulus by 6% [77,78]. However, a Li content above 1.3 wt.% results in a decrease in both yield stress and tensile strength, so the maximum strength of Al-Li alloy is always obtained in the range between 1.1-1.3 wt.% of Li [79].

Since 1920, three different generations of Al-Li alloy have been developed [80]. The industrial application of the 1st generation (including 2020, VAD 23 and 1420) was compromised by its limited ductility and toughness, while high anisotropy of mechanical properties and delamination issues during manufacturing in the short-transverse direction also hindered the use of the 2nd generation (including AA 2090, AA 2091 and AA 8090) [81]. In the early 1990s, the 3rd generation (2094, 2095, Weldalite, etc.) were introduced to overcome the previously mentioned limitations of Al-Li alloys, which featured a Li concentration between 1.0 wt.% and 1.8 wt.% [77,80,82]. 2055 and 2060 alloys are the newest 3rd generation among Al-Li alloy launched by Alcao Inc. at 2012 and 2011, respectively [83]. These alloys exhibit excellent corrosion resistance, high thermal stability, and a synergy of high strength and good toughness.

Although, Al-Li alloys have been widely used in the aerospace field [82], they still face some limitations. For instance, Al-Li alloys used for fuselage skins are susceptible to intergranular corrosion [73], which is due to the precipitate microstructure according to the Li concentration. Thus, Al-Li phase diagram serves as the basis for exploring the effects of alloying additions on precipitation.

The strengthening of Al-Li alloy is mainly derived from the formation of metastable ordered δ'-Al_3Li ($L1_2$) phase, a superlattice fcc structure of Cu_3Au-type, which acts as one of the major hardening precipitates in Al-Li alloy. The metastable two-phase boundary in the Al-Li phase diagram has been investigated extensively due to the important role of such metastable phase [84]. However, there is still significant disagreement in the solubility limits of δ' phases at low temperature, as shown in the results of Hallstedt [85] and Neibecker [86]. The Al-Li phase diagram was firstly predicted using Cluster Variation Method (CVM) by Sigli and Sanchez

[87], but their results showed large differences for the concentration of δ′ phase when compared with experimental data. The Al-Li phase diagram was studied using first-principles calculation in 1990 by Sluiter et al. [88]. The computed solid solubility of Li in the Al-rich solid solution was larger than the experimental one, and the fcc-Li appears to be a stable phase in the phase diagram, which is contrary to the experimental evidence. The analysis by Liu et al. [89], based on first-principles calculations, indicated that δ′ was a stable phase due to the fact that the effect of lattice vibration on the free energy was neglected, leading to the large discrepancies in the two-phase boundaries on the Al-rich compared with the experimental data. From the above discussion, it is clear that a reliable model capable to describe the thermodynamic properties and phase diagram information of the Al-Li system is not available. Thus, it is necessary to carry out a new thermodynamic assessment for the Al-Li system to overcome this limitation.

1.5.2. Ni-Al system

The evolution of aircraft that fly further and faster has been a consistent goal of aircraft designers. Achieving this goal has required new materials with other attributes in addition to strength and light weight. In particular, engines that can operate at higher temperatures result in higher efficiency and reduced gas emissions because the combustion cycle is more complete [90].

Currently, Ni-based superalloys are used for the manufacture of high temperature components in gas turbines, such as combustor, high-pressure turbine, shrouds, blades, etc., due to their exceptional strength at high temperatures [91,92]. Alloys based on the Ni-Al system are of interest for different engineering applications. The extraordinary properties of Ni-based superalloys are associated with the microstructure with the $L1_2$-ordered γ′ (Ni_3Al) precipitates coherently embedded in fcc γ (Ni) matrix [93]. The volume fraction, morphology and size distribution of γ′ will change during long-term service at elevated temperatures, which can significantly affect the mechanical properties (such as strength, fatigue and creep) of Ni-Al-based superalloys [94-96].

The development of Ni-Al superalloys has been subject to some limitations, such as low ductility at the ambient temperature and low strength and creep resistance at elevated temperatures [97]. It has been reported that the high-melting-point refractory element additions, such as Nb, Re, Ru, W and Mo, are particularly effective in improving the creep resistance, alloy strength and service temperature [99-101]. Unfortunately, high levels of refractory elements Mo, W, and Re are prone to form deleterious topologically close-packed (TCP) phase due to their limited solubility in γ matrix, which is harmful to the failure of the alloys [102-104]. Addition of Cr to Ni_3Al superalloy stabilizes the γ and γ′ region and improves the ductility and corrosion resistance but decreases the strength [104]. These studies indicate that the high-temperature performance of Ni-Al-based alloy can be improved by alloying additions and heat treatments. Thus, it is essential to know the Ni-Al phase diagram for guiding the design and development of novel Ni-Al-based superalloys.

The Ni-Al phase diagram was studied firstly using CVM in 1985 by Sigli and Sanchez [105]. Even though the vibrational contribution to the free energy of pure elementary phases and stoichiometric compounds was taken into account, the calculated phase diagram was not in agreement with the experimental one. Pasturel et al. [106] studied the Ni-Al phase diagram using first-principles calculations, which showed a better agreement with the experimental one. However, the Al_3Ni_2 was considered as a line compound in their version, and both Al_4Ni_3 and Al_3Ni_5 were neglected. Actually, Al_3Ni_5 is a frequently detected phase which was considered as a stoichiometric phase with two different crystal structures [107], while some experiments show significant composition range for Al_3Ni_5 [109-111]. In addition, there is significant controversy in the two-phase region between AlNi and $AlNi_3$. Overall, there is currently insufficient thermodynamic information to describe the thermodynamic properties of all phases in the Ni-Al system. Therefore, a new thermodynamic evaluation of the Ni-Al system is necessary to eliminate the shortage of reliable thermodynamic databases for this system.

1.5.3. Co-Al system

Co-based superalloys have been in use for several decades in the manufacturing of various components such as vanes or combustion chambers in gas turbines [111]. Co-based superalloys have a higher melting temperature (about 1450°C) than Ni-based superalloy, leading to excellent strength at high temperature as well as creep resistance [112,113]. Moreover, Co-based superalloys exhibit superior corrosion resistance, wear resistance, and weldability compared with Ni-base superalloys [114,115]. However, the strength of Co-based superalloy relies only on solid solution strengthening and carbide dispersion strengthening, that are not as effective as the γ′-Ni_3Al precipitate strengthening in Ni-based superalloys, and this fact hinders their applications in components subjected to high stresses [116,117].

A γ′-$Co_3(Al,W)$ ordered phase similar to γ′-Ni_3Al was firstly discovered in Co-Al-W-based alloys by Sato et al. [118]. It has a high melting point and high-temperature mechanical properties, paving the way for the use of Co-based superalloy in the next generation of high-temperature structural materials [120-122]. Recently, Makineni et al. [122] found a Co-Al-(Mo, Nb)-based alloy that exhibits higher solvus temperature and better mechanical strength than the commercial Ni-based and the Co-Al-W-based superalloys. The Co-Al-V-based superalloy with a high γ' phase stability and a low density developed by Chen et al. [123] showed that the hot-corrosion/oxidation resistance may be deteriorated due to the elevated V-content. They also confirmed that the addition of Cr reduces the γ/γ' lattice misfit as well as the γ' coarsening rate in Co-Al-Ta-based superalloy [124]. Overall, the γ' derived from Co_3Al in Co-Al system by adding different alloying elements is considered as the critical phase for the development of the next generation of Co-Al-based superalloy.

Currently, all available Co-Al phase diagrams are determined through the Calphad method. Shevchenko et al. [125] studied the Co-Al phase diagram by the Gibbs free energy description based on the model of ideal associated solutions. Ostrowska et al. [126] also assessed the Co-Al phase diagram by the Calphad method. It should be noted that a metastable two-phase region between Co and CoAl has been experimentally confirmed by Kozakai et al. [127,128], but it was not included in the existing Co-Al phase diagram due to the limitation in the Calphad method, where the thermodynamic information of metastable phases is hardly to obtain due to the kinetic factors. Therefore, a thermodynamic evaluation of the Co-Al system is necessary to eliminate the shortage of reliable thermodynamic databases for this system, and this thermodynamic information can also be used to design new Co-Al-based ternary and multi-component systems.

1.6. **Objectives**

Many of the component chemistries used in new alloy designs are largely the product of trial and error. The complex interactions among various elements make it difficult to understand exactly how changes in an alloy chemical composition will ultimately affect its performance. Understanding how composition affects phase fractions, phase composition, lattice parameters, and structural stability requires a comprehensive thermodynamic foundation that does not currently exist for multi-component systems. Therefore, the knowledge of phase equilibria across the whole concentration range of a binary phase diagram is crucial for the extrapolation of material properties and thermodynamic modeling to multi-component systems.

The present thesis aims to provide a method to predict accurately the solid-state region of the Al-Li, Ni-Al and Co-Al phase diagrams from first-principles calculations combined with MC simulations. The thermodynamic information obtained from these binary alloys can be used in the future to generate a database to extrapolate to the thermodynamic properties for multi-component system. This thesis is structured as follows:

Chapter 1 briefly illustrated the role of phase diagrams in the design of new alloys. By elaborating on the shortcomings of experimental and Calphad methods, the necessity of first-principles calculation combined with MC simulation for predicting phase diagrams was introduced

Chapter 2 introduced the research methodology used in this thesis. The total energy of a configuration was obtained by first-principles calculation based on DFT, which can be used to construct the CE. The lattice vibrational contribution to free energy was studied by L-S relationship. The magnetic excitation contribution to free energy was calculated using the effective Heisenberg Hamiltonian. The Gibbs free energy of each ground state phase in the phase diagram was obtained by MC simulation.

Chapter 3 presents the prediction of the solid-state region of Al-Li phase diagram using first-principles calculations and statistical mechanics principles including the effect of configurational disorder and lattice vibration. The formation enthalpies of many configurations were determined using first-principles calculations and the vibrational free energy of each configuration was included using the L-S relationship. Temperature-dependent CEs were fitted considering the formation enthalpy and vibrational free energy of each configuration, and they were used to predict the free energies of the different phases. The whole Al-Li phase diagram was predicted from this information and compared with the currently established phase diagrams [129,130]. In addition, the effect of vibrational entropy was assessed by comparison with our previous predictions of the Al-Li phase diagram without this contribution [89].

The whole solid-state region of the Ni-Al phase diagram was accurately predicted in Chapter 4 from first-principles calculations and MC simulations. In addition to the configurational and vibrational entropy, it should be noted that the stable phases ($AlNi_3$ and Ni) in the Ni-rich part of the Ni-Al phase diagram are ferromagnetic and the contribution of magnetic enthalpy has to be taken into account [85,131]. The magnetic entropy contribution is normally much smaller than the configurational and vibrational ones [132,133] and is neglected. The computed phase diagram is compared with the currently accepted Calphad phase diagram and the contributions of vibrational entropy and magnetic effects to the overall stability and solubility of the different phases were analyzed independently.

The solid-state region of the Co-Al phase diagram is calculated in Chapter 5 from first-principles calculations and statistical mechanics principles. Configurational entropic contributions to the free energy were included through MC simulations using the CE formalism. The vibrational entropy of each phase was determined through the L-S relationship associated with the lattice. The magnetic contribution was also included through the Heisenberg Hamiltonian [64]. The computed phase diagram was compared with the currently accepted experimental phase diagram and the different contributions to the stability of different phases are analyzed independently. The potential of this strategy to predict phase diagrams of magnetic systems is clearly established.

Finally, the main conclusions of this thesis and the avenues for future work are briefly summarized in Chapter 6.

2. Methodology

2.1. First-principles calculations

First-principle calculations is a computational method used to solve the Schrödinger equation [134] for materials in many-particle systems. The physical and chemical properties of materials are investigated through the interaction between nucleus and electrons, and their basic motion laws in the framework of quantum mechanics. It includes two categories of ab initio calculations based on Hartree-Fork self-consistent field [135] and DFT [136].

2.1.1. Density functional theory

DFT is a method based on two fundamental theorems, which was proposed in 1964 by Hohenberg and Kohn for Thomas-Fermi model of inhomogeneous electron gas [137]. These theorems state that: 1) the ground-state energy in Schrödinger's equation is uniquely determined by the number density of particles [138], and 2) the electron density that minimizes the energy of the overall functional at the condition of constant number of particles.

Schrödinger equation can be solved by finding the charge density wave function with three spatial variables for each atom [139]. However, it is extremely difficult to solve the equation for a many-body system. The widely used DFT-based calculations represents the state-of-the-art solution of the multi-body Schrödinger equation, which contains several approximations as follows [140,141]:

1) Adiabatic or Born-Oppenheimer approximation [140]. The nuclei can be assumed to be ‘frozen’ because they are much heavier than the electrons and only contribute to an external potential for the electrons. The electrons and nuclei are always in an instantaneous ground state.

2) Independent-electron approximation [141]. Each electron moves independently with respective to the others in an average effective potential collectively determined by all of the electrons. The many-body electron problems are replaced using independent electrons with an exchange-correlation functional of the electron density and an associated exchange-correlation energy and potential by Hohenberg and Kohn [137].

3) Exchange-correlation functional approximation by the local spin density approximation (LSDA) [142] and the generalized gradient approximation (GGA) [143,144]. In the LSDA, the exchange-correlation energy density at each point in space is assumed to be the same as in a homogenous electron gas with the same electron density. Exchange and correlation energies for a homogenous electron gas are available based on the Ceperley-Alder [142] and Perdew-

Zunger [145] fittings. In the GGA, the exchange-correlation energy density depends additionally on the gradient of the electron density. The GGA is accomplished by a low-order expansion of the exchange-correlation energy of an electron gas. Numerous approaches have been developed for this low-order expansion including the widely used PW91 [143] and Perdew-Burke-Ernzerhof (PBE) [144] implementations.

4) Replacement of the strong Coulomb potential of the nucleus and the tightly bound core electrons by a pseudopotential. Pseudopotentials obtained from atomic calculations are not unique and can be tailored to simplify calculations such as the commonly used ultrasoft pseudopotentials and the projector augmented wave (PAW) method [146].

With above approximations, the DFT-based first-principles calculations solve a set of one-electron Schrödinger equations, within which, each one is given by Kohn-Sham equations [147]:

$$[-\frac{\hbar^2}{2m_e}\nabla^2-\frac{e^2}{4\pi\varepsilon_0}\sum_{I=1}^{N}\frac{z_I}{|\vec{r}-\overrightarrow{R_I}|}+\frac{e^2}{4\pi\varepsilon_0}\int\frac{\rho(\vec{r}\,')}{|\vec{r}-\vec{r}\,'|}d^3\vec{r}\,'+V_{XC}[\rho(\vec{r}\,')]]\psi_i(\vec{r}\,')=\varepsilon_i\psi_i(\vec{r}) \tag{2.1}$$

where ε_i is the ith one-electron energy eigenvalue with $\psi_i(\vec{r})$ being the ith one-electron wavefunction. e is the electron charge, and ε_0 vacuum permittivity. $-\frac{\hbar^2}{2m_c}\nabla^2$ represents the electronic kinetic energy with $\hbar = h/2\pi$ being the reduced Planck constant. m_e the electronic mass, ∇ can be defined as follow

$$\nabla^2=\sum_{\alpha=1}^{3}\partial^2/\partial x_\alpha^2 \tag{2.2}$$

where x_α is the Cartesian coordinates of the electron. $\frac{e^2}{4\pi\varepsilon_0}\sum_{I=1}^{N}\frac{z_I}{|\vec{r}-\overrightarrow{R_I}|}$ defines the interaction between an electron and all of atomic nuclei. $\frac{e^2}{4\pi\varepsilon_0}\int\frac{\rho(\vec{r}')}{|\vec{r}-\vec{r}\prime|}d^3\vec{r}'$ is called the Hartree potential, which refers to the Coulomb interaction between the electron and itself. $V_{XC}[\rho(\vec{r}')]$ represents the exchange to the one-electron equations. It can be expressed as functional derivative of exchange correlation energy:

$$V_{XC}[\rho(\vec{r}')]=\frac{\delta E_{XC}[\rho(\vec{r}')]}{\rho(\vec{r}')} \tag{2.3}$$

where $E_{XC}[\rho(\vec{r}')]$ is the exchange correlation energy with the electron density of $\rho(\vec{r}')$.

2.1.2. Quantum espresso package

Quantum Espresso [148,149] is a free and open-source software for electronic-structure calculations and materials modeling based on DFT, where plane waves (PWs) are used to express the electronic wave functions and pseudopotentials (PPs) are employed to describe the interaction between valence electrons and atomic cores [150]. The Quantum Espresso is written by C++ and Fortran. The codes are constructed for periodic boundary conditions, which can deal with infinite crystal system directly and treat an efficient convergence of the thermodynamic limit for aperiodic but extended systems, such as liquids or amorphous materials. The basic computations can be performed including the energies for isolated or extended/periodic systems, structural optimizations (atomic coordinates and cell shape), ground state of spin-polarized or magnetic systems, second and third derivatives of the total energy at any arbitrary wavelength, ab initio molecular dynamics of thermodynamic ensembles, determining of saddle points and transition states via transition-path optimization, calculation of nuclear magnetic resonance and electronic paramagnetic resonance parameters [151]. Other utilities for data post-processing and advanced graphic application are available.

2.2. Lattice vibrations

2.2.1. Quasi-harmonic approximation

At finite temperature, atoms tend to fluctuate around the equilibrium positions, resulting in lattice vibrations. For a classical vibrating system, a harmonic approximation means only vibrations with small amplitude were considered. The potential energy *E* of the system can be expressed by a Taylor expansion up to second order in the atomic displacements *u* from the equilibrium positions [152].

$$E = E_0 + \sum_i \frac{\partial E}{\partial u_i} u_i + \frac{1}{2} \sum_{i,j} u_i \frac{\partial^2 E}{\partial u_i \partial u_j} u_j \tag{2.4}$$

in which E_0 is the potential energy where all atoms within are at their equilibrium positions. u_i and u_j stand for the displacements of atoms *i* and j. As all atoms within are at their equilibrium positions, the first derivatives of *E* vanish because it corresponds to the forces acting on atoms. Thus, the second order term only matters for the vibrational properties. The second derivatives of *E* with respect to *u* are called the force constant matrices, $\Psi(i,j)$:

$$\Psi(i,j) = \frac{\partial^2 E}{\partial u_i \partial u_j} \tag{2.5}$$

It should be noted that a structure will generally expand at elevated temperatures. The harmonic approximation performed at constant volume from eq. (2.4) neglects the thermal expansion, which results in an overestimation of the energy. This limitation can be overcome by quasi-harmonic approximation [50,153] that contains the volume-dependent free energy contribution, in which each strained volume agrees the harmonic regime.

The dynamical matrix, $D_{i,j}(\mathrm{q})$ can be obtained by the Fourier transform of $\Psi(i,j)$ at wavevector q [50,154].

$$\mathrm{D}_{i,j}^{kk'}(\mathrm{q}) = \frac{1}{\sqrt{M_k M_{k'}}} \sum_{l'} \Psi_{i,j}(0k, l'k')\, e^{iq\cdot[\mathrm{r}(l'k') - r(0k)]} \tag{2.6}$$

where $r(l\kappa)$ is the equilibrium atomic position, M_κ is the atomic mass of type κ. Usually $D(\mathrm{q})$ is arranged to be a $3n_a \times 3n_a$ matrix, where 3 comes from the freedom of the Cartesian indices for crystal and n_a is the number of atoms in a unit cell.

The phonon frequencies $\omega(q)$ as a function of wavevector q are obtained from the eigenvalues of $D(\mathrm{q})$ [50,154,155] according to:

$$det\left|\frac{1}{\sqrt{M_k M_{k'}}} D_{i,j}^{kk'}(\mathrm{q}) - \omega^2(q)\right| = 0 \tag{2.7}$$

The phonon density of states (DOS), $g(\omega)$, is obtained by an integration over the first Brillouin zone Ω of the crystal structure:

$$g(\omega) = \frac{1}{\Omega}\int_\Omega dq\delta(\omega - \omega(q)) \tag{2.8}$$

The supercell method [156] is one of the techniques most widely used to calculate the force constant tensor. In this method, supercells are constructed from the fully relaxed primitive unit cell containing perturbations of atomic displacement under symmetry constraints. By relating the atomic displacements to the resulted interatomic forces obtained using first-principles calculations, a set of equations (eq. (2.4)) is generated. The solutions of this set of equations are the force constants, the eigenvalues of the corresponding dynamical matrix correspond to the normal modes of oscillation (phonons) of the structure, that is phonon frequency. By sampling a great number of *k*-points within the irreducible Brillouin zone, the phonon DOS can be obtained by eq. (2.8). For the actual implementation of the supercell method, the force constants were obtained using the Phonopy code [50].

2.2.2. **Vibrational free energy**

In the quasi-harmonic approximation, the vibrational entropic contribution to the free energy is determined by Born-von Karman model according to [157]:

$$F_{vib}(V,T) = -TS_{vib}(V,T) \tag{2.9}$$

where T is the absolute temperature. $S_{vib}(V,T)$ is the vibrational entropy at the given temperature and volume that expressed as [55]

$$S_{vib}(V,T) = -k_B \int \frac{g(\omega)}{1-\vartheta} [\vartheta \log(\vartheta) + (1-\vartheta)\log(\vartheta)]\, \mathrm{d}\omega \tag{2.10}$$

where $\hbar$ is the reduced Planck's constant, k_B the Boltzmann constant, $\vartheta = \mathrm{e}^{-\frac{\hbar\omega}{k_B T}}$ and $g(\omega)$ is calculated from eq. (2.8).

2.2.3. **Bond length vs. bond stiffness**

The contribution of the lattice vibration to the free energy can be described by using L-S relationship. This calculation method has the advantage of reducing the computational burden of calculating phonon DOS for each supercell configuration that is used to fit the CE.

The L-S relationship can be determined as follows. Several different configurations in each lattice (since these relationships are transferable in configurations within the same lattice) were expanded up to 10% in volume with an increment of 2% after full relaxation to generate different atomic bond lengths using Alloy Theoretic Automated Toolkit (ATAT) code [158]. Supercells of the expanded configurations were constructed, and a displacement of 0.1 Å was applied to each symmetrically distinguished atom within. Then, self-consistent calculations were performed to obtain the forces acted on each atom due to the displacements.

Three assumptions are made to obtain the desired transferable properties in the L-S relationship [159,160]. Only the nearest neighbor interactions are considered because the longer ranged force constants do not exhibit good transferability. The bending stiffnesses b are averaged over various spatial directions, and off-diagonal terms in the bond stiffness tensor are constrained to be zero. Hence, the resulting force constant matrix Ψ between pairs of symmetrically different atoms has only two independent terms, namely the stretching stiffness s and the isotropic bending stiffness b:

$$\Psi(\mathrm{i},\mathrm{j}) = \begin{pmatrix} b & 0 & 0 \\ 0 & b & 0 \\ 0 & 0 & s \end{pmatrix} \tag{2.11}$$

A L-S relationship was fitted for each chemical bond from the stiffness values obtained for the same chemical bonds with different length. The phonon DOS of any configuration can be easily obtained from the L-S relationship fitted for a given lattice, instead of using expensive supercell calculations for each configuration. Finally, the vibrational free energies of all configurations generated using ATAT code [158] that kept the original symmetry can be calculated from eqs. (2.9) and (2.10).

2.3. **Magnetic excitation**

2.3.1. **Heisenberg Hamiltonian**

An effective Heisenberg Hamiltonian is firstly obtained to capture the magnetic free energy contribution of a given configuration with localized magnetic moments in the magnetic system. This is achieved by mapping the enthalpy at 0 K onto the following relationship [161,162]:

$$H_{mag} = -\sum_{ij}(N_{nn}^{\uparrow\uparrow} - N_{nn}^{\uparrow\downarrow})J_{ij}S_iS_j \tag{2.12}$$

where $H_{mag} = E_{FM} - E_{AFM}$, E_{FM} and E_{AFM} are total energy of one configuration with ferromagnetic (FM) and antiferromagnetic (AFM) behavior, respectively. $N_{nn}^{\uparrow\uparrow}$ and $N_{nn}^{\uparrow\downarrow}$ denote the number of the nearest-neighbor atomic pairs with parallel and antiparallel spins aligned with respect to each other. The unit vectors S_i and S_j are the operators for the spin angular momentum of atoms i and j. J_{ij} is the coupling constant between atom i and j. $J_{ij} > 0$ for FM interactions and $J_{ij} < 0$ for AFM interactions. At elevated temperature, the spins may flip while the coupling constants remain constant.

The Heisenberg Hamiltonian can be combined with MC simulations to obtain the magnetic free energy F_{mag} and magnetic entropy $S_{mag}(T)$ at elevated temperature:

$$F_{mag}(T) = -TS_{mag}(T) \tag{2.13}$$

$$S_{mag}(T) = \int_0^T \frac{C_{mag}}{T} dT \tag{2.14}$$

where C_{mag} stands for the magnetic specific heat, which was obtained from the averaging stage according to [163]:

$$C_{mag} = \frac{|\langle E^2\rangle - \langle E\rangle^2|}{k_B T^2} \tag{2.15}$$

where E is the average magnetic exchange energy that can be expressed as

$$\langle E \rangle = \frac{1}{N} \sum_i H_{mag}^i \tag{2.16}$$

and H_{mag}^i stands for the magnetic enthalpy contribution of each possible spin microstate i, as given by eq. (2.12). The Curie temperature T_C can be determined by the peak of magnetic specific heat C_{mag} as a function of temperature [68].

2.3.2. **VAMPIRE package**

VAMPIRE [164] is an open source atomistic spin simulation package. The code was created by the University of York and is designed to be accessible without requiring in-depth technical or programming knowledge. VAMPIRE is a state-of-the-art atomistic simulator for magnetic nanomaterials, capable of simulating many different systems and determining parameters such as coercivity [165], Curie point [166], inversion dynamics [167], statistical behavior, and more.

The features of VAMPIRE are split into three main categories: material parameters, structural parameters, and simulation parameters. Material parameters essentially define the magnetic properties of a class of atoms, including magnetic moments, exchange interactions, damping constants etc. Structural parameters define properties such as the system size, shape, particle size, or Voronoi grain structures. Combined with the material parameters, they essentially define the system to be simulated. VAMPIRE includes a number of built-in simulations for determining the most common magnetic properties of a system, such as Curie temperature T_C and hysteresis loops.

2.4. **Cluster expansion approach**

2.4.1. **Parent crystal structure**

Enumerating configurations using the ATAT code requires the specification of parent crystal structure [168]. The parent crystal structure serves as the reference to which chemical and structural perturbations are applied. Usually the parent crystal structure is a high symmetry phase, making it possible to study group/subgroup symmetry breaking ordering and structural transitions. Taking fcc Al-Li system as an example, its input format is shown in Table 2.1. A crystal is determined by a unit cell and a collection of basis sites. The unit cell vectors, $\vec{l}_1$, $\vec{l}_2$ and $\vec{l}_3$ determine a lattice. The basis sites have coordinates $\vec{b}_1$, $\vec{b}_2$, … and represents a motif within the unit cell that is translated to all the lattice sites to generate the full crystal. A site *i* in the full crystal with coordinates $\vec{r}_i = \vec{n}_1\vec{l}_1 + \vec{n}_2\vec{l}_2 + \vec{n}_3\vec{l}_3 + \vec{b}_N$, is completely specified by the integer vectors $\vec{n}_1$, $\vec{n}_2$ and $\vec{n}_3$, which determine the lattice site, and N, which is an index that specifies the basis site. A typical example is the B_2 crystal structure, which is a simple chemical ordering over the sites of a body-centered cubic (bcc) parent crystal structure. Similarly, the common $L1_2$ crystal structure correspond to periodic orderings of two chemical species over the sites of a fcc parent crystal structure.

Table 2.1: Input file lat.in of parent crystal structure used in the fcc Al-Li

Parent crystal structure (lat.in)	Explanation
0 2.00781403 2.00781403 2.00781403 0 2.00781403 2.00781403 2.00781403 0	unit cell vectors $\vec{l}_1$, $\vec{l}_2$ and $\vec{l}_3$
1 0 0 0 1 0 0 0 1	Lattice vector $\vec{n}_1$, $\vec{n}_2$ and $\vec{n}_3$
0 0 0 Al, Li	Basis sites $\vec{b}$

2.4.2. **Mixing enthalpy**

The mixing enthalpy H_{conf} at 0 K due to the atomic occupation of an $A_{1-x}B_x$ configuration in a given lattice s is given by [169]

$$H_{conf}^{A_{1-x}B_x} = E_s^{A_{1-x}B_x} - (1-x)E_s^A - xE_s^B \tag{2.17}$$

where $E_s^{A_{1-x}B_x}$, E_s^A and E_s^B stand for the energy of the relaxed $A_{1-x}B_x$, A and B in the corresponding lattice s.

Lattice vibrations will contribute to the free energy at elevated temperature, changing the relative stability of each configuration with respect to that at 0 K. The mixing enthalpy contribution due to lattice vibrations in each configuration is given by:

$$H_{vib}^{A_{1-x}B_x}(T) = F_{vib,s}^{A_{1-x}B_x}(T) - (1-x)F_{vib,s}^A(T) - xF_{vib,s}^B(T) \tag{2.18}$$

where $F_{vib,s}^{A_{1-x}B_x}(T)$, $F_{vib,s}^A(T)$ and $F_{vib,s}^B(T)$ stand for the vibrational free energy of $A_{1-x}B_x$, A and B in the corresponding lattice s at temperature T.

Similarly, the mixing enthalpy contribution due to magnetic excitation is given by:

$$H_{mag}^{A_{1-x}B_x}(T) = F_{mag,s}^{A_{1-x}B_x}(T) - (1-x)F_{mag,s}^{A}(T) - xF_{mag,s}^{B}(T) \tag{2.19}$$

where $F_{mag,s}^{A_{1-x}B_x}(T)$, $F_{mag,s}^{A}(T)$ and $F_{mag,s}^{B}(\mathrm{T})$ stand for the magnetic free energy of $A_{1-x}B_x$, A and B in the corresponding lattice s at temperature T.

Therefore, the temperature-dependent mixing enthalpy H_{mix} - including the configurational and vibrational contributions - of an $A_{1-x}B_x$ configuration in each lattice can be summarized from eqs. (2.17) and (2.18) as

$$H_{mix}^{A_{1-x}B_x}(T) = H_{conf}^{A_{1-x}B_x} + H_{vib}^{A_{1-x}B_x}(T) \tag{2.20}$$

while that including the configurational, vibrational, and magnetic contribution can be expressed from eqs. (2.17)-(2.19) as

$$H_{mix}^{A_{1-x}B_x}(T) = H_{conf}^{A_{1-x}B_x} + H_{vib}^{A_{1-x}B_x}(T) + H_{mag}^{A_{1-x}B_x}(T) \tag{2.21}$$

2.4.3. **Cluster expansion**

CE [38-40] including the different contributions for each lattice can be fitted from the mixing enthalpies. The CE only including the configurational contribution is expressed as

$$E = \sum_{\alpha} m_{\alpha} J_{\alpha} \langle \varphi_{\alpha}(\vec{\sigma}) \rangle \tag{2.22}$$

where $\vec{\sigma} = \{\sigma_1, \sigma_2, \dots, \sigma_N\}$ is the vector of occupation variables that indicates which type of atom locates on lattice site i. σ_i = -1 when site i accommodates an A atom and σ_i = +1 when the site *i* accommodates a B atom. m_{α} are multiplicities indicating the number of clusters equivalent to α by symmetry. The coefficients J_{α} are called effective cluster interaction (ECI) with cluster α whose values are determined by the specific chemical properties of the alloy. The sum is over all possible clusters α that are mutually symmetrically distinct under the space group of the underlying lattice. The average $\langle \dots \rangle$ is over all clusters α' that are equivalent by symmetry to cluster α. $\varphi_{\alpha}(\vec{\sigma})$ is the cluster function. Any function of the discrete occupation variables σ can be expanded in polynomials called cluster functions $\varphi_{\alpha}(\vec{\sigma})$. In a binary A-B alloy, the $\varphi_{\alpha}(\vec{\sigma})$ is simply defined as the product of occupation variable σ_i which form a cluster α,

$$\varphi_{\alpha}(\vec{\sigma}) = \prod_{i \epsilon \alpha} \sigma_i \tag{2.23}$$

The φ_α of eq. (2.23) can be shown to form a complete basis for any scalar function of the configuration, $(\vec{\sigma})$, of the crystal. For a binary alloy on a parent crystal structure with N sites, there are exactly 2^N configurations $\vec{\sigma}$, and there are an equal number of φ_α, one for each distinct cluster of sites within the crystal. While the cluster expansion, Eq. (2.22), extends over all 2^N clusters, in practice it must be truncated beyond some maximally sized cluster. The expansion coefficients of a truncated CE can then be trained to a large data set of energies for different configurations as calculated with a first-principles electronic structure method.

A CE formalism including both the configurational and vibrational contribution can be expressed as

$$H_{mix}(\vec{\sigma},T) = \sum_{\alpha} m_\alpha \langle \varphi(\vec{\sigma}) \rangle_\alpha (J_\alpha + J_\alpha^{vib}(T)) \tag{2.24}$$

where $J_\alpha^{vib}(T)$ are the ECIs due to vibrational effect at temperature T where the same clusters included in eq. (2.23) are used. Similarly, a CE formalism including the configurational, vibrational, and magnetic contributions is expressed as

$$H_{mix}(\vec{\sigma},T) = \sum_{\alpha} m_\alpha \langle \varphi(\vec{\sigma}) \rangle_\alpha (J_\alpha + J_\alpha^{vib}(T) + J_\alpha^{mag}(T) \tag{2.25}$$

where $J_\alpha^{mag}(T)$ are the ECIs due to magnetic effect at temperature T and the same clusters included in eq. (2.23) are used.

The ECIs were fitted from the mixing enthalpy by the least square method. The accuracy of the CEs was assessed by cross-validation score as well as by the accurate prediction of the mixing enthalpies of ground state configurations. Focused on a CE for mixing enthalpies, the cross validation (CV) is expressed as the root mean square of differences between those calculated from first-principles and the energies predicted from the CE [170,171],

$$\mathrm{CV} = \frac{1}{n} \sum_{i=1}^{n} \left(E_i - \hat{E}_i\right)^2 \tag{2.26}$$

where E_i is the calculated energy of configuration i by DFT calculation, while $\hat{E}_i$ is the predicted energy of configuration *i* obtained from a least-squares fit to the (n-1) other structural energies.

2.5. Monte Carlo simulations

Once the CE for an alloy system has been obtained, MC simulations on a lattice model can be used to efficiently calculate thermodynamic properties [172,173]. MC simulations readily provide thermodynamic quantities such as energy and composition by averaging over a huge number of ensemble of microscopic states using the Metropolis MC algorithm [174].

A very convenient way to obtain thermodynamic information regarding an alloy system is to perform MC simulations which sample a semi-grand-canonical ensemble [175]. In this ensemble, the energy and concentration of an alloy with a fixed total number of atoms (N) are allowed to fluctuate while temperature and chemical potentials are externally imposed. For an A-B alloy, only the composition x of element A and the difference in chemical potential ($\Delta\mu = \mu_A - \mu_B$) between the two species needs to be specified.

The grand potential $\emptyset$ of the system can then be summarized in a partition function of the form [176]

$$\beta\emptyset(\beta, \Delta\mu) = -\ln Z \tag{2.27}$$

where $\beta = \frac{1}{k_B T}$, is the reciprocal of the temperature T and k_B is Boltzmann's constant. Z is partition function and can be expressed as [172]

$$Z = \sum_{\mathrm{i}} \exp\left(-\beta N\left(\langle H_f^i\rangle - \Delta\mu x\right)\right) \tag{2.28}$$

where $\langle H_f^i\rangle$ is the average formation enthalpy of each microstate i, which can be parametrized in a compact form with the help of the CE. N is the number of sites in the crystal lattice.

From eqs. (2.27) and (2.28), the derivative of the grand potential for each phase can be written as:

$$\mathrm{d}(\beta\emptyset) = N\left(\langle H_f\rangle - \Delta\mu x\right)\mathrm{d}\beta - N\beta x \,\mathrm{d}(\Delta\mu) \tag{2.29}$$

where $\langle H_f\rangle$ stands for the average formation enthalpy.

For a given $\Delta\mu$, $\emptyset$ can be calculated as [172]:

$$\emptyset(\beta_1, \Delta\mu) = \emptyset(\beta_0, \Delta\mu) + \frac{N}{\beta}\int_{\beta_0}^{\beta_1}(\mathrm{H_f} - \Delta\mathrm{\mu x})\,\mathrm{d}\beta \tag{2.30}$$

and for a given β, $\emptyset$ can be calculated as:

$$\emptyset(\beta, \Delta\mu_1) = \emptyset(\beta, \Delta\mu_0) - N\int_{\Delta\mu_0}^{\Delta\mu_1} x \,\mathrm{d}\Delta\mu \tag{2.31}$$

where the integral is performed along a continuous path joining points (β_0, $\Delta\mu_0$) and (β_1, $\Delta\mu_1$) that does not encounter a phase transition.

The difference between Gibbs and Helmholtz free energies can be neglected during solid-state transformations, so the Gibbs free energy G is expressed as [178]

$$G = \emptyset + \Delta\mu x \tag{2.32}$$

The two-phase boundary between phases that share the same lattice can be determined by the intersection of $\emptyset$ obtained from increasing and decreasing $\Delta\mu$. For two adjacent phases with different lattice structures, the two-phase equilibrium region in the phase diagram can be determined by the common tangent of their Gibbs free energies curves at a given temperature.

3. Prediction of the Al-Li phase diagram

3.1. Introduction

The strength/weight ratio was the prime driver for materials selection for both engines and aircraft [73,179]. Al-Li alloys have gained attention for their use in weight and stiffness-critical structures used in aircraft, aerospace and military applications because they exhibit better properties, such as a low density and high specific strength, than those of commercial Al alloys [77,79,180].

The main strengthening in Al-Li alloys is generally achieved from the existence of a huge volume fraction of the Al_3Li (δ') phase [77,181,182], which is the main reason for high elastic modulus observed in these alloys, since Al_3Li itself has a large intrinsic modulus. δ' precipitates are considered metastable [183]. This conclusion does not come from free energy calculations, but from experimental observations: the equilibrium δ (AlLi) phase precipitates at grain boundaries and its growth depends on the coarsening and eventual disappearance of δ' precipitates [183,184]. This process leads to the apparition of a precipitate-free zone, devoid of δ' precipitates, adjacent to the grain boundaries. It was initially assumed that δ formation was due to a martensitic transformation from δ', but this hypothesis was not in agreement with transmission electron microscopy observations which showed evidence of the heterogeneous nucleation of δ precipitates at grain boundaries and dislocations, independent of δ' [185]. Nevertheless, the growth of the δ precipitates was carried out at the expense of the Li in solid solution and in the δ' precipitates. This latter mechanism assumes that δ' is metastable, but this result should be confirmed by free energy data.

In this chapter, the Al-Li phase diagram is predicted by first-principles calculations and statistical mechanics principles including the effect of vibrational entropy. To this end, the L-S relationships of nearest-neighbor bonds in the Al-Li system were obtained from several ordered configurations, and the accuracy of this approach to calculate the phonon density of states was proven by comparison with the full phonon calculations. Then, the formation enthalpies of many configurations were determined using first-principles calculations and the vibrational free energy of each configuration was included using the L-S relationship. Temperature-dependent CEs were fitted by taking into account the formation enthalpy and vibrational free energy of each configuration, and they were used to predict the free energies of the different phases. The whole Al-Li phase diagram was predicted from this information and compared with the currently established phase diagram [129,130]. In addition, the effect of vibrational entropy was assessed by comparison with our previous predictions of the Al-Li phase diagram without this contribution [89].

3.2. **Methodology**

3.2.1. **DFT calculations**

The first step to calculate the Al-Li diagram is to determine the ground state phases at 0 K from the formation energies of the different Al-Li intermetallic compounds. Al and Li exhibit fcc and bcc structures, respectively, in the stable configurations. Thus, symmetrically distinct fcc and bcc $Al_{1-x}Li_x$ configurations with Al and Li atoms randomly placed in fcc and bcc lattice sites were generated with up to 8 atoms per unit cell using ATAT code [158].

The relaxed energy of each $Al_{1-x}Li_x$ configuration was calculated by DFT using Quantum Espresso [148,149] in the ultra-soft pseudopotential mode [186]. The atomic positions, lattice parameters and angles of each configuration were fully relaxed at pressure P=0. The exchange correlation energy was evaluated using the PBE approach [144] with 114 Ry as the energy cut-off. The Brillouin zone was sampled using a Monkhorst-Pack grid with a density of 40 points/$Å^{-1}$.

3.2.2. **Vibrational free energy calculation**

The L-S relationship is related to the lattice symmetry [159] and only fcc and bcc lattices need to be considered because all phases in the Al-Li system are either fcc or bcc. All configurations were relaxed by DFT calculation in section 3.2.1, four ordered configurations were used to determine the L-S relationship for the fcc lattice and only three for the bcc lattice. They were compressed and expanded up to 10% with increment of 2.5% in volume to create cells with different bond lengths. For each volume, a supercell of 3×3×3 unit cell was used and a displacement of 0.2 Å was applied for each symmetrically different atom in the unit cell to calculate the force acted on each atom because small atomic displacement. Therefore, a L-S relationship for each type of bonding interaction (either Al-Al, Li- Li or Al-Li) was fitted from the values b and s obtained for each lattice, which can be used to obtain the force constant matrices of all configurations enumerated by ATAT code.

Following the quasi-harmonic approximation, the vibrational free energy of a configuration is determined by Born-von Karman model according to [156]

$$F_{vib}(V,T) = E(V) - TS_{vib}(V,T) \tag{3.1}$$

where $E(V)$ is the volume-dependent energy of the configuration, T the absolute temperature and $S_{vib}(V,T)$ the vibrational entropy. $E(V)$ and $S_{vib}(V,T)$ at a given volume can be expressed as [187,188]

$$E(V) = \int \hbar\omega \, g(\omega) \left[\frac{1}{2} + \frac{\vartheta}{1+\vartheta}\right] d\omega \tag{3.2}$$

$$S_{vib}(V,T) = -k_B \int \frac{g(\omega)}{1-\vartheta} [\vartheta log(\vartheta) + (1-\vartheta) log(\vartheta)] \, d\omega \tag{3.3}$$

3.2.3. **Cluster expansion**

The temperature-dependent mixing enthalpy H^{mix} of a configuration with composition $Al_{1-x}Li_x$ - including the vibrational entropy contribution - can be expressed as [189]

$$H^{mix}_{Al_{1-x}Li_x}(T) = F_{vib}^{Al_{1-x}Li_x}(T) - (1-x)F^{Al}_{vib,s}(T) - xF^{Li}_{vib,s}(T) \tag{3.4}$$

where $F^{Al}_{vib,s}(T)$ and $F^{Li}_{vib,s}(T)$ stand for the vibrational free energy of pure Al and Li in the corresponding lattice at temperature T. It should be noted that the mixing enthalpy given by eq. (3.4) will be used to fit the CE but it does not correspond to the actual formation enthalpy, H^f, that is expressed as

$$H^{f}_{Al_{1-x}Li_x}(T) = F_{vib}^{Al_{1-x}Li_x}(T) - (1-x)F^{Al}_{vib}(T) - xF^{Li}_{vib}(T) \tag{3.5}$$

where $F^{Al}_{vib}(T)$ and $F^{Li}_{vib}(T)$ stand for vibrational free energy of pure Al and Li in their equilibrium structure, namely fcc Al and bcc Li.

The temperature-dependent CE formalisms for the fcc and bcc lattices can be fitted from the temperature-dependent mixing enthalpies of the configurations in fcc and bcc lattices by eq. (2.24), respectively. The number of clusters and the ECI coefficients for them were fitted using the ATAT package [158]. The lattice distortion of each configuration after relaxation was determined to assess whether the lattice symmetry changed. Following the criteria reported in the literature [190], only configurations whose distortion was below 10% were considered to keep the original lattice symmetry and used to fit the CE for each lattice.

3.2.4. **Monte Carlo simulations**

The semi-grand canonical MC simulations [191] of fcc and bcc Al-Li systems were carried out using ATAT package in periodic supercells of dimensions 20×20×20 primitive unit cells. The temperature range varied from 10 K to 1000 K with a temperature increment of 10 K for each chemical potential. At each temperature, MC simulations were carried out from the ground state phases with increasing and decreasing $\Delta\mu$ with an increment of 0.005 eV/atom in the chemical potential, where $\Delta\mu$ represents the difference in chemical potential between the Al and Li. For each value of T and $\Delta\mu$, a MC simulation included 2000 passes for equilibrium, followed by 5000 passes for calculating the thermodynamic averages. The grand potential and Gibbs free energy of each phase can be calculated from eqs. (2.30)-(2.32).

For two adjacent phases with the same lattice structure, the two-phase equilibrium region in the phase diagram can be determined by the intersection of $\emptyset$ obtained from increasing and decreasing $\Delta\mu$. For two adjacent phases with different lattice structures, the two-phase equilibrium region in the phase diagram can be determined by the common tangent of their Gibbs free energies curves at a given temperature.

3.3. **Results**

3.3.1. **Bond length *vs.* bond stiffness relationship**

There are three types of chemical bonds between different atomic species in Al-Li alloys, namely Al-Al, Li-Li and Al-Li bonds. Their L-S relationships in the fcc lattice were obtained from the ordered Al, Al_3Li, AlLi and Li compounds, whose structures are shown in Figure 3.1. Their space groups are FM-3M, PM-3M, R-3M and FM-3M, respectively. The first-nearest neighbor bonds in fcc Al and fcc Li (Figures. 3.1(a) and (d)) are Al-Al and Li-Li and their equilibrium bond lengths are 2.837 Å and 3.05 Å, respectively. The first-nearest neighbor bonds in fcc Al_3Li (Figure 3.1(b)) are Al-Al and Al-Li with the same equilibrium bond length of 2.828 Å. Finally, the first-nearest neighbor bonds in fcc AlLi (Figure 3.1(c)) are Al-Al (2.820 Å), Li-Li (2.820 Å) and Al-Li (2.839 Å). They were also used to fit the L-S relationships to ensure that they are transferable.

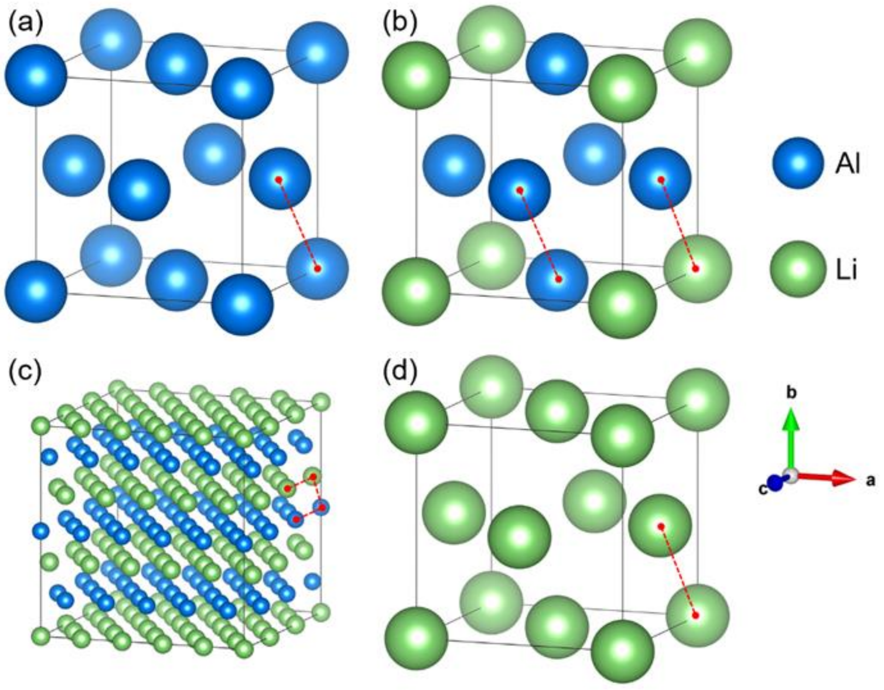

Figure 3.1: Crystal structures of ordered Al-Li configurations with fcc lattice. (a) Al. (b) Al_3Li.(c) AlLi. (d) Li. The first nearest-neighbor bonds are indicated with red lines.

The force constant matrix of the three types of bonds in the ordered fcc Al-Li configurations with different volumes were determined from full phonon calculations and the corresponding L-S relationships. The stretching and bending stiffnesses of each bond are depicted in Figure 3.2. The stretching stiffness decreases dramatically with bond length in the three bonds, while the bending stiffness increases slightly. The stretching and bending stiffness terms for the three types of bonds (Al-Al, Al-Li and Li-Li) are very close, regardless of the ordered configuration, and this result indicates that the force constant matrix is transferable for different configurations with the same lattice. The L-S relationships of stretching and bending stiffness for each type of bond were fitted by quadratic polynomials using the least-squares method and they are plotted as solid lines in Figure 3.2. They can be used to predict the force constant matrix of configurations with many atoms arranged in a fcc lattice.

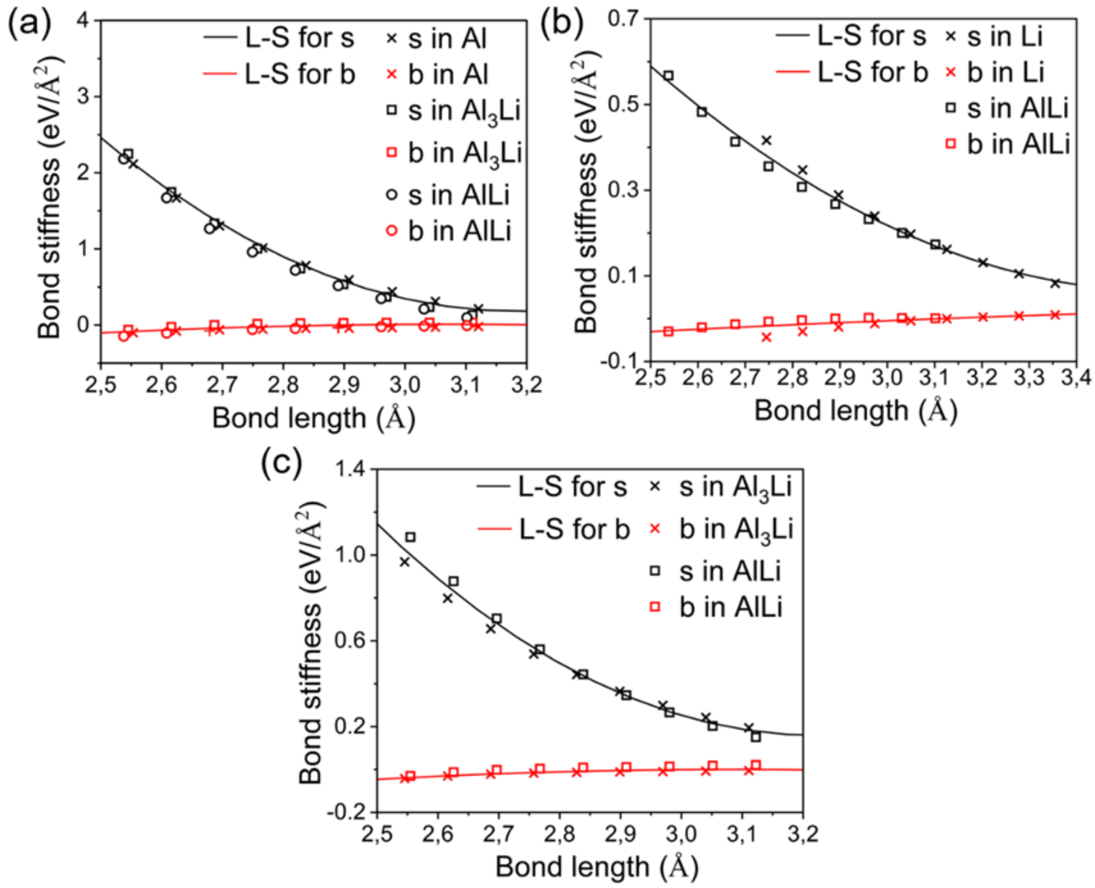

Figure 3.2: Bond stiffness vs. bond length relationships fitted from ordered fcc Al-Li configurations. The symbols stand for the results obtained from full phonon calculations according to eq. (2.11). The solid lines are the fitted polynomials. (a) Al-Al bond. (b) Li-Li bond. (c) Al-Li bond. s stands for the stretching stiffness and b for the bending stiffness.

The Al, AlLi and Li ordered configurations, whose structures are displayed in Figure 3.3, were used to determine the L-S relationships in the bcc lattice. Their space groups are IM-3M, FD-3M and IM-3M, respectively. The first-nearest neighbor bonds in bcc Al and Li are Al-Al and Li-Li (Figures. 3.3(a) and (c)) and their equilibrium bond lengths are 2.778 Å and 2.968 Å, respectively. The first-nearest neighbor bonds in bcc AlLi (Figure 3.3(b)) are Al-Al, Al-Li and Li-Li with the same equilibrium bond length of 2.736 Å in all cases.

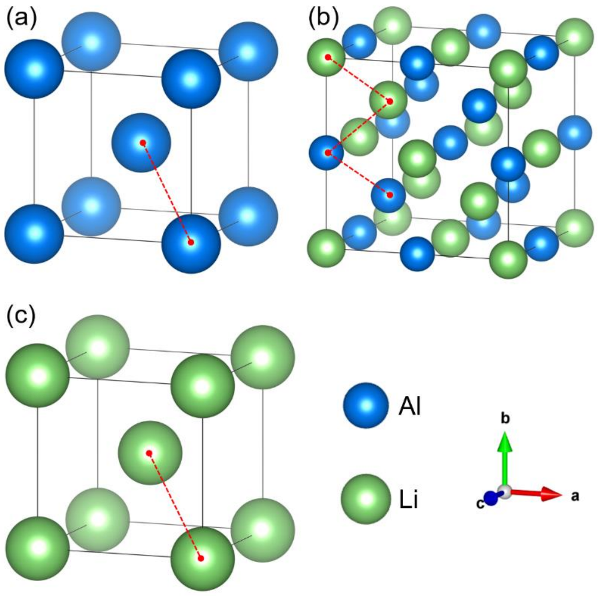

Figure 3.3: Crystal structure of ordered Al-Li configurations with bcc lattice. (a) Al. (b) AlLi. (c) Li. The first nearest-neighbor bonds are indicated with red lines.

The force constant matrix of the three types of bonds in the ordered bcc Al-Li configurations with different volumes were determined from full phonon calculations. The corresponding L-S relationships are depicted in Figure 3.4. The stretching and bending stiffnesses in the three bonds follow the same trends found previously in the fcc ordered configurations (Figure 3.2). The L-S relationships of stretching and bending stiffness for each type of bond were fitted into quadratic polynomials using the least-squares method and they are plotted as solid lines in Figure 3.4. They were used to predict the force constant matrix of configurations with the bcc lattice.

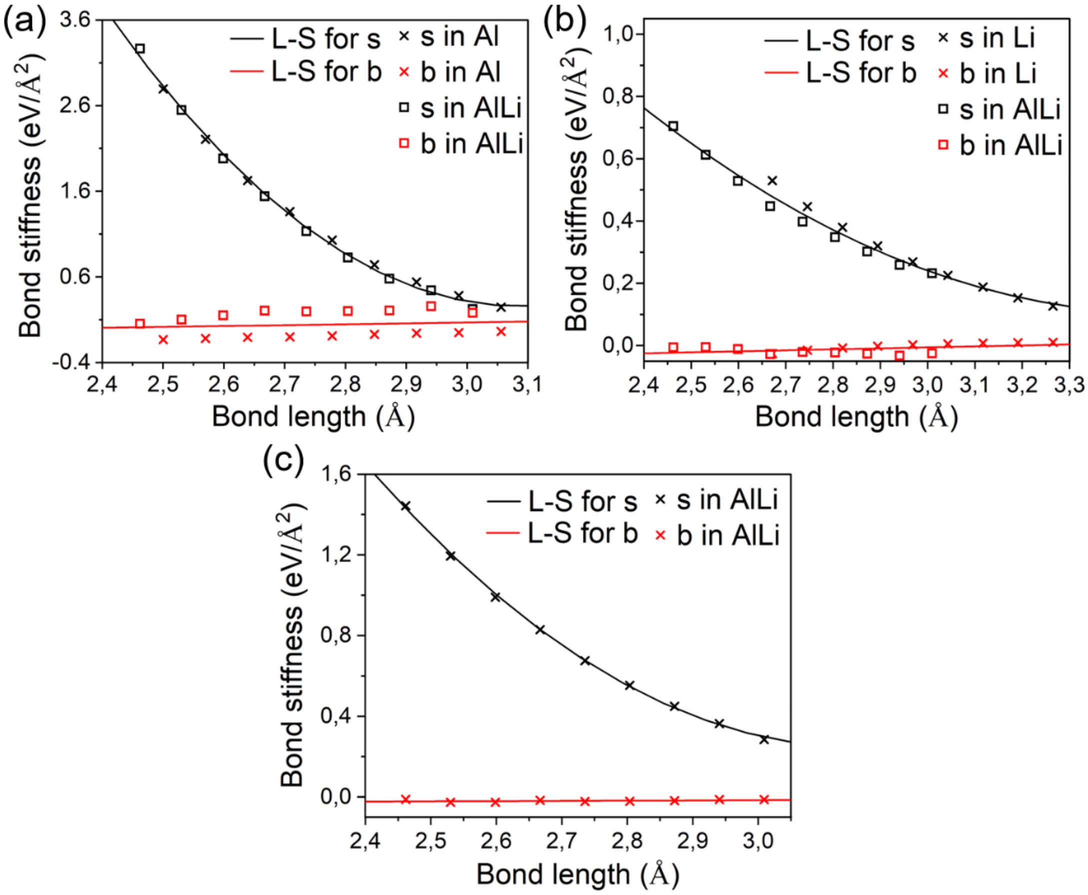

Figure 3.4: Bond stiffness vs. bond length relationships fitted from ordered bcc Al-Li configurations. The symbols stand for the results obtained from full phonon calculations according to eq. (2.11). The solid lines are the fitted polynomials. (a) Al-Al bond. (b) Li-Li bond. (c) Al-Li bond. s stands for the stretching stiffness and b for the bending stiffness.

3.3.2. **Vibrational free energy**

The accuracy of the L-S relationship to obtain the phonon DOS and the vibrational entropy contribution to the Gibbs free energy can be assessed by comparison with the results obtained from full phonon calculations for the most relevant phases in the Al-Li system. The vibrational free energies, F_{vib}, of Al, Al_3Li, AlLi, Al_2Li_3, Al_4Li_9 and Li calculated using both approaches are plotted as a function of temperature in Figures. 2.5(a) to 2.5(f), and the corresponding phonon DOS are inserted in each Figure. The red curves stand for the results obtained from full phonon calculations while the black curves indicate the vibrational free energy and phonon DOS predicted with the L-S relationships. The phonon DOS predicted with the L-S relationships are consistent with those obtained from full phonon calculations for all the different intermetallic compounds with fcc and bcc lattices. As a result, the vibrational entropic contribution - that is obtained by the integration of the phonon DOS through eq. (2.8) - obtained with the L-S relationships is very close to the actual one determined from the full phonon calculations. The small differences are similar for all phases and are not significant from the viewpoint of accuracy in the formation enthalpy.

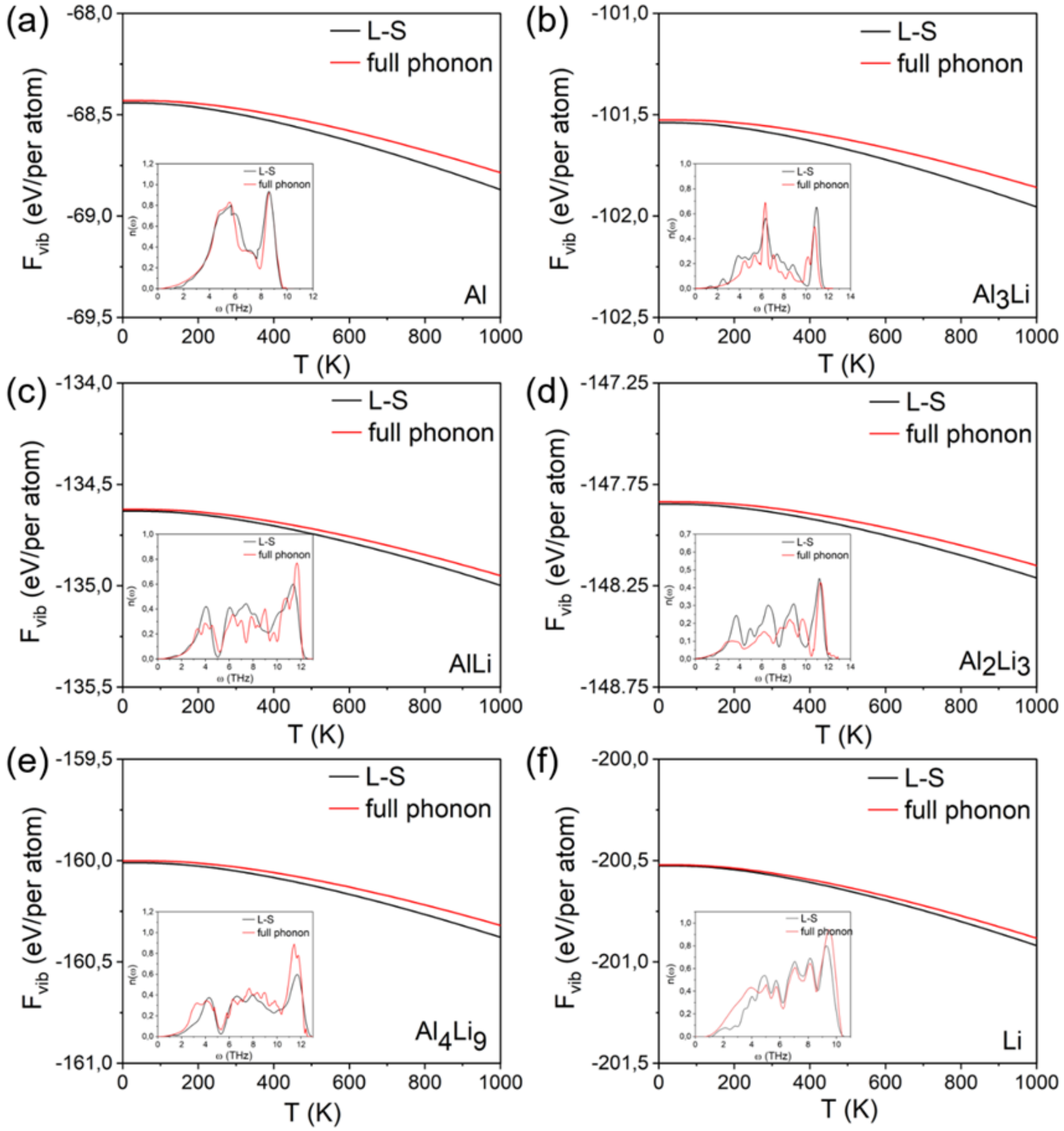

Figure 3.5: Vibrational free energy of phases in Al-Li system determined by full phonon calculations and predicted with the L-S relationships. (a) Al. (b) Al_3Li. (c) AlLi. (d) Al_2Li_3. (e) Al_4Li_9. (f) Li.

3.3.3. **Temperature-dependent cluster expansions**

Temperature-dependent CEs for fcc and bcc Al-Li systems were fitted and the ECI coefficients as well as the cluster features are listed in Tables A1, A2, A3 and A4 in the Annex A. The formation enthalpies, H^f, of different configurations determined from the combination of first-principles calculations and the L-S relationships and predicted with the CEs are compared in Figure 3.6 for three different temperatures: 0 K, 500 K and 1000 K. The red crosses and open symbols stand for the bcc configurations calculated using both strategies while the blue crosses and open symbols provide the same information for the fcc configurations. The H^f predicted with the CE formalism are in good agreement with those obtained from first-principles calculations and the L-S relationships. The cross-validation scores for the fcc and bcc configurations were 0.0067 eV/atom and 0.0148 eV/atom, respectively.

The ground state phases located on the convex hull at 0 K can be found in Figure 3.6(a). They are Al, Al_3Li (δ'), AlLi (δ), Al_2Li_3, $AlLi_2$, Al_4Li_9 and Li. Al and Al_3Li (δ') have fcc structures while the others are bcc. Among them, the space groups of Al_2Li_3, $AlLi_2$, Al_4Li_9 are R-3M, CMCM, and C2/M, respectively. At higher temperature, H^f provides information about the stability of the phases including the contribution from vibrational entropy and the same phases are found in convex hull at 500 K (Figure 3.6(b)) and 1000 K (Figure 3.6(c)). Al_3Li (δ') is located almost on the tie-line connecting Al and AlLi (δ) at 0K, and its formation enthalpy is only 4.17 meV/atom lower than that of the straight line connecting Al and AlLi, which is the same order of the accuracy in first-principles calculations. Thus, it is difficult to establish whether Al_3Li (δ') is ground state phase at 0 K. Nevertheless, the stability of Al_3Li (δ') is slightly increased with temperature due to the vibrational entropy contribution. In fact, the difference between the formation enthalpy of Al_3Li and that of the straight line connecting Al and AlLi is increased to 6.172 meV/atom at 500 K (Figure 3.6(b)), and to 10.942 meV/atom at 1000 K (Figure 3.6(c)).

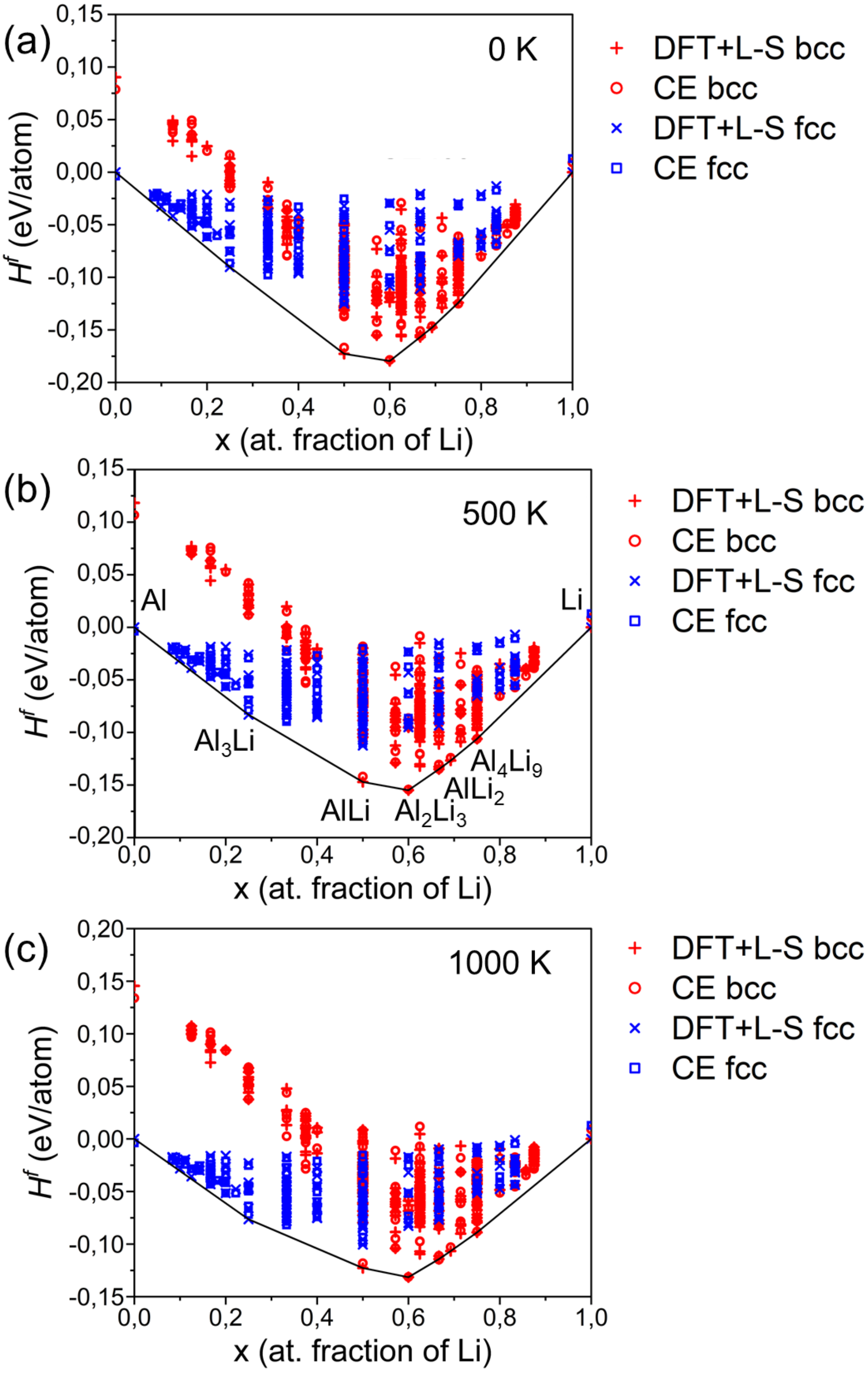

Figure 3.6: Formation enthalpies H^f of different configurations in the Al-Li system at different temperatures. (a) 0 K. (b) 500 K. (c) 1000 K. Crosses stand for the enthalpies calculated using first-principles calculations and the L-S relationships while open symbols provide the results given by the CE formalism. Red symbols stand for bcc configurations and blue symbols for fcc.

3.4. Phase diagram

3.4.1. Al-Al_3Li phase boundary

The semi-grand canonical MC calculations were performed from each ground state phase in the direction of both increasing and decreasing $\Delta\mu$. In the Al-rich part, Al and Al_3Li are the two ground state phases which share the same fcc lattice (Figure 3.6). Their phase boundaries can be determined by the grand potential $\emptyset$, which was obtained by thermodynamic integration from $\Delta\mu$ and T, as indicated in Section 2.5 and Section 3.2.4.

The grand potentials $\emptyset$ are plotted as a function of $\Delta\mu$ at T=500 K in Figure 3.7(a) as an example. The black curve is calculated from Al by increasing $\Delta\mu$, while the red one is calculated from Al_3Li by decreasing $\Delta\mu$. The intersection $\emptyset_{Al}$ = $\emptyset_{\delta'}$ corresponds to $\Delta\mu$ where Al and δ' coexist. On the left of the intersection, $\emptyset_{Al}$< $\emptyset_{\delta'}$, which indicates that Al is the stable phase in this $\Delta\mu$ range, while $\emptyset_{\delta'} < \emptyset_{Al}$ on the right of the intersection, and Al_3Li is the stable phase. The two-phase equilibrium region of Al and Al_3Li, expressed by $\emptyset_{Al}$ = $\emptyset_{\delta'}$, can be mapped on to the conjugated relationship between composition x and chemical potential $\Delta\mu$, as shown in Figure 3.7(b), from which the composition of Al and Al_3Li at equilibrium can be determined. Thus, the phase boundary between Al and Al_3Li at 500K can be constructed and is marked by the dashed line in Figure 3.7(c). Following the same methodology, the phase boundary between Al and Al_3Li can be determined as a function of temperature and the phase diagram in this region is constructed, as shown in Figure 3.7(c). The two-phase equilibrium region of Al and Al_3Li exists up to T = 680 K. The $\emptyset - \Delta\mu$ and $x - \Delta\mu$ curves obtained by increasing $\Delta\mu$ and decreasing $\Delta\mu$ overlap when the temperature is higher than 680 K, which means Al and Al_3Li cannot be distinguished from a thermodynamic viewpoint.

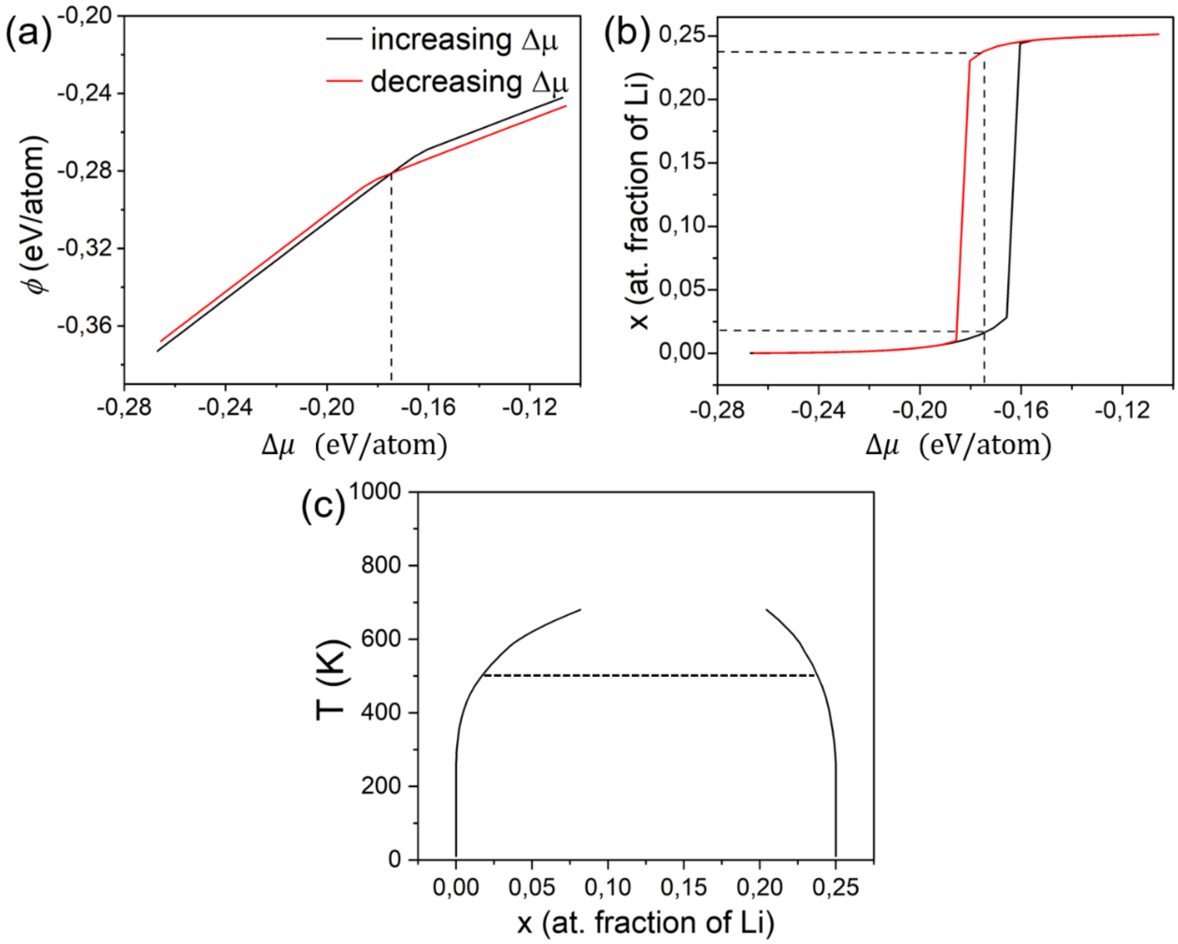

Figure 3.7 (a) Grand potentials Ø of Al and Al_3Li as a function of chemical potential $\Delta\mu$ at 500 K. (b) Li content (expressed by x) as a function of $\Delta\mu$ at 500 K. (c) Phase boundary between Al and Al_3Li.

3.4.2. Al_3Li-AlLi phase boundary

The other adjacent phase to Al_3Li is AlLi (Figure 3.6), which has a bcc lattice structure. Therefore, the phase boundary between AlLi and either Al or Al_3Li can only be determined by the common tangent to their Gibbs free energy G, which were calculated by according to eq. (2.32). Since the Gibbs free energy of Al_3Li is almost on the tie-line connecting Al and AlLi at 0 K (Figure 6(a)), it is difficult to establish whether Al_3Li (δ') is ground state phase at 0 K, and the Gibbs free energy of Al_3Li is also compared. The dash lines in Figure 8(a) stand for the common tangent to the Gibbs free energies of Al and AlLi at each temperature, and they indicate the chemical potential at equilibrium between Al and AlLi. The Gibbs free energies of Al_3Li are always above the common tangent to the Gibbs free energies of Al and AlLi at each temperature, and this result indicates the Al_3Li is a metastable phase, mainly due to the configurational entropic contribution to the free energy because the vibrational entropic contribution enhanced the stability of Al_3Li.

The composition of Al and AlLi at equilibrium can be obtained for each temperature from the common tangent at the Gibbs free energy curves, and the phase boundary between them is constructed (Figure 3.8(b)). The two-phase equilibrium region of Al and AlLi exist up to T = 850 K, in good agreement with experimental results [129,130]. The Gibbs free energies of Al and AlLi overlap at T > 850 K (Figure 3.8(a)), and they become solid solutions above this temperature.

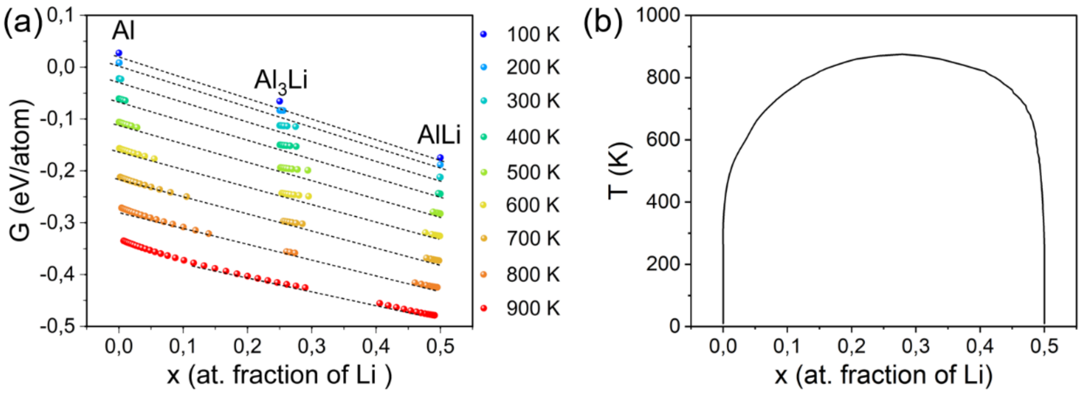

Figure 3.8: (a) Gibbs free energy of Al, Al_3Li and AlLi phases as a function of the Li content (expressed by x) at different temperatures. (b) Phase boundary between Al and AlLi.

3.4.3. AlLi-Al_2Li_3 and Al_2Li_3-$AlLi_2$ phase boundaries

AlLi and Al_2Li_3 share the bcc lattice structure, and their phase boundary was determined from the thermodynamic grand potentials $\emptyset$, as in the case of Al and Al_3Li. Their grand potentials are plotted as a function of $\Delta\mu$ at T = 600 K in Figure 3.9(a) as another example. The black curve is obtained from AlLi by increasing $\Delta\mu$, while the red one is obtained from Al_2Li_3 by decreasing $\Delta\mu$. On the left of the intersection, $\emptyset_{\mathrm{AlLi}} < \emptyset_{\mathrm{Al_2Li_3}}$, which indicates the Al_2Li_3 is the stable phase in this $\Delta\mu$ range, while $\emptyset_{\mathrm{AlLi}} > \emptyset_{\mathrm{Al_2Li_3}}$ on the right of the intersection, and Al_2Li_3 is the stable phase. The intersection of the grand potentials can be mapped on to the conjugated relationship between composition x and $\Delta\mu$, as shown in Figure 3.9(b), which determines the composition of AlLi and Al_2Li_3 at equilibrium. Thus, the phase boundary between AlLi and Al_2Li_3 at T = 600 K can be constructed, and is indicated by the dashed line in Figure 3.9(c). Following this strategy, the phase boundary between both phases was built as a function T and is plotted in Figure 3.9(c).

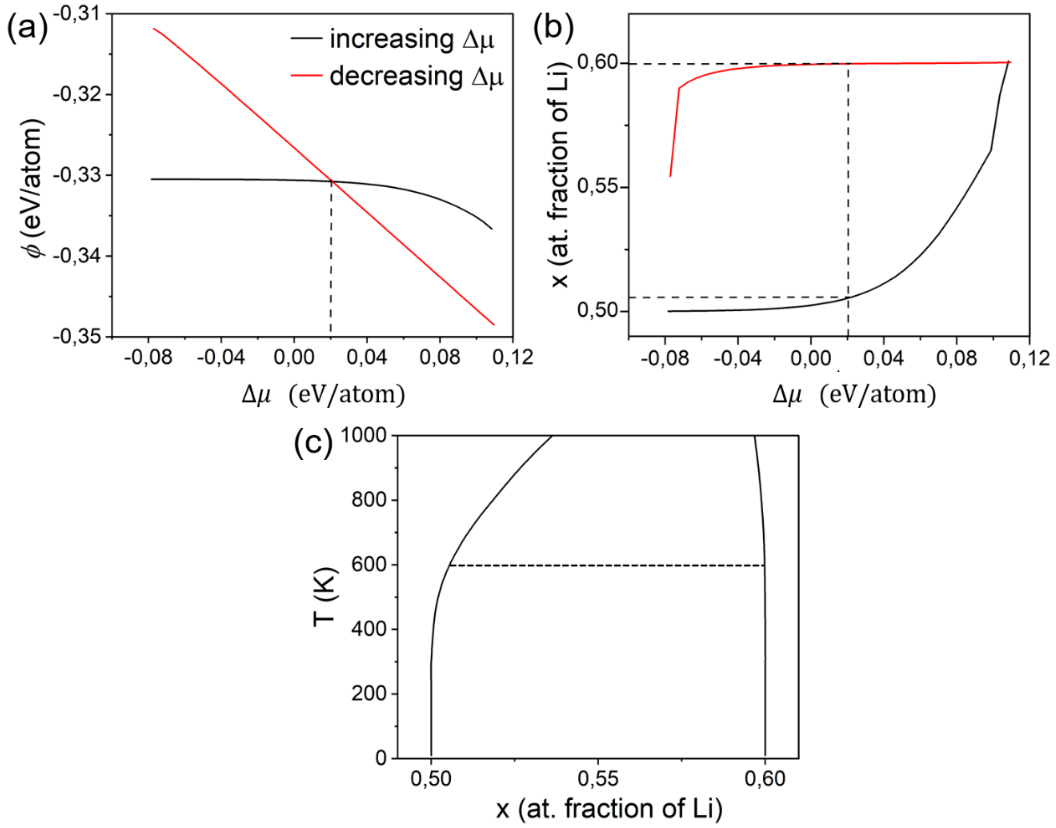

Figure 3.9: (a) Grand potentials Ø of AlLi and Al_2Li_3 as a function of the chemical potential $\Delta\mu$ at 600 K. (b) Li content (expressed by x) as a function of $\Delta\mu$ at 600 K. (c) Phase boundary between AlLi and Al_2Li_3.

The strategy to obtain the phase boundaries between Al_2Li_3 and $AlLi_2$ is identical to the one presented above for AlLi and Al_2Li_3. The ascending and descending curves of the thermodynamic grand potentials Ø as a function of $\Delta\mu$ at T = 500 K are plotted in Figure 10(a). The composition of Al_2Li_3 and $AlLi_2$ at equilibrium could be determined from their intersection (Figure 3.10(b)) and this construction is repeated at different temperatures to plot the phase boundaries, which are plotted in Figure 3.10(c).

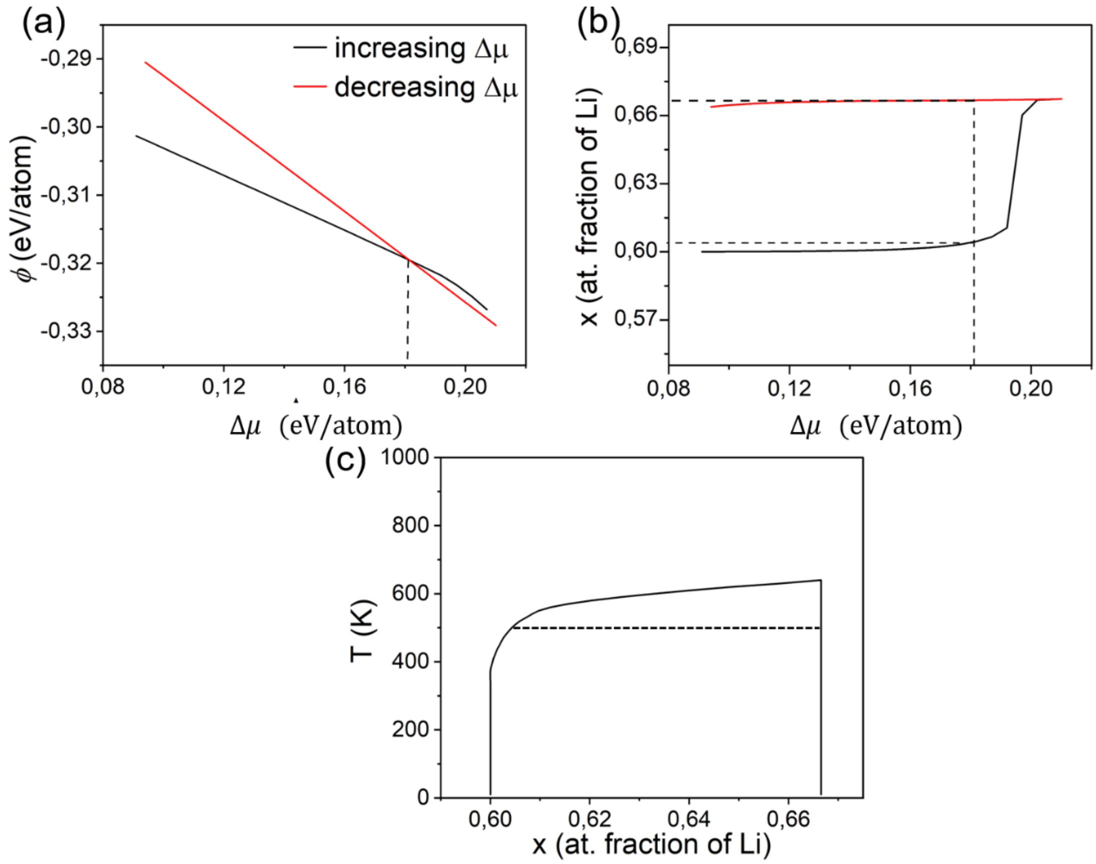

Figure 3.10: (a) Grand potentials $\emptyset$ of Al_2Li_3 and $AlLi_2$ as a function of the chemical potential $\Delta\mu$ at 500 K. (b) Li content (expressed by x) as a function of $\Delta\mu$ at 500 K. (c) Phase boundary between Al_2Li_3 and $AlLi_2$.

3.4.4. $AlLi_2$-Al_4Li_9 and Al_4Li_9-Li phase boundaries

The phase boundaries between $AlLi_2$ and Al_4Li_9 were also determined from their thermodynamic grand potentials $\emptyset$ and they are plotted in Figure 3.11(a) as a function of $\Delta\mu$ at T = 450 K as an example. Again, the intersection between the ascending and descending grand potentials was mapped on to the conjugated relationship between Li content (expressed by x) and chemical potential $\Delta\mu$, as shown in Figure 3.11(b). Thus, the composition of $AlLi_2$ and Al_4Li_9 at equilibrium was determined and the phase boundary between $AlLi_2$ and Al_4Li_9 at T = 450 K was obtained and is plotted with the dashed line in Figure 3.11(c). The phase boundary in this region was constructed from the grand potentials at each temperature and is shown in Figure 3.11(c), from which the $AlLi_2$ and Al_4Li_9 are both line compounds. The two-phase equilibrium region of $AlLi_2$ and Al_4Li_9 exists up to T = 520 K, and $AlLi_2$ and Al_4Li_9 cannot be distinguished above 520 K.

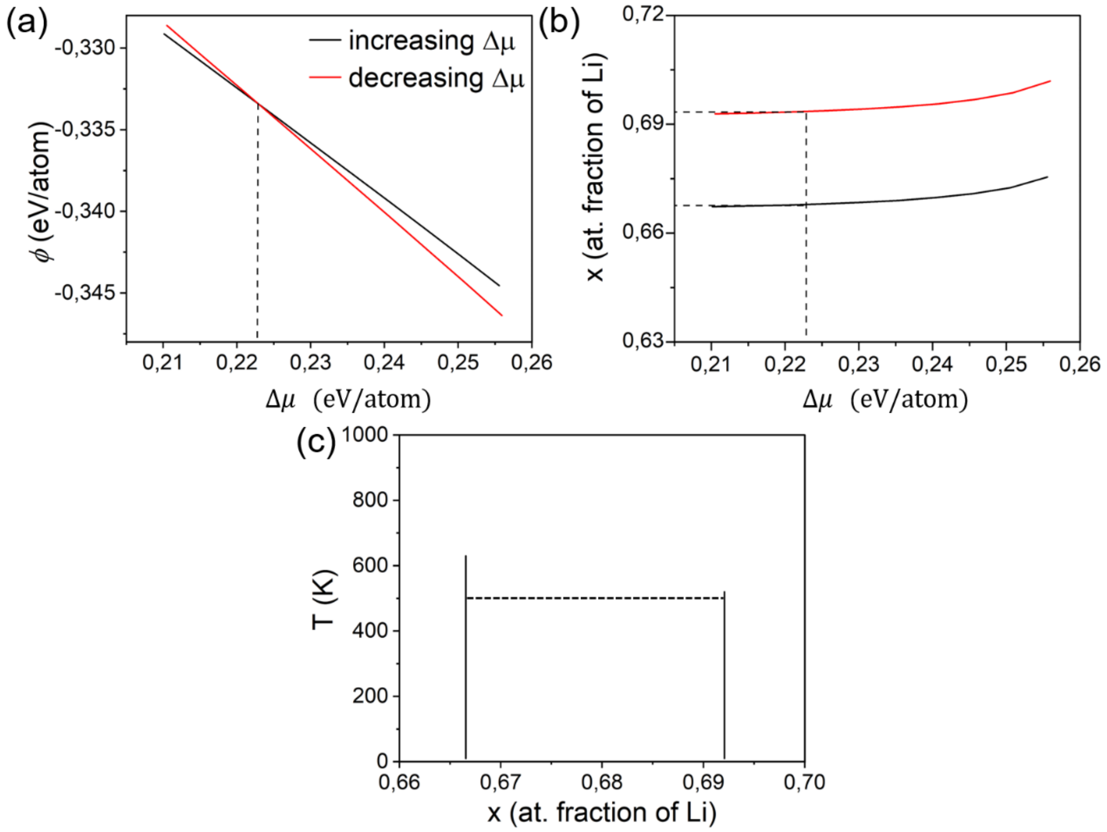

Figure 3.11: (a) Grand potentials ∅ of $AlLi_2$ and Al_4Li_9 as a function of the chemical potential $\Delta\mu$ at 450 K. (b) Li content (expressed by x) as a function of $\Delta\mu$ at 450 K. (c) Phase diagram between $AlLi_2$ and Al_4Li_9.

Exactly the same construction was used to obtain the phase boundaries between Al_4Li_9 and Li. The corresponding ascending and descending ∅ vs. $\Delta\mu$ curves (Figure 12(a)), the composition at equilibrium of both phases at T = 400 K (Figure 3.12(b)) and the phase boundaries as a function of temperature (Figure 3.12(c)) were obtained. are shown in Figure 3.12(a). The two-phase equilibrium region of Al_4Li_9 and Li exists up to T=520 K.

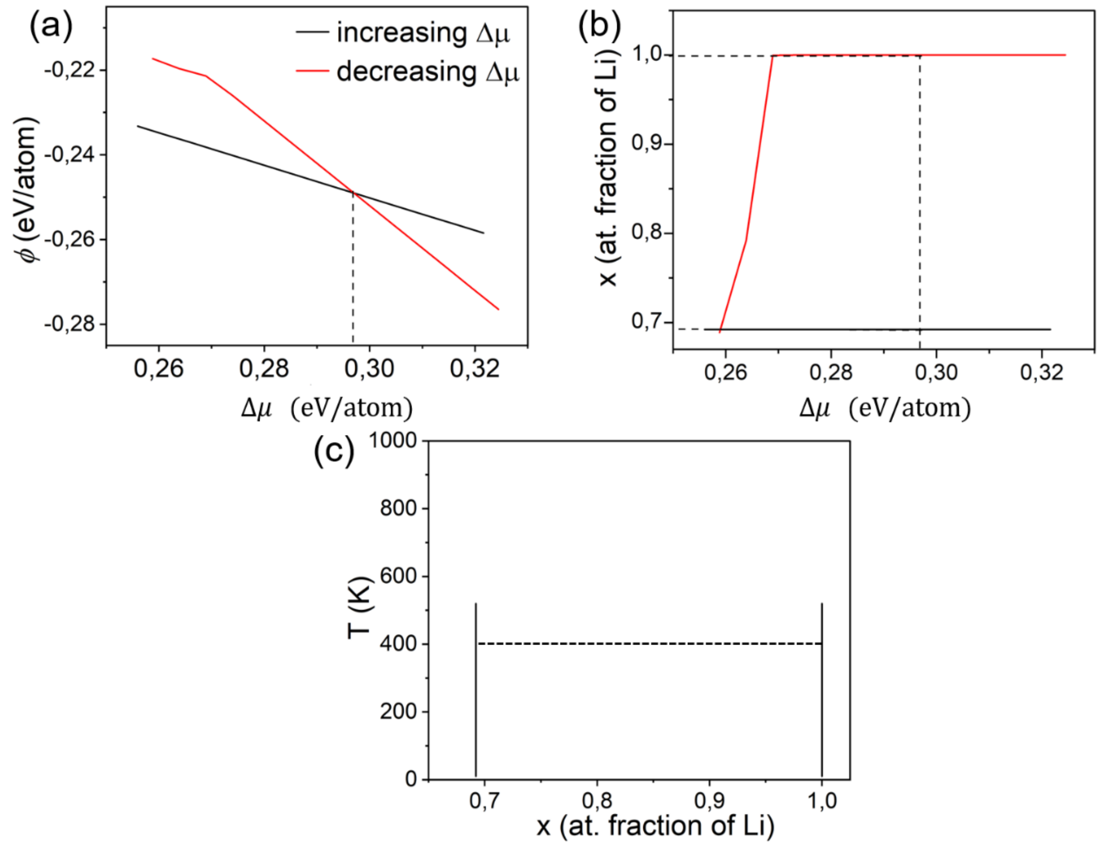

Figure 3.12: (a) Thermodynamics grand potentials $\emptyset$ of Al_4Li_9 and Li as a function of the chemical potential $\Delta\mu$ at 400 K. (b) Li content (expressed by x) as a function of $\Delta\mu$ at 400 K. (c) Phase diagram between Al_4Li_9 and Li.

3.5. Discussion

The phase boundaries between each two adjacent phases were integrated to build the Al-Li phase diagram which is plotted in Figure 3.13(a) together with the previous one that was obtained including only the configurational entropy contribution to the free energy [89]. Al_3Li is considered as a stable phase in the previous phase diagram that only includes configurational disorder and, thus, there are two Al-Al_3Li and Al_3Li-AlLi two-phase equilibrium regions (in red). However, since Al_3Li is a metastable phase in the phase diagram including both vibrational and configurational entropy, the Al_3Li-AlLi two-phase equilibrium region has disappeared and only one Al-AlLi two-phase equilibrium region exists. Moreover, the critical temperature of Al-Al_3Li two-phase region (maximum of the red dashed line) was 730 K in the phase diagram with only configurational disorder, but this value is higher than the experimental ones (620 K) [130]. This discrepancy could be expected because neglecting the vibrational contribution often leads to overestimate of phase transition temperatures[172,191]. The phase diagram including both vibrational and configurational contributions leads to a wider two-phase equilibrium region between Al and Al_3Li (black dashed lines) than the one without considering vibrational effect, and the critical temperature also decreases to 670 K, which is in better agreement with the experimental data.

$AlLi_2$ and Al_4Li_9 appear as line compounds in the phase diagrams with or without vibrational entropy. Nevertheless, $AlLi_2$ and Al_4Li_9 are only stable up to 300 K and 500 K, respectively, when vibrational disorder is not included. They reach 640 K and 520 K, respectively, when vibrational entropy is taken into account, which is much closer to the experimental data (600 K and 545 K, respectively). The solubilities of AlLi and Al_2Li_3 are also influenced by the vibrational entropy. The Li content in the two phase AlLi- Al_2Li_3 region reaches 0.6 at 700 K if only configurational disorder is included but is dramatically reduced at this temperature if vibrational entropy is taken into account. In addition, Al_2Li_3 is a line compound if only configurational disorder is included but it forms a two-phase region with $AlLi_2$ if vibrational entropy is considered.

The phase diagram calculated taking into account both vibrational and configurational entropic contributions is also compared with the accepted experimental phase diagram [172,191] in Figure 13(b). Both phase diagrams predict that Al_3Li is a metastable phase. The Al-AlLi two-phase equilibrium regions in the both phase diagrams are almost superposed and a small difference only appears at high temperature. The phase boundary between AlLi and Al_2Li_3 is also accurately predicted in the phase diagram. Moreover, $AlLi_2$ and Al_4Li_9 appear as lines compounds in both phase diagrams and the maximum temperatures at which both disappear are also very close in both phase diagrams. Al_2Li_3 is a line compound in the experimental phase diagram while it is only a line compound up to 500 K in the calculated phase diagram and forms a solid solution at higher temperature.

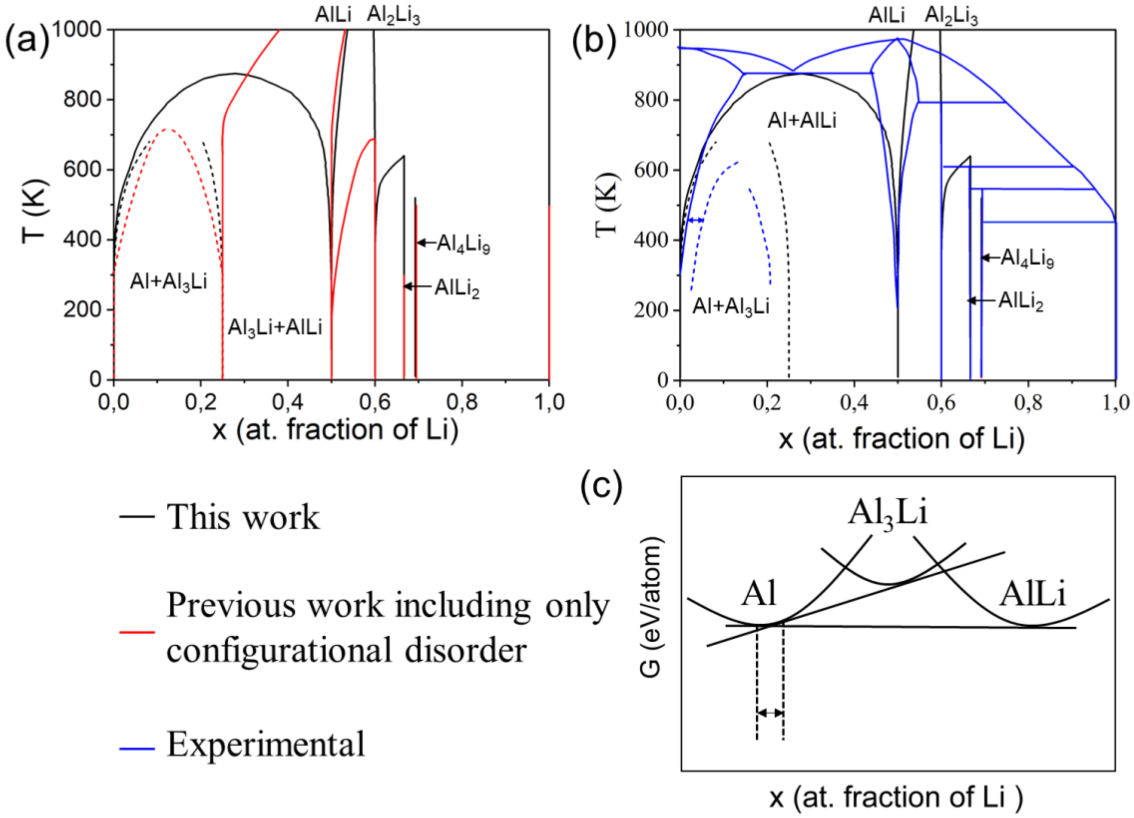

Figure 3.13: (a) Comparison between Al-Li phase diagrams calculated in this work (black lines) and in a previous investigation (red lines) [130]. The phase diagram calculated in [130] only considered the configurational disorder contribution to the free energy. (b) Comparison between the Al-Li phase diagrams calculated in this work (black lines) and the experimental one (blue lines) [172,191]. (c) Schematic illustration of the gap between the solvus lines of AlLi and Al_3Li.

Overall, the calculated phase diagram is in very good agreement with the experimental data and the only remarkable difference is the gap between the solvus lines of AlLi and Al_3Li, which is indicated by the arrow in Figure 3.13(b). This gap is very small in our calculated phase diagram as compared with the experimental data. A schematic illustration in the formation of gap is displayed in Figure 3.13(c), which shows the three curves of the Gibbs free energy of the stable Al and AlLi phases and of metastable Al_3Li at a given temperature. The gap is given by the difference in the composition of Al determined by the common tangent, which is marked by the arrows. A large gap will be formed if the Gibbs free energy of metastable Al_3Li is much higher than the common tangent between the Gibbs free energy of the stable Al and AlLi, (as shown in Figure 3.13(c)). However, based on our accurate calculations, the Gibbs free energy of metastable Al_3Li is only slightly higher than the common tangent between the Gibbs free energies of Al and AlLi (Figure 3.8), and a large gap cannot be formed. The large gap in the experimental phase diagram is probably an error caused by sluggish kinetics and uncertainties during experiments. Therefore, our calculation provides an accurate solvus line for Al_3Li, which is very important for the heat treatment of Al-Li alloy.

3.6. Conclusions

The whole phase diagram of the Al-Li system is predicted from first-principles calculations and statistical mechanics taking into account the influence of the configurational and vibrational entropy. To this end, the formation enthalpy of different configurations with either fcc or bcc lattices at different temperatures was accurately predicted by means of cluster expansion formalisms that were fitted from density functional theory simulations. The vibrational entropic contribution of each configuration was determined from the L-S relationship for each type of bond (either Al-Al, Li-Li and Al-Li) for each lattice that were obtained from full phonon calculations of various compounds. Thus, the thermodynamic grand potential and the Gibbs free energy of the different phases in the convex hull were obtained as a function of temperature by means of MC simulations and the phase diagram was determined.

The calculated phase diagram was in excellent agreement with the experimental data and provides accurate predictions of the stable (AlLi, Al_2Li_3, $AlLi_2$, Al_4Li_9) and metastable (Al_3Li) phases, of the phase boundaries between them and of the maximum stability temperature of $AlLi_2$ and Al_4Li_9 which are line compounds. In addition, the calculated phase diagram shows that Al_2Li_3 is a line compound only up to 500 K and forms a solid solution at higher temperature. It also indicates that gap between the solvus lines of AlLi and Al_3Li is narrower than that found in the accepted experimental phase diagram, an information that is important to design precipitation high treatments for these alloys. Finally, the large influence of the vibrational entropic contribution to assess the metastability of Al_3Li, the phase boundaries and the maximum stability temperature of different phases is revealed by comparison with predictions of the phase diagram that only considered the configurational entropy contribution. Overall, the methodology presented in this paper shows that accurate phase diagrams of alloys of technological interest can be predicted from first-principles calculations.

Data availability

The computational data generated in this chapter can be found at https://zenodo.org/doi/10.5281/zenodo.12528018.

4. Prediction of the Ni-Al phase diagram

4.1. Introduction

Alloys based on the Ni-Al system are of interest for different engineering applications. Ni-based superalloys present outstanding mechanical properties and high corrosion resistance at high temperature and are widely used in gas-turbine engines for propulsion and energy generation. They contain many elements but are built on the Ni-Al binary system [192] because the main strengthening contribution comes from the dispersion of γ' ($AlNi_3$) precipitates. Similarly, addition of small amounts of Ni to Al and Al alloys leads to the formation of diverse Ni-based intermetallic compounds that improve the wear resistance and high temperature strength. Thus Ni-Al alloys are suitable for high temperature structural components as well as for friction and corrosion resistant coatings to protect from aggressive liquids and gases [194-196]. In addition, intermetallic compounds based on Ni and Al (mainly $AlNi_3$ and AlNi) present low-density, good thermal conductivity, oxidation resistance and high melting temperature [193] and have applications as coatings and high temperature structural elements when they are alloyed with other elements [197-199] to overcome the brittleness associated with their ordered lattice structure [199]. Other applications of Ni-Al alloys are found in catalytic devices [200,201] nanotechnology [202], and so on.

Obviously, the Ni-Al phase diagram is a crucial factor to design and improve mechanical and functional properties of alloys based in these chemical elements. The Ni-Al phase diagrams determined in traditional Calphad method have been reported in literatures [204-207]. The presence of impurities and the precision of the measurements will affect the phase diagrams [17], and a long annealing time is necessary to reach the stability or to discriminate metastable from stable phases because the convergence towards thermodynamic equilibrium can be hindered by slow kinetics [20,21]. Although some efforts, such as substituting some experimental data with first-principles calculated single phase quantities [205], have been made to reduce time and expense, the effort saving is still limited. Moreover, there are often regions in the phase diagram in which the experimental information is limited. For instance, the Al_3Ni_5 phase has been reported to proceed from a peritectoid reaction between $AlNi_3$ and AlNi phases but there are some uncertainties about the formation mechanism as well as about the range of Ni solubility in the phase diagram [208-212]. Robertson et al. [208] found that the maximum temperature for stable Al_3Ni_5 phase is 973 K and its solubility is (62~69.5) at.% Ni while Li et al. [212] reported that Al_3Ni_5 is only stable below 923 K and the solubility range is (54.7~59.4) at.% Ni. Moreover, other researchers considered Al_3Ni_5 a line compound [213]. Additionally, two morphologies of Al_3Ni_5 have been observed by optical microscopy, namely striped and lath-like, which point out to two different routes to form Al_3Ni_5 [214]. One path starts with metastable AlNi ($L1_0$) phase [211] and the other with the stable AlNi (B_2) phase [210]. However, the transformation mechanism for each one is not clear.

In this chapter, the whole solid Ni-Al phase diagram is accurately predicted from first-principles calculations and MC simulations. In addition to the configurational and vibrational entropy, it should be noted that the stable phases ($AlNi_3$ and Ni) in the Ni-rich part of the Ni-Al phase diagram are ferromagnetic and the contribution of magnetic enthalpy has to be taken into account [85,131]. The magnetic entropy contribution is normally much smaller than the configurational and vibrational ones [132,133] and is neglected. The computed phase diagram is compared with the currently accepted Calphad phase diagram and the contributions of vibrational entropy and magnetic effects to the overall stability and solubility of the different phases are analyzed independently. Thus, the capability of this methodology to predict accurate phase diagrams of alloys of technological interest is clearly established.

4.2. **Methodology**

4.2.1. **DFT calculations**

All configurations enumerated by the ATAT code [158] were optimized using first-principles calculations. The electron exchange-correlation was described by the generalized gradient approximation with the PBE exchange-correlation functional and ultrasoft pseudopotentials, as implemented in Quantum Espresso [148,149]. An energy cutoff of 60 Ry was adopted for the plane-wave expansion of the electronic wave functions. The Brillouin zone was sampled by the Monkhorst-Pack scheme with a k-point density of 40 points/$Å^{-1}$. Two stable phases with ferromagnetism appear in the Ni-Al phase diagram, namely Ni_3Al and Ni, while all other stable phases are nonmagnetic. Therefore, an initial magnetic moment was set to 0.28 μB for Ni atoms, and 0 μB for Al atoms in collinear calculations was included in the simulations for the configurations with >75 at.% Ni [132]. All degrees of freedom of each configuration including volume, shape, and internal atomic positions, were allowed to relax under zero pressure.

4.2.2. **Vibrational free energy calculation**

The L-S relationship for each lattice was determined from different configurations. Since the relationship is transferable [55,159,215] in configurations within the same lattice, any configuration can be used for fitting. All configurations were relaxed by DFT calculation, four configurations including the elementary ones for two different lattices were used, respectively. The relaxed configurations were expanded up to 10% in volume in increments of 2%, in order to generate bonds with different lengths. Then, supercells of the expanded configurations were constructed. The supercells of fcc Al and fcc Ni contain 60 atoms, those of bcc Al, bcc Ni, bcc AlNi and fcc $AlNi_3$ contain 64 atoms and those of bcc Al_3Ni_5 and fcc Al_3Ni contain 96 atoms. A displacement of 0.1 Å was applied for each symmetrically different atom within each supercell. The force acted on each atom in each supercell is calculated by self-consistent field (scf) calculation using same parameter as section 4.2.1. Therefore, the force constant matrices between all atomic pair in a configuration can be obtained from eqs. (2.5) and (2.11). The vibrational free energy was calculated from eqs. (2.9)-(2.10).

4.2.3. **Cluster expansion**

The temperature-dependent mixing enthalpy H_{mix} - including the vibrational entropic contribution - of an $Al_{1-x}Ni_x$ configuration (in which all sites accommodate either Al or Ni atoms) in a bcc or fcc lattice can be calculated as [216]

$$H_{mix}^{Al_{1-x}Ni_x}(T) = \left(E_s^{Al_{1-x}Ni_x} - TS_{vib,s}^{Al_{1-x}Ni_x}(T)\right) - (1-x)\left(E_s^{Al} - TS_{vib,s}^{Al}(T)\right) - \\ - x\left(E_s^{Ni} - TS_{vib,s}^{Ni}(T)\right) \tag{4.1}$$

where x is the atomic fraction of Ni, and $E_s^{Al_{1-x}Ni_x}$, E_s^{Al} and E_s^{Ni} stand for the energy of the relaxed $Al_{1-x}Ni_x$, Al and Ni in the corresponding lattice s. $S_{vib,s}^{Al_{1-x}Ni_x}$, $S_{vib,s}^{Al}(T)$ and $S_{vib,s}^{Li}(T)$ stand for the vibrational entropy of $Al_{1-x}Ni_x$, Al and Ni in the corresponding lattice s at temperature T.

The temperature-dependent mixing enthalpy of an $AlNi_{1-y}Va_y$ configuration (Ni sublattice sites in AlNi can accommodate either Ni atoms or vacancies) in the bcc lattice can be calculated as:

$$H_{mix}^{AlNi_{1-y}Va_y}(T) = \left(E_{bcc}^{AlNi_{1-y}Va_y} - TS_{vib,bcc}^{AlNi_{1-y}Va_y}(T)\right) - (1-y)\left(E_{bcc}^{AlNi} - \\ - TS_{vib,bcc}^{AlNi}(T)\right) - x\left(E_{bcc}^{AlVa} - TS_{vib,bcc}^{AlVa}(T)\right) \tag{4.2}$$

where y is the atomic fraction of vacancy on the Ni sublattice, and $E_{bcc}^{AlNi_{1-y}Va_y}$, E_{bcc}^{AlNi} and E_{bcc}^{AlNi} stand for the energy of the relaxed bcc $AlNi_{1-y}Va_y$, AlNi and AlVa. $S_{vib}^{AlNi_{1-y}Va_y}$, $S_{vib,s}^{AlNi}(T)$ and $S_{vib,s}^{AlVa}(T)$ stand for the vibrational entropy of $AlNi_{1-y}Va_y$, AlNi and AlVa in the corresponding bcc lattice at temperature T. Here we should note that AlNi and AlVa are used as the reference systems because of the atomic occupancy of the lattice.

The temperature-dependent CE can be fitted from the temperature-dependent mixing enthalpies of a set of configurations in the same lattice by eq. (2.24). For bcc and fcc lattices, σ_i = -1 when site i accommodates an Al atom and σ_i = +1 when the site i accommodates a Ni atom for a lattice without vacancies. For the AlNi bcc lattice with vacancies, only the Ni sublattice sites have occupation variables: σ_i = -1 when site *i* accommodates a Ni atom and σ_i = +1 when site *i* accommodates a vacancy.

It should be noted that the mixing enthalpies given by eqs. (4.1) and (4.2) are the actual formation enthalpies only in the case of the fcc lattice because the stable reference phases are fcc Al and Ni. The temperature-dependent formation enthalpies of the bcc configurations can be obtained from the formation energies and vibrational entropic contribution of the configurations with respect to those of fcc Al and Ni. Moreover, the actual stoichiometry of the configuration should be included in the case of the bcc AlNi with vacancies. Thus, the temperature-dependent formation enthalpy of bcc configurations, H_f, can be calculated as:

$$H_f^{Al_{1-x}Ni_x}(T) = \left(E_{bcc}^{Al_{1-x}Ni_x} - TS_{vib,bcc}^{Al_{1-x}Ni_x}(T)\right) - (1-x)\left(E_{fcc}^{Al} - TS_{vib,fcc}^{Al}(T)\right) - \\ -x\left(E_{fcc}^{Ni} - TS_{vib,fcc}^{Ni}(T)\right) \quad (4.3)$$

4.2.4. **Monte Carlo simulations**

The semi-grand canonical MC simulations of bcc and fcc lattices as well as of bcc lattices with vacancies were performed using the ATAT package. 20x20x20 supercells were used for each ground state phase. The fitted CE of each lattice was used to predict H_f^i from H_{mix}^i, eqs. (4.2) and (4.3). MC simulations were performed at different T (from 10 K up to 1800 K) with a temperature increment of 10 K for each chemical potential and within a given range of Δμ for each phase with increments of 0.005 eV/component in the chemical potential for each temperature, where Δμ are chemical potential differences between Al and Ni for lattices without vacancies, and AlNi and AlVa for bcc lattices with vacancies. For each value of T and Δμ, a MC simulation included 2000 passes for equilibrium, followed by 5000 passes for calculating the thermodynamic averages. The Gibbs free energy and grand potential at different temperature can be calculated from eqs. (2.30)-(2.31). Thus, all two adjacent phase boundaries can be determined by Gibbs free energy or Grand potential.

4.3. **Results**

4.3.1. **Phases in Ni-Al alloy**

The stables phases according to the accepted Ni-Al phase diagram are Al, Al_3Ni, Al_3Ni_2, AlNi, Al_3Ni_5, $AlNi_3$ and Ni [193,204]. Their crystal structures are depicted in Figure 4.1 and the corresponding structural information is listed in Table 4.1. Based on our previous experience, some phases with complex structure can be treated as a distorted configuration on a simpler lattice. After careful analysis, it was concluded that all phases in Ni-Al phase diagram - with the exception of Al_3Ni - can be treated as configurations existing on fcc or bcc lattices, with the atomic sites accommodating Al and Ni atoms. Al_3Ni_2 can also be treated as a configuration on a bcc lattice, with the Ni sublattice sites of AlNi (which is CsCl type B_2 structure) accommodating Ni atoms and vacancies, while the Al sublattice site of AlNi only accommodates Al atoms. In the case of δ-Al_3Ni_5, the orthorhombic lattice is slightly distorted and one the three angles between the principal axes of the lattice is not 90º (γ=97.46º, Table 1).

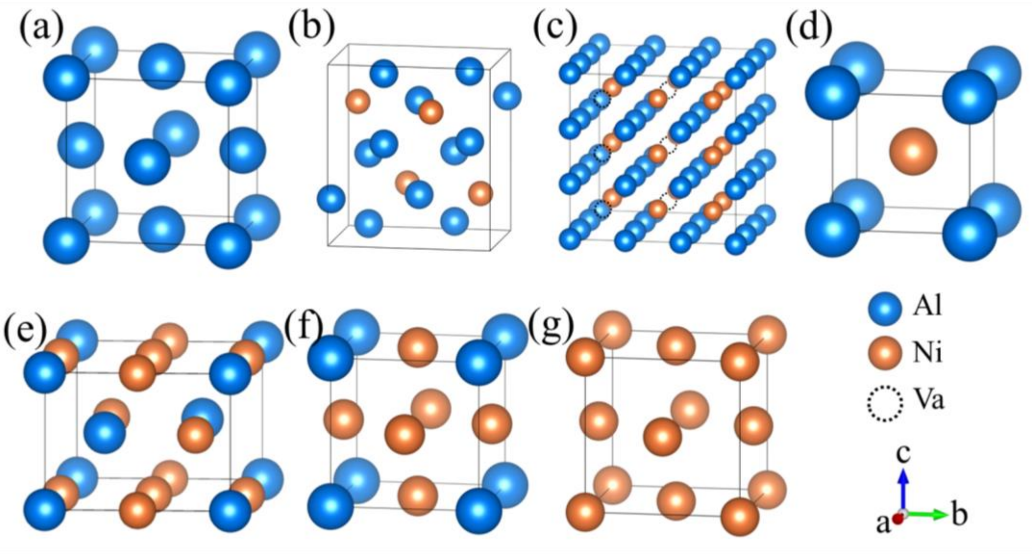

Figure 4.1: Stable phases in Ni-Al alloys. (a) γ-Al. (b) DO_{11}-Al_3Ni. (c) $D5_{13}$-Al_3Ni_2. (d) β-AlNi. (e) δ-Al_3Ni_5. (f) γ'-$AlNi_3$. (g) γ-Ni.

Table 4.1: Structural information of the stable phases in the Ni-Al phase diagram

Composition	Symmetry	Lattice constants (Å)	phase
Al	Fm3m	a =b=c=3.48	γ
Al_3Ni	Pnma	a =4.77, b=6.56, c=7.30	DO_{11}
Al_3Ni_2	$P\bar{3}m1$	a =b=3.99, c=4.88	$D5_{13}$
AlNi	$Pm\bar{3}m$	a =b=c=2.86	B_2 (β)
Al_3Ni_5	Cmmm	a =4.996, b=4.996, c=3.740, α=β=90º, γ=97.46º	δ
$AlNi_3$	$Pm\bar{3}m$	a =b=c=3.52	$L1_2$ (γ')
Ni	Fm3m	a =b=c=3.48	γ

4.3.2. **Cluster expansion at 0 K**

631 configurations with the fcc lattice, 437 configurations with the bcc lattice and 167 configurations with the bcc lattice with vacancies were fully relaxed at zero pressure using Quantum Espresso. The lattice distortion after relaxation was determined to assess whether the lattice symmetry changed. Only configurations whose distortion was below 10% were

considered to keep the original lattice symmetry and used to fit the CE for each lattice, following the criteria in the literature [190,217]. Thus, the mixing enthalpies were calculated for 485 fcc configurations and 170 bcc configurations, following eq. (4.1), and for 163 bcc configurations with vacancies following eq. (4.2). They are plotted with solid symbols in Figures 4.2(a)-(c), respectively.

The optimized ECIs were obtained for each lattice. Those for the fcc lattice include 25 pair cluster interactions, 20 triplet cluster interactions and 35 quadruplet cluster interactions. The optimized ECIs for the bcc lattice include 1 empty cluster interaction, 1 point cluster interaction, 12 pair cluster interactions, 17 triplet cluster interactions and 7 quadruplet cluster interactions. Finally, the optimized ECIs for the bcc lattice with vacancies include 11 pair cluster interactions, 21 triplet cluster interactions and 12 quadruplet cluster interactions. The values of the ECI at 0 K are depicted in Tables B1, B2 and B3 in the Annex B. The mixing enthalpies for each lattice calculated with the CE formalism are plotted with open symbols in Figures 4.2(a) to 4.2(c). They were in good agreement with the DFT results and the cross-validation scores of the CE predictions were 0.0125 eV/atom, 0.0184 eV/atom and 0.0126 eV/atom for the fcc, bcc and bcc with vacancies configurations, respectively.

The formation enthalpies at 0 K of all configurations (that are equal to the mixing enthalpies for the fcc lattice and are calculated from eq. (4.1) for the bcc lattices) are plotted in Figure 4.3. The formation enthalpy of Al_3Ni is also included with a green symbol in this Figure. The primitive cell of the orthorhombic Al_3Ni phase contains 16 atoms, and the computational work to fit the CE for this lattice will be huge. This effort is not justified because the configurational entropy of this phase with low symmetry is very limited [218]. Thus, Al_3Ni is assumed to be a line compound and corresponding configurational entropy is neglected. The Gibbs free energy of Al_3Ni at different temperatures is replaced by corresponding formation enthalpy at the same temperature, including the vibrational entropic contribution. The ground state phases in the convex hull are connected by the black line in Figure 4.3(a). They include Al, Al_3Ni, Al_3Ni_2, Al_4Ni_3, AlNi, Al_3Ni_5, $AlNi_3$ and Ni. In most experimental and Calphad Ni-Al phase diagrams, all of them were included with the exception of Al_4Ni_3, which is an ordered configuration in the bcc lattice with vacancies, whose structure is displayed in Figure 4.3(b). All vacancies appeared at the Ni sublattice and are arranged so that only one site was occupied by a vacancy in any row of the Ni sublattice along of x, y, or z directions. Actually, Al_4Ni_3 has been experimentally discovered for several times [220-222], and the reported structure is the same as Figure 4.3(b). In addition, it should be noted that different configurations with energies very close to the convex hull (just a few meV/atom) were found for Ni contents between 0.65 and 0.9, in agreement with previous calculations [107].

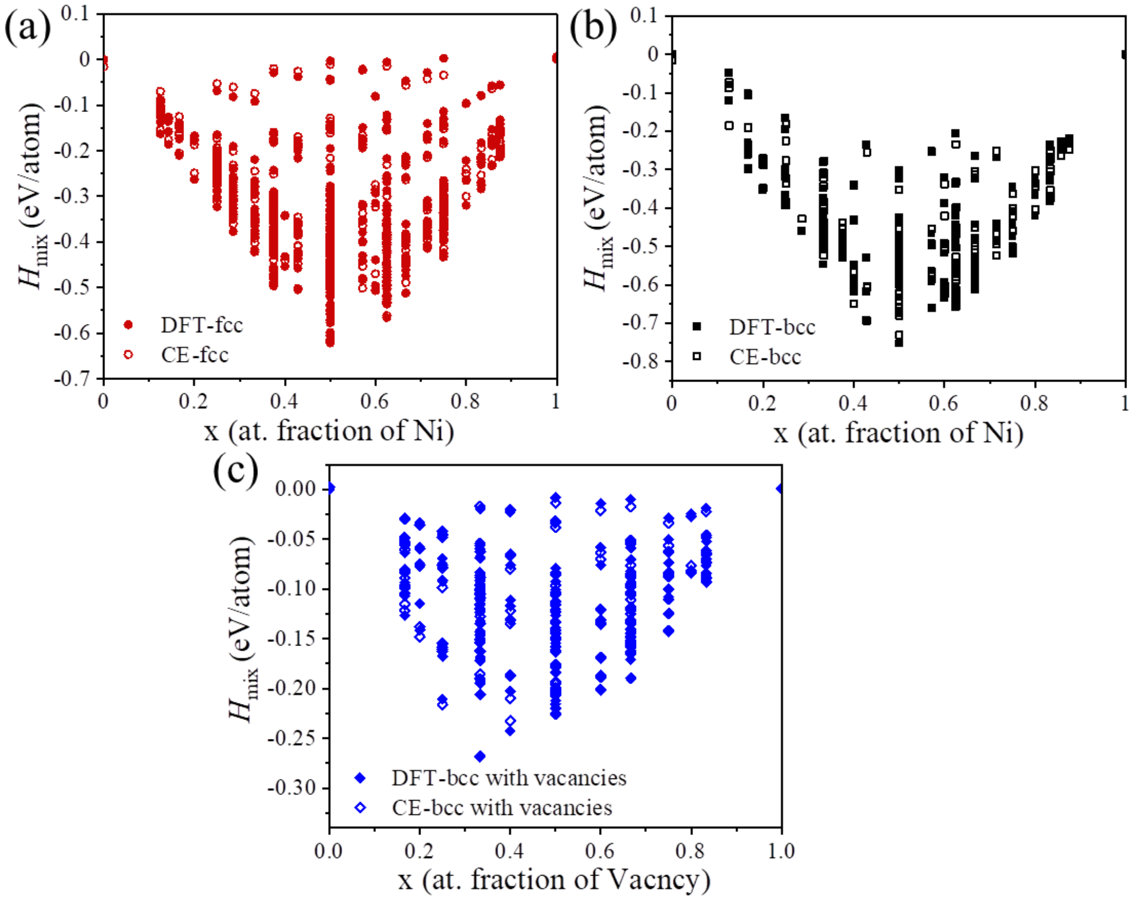

Figure 4.2: Mixing enthalpy of configurations with different lattice symmetry at 0 K. (a) fcc lattice (b) bcc lattice and (c) bcc lattice with vacancies. The mixing enthalpies calculated by DFT are represented by solid symbols, while the predictions using the CE are represented by open symbols.

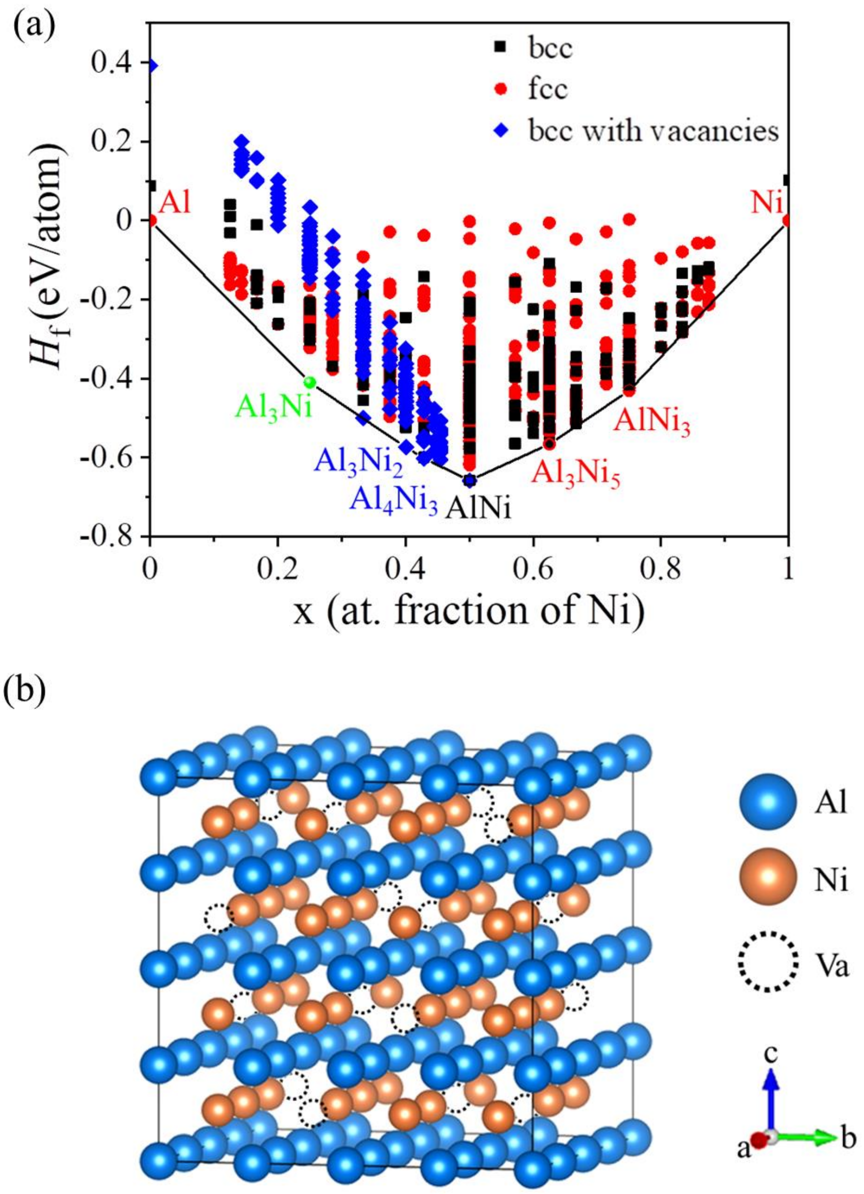

Figure 4.3: (a) Formation enthalpies of all configurations at 0 K. The ground state phases in the convex hull are connected by the black line. Al_3Ni is neither in the bcc nor the fcc lattice, so it is depicted with a green point. Thus, the ground state phases are Al, Al_3Ni, Al_3Ni_2, Al_4Ni_3, AlNi, Al_3Ni_5, $AlNi_3$ and Ni, respectively. (b) Crystal structure of the predicted ground state phase Al_4Ni_3.

The DFT calculations showed that two configurations enumerated in fcc and bcc lattices (depicted in Figures. 4.4(b) and 4(c), respectively) relaxed into the δ-Al_3Ni_5 phase (Figure 4.4(a)). The energy variation during relaxation shown in Figure 4.4(f) reveals that the bcc and fcc Al_3Ni_5 configurations do not coincide with any local minima and will spontaneously collapse to δ-Al_3Ni_5. According to the literature [222], two different routes for the formation of Al_3Ni_5 have been observed: one starts from the $L1_0$ (NiAl) martensite in the fcc lattice (Figure 4.4(d)) and the other from the B_2 (NiAl) in the bcc lattice (Figure 4.4(e)). Moreover, the formation of Al_3Ni_5 appears to be diffusion-controlled [223]. The transformation from $L1_0$ martensite (Figure 4.4(d)) to fcc Al_3Ni_5 (Figure 4.4(b)) only needs short-range diffusion of the Ni atoms in the Al sublattice and leads to small changes in the c/a ratio (from 0.711 in $L1_0$ to 0.749 in fcc Al_3Ni_5). The transformation from B_2 (AlNi) (Figure 4.4(e)) to bcc Al_3Ni_5 (Figure 4.4(c)) involves atomic diffusion plus a Bain-type distortion [210,224-226] to change the c/a ratio from 0.5 in B_2 (AlNi) to 0.749 in bcc Al_3Ni_5. Afterwards, both fcc and bcc bcc Al_3Ni_5 will collapse to δ-Al_3Ni_5 by adjusting the crystal shape (γ from 90° to 97.46°), which is shear controlled. However, the transformation path from $L1_0$ martensite has a steeper slope (Figure 4.4(e)) and the changes in the lattice parameters from $L1_0$ to δ-Al_3Ni_5 (Figure 4.4(b) to (a)) are smaller than from B_2 to δ-Al_3Ni_5 (Figure 4.4(c) to (a)). So, Al_3Ni_5 is treated as a fcc configuration.

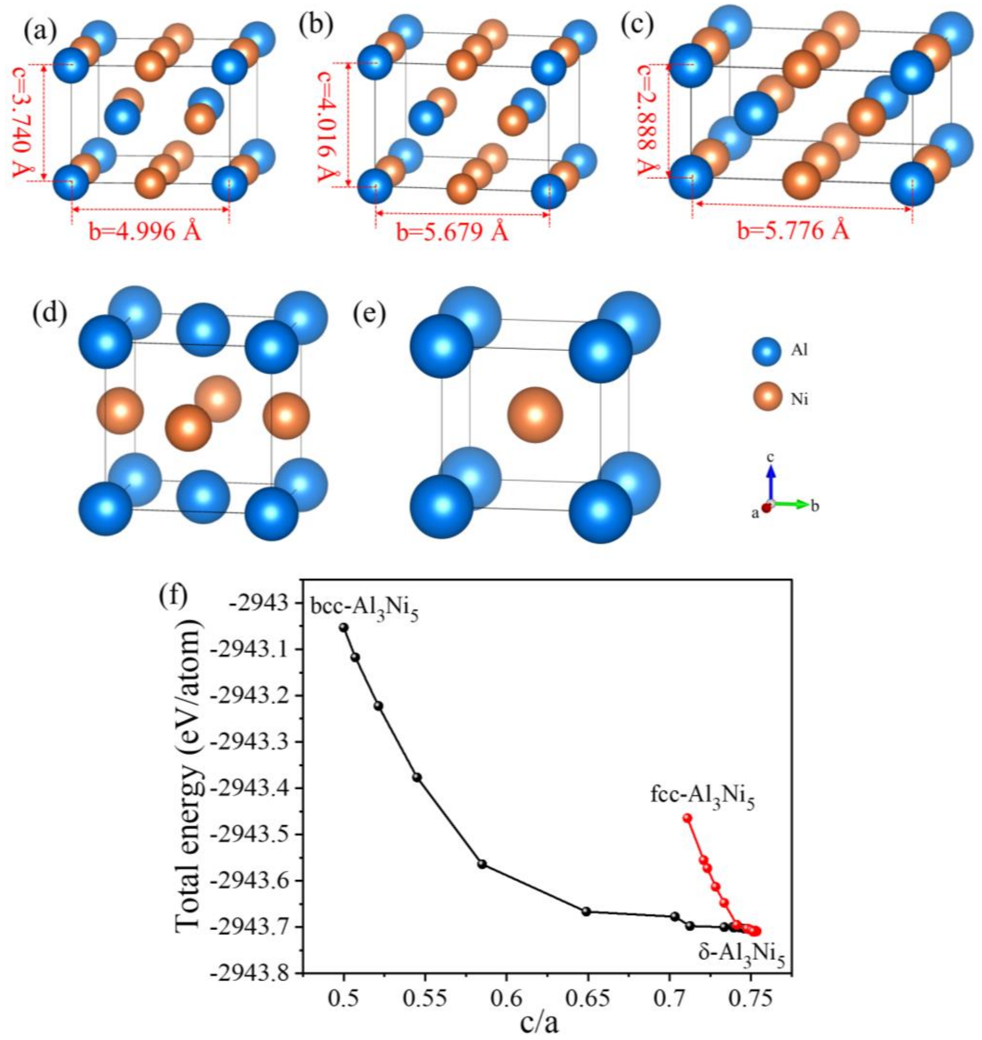

Figure 4.4: Crystal structures of (a) δ-Al_3Ni_5. (b) fcc Al_3Ni_5. (c) bcc Al_3Ni_5. (d) $L1_0$ (NiAl) martensite, (e) B_2 (NiAl). (f) Transformation path (marked by the change in c/a ratio) from bcc-Al_3Ni_5 and fcc- Al_3Ni_5 to δ-Al_3Ni_5.

4.3.3. Bond length vs. bond stiffness relationship

There are three types of chemical bonds between different species in Ni-Al alloys, namely Al-Al, Ni-Ni and Al-Ni bonds. Their L-S relationships in the bcc lattice were obtained from four ordered configurations Al, AlNi, Al_5Ni and Ni, whose structures are shown in Figure 5. The nearest-neighbor (NN) bonds in each lattice are the ones that contribute most to the vibrational free energy [55,227,228], so only the NN bonds were considered. The NN bonds in bcc Al (Figure 4.5(a)) and bcc Ni (Figure 4.5(d)) are Al-Al and Ni-Ni, and their equilibrium bond lengths are 2.782 Å and 2.387 Å, respectively. The NN bonds in bcc AlNi (Figure 4.5(b)) are Al-Al, Ni-Ni and Al-Ni, and the respective equilibrium bond lengths are 2.481 Å, 2.864 Å and 2.864 Å. The NN bonds in bcc Al_5Ni (Figure 4.5(c)) are two kinds of Al-Al (equilibrium bond lengths of 2.850 Å and 2.778 Å), Ni-Ni (equilibrium bond length is 2.778 Å) and Al-Ni (equilibrium bond length is 2.464 Å).

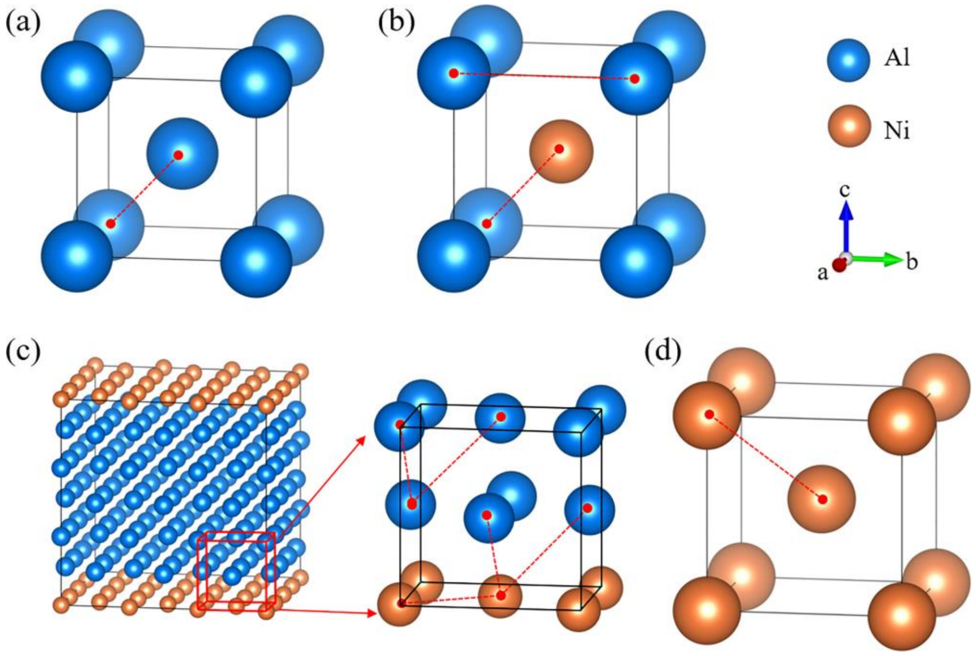

Figure 4.5: Crystal structures of ordered bcc Ni-Al configurations. (a) Al. (b) AlNi. (c) Al_5Ni. (d) Ni. The NN bonds in each crystal structure are indicated by red lines.

The ordered bcc Ni-Al configurations were expanded to different volumes and the force constant matrices of Al-Al, Ni-Ni and Al-Ni bonds in different volumes were determined from full phonon calculations. The stretching and bending stiffnesses of each bond as a function of the bond length are depicted with different symbols in Figure 4.6. The stretching stiffness of the three bonds decrease as bond length increases, while the bending stiffness increases slightly. The L-S relationships of stretching and bending stiffness for each chemical bond were fitted with quadratic polynomials using the least-squares method. They are represented by the black and red curves in Figure 4.6. It is obvious that the L-S relationship for a given chemical bond holds the same trend in different configurations and, thus, the force constant matrix is transferable to different configurations in the bcc lattice.

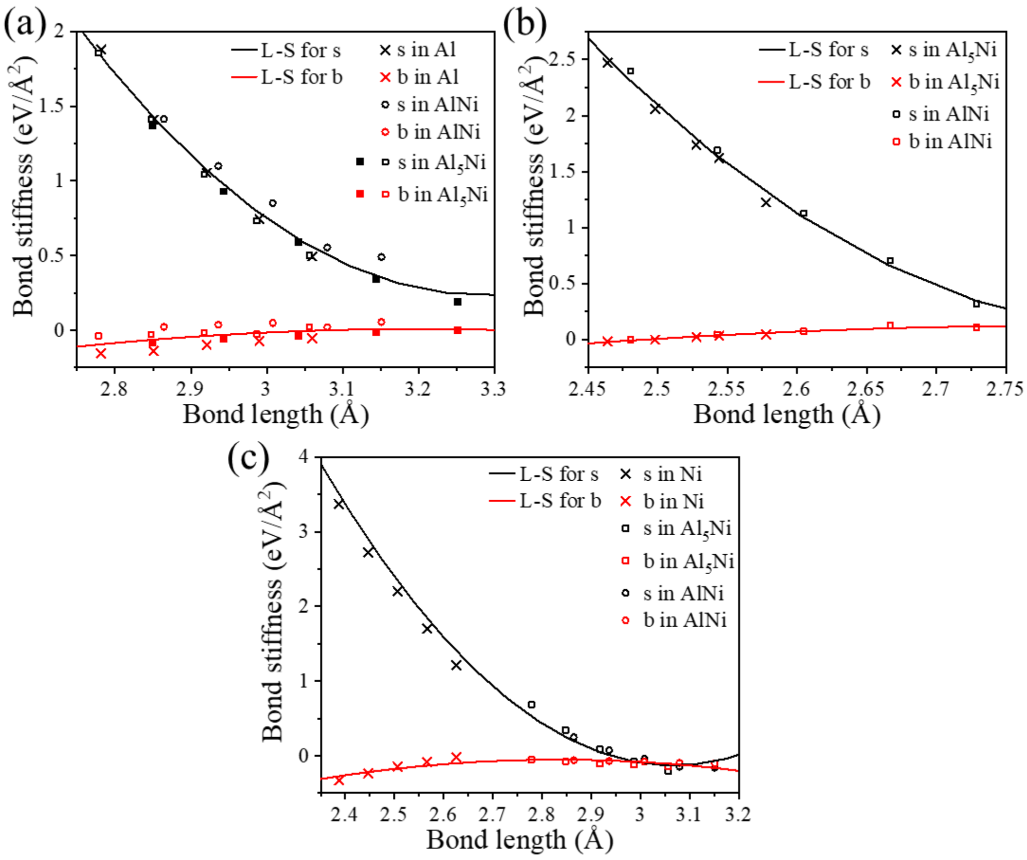

Figure 4.6: Bond length vs. bond stiffness relationships in the bcc lattice. (a) Al-Al bond. (b) Al-Ni bond. (c) Ni-Ni bond. The symbols stand for the results obtained from ordered bcc Ni-Al configurations by full phonon calculations according to eq. (2.11). The black and red curves stand for the fitted quadratic polynomials.

The L-S relationships of Al-Al, Ni-Ni and Al-Ni bonds in the fcc lattice were obtained from four ordered configurations, namely Al, Al_3Ni, $AlNi_3$ and Ni, whose structures are shown in Figure 4.7. The NN bonds in fcc Al and Ni are Al-Al and Ni-Ni (Figures. 4.7(a) and (d)) and their equilibrium bond lengths are 2.837 Å and 2.448 Å, respectively. The NN bonds in fcc $AlNi_3$ (Figure 4.7(c)) are Al-Al and Al-Ni, whose equilibrium bond lengths are both 2.495 Å. The NN bonds in fcc Al_3Ni (Figure 4.7(b)) are two kinds of Al-Al (whose equilibrium bond lengths are 2.588 Å and 2.726 Å), two kinds of Al-Ni (whose equilibrium bond lengths are 2.604 Å and 2.819 Å) and Ni-Ni (whose equilibrium bond length is 2.746 Å).

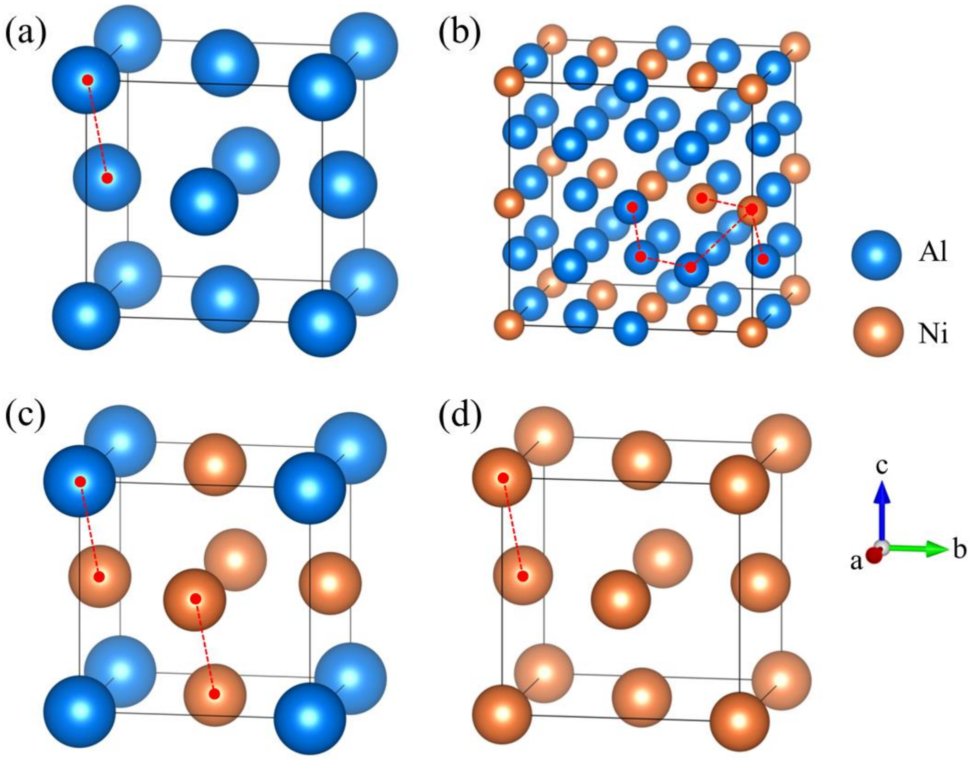

Figure 4.7: Crystal structures of ordered fcc Ni-Al configurations. (a) Al. (b) Al_3Ni. (c) $AlNi_3$. (d) Ni. The NN bonds in each crystal structure are indicated by red lines.

The ordered fcc Ni-Al configurations were expanded to different volumes and the force constant matrix of Al-Al, Ni-Ni and Al-Ni bonds in different volumes were determined by full phonon calculations. The stretching and bending stiffnesses of each bond as a function of the bond length are depicted with different symbols in Figure 4.8, and they show similar trends to those in Figure 4.6. The L-S relationships of stretching and bending stiffness of each chemical bond were fitted into quadratic polynomials using the least-squares method, and the represented by the black and red curves in Figure 4.8.

It should be noted that equivalent simulations were carried out assuming the Ni is non-magnetic. The L-S relationships fitted under this assumption are depicted in Figure B1 in the Annex B. The values of the stretching and bending stiffnesses of the non-magnetic configurations were very close to those obtained with magnetism, and it was concluded that the same L-S relationship can be used for magnetic and non-magnetic configurations.

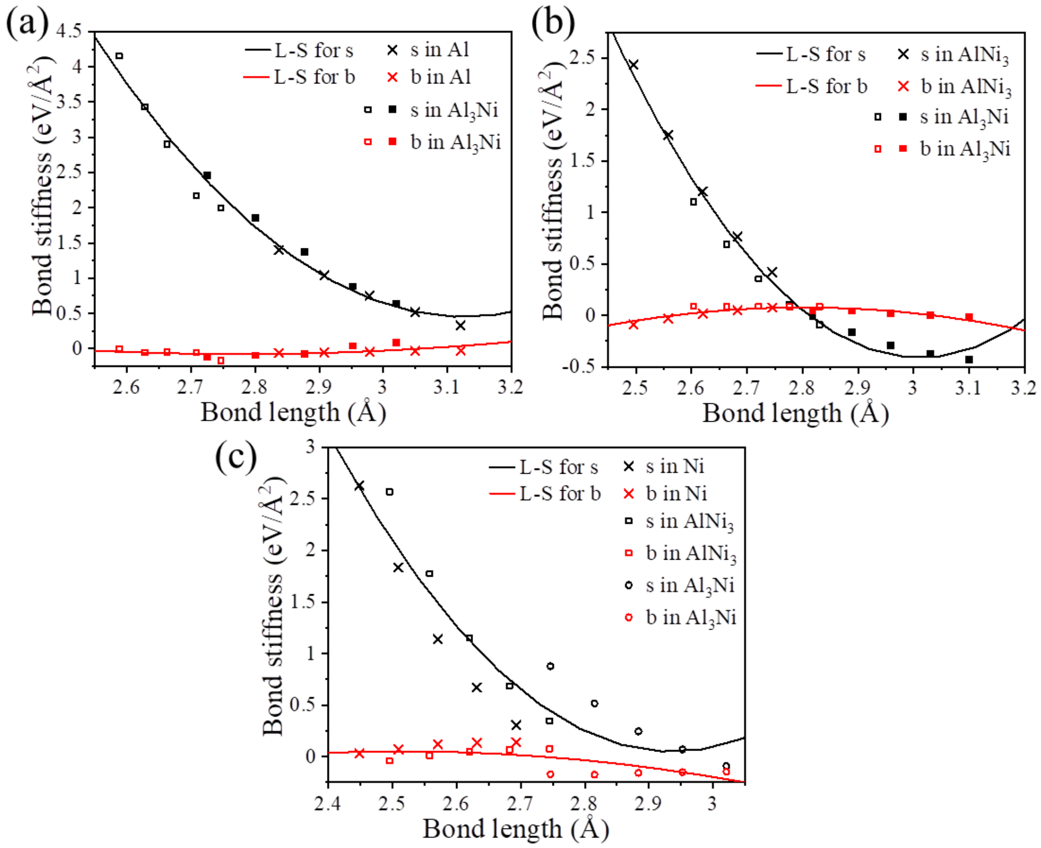

Figure 4.8: Bond length vs. bond stiffness relationships in fcc lattice. (a) Al-Al bond. (b) Al-Ni bond. (c) Ni-Ni bond. The symbols stand for the results obtained from ordered fcc Ni-Al configurations by full phonon calculations according to eq. (2.11). The black and red curves are the fitted quadratic polynomials.

4.3.4. **Vibrational free energy**

The quadratic polynomials in Figures 4.6 and 4.8 can be used to predict the force constant matrix of any bcc and fcc configuration, and as a result, the corresponding vibrational free energy can be obtained through the integration of the phonon DOS through eqs. (2.7) and (2.10). The accuracy of the fitted L-S relationships can be assessed by comparison with the results obtained from full phonon calculations on the most relevant phases of the Ni-Al system. The phonon DOS of Al, Al_3Ni_2, AlNi, Al_3Ni_5, $AlNi_3$ and Ni phases obtained from the L-S relationships (black lines) and from full phonon calculations (red lines) are plotted in Figure 4.9, together with the vibrational free energies, F_{vib}, obtained as a function of temperature. The phonon DOS and vibrational free energies predicted by the L-S relationships are consistent with those obtained from full phonon calculations, including in the case of configurations with vacancies, such as Al_3Ni_2. It should be noted that Al_3Ni is not included in Figure 4.9 because it has an orthorhombic structure and the corresponding L-S relationship was not calculated. The phonon DOS and vibrational free energy of this phase as a function of temperature was only determined from full phonon calculations and it is plotted in Figure 4.10. Additionally, the vibrational free energies of ferromagnetic Ni and $AlNi_3$ are also compared with those of non-magnetic Ni and $AlNi_3$ in Figure B2 in the Annex B. They are superposed, indicating the effect of magnetism on vibrational entropy can be neglected.

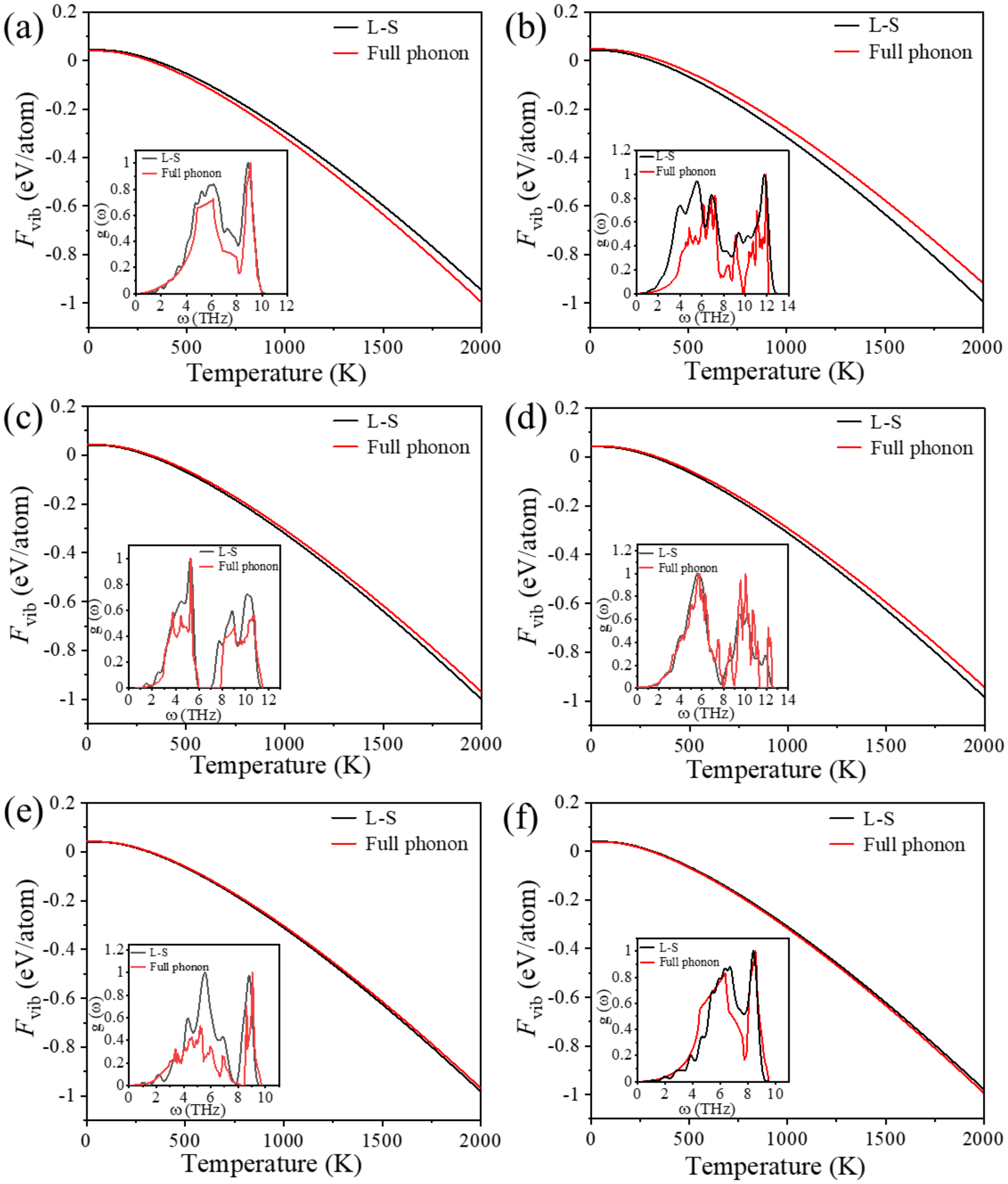

Figure 4.9: Vibrational free energies of the different stable phases in the Ni-Al system obtained from full phonon calculations (red lines) and from the L-S relationships (black lines). (a) γ-Al. (b) $D5_{13}$-Al_3Ni_2. (c) B_2(β)-AlNi. (d) δ-Al_3Ni_5. (e) γ’-$AlNi_3$. (f) γ-Ni. The DOS predicted for each phase using both strategies is plotted in the inset of each Figure.

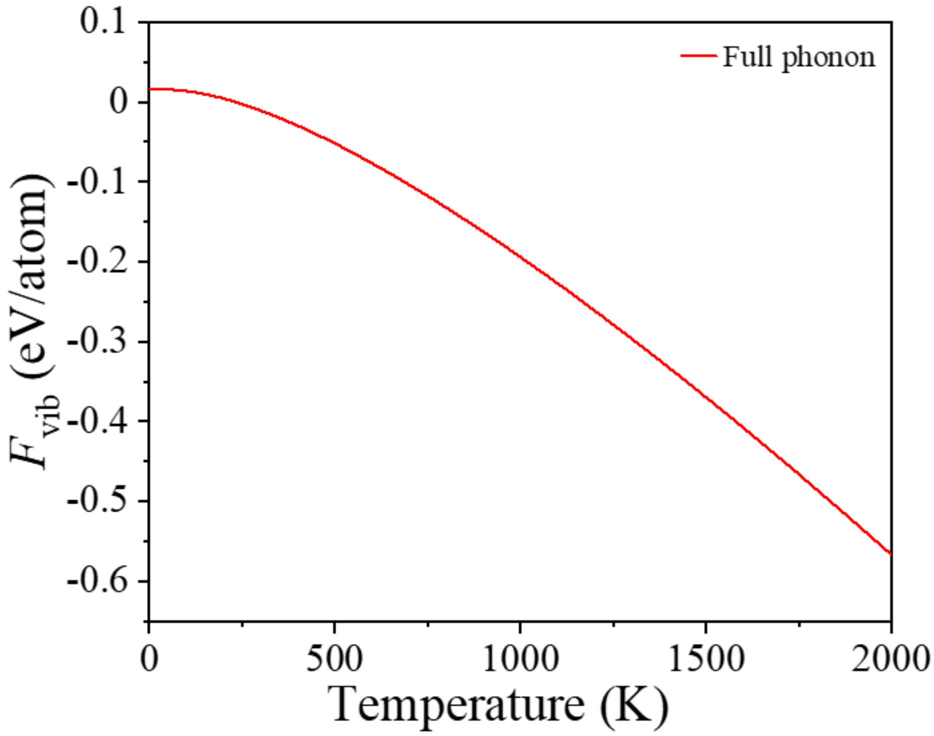

Figure 4.10: Vibrational free energy of Al_3Ni obtained by full phonon calculations.

4.3.5. **Temperature-dependent cluster expansions**

The temperature-dependent ECI of the cluster interactions used in section 4.3.2 for each lattice were fitted based on the vibrational free energy of the configurations. The temperature-dependent ECI coefficients for fcc lattice, bcc lattice and bcc lattice with vacancies are also listed in Tables B4, B5 and B6 in the Annex B. The formation enthalpies at different temperatures (300 K, 600 K, 900 K and 1200 K) of all configurations in the three lattices are plotted in Figure 4.10. They were obtained from the DFT simulations of the formation energy plus the vibrational entropic contribution obtained from the L-S relationships. They are compared with the formation enthalpies predicted by the temperature-dependent CEs in Figure B3, Figure B4 and Figure B5 in the Annex B. Both were in good agreement and the corresponding cross-validation scores were similar to those obtained for the CE at 0 K.

The formation enthalpies in Figure 4.10 include the contribution of formation enthalpy at 0 K and the vibrational entropy at different temperatures. Thus, the convex hulls at different temperatures provide information about the stability change of each phase due to lattice vibration. The phases on the convex hulls at 300 K (Figure 4.11(a)) and 600 K (Figure 4.11(b)) are the same as at 0 K (Figure 4.3(a)). Nevertheless, Al_3Ni (marked with a green symbol) is no longer located in the convex hull at 900 K (Figure 4.11(c)), and this change is due to the vibrational entropy. The vibrational free energy of Al_3Ni is displayed in Figure 4.10 as a function of temperature. The reduction in the vibrational free energy of Al_3Ni with temperature is much smaller than that found for all other stable phases in Figure 4.9, leading to the instability of this phase at high temperature. Other phases including Al, Al_3Ni_2, Al_4Ni_3, AlNi, Al_3Ni_5, $AlNi_3$ and Ni are always on the convex hull.

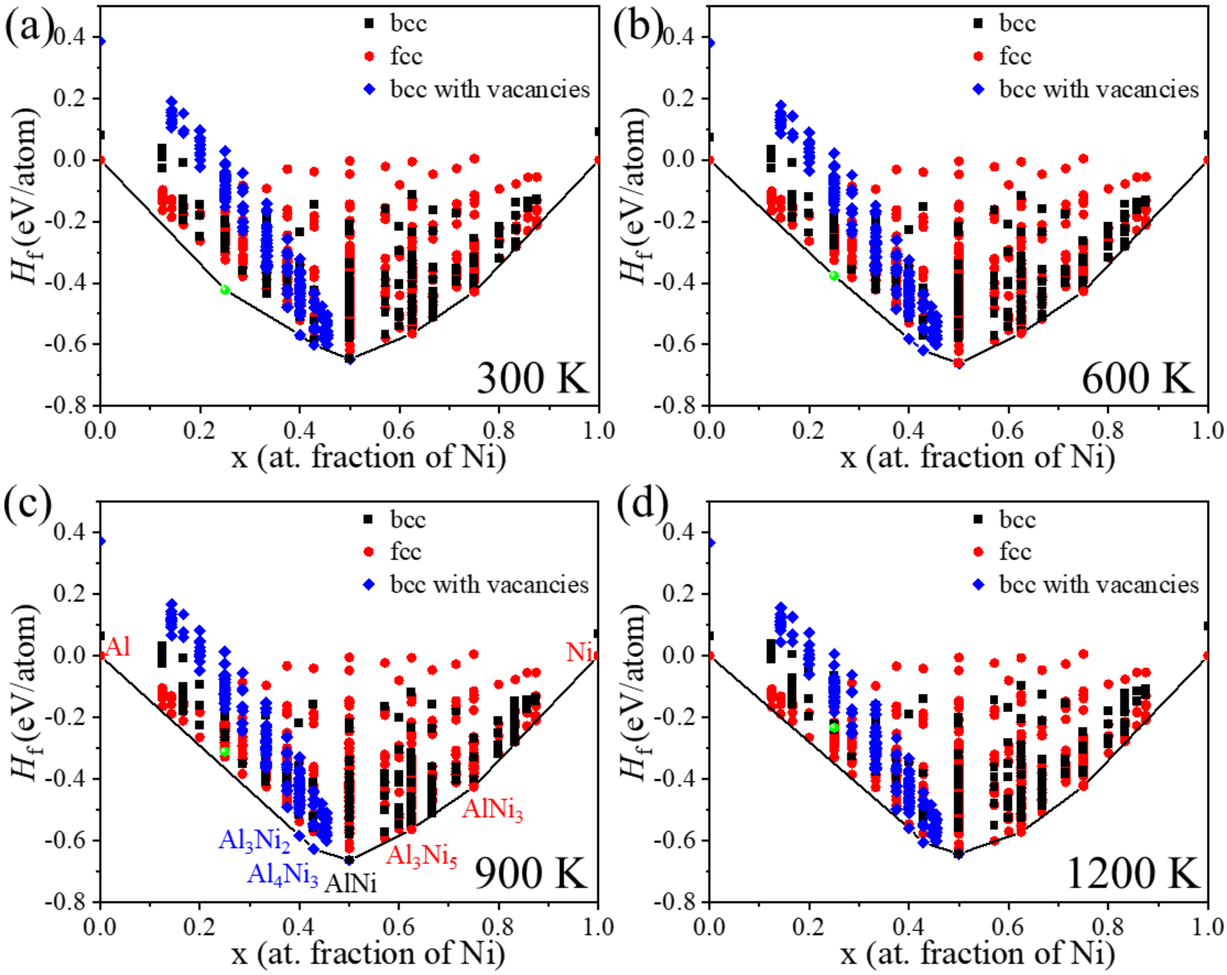

Figure 4.11: Formation enthalpies of all configurations in the Ni-Al system at different temperatures. (a) 300 K. (b) 600 K. (c) 900 K. (d) 1200 K. The red symbols stand for the fcc configurations, the black symbols for the bcc configurations, and the blue symbols symbols for the bcc configurations with vacancies. The green symbol stands for Al_3Ni.

4.4. Phase diagram construction

4.4.1. Al-Al_3Ni phase boundary

Semi-grand canonical MC simulations were performed from each ground state phase. In the Al-rich solid region of the phase diagram, the adjacent phase to fcc Al is Al_3Ni, which has an orthorhombic lattice. Therefore, the solid phase boundary between Al and Al_3Ni can only be determined by the common tangent of their Gibbs free energies. The Gibbs free energy of Al was calculated from eq. (2.32), the Gibbs free energy of Al_3Ni at different temperatures was replaced by the formation enthalpy at different temperatures because it is a line compound. The dash line in Figure 4.12(a) shows the common tangent at 800 K, from which the composition of each phase at this temperature is determined. This strategy was used to obtained the two-phase region between Al and Al_3Ni in Figure 4.12(b). There is no common tangent between both phases, above 930 K, which means that they become solid solutions.

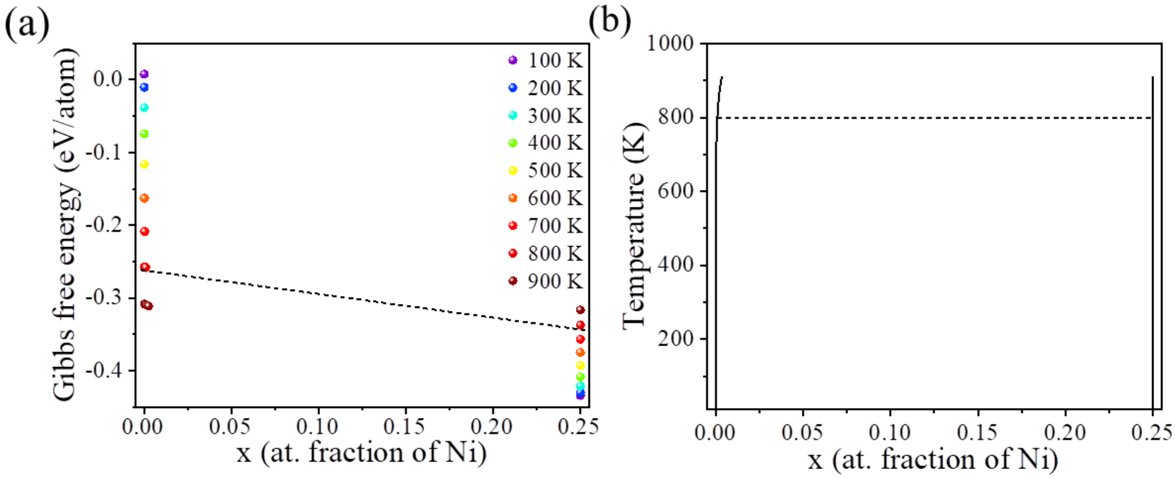

Figure 4.12: (a) Gibbs free energies of Al and Al_3Ni at different temperatures. (b) Phase boundary between Al and Al_3Ni.

4.4.2. Al_3Ni-Al_3Ni_2 phase boundary

The other adjacent phase to Al_3Ni is Al_3Ni_2 and the phase boundary between them also can be determined through the common tangent to their Gibbs free energies because both phases have different lattice structure. The Gibbs free energies of Al_3Ni and Al_3Ni_2 are plotted as a function of temperature in Figure 4.13(a). The dashed line represents the common tangent at 900 K. Above 900 K, the common tangent to their Gibbs free energy does not exist, indicating that they become solid solutions. According to Figure 4.13(a), the two-phase region between Al_3Ni and Al_3Ni_2 is drawn in Figure 4.13(b).

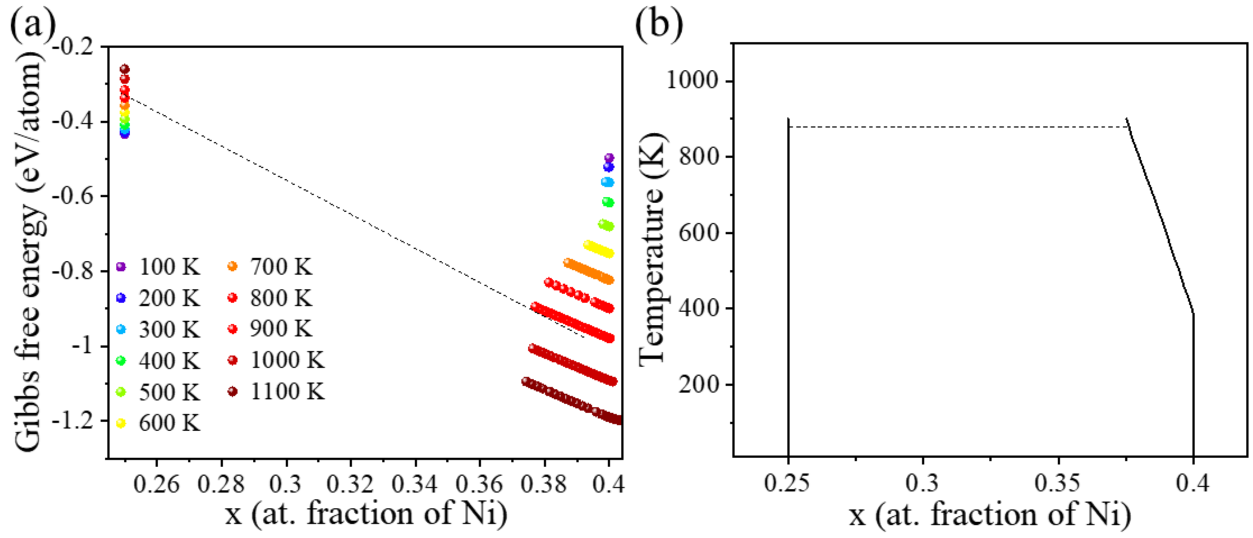

Figure 4.13: (a) Gibbs free energies of Al_3Ni and Al_3Ni_2 at different temperatures. (b) Phase boundary between Al_3Ni and Al_3Ni_2.

4.4.3. Al_3Ni_2-Al_4Ni_3 phase boundary

Al_3Ni_2 and Al_4Ni_3 phases are both in the bcc lattice with vacancies, and the phase boundary between them can be determined from the intersection of the grand potentials. They are plotted as a function of $\Delta\mu$ at 600 K in Figure 4.14(a). It should be noted that the conjugated of $\Delta\mu$ in Figure 4.14(b) is the composition of AlVa because of the sites accommodation in the bcc lattice with vacancies. The composition of AlVa for Al_3Ni_2 is 1/3 while that of Al_4Ni_3 is 0.2485713, which correspond to a Ni content of 0.4 and 0.42857, respectively. The black curves in Figure 4.14(a) and(b) are obtained from Al_3Ni_2 by decreasing $\Delta\mu$, while the red ones are obtained from Al_4Ni_3 by decreasing $\Delta\mu$. $\emptyset_{Al_4Ni_3}$ and $\emptyset_{Al_3Ni_2}$ intersect in Figure 4.14(a). On the left of the intersection, $\emptyset_{Al_4Ni_3} < \emptyset_{Al_3Ni_2}$, which indicates that Al_4Ni_3 is more stable. On the right, $\emptyset_{Al_4Ni_3} > \emptyset_{Al_3Ni_2}$ and Al_3Ni_2 is more stable. The intersection is mapped onto the conjugated composition of AlVa, which is shown in Figure 4.14(b). Then, he atomic fraction of Ni in Al_3Ni_2 and Al_4Ni_3 can be obtained and the phase boundary between Al_3Ni_2 and Al_4Ni_3 at 600 K can be constructed, and it is shown by the dashed line in Figure 4.14(c). In this way, the phase boundary between Al_3Ni_2 and Al_4Ni_3 is built. It shows that Al_4Ni_3 is a line compound. Above 1370 K, the grand potentials for Al_3Ni_2 and Al_4Ni_3 are overlapped, indicating that they become a solid solution.

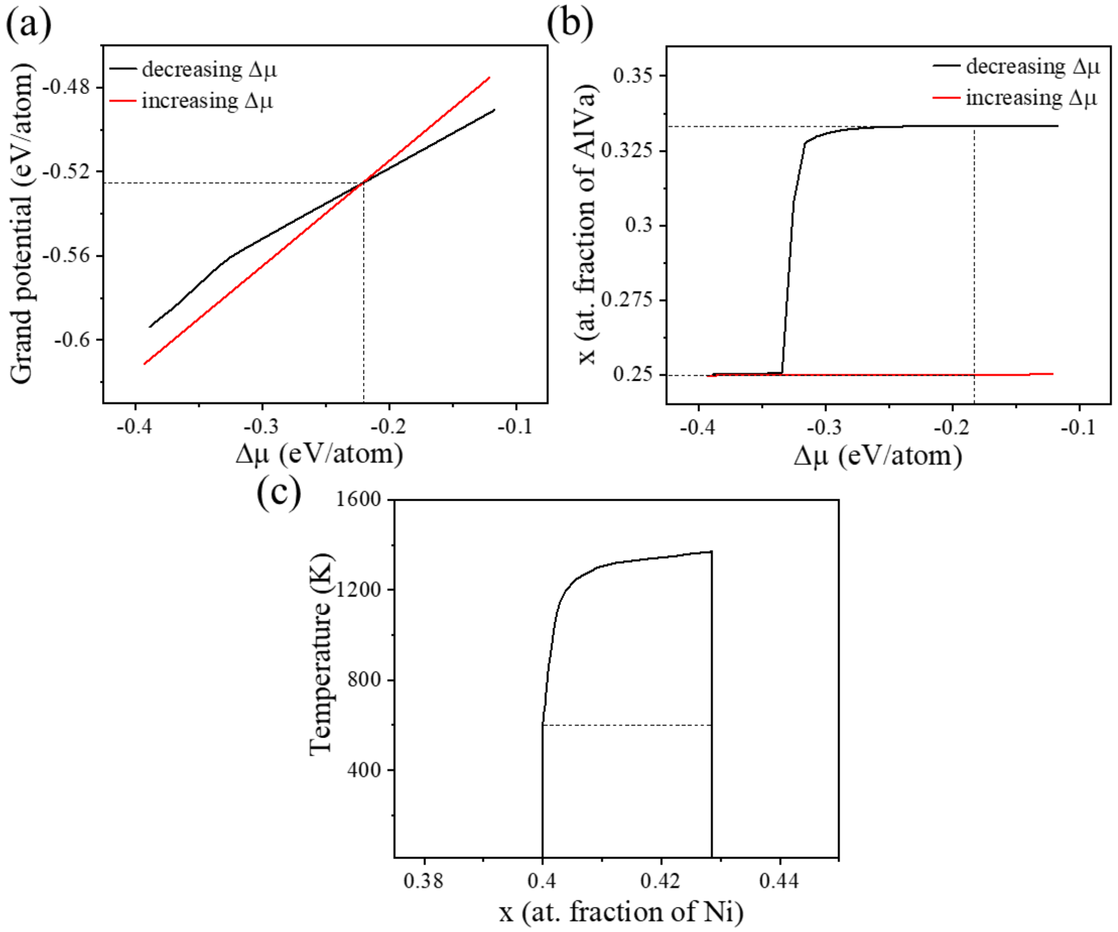

Figure 4.14: (a) Grand potentials of Al_3Ni_2 and Al_4Ni_3 as a function of chemical potential $\Delta\mu$ at 600 K. (b) Composition of AlVa as a function of chemical potential at 600 K. (c) Phase boundary between Al_3Ni_2 and Al_4Ni_3.

4.4.4. Al_4Ni_3-AlNi phase boundary

Al_4Ni_3 is also adjacent to AlNi. Even though AlNi has a bcc lattice, it can also be considered a particular bcc lattice with vacancies, in which the fraction of AlVa is equal to zero. Therefore, the phase boundary between Al_4Ni_3 and AlNi can be obtained from the grand potential obtained by MC simulations in the bcc lattice with vacancies. The grand potentials at 750 K are shown Figure 4.15(a). The black curve corresponds to Al_4Ni_3 by decreasing $\Delta\mu$, while the red one is obtained from AlNi by decreasing $\Delta\mu$. The conjugated composition of AlVa is shown in Figure 4.15(b), where the composition of AlVa for Al_4Ni_3 is 0.2485713 and 0 for AlNi. The equilibrium composition of Ni in Al_4Ni_3 and AlNi is determined by the intersection of both curves and the phase boundary between Al_4Ni_3 and AlNi is plotted in Figure 4.15(c). Above 1370 K, the grand potentials of Al_4Ni_3 and AlNi are overlapped and they become a solid solution.

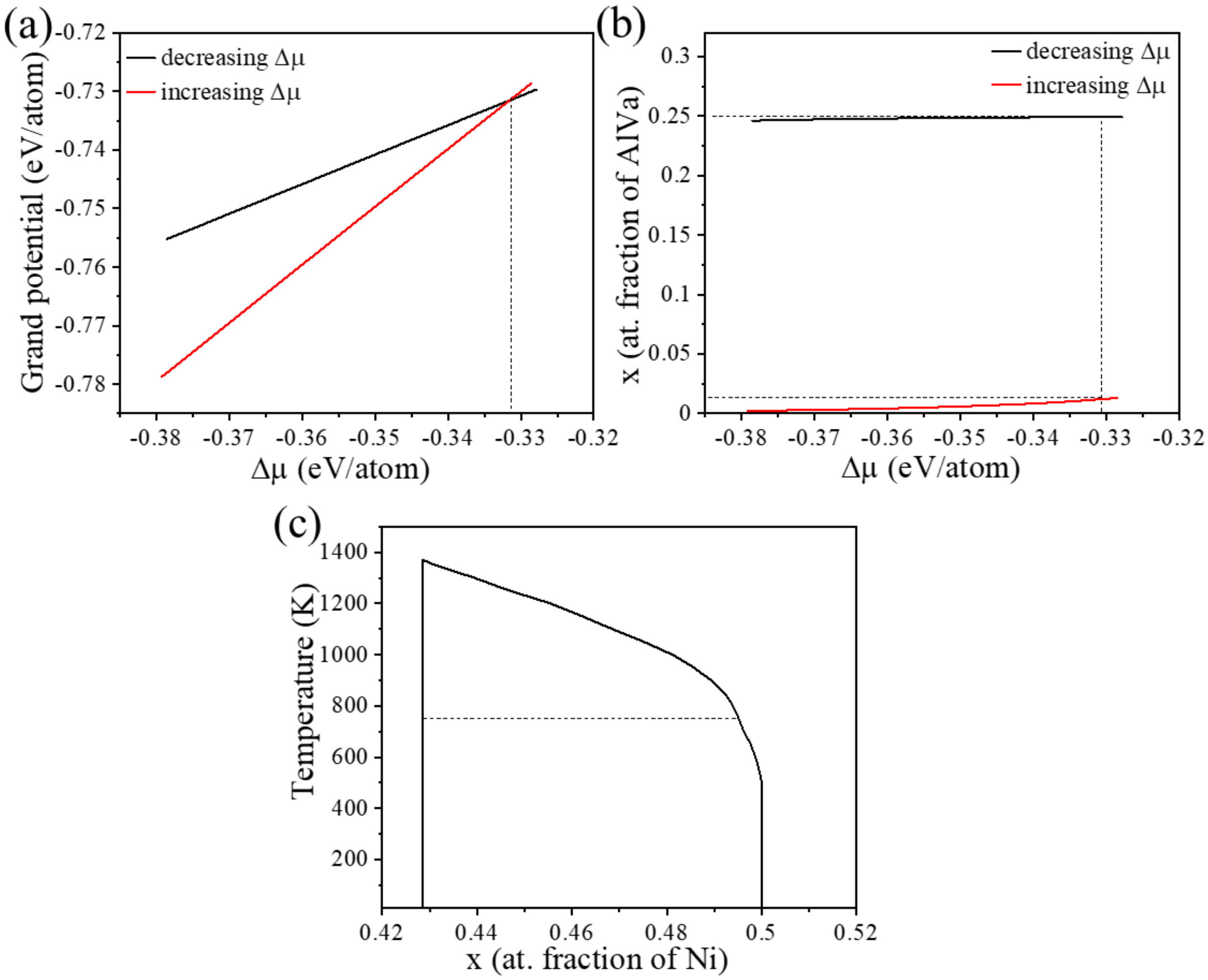

Figure 4.15: (a) Grand potentials of Al_4Ni_3 and AlNi as a function of the chemical potential $\Delta\mu$ at 750 K. (b) Composition of AlVa as a function of chemical potential at as a function of $\Delta\mu$ at 750 K. (c) Phase boundary between Al_4Ni_3 and AlNi.

4.4.5. **AlNi-Al_3Ni_5 phase boundary**

The adjacent phase to AlNi on the other side of the phase diagram is Al_3Ni_5, which has a fcc lattice. Therefore, the phase boundary between AlNi and Al_3Ni_5 can only be determined by the common tangent of their Gibbs free energy. The dash black line in Figure 4.16(a) stands for the common tangent at 900 K, which indicates the equilibrium chemical potential of AlNi and Al_3Ni_5. The common tangent always cuts the Gibbs free energy of Al_3Ni_5 at $x = 0.625$, which indicates AlNi does not have any solubility in Al_3Ni_5. The two-phase region of AlNi and Al_3Ni_5 exists up to 1020 K, which is slightly higher than that in experimental phase diagram (973 K) [208]. The Gibbs free energies of AlNi and Al_3Ni_5 overlap with each other above 1020 K.

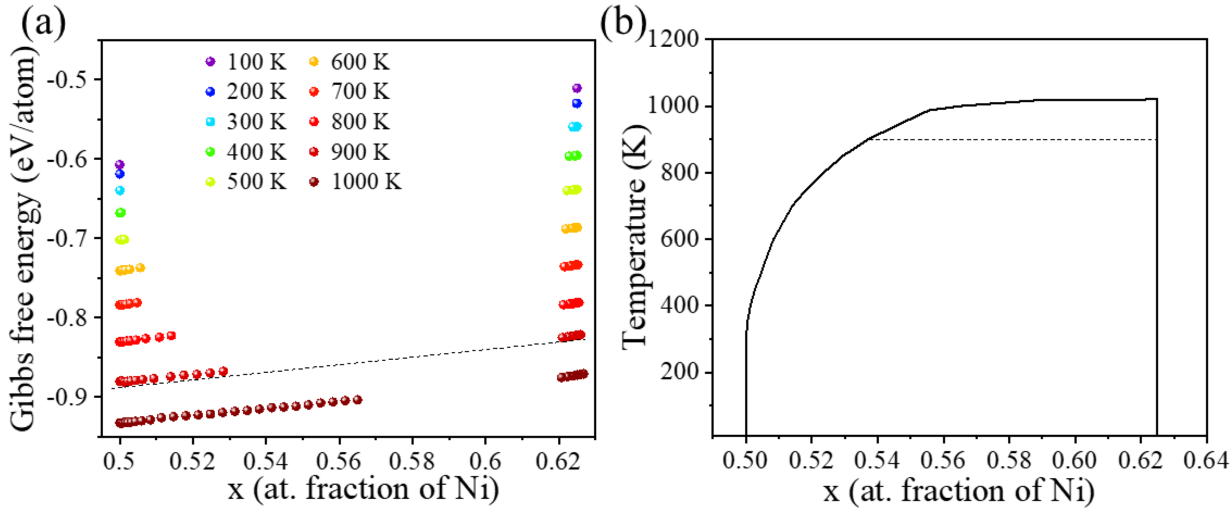

Figure 4.16: (a) Gibbs free energy of AlNi and Al_3Ni_5 at different temperatures. (b) Phase boundary between AlNi and Al_3Ni_5.

4.4.6. **Al_3Ni_5-$AlNi_3$ phase boundaries**

Al_3Ni_5 and $AlNi_3$ are both in the fcc lattice, so their phase boundary can be determined by the intersection of their grand potentials, which is shown in Figure 4.17(a) at 700 K. The black curve indicates the grand potential obtained from Al_3Ni_5 by increasing chemical potential, while the red curve indicated that obtained from $AlNi_3$ by decreasing chemical potential. The intersection is mapped onto the conjugated composition of Ni (Figure 4.17(b)) and the equilibrium composition of Ni in Al_3Ni_5 and $AlNi_3$ at 700 K was determined. The phase boundary between Al_3Ni_5 and $AlNi_3$ is plotted in Figure 4.17(c).

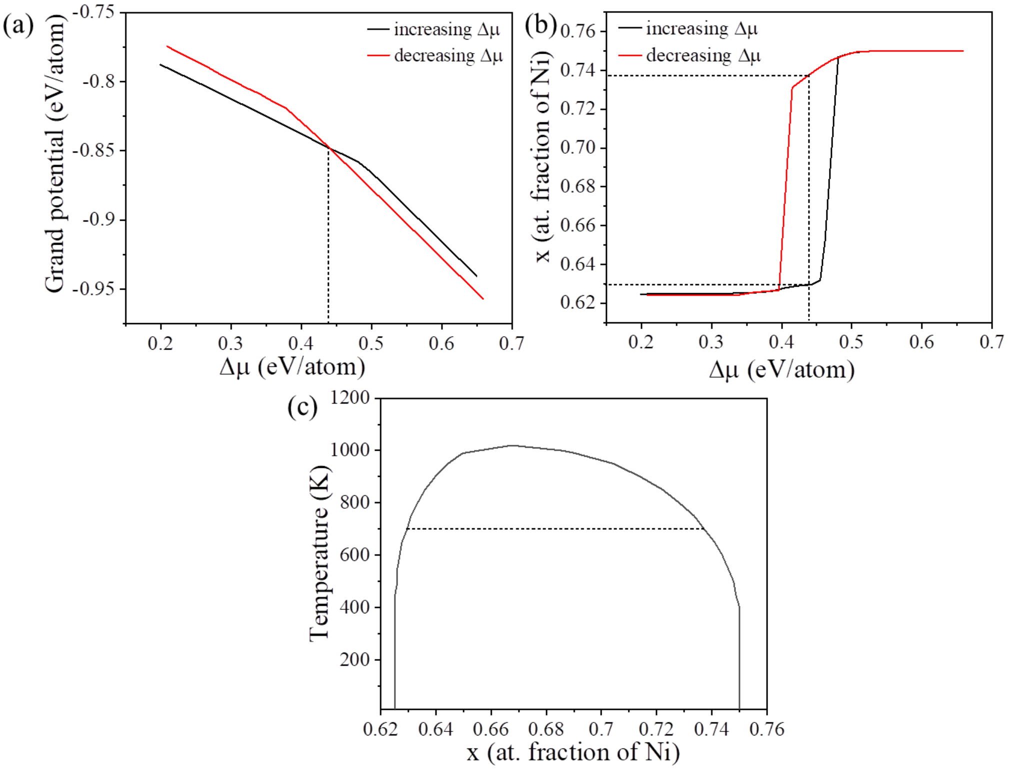

Figure 4.17: (a) Grand potentials of Al_3Ni_5 and $AlNi_3$ as a function of chemical potential at 700 K. (b) Composition of Ni as a function of chemical potential at 700 K. (c) Phase boundary between Al_3Ni_5 and $AlNi_3$.

4.4.7. **AlNi-AlNi$_3$ phase boundary**

According to literature, the two-phase region between AlNi and $AlNi_3$ was observed at high temperature. Therefore, the phase boundary between them was constructed according to their Gibbs free energy. The result is shown in Figure 4.18.

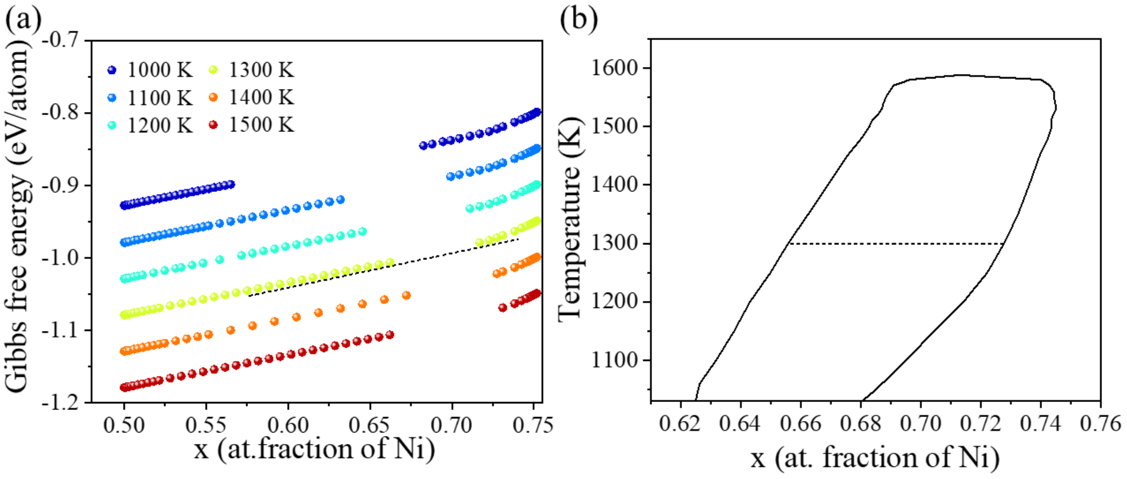

Figure 4.18: (a) Gibbs free energy of AlNi and $AlNi_3$ at temperature above 1300 K; (b) Phase boundary between AlNi and Al_3Ni_5.

4.4.8. $AlNi_3$-Ni phase boundary

Finally, the intersection of the grand potential was used to obtain the phase boundary between $AlNi_3$ and Ni, since both share the fcc lattice. The grand potentials obtained by increasing and decreasing chemical potential at 600 K are plotted in Figure 4.19(a) and the conjugated composition of Ni is plotted in Figure 4.19(b), from which the phase boundary between $AlNi_3$ and Ni is obtained (Figure 4.19(c)). The two-phase region between $AlNi_3$ and Ni exists up to 1640 K, which is slightly higher than that in experimental phase diagram (1623 K) [204].

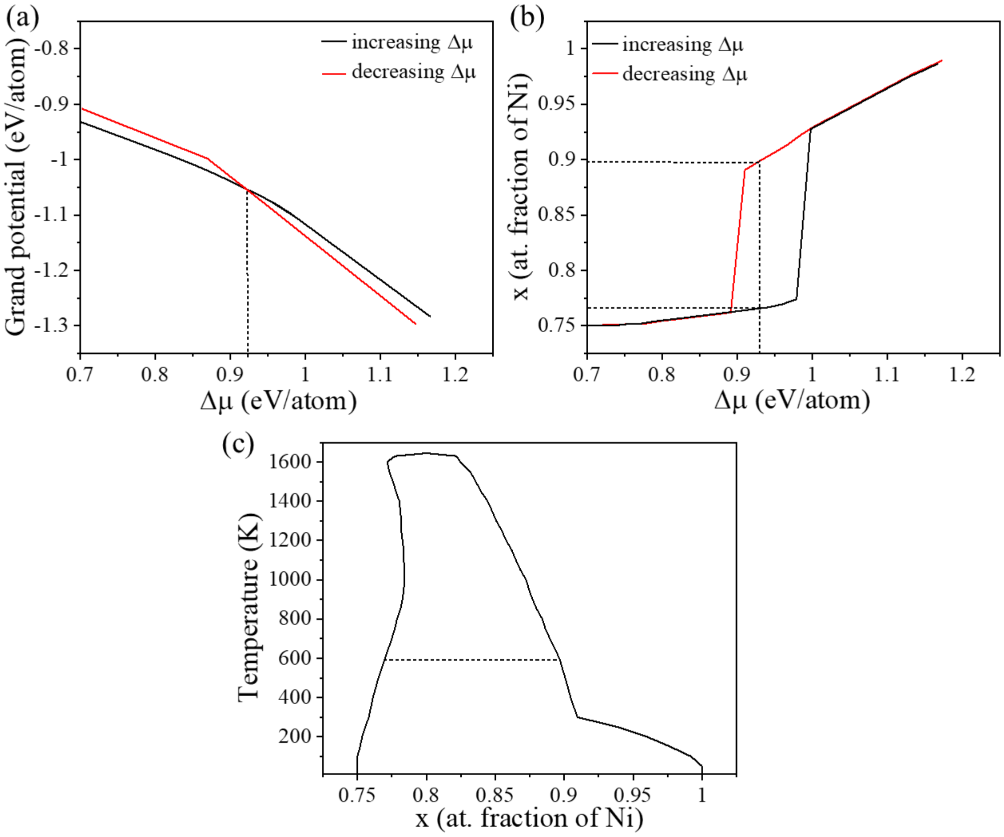

Figure 4.19: (a) Grand potentials of $AlNi_3$ and Ni as a function of chemical potential at 600 K. (b) Composition of Ni as a function of chemical potential at 600 K. (c) Phase boundary between $AlNi_3$ and Ni.

4.5. Discussion

4.5.1. Comparison with the experimental phase diagram

The phase boundaries between adjacent phases were integrated to build the Ni-Al phase diagram, which is plotted in Figure 4.20(a) with red lines. The black lines in Figure 4.20 stand for the accepted experimental phase diagram [204]. Overall, the calculated phase diagram is in excellent agreement with the experimental one, and this result demonstrates the potential of this methodology to determine the thermodynamic properties of each phase by including configurational and vibrational entropic contributions as well as the magnetic enthalpy. The calculated Al-Al_3Ni two-phase region and the Al_3Ni-Al_3Ni_2 two-phase regions are practically superposed to the experimental ones up to 900 K. The solubility of Ni in α-Al matrix is very low: simulations predicted a maximum solubility of 3.5 at.% at 930 K while the experimental phase diagram reaches 4.5 at.% at 916 K. The Al_3Ni phase is a line compound with a critical equilibrium temperature of 930 K according to our calculations, which is very close to 916 K in the experimental phase diagram. Moreover, the phase boundaries concerning Al_4Ni_3 phase were determined in the Al-rich region of the phase diagram by our simulations. This line compound with a critical equilibrium temperature of 1370 K was recently reported experimentally [206,229].

An AlNi single-phase region appears in the phase diagram at high temperature, which is facilitated by different mechanisms, namely vacancies on the Ni sublattice in the Al-rich part and the substitution of Al atoms by Ni atoms on the Al sublattice in the Ni-rich part. The right boundary of the AlNi single-phase region (which is also the left boundary of the AlNi-Al_3Ni_5 two-phase region) is not fully consistent with the experimental one. The discrepancy can be attributed transformation mechanism responsible for the nucleation of Al_3Ni_5. Al_3Ni_5 is an intermediate product of the reversible martensitic transformation from B_2 to $L1_0$ and the presence and composition of Al_3Ni_5 is controlled by the aging temperature and the heating rate. For instance, the Al_3Ni_5 phase may come directly from the $L1_0$ martensite during a heating-up stage if the heating rate was not fast enough [230]. The Al_3Ni_5 phase can also be formed from B_2 after aging at 500 °C [225]. Different formation mechanisms may lead to large discrepancies in the experimental left boundary of the AlNi-Al_3Ni_5 two-phase region boundary and the Al_3Ni_5 phase was not even observed in some experiments [231]. In our calculation, Al_3Ni_5 is formed from either fcc ordering or bcc ordering (the former one is more likely) by atomic diffusion and shear transformation, as explained in Section 4.3.2. The calculated maximum temperature for the two phase AlNi-Al_3Ni_5 region is 1020 K, close to the experimental value of 973 K. Approaching the Ni-rich part, the calculated critical equilibrium temperature of $AlNi_3$ phase (1640 K) as well as the solvus line are in good agreement with the experimental data. It should be noted that the calculated phase diagram provides novel information about the solvus line below 300K. This information is not available experimentally.

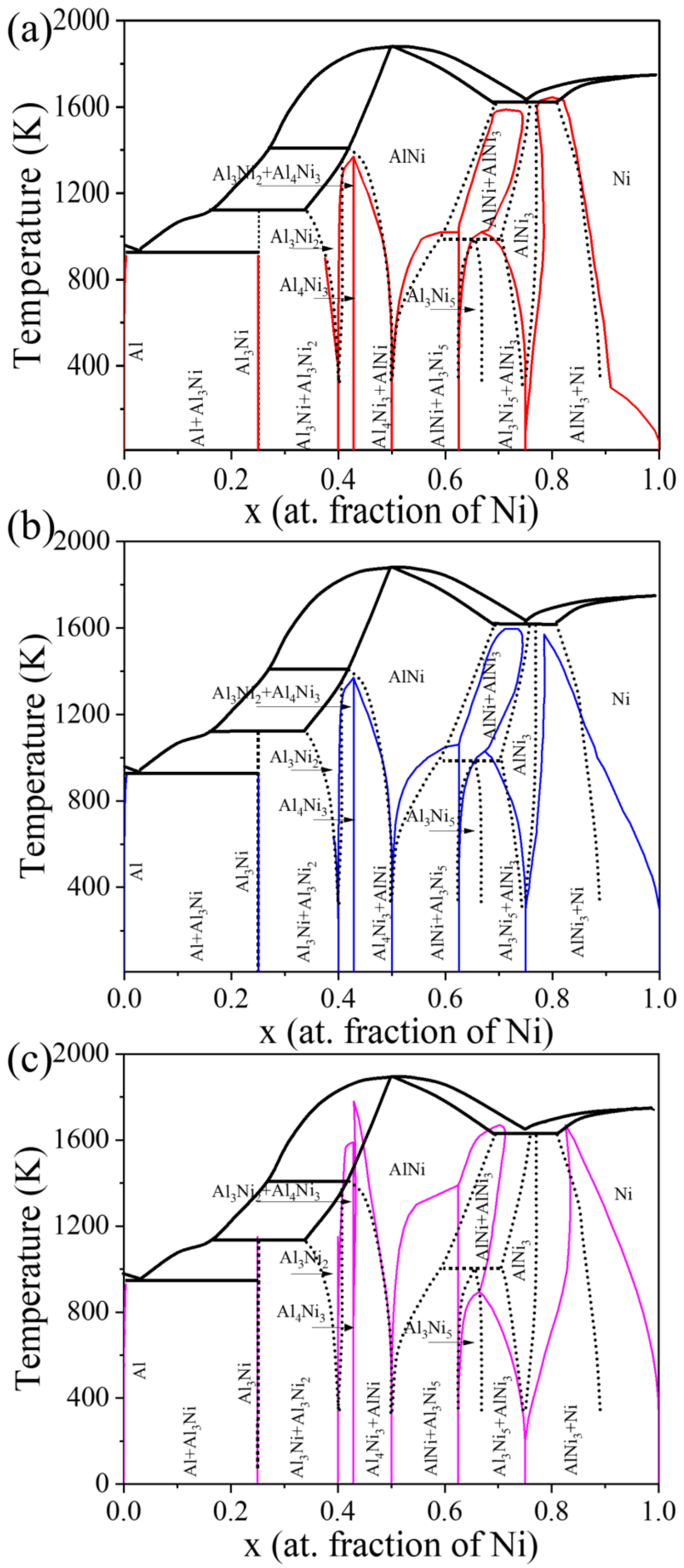
(a)
(b)
(c)
Temperature (K)
x (at. fraction of Ni)
2000
1600
1200
800
400
0
0.0
0.2
0.4
0.6
0.8
1.0
AlNi
Ni
Al
Al+Al3Ni
Al3Ni
Al3Ni+Al3Ni2
Al4Ni3+AlNi
AlNi+Al3Ni5
Al3Ni5+AlNi3
AlNi3+Ni
Al3Ni2+Al4Ni3
Al3Ni2
Al4Ni3
Al3Ni5
AlNi+AlNi3
AlNi3

Figure 4.20: Comparison of the experimental Ni-Al phase diagram [204] (black lines) with those obtained for first-principles calculations Phase diagrams by calculation and by experiments. (a) Calculated phase diagram including magnetic enthalpy as well as configurational and vibrational entropy (red lines). (b) Calculated phase diagram including only configurational and vibrational entropy (blue lines) and neglecting the magnetic enthalpy (c) Calculated phase diagram including only configurational entropy (purple lines).

4.5.2. Influence of magnetism and vibrational entropy

One advantage of the simulations is that the different contributions to the thermodynamic properties of the phases can be turned off to ascertain their influence. Thus, the Ni-Al phase diagram can be obtained following exactly the same methodology but neglecting the effect of magnetic enthalpy. This is achieved by assuming that the stable phase reference phases in the Ni-rich part of the Ni-Al phase diagram (γ-Ni and γ’-$AlNi_3$) are non-magnetic. The Energy difference (ΔE), magnetism moment and volume of ferromagnetic and non-magnetic $AlNi_3$ and Ni are compared in Table 4.2. The total magnetic moments of the ferromagnetic phases are in a good agreement with experimental and calculated data in the literature references. Moreover, the total energy of ferromagnetic Ni slightly lower than that of non-magnetic Ni (the energy difference between them is in Table 4.2) indicating that the former is more stable. The differences in the total energy between ferromagnetic and non-magnetic $AlNi_3$ are, however, negligible. Therefore, neglecting the magnetic contribution can lead to important errors in the calculation of the Ni-rich region of the phase diagram. The whole solid phase diagram was built without considering the magnetic enthalpy and it is plotted in Figure 4.20(b). The corresponding phase boundaries between adjacent phases are depicted in Figure B6-B11 in the Annex B. As expected, the calculated $AlNi_3$-Ni boundary in the phase diagram show large discrepancies with the experimental one. It should be noted that at higher temperature, the spins will fluctuate, which will lead to an entropy contribution from magnetism. This contribution is smaller than the configurational and vibrational contribution so it was ignored in this work.

Table 4.2: Energy difference (ΔE) between non-magnetic and ferromagnetic phases, magnetic moment and volume of ferromagnetic and non-magnetic $AlNi_3$ and Ni.

Composition	ΔE (eV/atom)	Volume/atom (Å^3)	Magnetic moment (μ_B)	
			This work	Experimental Calculated
Ferromagnetic $AlNi_3$	0	10.896	0.76	0.71 [232]

				0.73 [233]
Non-magnetic $AlNi_3$	0.004	10.883	-	-
Ferromagnetic Ni	0	10.369	0.6	0.605 [222] 0.65 [234]
Non-magnetic Ni	0.061	10.312	-	-

The predicted Ni-Al phase diagram only considering the configurational entropic contribution is shown by the green lines in Figure 4.20(c). The corresponding phase boundaries between adjacent phases are depicted in Figure B12-B19 in the Annex B. Overall, the phase diagram at low temperatures is very similar to the one in Figure 4.20(a) because the configurational enthalpy (namely the formation energy) dominates over the entropic contributions. Nevertheless, large discrepancies arise in the critical equilibrium temperatures. For instance, the maximum temperature of Al_3Ni_2-Al_4Ni_3, Al_4Ni_3-AlNi and AlNi-Al_3Ni_5 two phase regions are overestimated by several hundred K, while the Al_3Ni_5-$AlNi_3$ two phase region is several hundred K below the experimental one. The solubility of phases is also affected by the vibrational entropic contribution, especially in the Ni-rich part. Therefore, the formation enthalpy can provide the information about the stoichiometry and the lattice of stable phases, while the addition of the configurational entropy allows good enough predictions of the low temperature region of the phase diagram. However, the lattice vibration contribution has to be taken into account if accuracy is needed at high temperature.

4.6. Conclusions

The phase diagram of the Ni-Al system was predicted by means of first principle simulations and statistical mechanics. it was found that all phases - with the exception of Al_3Ni - can be treated as configurations existing on fcc or bcc lattices, with the atomic sites accommodating Al and Ni atoms, or - in the case of Al_3Ni_2 - bcc lattices with the Ni sublattice sites of AlNi accommodating Ni atoms and vacancies. The temperature-dependent mixing enthalpies of the configurations in each lattice were approximated by the cluster expansion formalism, including the effect of magnetisms and of vibrational entropy which was calculated from the corresponding length-stiffness relationships. The thermodynamic grand potential of each phase and the Gibbs free energy were calculated from MC simulations and used to predict the phase diagram.

Seven ground state phases were found at 0 K, namely Al, Al_3Ni, Al_3Ni_2, Al_4Ni_3, AlNi, Al_3Ni_5, $AlNi_3$ and Ni. Among them, Al_4Ni_3 and Al_3Ni were line compounds. The predicted phase diagram was in excellent agreement with the current experimentally accepted Al-Ni phase diagram and provided accurate predictions of the two-phase boundaries, critical equilibrium temperatures and solubility of the phases. Moreover, the phase boundary between $AlNi_3$ and Ni below 300 K was reported. Overall, these results demonstrate the accuracy of the methodology employed to predict accurately the phase diagram of alloys of technological interest.

Predictions of the phase diagram were carried out neglecting the effect of magnetism and of vibrational entropy. They showed that the former is important to predict the phase boundaries and the critical equilibrium temperatures in the Ni-rich of the phase diagram (> 75% Ni) while vibrational entropy is necessary to predict accurately the features of the phase diagram (two phase boundaries, solubilities, critical equilibrium temperatures) above 400 K.

Data availability

The computational data generated in this chapter can be found at https://zenodo.org/doi/10.5281/zenodo.12527913.

5. Prediction of the Co-Al phase diagram

5.1. Introduction

Advanced superalloys with excellent mechanical properties at high temperature as well as wear and corrosion resistance, chemical stability and low thermal expansion coefficient are necessary to improve the performance of gas turbines [235]. In particular, novel Co-based superalloys have attracted widespread attention because they have higher melting temperature than Ni-based superalloys, which endow Co-based superalloys with excellent strength at high temperature [114,118] as well as creep resistance [236]. Moreover, Co-based superalloy exhibit superior corrosion resistance, wear resistance, and weldability compared with Ni-base superalloys [115]. Precipitates based on the $Co_3(Al, X)$ (X= W, Cr, Mo, Ni) [238-240] phase are the main strengthening phases, particularly at high temperature. They come from the unstable Co_3Al (γ’) phase, that is stabilized by replacing with X the Al sublattice in the Co_3Al structure. These potential advantages open up a pathway to the exploitation of novel Co-based superalloy as the next generation of high-temperature materials. But a thorough understanding of the Co-Al phase diagram is necessary to optimize the stability and mechanical properties of Co-based superalloys.

In this chapter, the solid-state region of the Co-Al phase diagram is accurately predicted from first-principles calculations and statistical mechanics principles. Configurational entropic contributions to the free energy were included through MC simulations using the CE formalism. The vibrational entropy of each phase was determined through the L-S relationship associated with the lattice. The magnetic contribution was also included through the Heisenberg Hamiltonian[64]. The computed phase diagram is compared with the currently accepted experimental phase diagram and the different contributions to the stability of different phases are analyzed independently. The potential of this strategy to predict phase diagrams of magnetic systems is clearly established.

5.2. Methodology

5.2.1. DFT calculations

Different configurations in fcc, bcc and hcp lattices of the Co-Al system were enumerated using the ATAT code [158], and their enthalpy at 0 K was obtained by first-principles calculations based on DFT with Quantum Espresso [240]. The electronic exchange-correlation contributions were described by the generalized gradient approximation, as parameterized by the PBE method and ultrasoft pseudopotentials [186]. The Brillouin zone was sampled by using a Monkhorst-Pack scheme [241] with a k-point density of 40 points/Å^{-1}. A cutoff energy of 90 Ry was used in all calculations. Each configuration was fully relaxed under zero pressure, where the cell and the atomic degrees of freedom were allowed to change until energy difference was below 10^{-7} eV and the forces difference was smaller than 10^{-4} eV/Å. An initial spin polarization was set for Co atoms and collinear calculations on magnetism were included during relaxation. Thus, the following fitted CEs contain the magnetic contribution to enthalpy.

5.2.2. **Vibrational free energy calculation**

For each lattice, a L-S relationship was fitted to predict the phonon DOS of each configuration. The L-S relationship was determined as follow. Three or four different configurations in each lattice (since these relationships are transferable in configurations within the same lattice) were expanded up to 10% in volume with an increment of 2% after full relaxation to generate different atomic bond lengths. Supercells of the expanded configurations were constructed, and a displacement of 0.1 Å was applied to each symmetrically distinguished atom within. Then, self-consistent calculations were performed to obtain the forces acted on each atom due to the displacements. The configurations used in each lattice and the corresponding supercell size are listed in Table 5.1.

A L-S relationship was fitted for each chemical bond (namely Al-Al, Co-Co or Al-Co) from the stiffness values obtained for the same chemical bonds with different length. The eigenvalues of dynamical matrix $D_{i,j}(q)$ can be obtained from the Fourier transform of $\Psi(i,j)$ at wavevector q [242], and this information is used to determine the phonon DOS. Therefore, the phonon DOS of any configuration can be easily obtained from the L-S relationship fitted for a given lattice, instead of using expensive phonon calculations of supercells.

Table 5.1: Supercell size and k points for fcc, hcp and bcc configurations used to determine the L-S relationship.

fcc	Supercell size	hcp	Supercell size	bcc	Supercell size
Al	4×4×4	Al	4×4×4	Al	3×3×4
AlCo	3×3×3	$AlCo_3$	3×3×3	Al_2Co	3×3×4
Co	4×4×4	Co	4×4×4	AlCo	3×3×4

	Co	3×3×4

5.2.3. Magnetic free energy calculation

Only the coupling constant between Co-Co pair is needed in the Co-Al system, while those between Al-Al and Al-Co atoms are considered as 0 because Al is non-magnetic. The coupling constants between Co-Co pairs in different lattices can be obtained from pure Co from eq. (2.12). To this end, bcc, fcc and hcp pure Co in different magnetic states (Figure 5.1) were fully relaxed using the same parameters and convergence criteria. All spins are aligned along the positive z-direction for the FM configurations (Figure 5.1(a)-(c)), while spins on adjacent layers have opposite orientations for the AFM ones (Figure 5.1(d)-(f)). The number of parallel and antiparallel nearest-neighboring pairs is listed in Table 5.2.

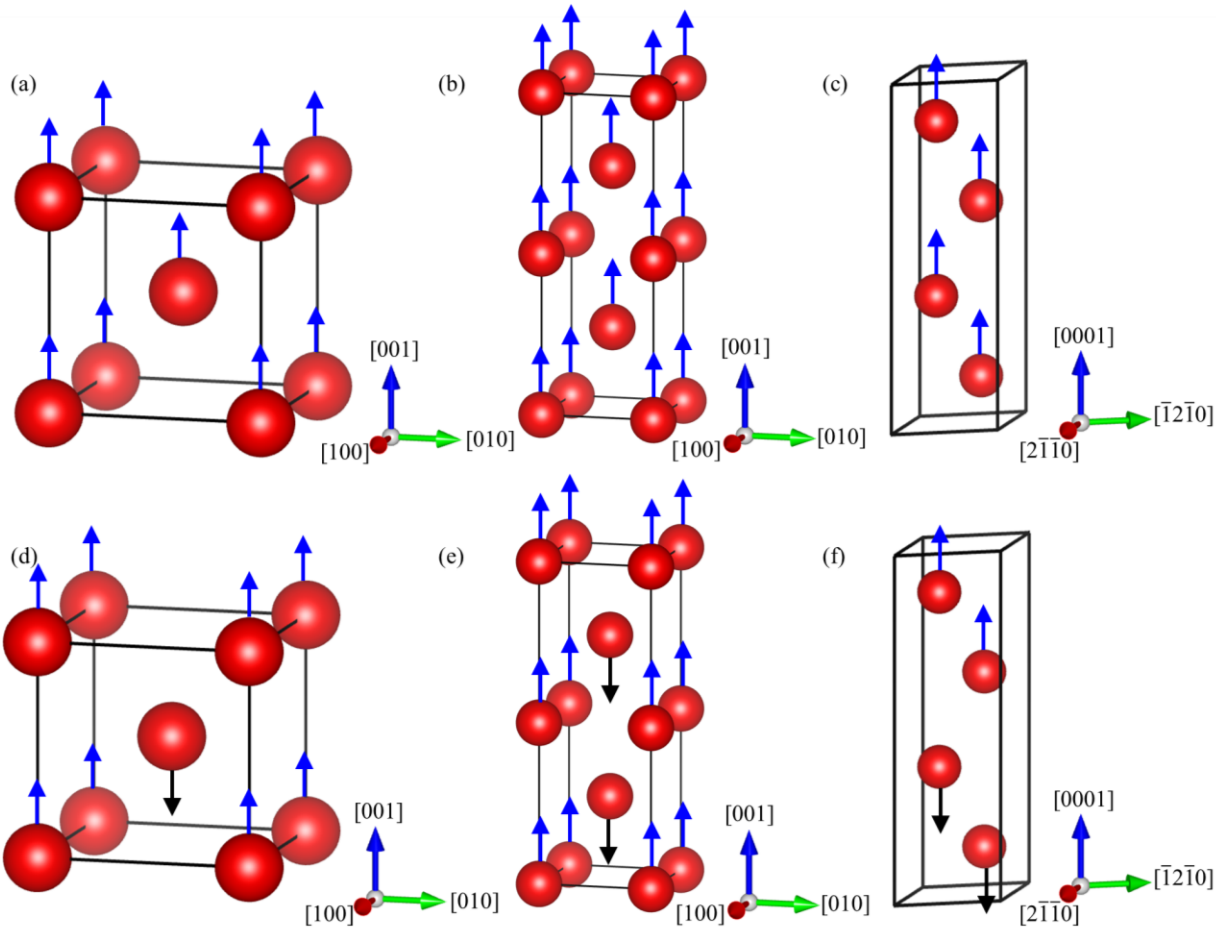

Figure 5.1: Ferromagnetic structures of bcc (a), fcc (b) and hcp Co (c). Antiferromagnetic structures of bcc (d), fcc (e) and hcp Co (f). The arrows denote the spin of each atom.

Table 5.2: Number of parallel ($N_{nn}^{\uparrow\uparrow}$) and antiparallel ($N_{nn}^{\uparrow\downarrow}$) nearest-neighboring pairs in the magnetic configurations displayed in Figure 5.1.

	bcc		fcc		hcp	
	FM	AFM	FM	AFM	FM	AFM
$N_{nn}^{\uparrow\uparrow}$	8	0	12	8	12	9
$N_{nn}^{\uparrow\downarrow}$	0	8	0	4	0	3

5.2.4. **Cluster expansion**

The mixing enthalpy H_{conf} at 0 K due to the atomic occupation of an $Al_{1-x}Co_x$ configuration in a given lattice *s* (in which the lattice sites accommodate either Al or Co atoms) is given by [169]

$$H_{conf}^{Al_{1-x}Co_x} = E_s^{Al_{1-x}Co_x} - (1-x)E_s^{Al} - xE_s^{Co} \tag{5.1}$$

where $E_s^{Al_{1-x}Co_x}$, E_s^{Al} and E_s^{Co} stand for the energy of the relaxed $Al_{1-x}Co_x$, Al and Co in the corresponding lattice s.

The mixing enthalpy contribution due to lattice vibrations in each configuration is given by:

$$H_{vib}^{Al_{1-x}Co_x}(T) = F_{vib,s}^{Al_{1-x}Co_x}(T) - (1-x)F_{vib,s}^{Al}(T) - xF_{vib,s}^{Co}(T) \tag{5.2}$$

where $F_{vib,s}^{Al_{1-x}Co_x}(T)$, $F_{vib,s}^{Al}(T)$ and $F_{vib,s}^{Co}(T)$ stand for the vibrational free energy of $Al_{1-x}Co_x$, Al and Co in the corresponding lattice s at temperature T.

Similarly, the mixing enthalpy contribution due to magnetism is given by:

$$H_{mag}^{Al_{1-x}Co_x}(T) = F_{mag,s}^{Al_{1-x}Co_x}(T) - (1-x)F_{mag,s}^{Al}(T) - xF_{mag,s}^{Co}(T) \tag{5.3}$$

where $F_{mag,s}^{Al_{1-x}Co_x}(T)$, $F_{mag,s}^{Al}(T)$ and $F_{mag,s}^{Co}(\mathrm{T})$ stand for the magnetic free energy of $\mathrm{Al}_{1-\mathrm{x}}\mathrm{Co}_\mathrm{x}$, Al and Co in the corresponding lattice s at temperature T.

Therefore, the temperature-dependent mixing enthalpy H_{mix} - including the configurational and vibrational contributions - of an $Al_{1-x}Co_x$ configuration in each lattice can be summarized from eqs. (5.1) and (5.2) as

$$H_{mix}^{Al_{1-x}Co_x}(T) = H_{conf}^{Al_{1-x}Co_x} + H_{vib}^{Al_{1-x}Co_x}(T) \tag{5.4}$$

while that including the configurational, vibrational, and magnetic contribution can be expressed from eqs. (5.1)-(5.3) as

$$H_{mix}^{Al_{1-x}Co_x}(T) = H_{conf}^{Al_{1-x}Co_x} + H_{vib}^{Al_{1-x}Co_x}(T) + H_{mag}^{Al_{1-x}Co_x}(T) \tag{5.5}$$

CE including the different contributions (configurational, vibrational and magnetic) for each lattice can be fitted from the mixing enthalpies by eqs. (2.22), (2.24) and (2.25). It should be noted that the mixing enthalpies mentioned above are only relative to pure Al and Co in the corresponding lattice, so they are not the real formation enthalpies H_f with respective to fcc Al and hcp Co. To compare the relative stability of configurations in different lattices, the actual formation enthalpies including the configurational contribution are obtained as follows:

$$H_f^{Al_{1-x}Co_x}(T) = \left(E_s^{Al_{1-x}Co_x} - (1-x)E_{fcc}^{Al} - xE_{hcp}^{Co}\right) \tag{5.6}$$

where E_{fcc}^{Al} and E_{hcp}^{Co} stand for the energy of the relaxed fcc Al and hcp Co.

The actual formation enthalpy including both the configurational and vibrational contribution is obtained by:

$$H_f^{Al_{1-x}Co_x}(T) = \left(E_s^{Al_{1-x}Co_x} - (1-x)E_{fcc}^{Al} - xE_{hcp}^{Co}\right) + \Big(F_{vib,s}^{Al_{1-x}Co_x}(T) - (1-x)F_{vib,fcc}^{Al}(T) - \\ - xF_{vib,hcp}^{Co}(T)\Big) \tag{5.7}$$

while that including configurational, vibrational, and magnetic contributions is expressed as:

$$H_f^{Al_{1-x}Co_x}(T) = \left(E_s^{Al_{1-x}Co_x} - (1-x)E_{fcc}^{Al} - xE_{hcp}^{Co}\right) + \Big(F_{vib,s}^{Al_{1-x}Co_x}(T) - (1-x)F_{vib,fcc}^{Al}(T) - \\ - xF_{vib,hcp}^{Co}(T)\Big) + \Big(F_{mag,s}^{Al_{1-x}Co_x}(T) - (1-x)F_{mag,fcc}^{Al}(T) - xF_{mag,hcp}^{Co}(T)\Big) \tag{5.8}$$

5.2.5. **Monte Carlo simulations**

A simulation box with a size of 18×18×18 was built for each ground state phase found in the convex hull. Then, MC simulations in semi-grand canonical ensemble were performed using the ATAT code [158] at different T (from 10 K to 2000 K) with an increment of 10 K under a given chemical potential difference with an increment of 0.005 eV/atom. For each value of T and $\Delta\mu$, where $\Delta\mu$ is chemical potential difference between the MC simulation includes 2000 passes for equilibrium, followed by 5000 passes for calculating the thermodynamic averages.

5.2.6. **Magnetic phase transition**

An important feature of the Co-Al phase diagram is the ferromagnetic to paramagnetic phase transition in the Co-rich fcc solid solution. For an ideal solid solution, in which the different species are randomly located on the lattice sites, the correlation function of each cluster α is given by a statistical value expressed by [243]:

$$\rho_\alpha(\sigma^{rnd}) = \prod_i \langle \gamma(\sigma_i) \rangle_\alpha \tag{5.9}$$

where $\langle \gamma(\sigma_i) \rangle_\alpha$ is the averaged probability of the appearance of α on each site i. The correlation functions of each cluster for an ideal solid solution with a given composition are listed in Table C1 in the Annex C.

Supercells of 80 atoms with different Co content (88.5~100 at.%) were constructed with the ATAT code [65,243] to represent the ideal solid solution. The correlation functions of the included clusters were calculated as [243]:

$$\rho_\alpha(\sigma^{SQS}) \equiv \langle \Gamma(\sigma) \rangle_\alpha \tag{5.10}$$

where $\Gamma(\sigma)$ is a cluster function.

The correlation functions of these supercells are listed in Table C1 in the Annex C, where they can be compared with those of the ideal solid solution with the same Co content. They were close and then the corresponding supercells can be recognized as special quasi-random structure (SQS) to represent the ideal solid solution. These SQSs were fully relaxed by DFT calculations to obtain the total energies, equilibrium volumes and magnetic moments. Then, a 10×10×10 supercell was built for each SQS, and MC simulations were performed in the VAMPIRE package [244] to obtain the magnetic free energy, as indicated above. Finally, T_C were determined by finding the peak value of C_{mag} in each SQS with different Co content, and the FM-PM (paramagnetic) phase boundary was determined.

5.3. **Results**

5.3.1. **Formation enthalpy due to configurational occupation**

623 configurations in the bcc lattice, 696 in the fcc lattice and 397 in the hcp lattice were fully relaxed. The configurations whose deformation after relaxation (including shape and atomic position) was < 10% were retained to fit the CE, following the standard criteria [245]. These conditions were fulfilled in 193 configurations in the bcc lattice, 554 in the fcc lattice and 317 in the hcp lattice. The average magnetic moment of each configuration is shown in Figure 5.2. The average magnetic moments of almost all configurations are zero in the Al-rich region, but they are different from 0 in the Co-rich region. Thus, the configurations on the Co-rich side exhibit ferromagnetism. The magnetic moments of pure bcc Co, fcc Co and hcp Co are 1.76 μ_B, 1.64 μ_B and 1.605 μ_B, respectively, and they are close to the data reported in the literature, i.e. 1.77 μ_B [246], 1.67 μ_B [247] and 1.58 μ_B [248], respectively.

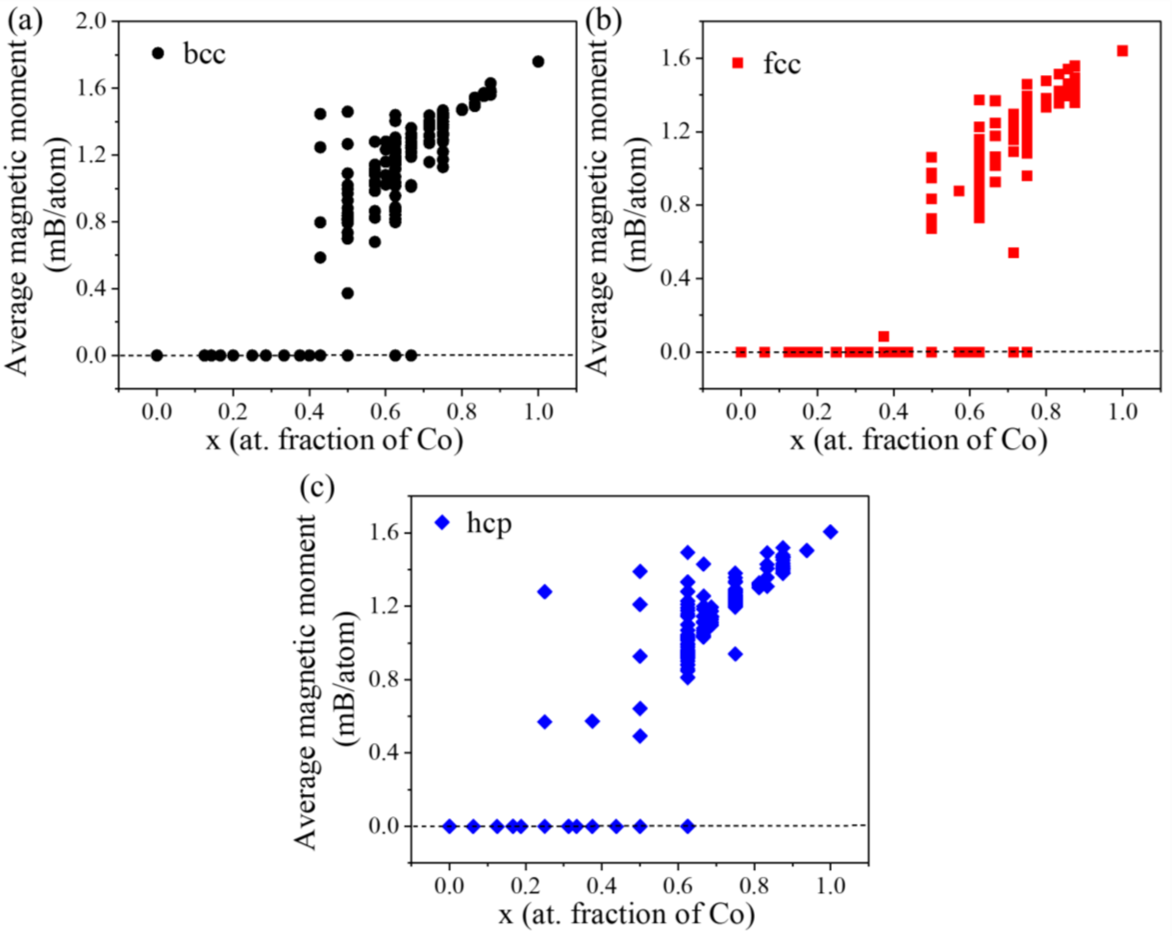

Figure 5.2: Average magnetic moment of all configurations in the Co-Al system at 0 K. (a) bcc lattice. (b) fcc lattice. (c) hcp lattice.

The mixing enthalpy of each configuration, H_{conf}, was obtained from eq. (5.1) and they are plotted with open symbols in Figure 5.3. The ECI parameters of the CE were fitted for each lattice by eq. (2.22) using the ATAT code [158]. The CE for the bcc lattice includes 9 pair cluster interactions, 17 triplet cluster interactions and 1 quadruplet cluster interactions. The CE for the fcc lattice includes 9 pair cluster interactions, 3 triplet cluster interactions and 52 quadruplet cluster interactions. The CE for the hcp lattice includes 15 pair cluster interactions, 11 triplet cluster interactions and 24 quadruplet cluster interactions. Their ECIs are depicted in Tables C2, C3 and C4 in the Annex C. The mixing enthalpies predicted by the CEs (solid symbols) are compared with those obtained by DFT (open symbols) in Figure 5.3. They are in good agreement, and the corresponding cross-validation scores are 0.01749 eV/atom, 0.0168 eV/atom and 0.01306 eV/atom for the bcc, fcc and hcp lattices, respectively.

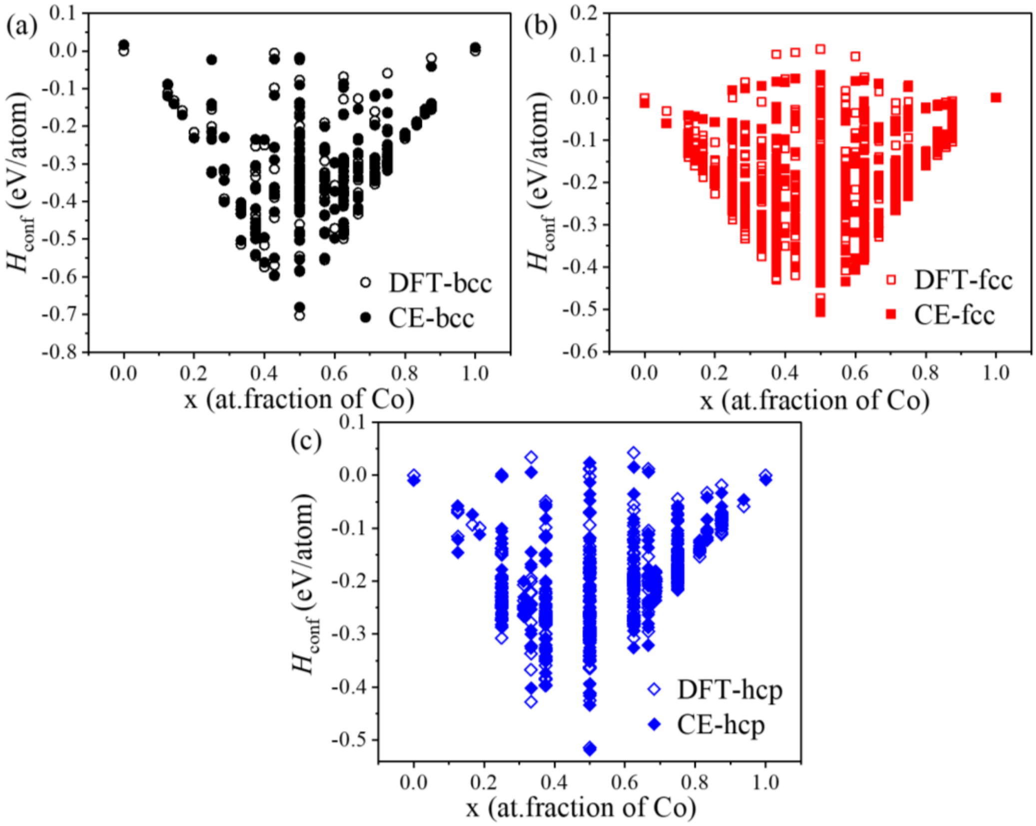

Figure 5.3: Mixing enthalpy at 0 K due to configurational occupation, H_{conf}, of configurations in different lattices. (a) bcc lattice. (b) fcc lattice. (c) hcp lattice. The values calculated by DFT are represented with open symbols, while the values predicted by CE are represented with solid symbols.

The actual formation enthalpies at 0 K, H_f^{conf}, of all configurations in the three lattices were obtained from eq. (5.1), and they are plotted in Figure 5.4. The formation enthalpies of other complex crystal structures in Co-Al system (namely Al_9Co_2, $Al_{13}Co_4$, Al_3Co and Al_5Co_2, which were reported experimentally [250-252]) are also included in the Figure and their structures are displayed in Figure 5.5. The primitive cells of these four phases contain 28, 22, 16 and 102 atoms, respectively, they were assumed to be line compounds. Their configurational entropy was neglected to calculate the free energy because it is known to be very small in phases with low symmetry [252]. Thus, their Gibbs free energy at different temperatures only include the vibrational and magnetic contributions.

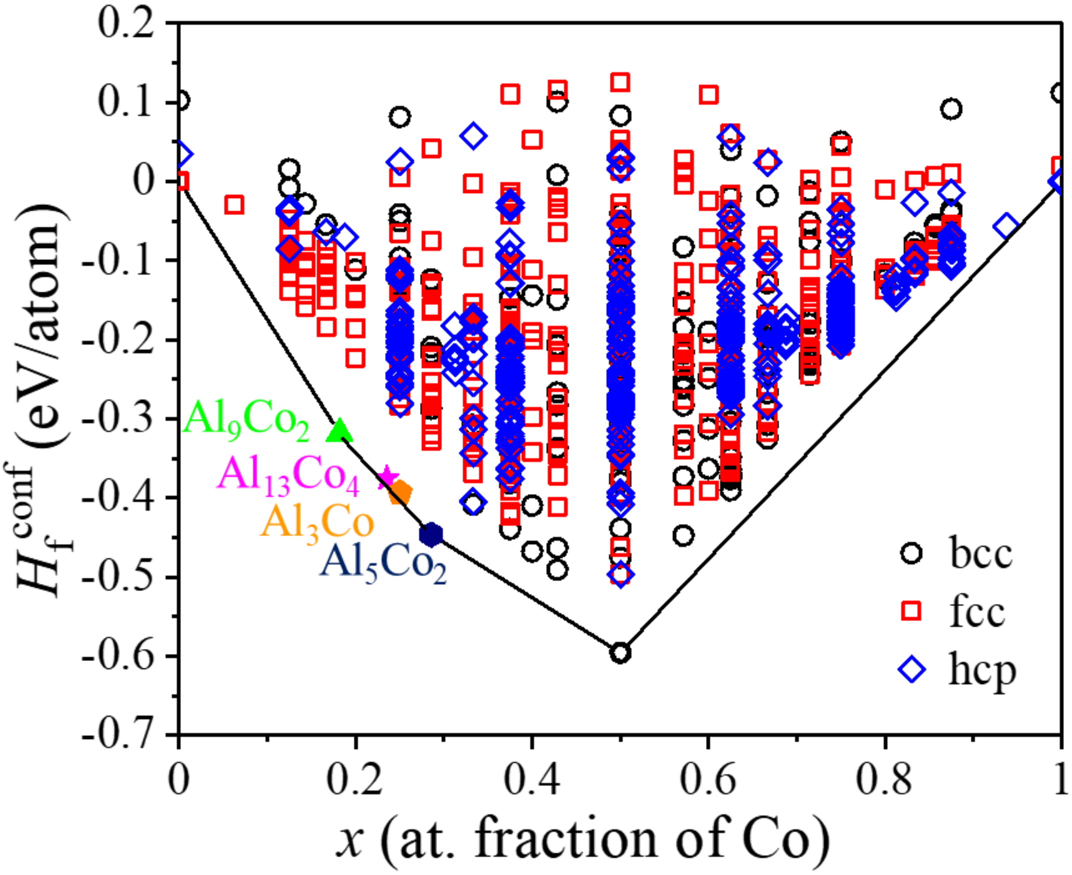

Figure 5.4: Formation enthalpies at 0 K of configurations with different lattices in the Co-Al system. The ground state phases on the convex hull are connected by the black line. They are Al, Al_9Co_2, Al_5Co_2, AlCo and hcp Co, respectively. Complex phases, such as Al_9Co_2, $Al_{13}Co_4$, Al_3Co and Al_5Co_2, are depicted with solid symbols.

The ground state phases on the convex hull are connected by the black line in Figure 5.4. They are fcc Al, Al_9Co_2, Al_5Co_2, bcc AlCo and hcp Co, respectively, which are in agreement with available experimental data [253]. $Al_{13}Co_4$ and Al_3Co are located almost on the tie-line connecting Al_9Co_2 and Al_5Co_2, with formation enthalpies only 8.961 meV/atom and 9.026 meV/atom above the tie-line. Both have been reported as metastable phases formed at high-temperature in some investigations [249,254].

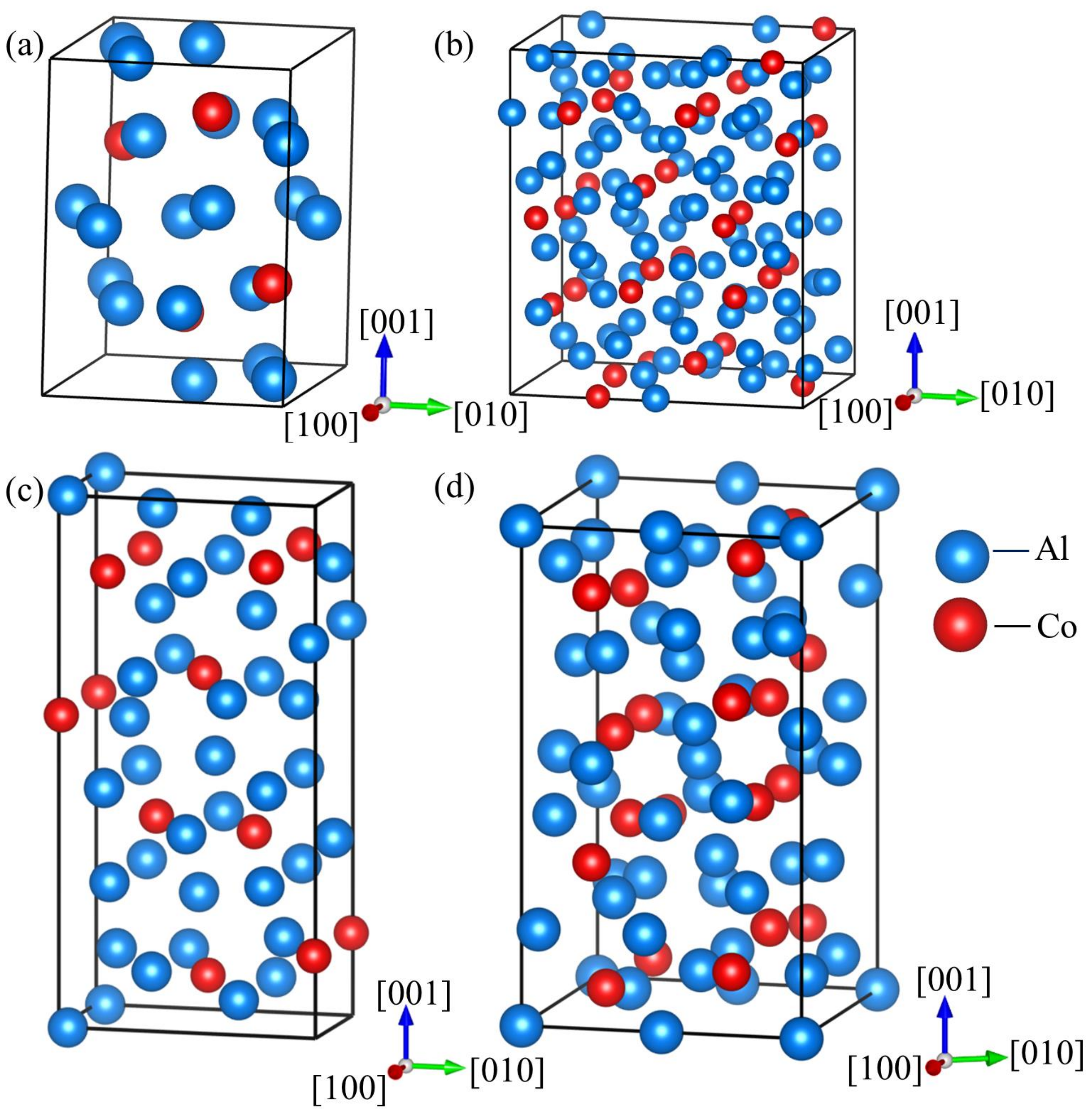

Figure 5.5: Crystal structure of complex phases in the Co-Al system. (a)Al$_9$Co$_2$ (space group: P2$_1$/c). (b) Al$_{13}$Co$_4$ (space group: Pmn2$_1$). (c) Al$_3$Co (space group: C2/m). (d) Al$_5$Co$_2$ (space group: P6$_3$/mmc).

5.3.2. Bold length vs. bond stiffness relationships

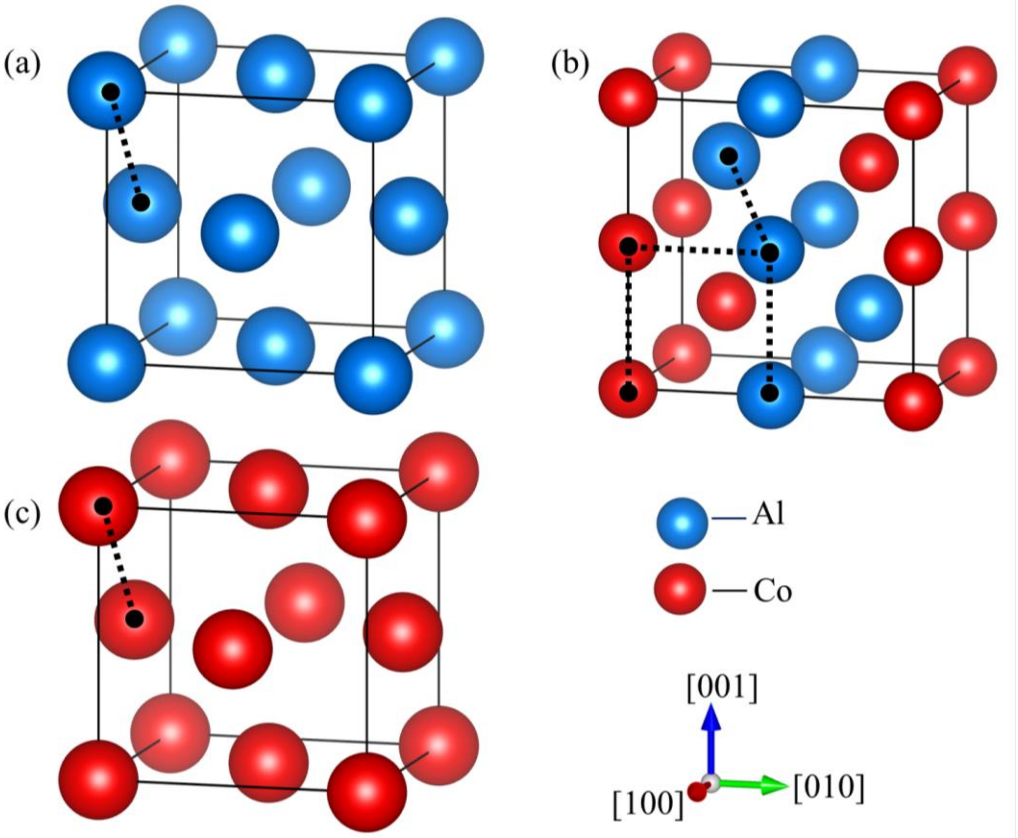

Figure 5.6: Crystal structures of ordered fcc Al-Co configurations. (a) Al. (b) AlCo. (c) Co. The nearest-neighboring bonds in each crystal structure are indicated by black lines.

The L-S relationships of the nearest-neighboring Al-Al, Co-Co and Al-Co bonds in the fcc lattice were obtained from three ordered fcc configurations, namely Al, $AlCo_3$, and Co, whose structures are depicted in Figure 5.6. The nearest-neighboring bonds are marked with dashed lines. The stretching and bending stiffnesses of each bond in fcc lattice as a function of the bond length are depicted with different symbols in Figure 5.7. The stretching stiffness of the three bonds decrease as bond length increases, while the bending stiffness increases slightly. The L-S relationships for each chemical bond were fitted by quadratic polynomials using the least-squares method. They are represented by the black and red curves in Figure 5.7. It is obvious that the L-S relationship for a given chemical bond is equivalent in different configurations and, thus, the force constant matrix is transferable to different configurations in the fcc lattice. Similarly, the configurations in the bcc lattice (Al, Al_2Co, AlCo and Co) and in the hcp lattice (Al, $AlCo_3$ and Co) used to calculate the stretching and bending stiffness between Al-Al, Al-Co and Co-Co bonds are shown in Figure 5.8 and Figure 5.10, respectively. The corresponding L-

S relationships for the bcc and hcp lattices are plotted in Figure 5.9 and Figure 5.11, respectively. As in the fcc lattice, the L-S relationship for a given chemical bond is equivalent for different configurations in the same lattice and, thus, the force constant matrix is transferable to different configurations in the same lattice.

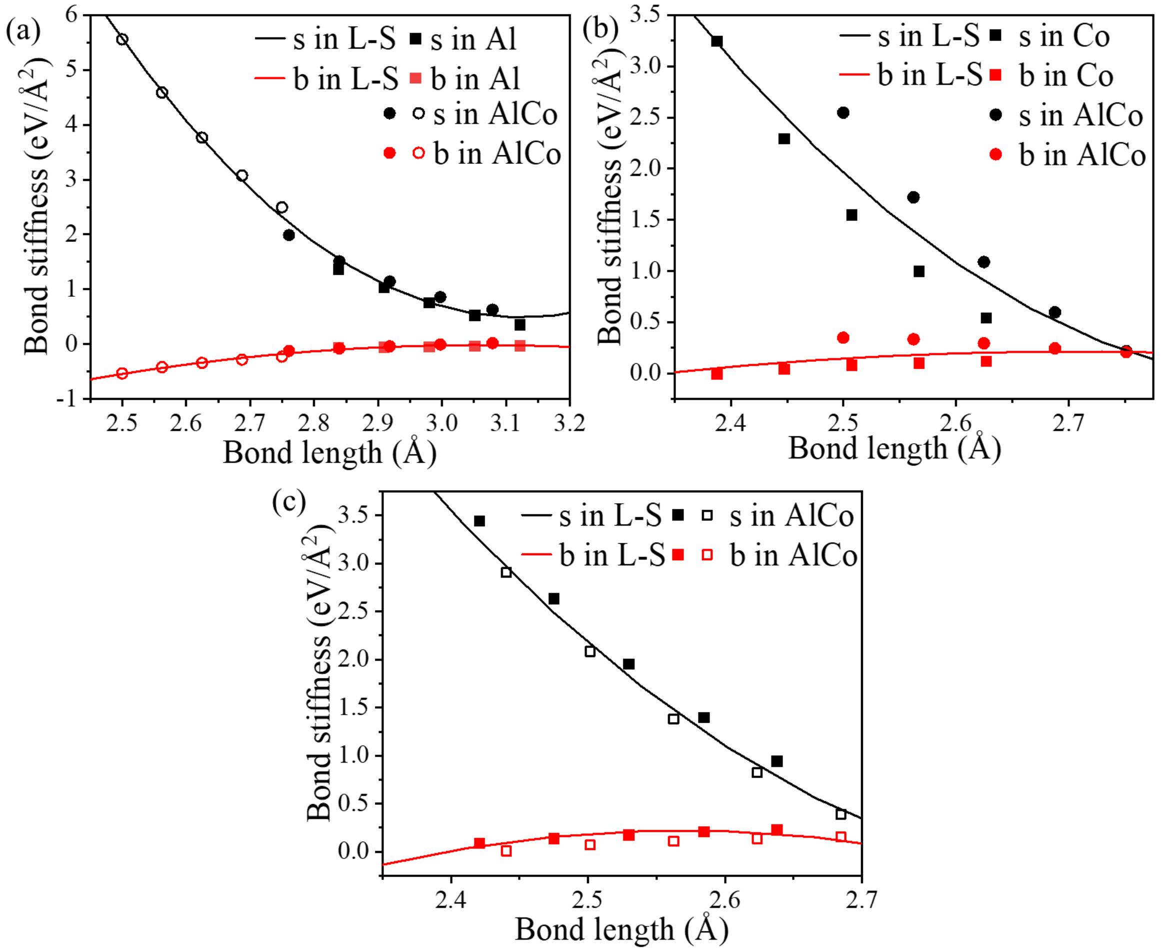

Figure 5.7: Bond length vs. bond stiffness relationships in the fcc lattice. (a) Al-Al bond. (b) Al-Co bond. (c) Co-Co bond. The symbols stand for the results obtained from ordered fcc Al-Co configurations by full phonon calculations according to eq. (2.11). The black and red curves stand for the fitted quadratic polynomials.

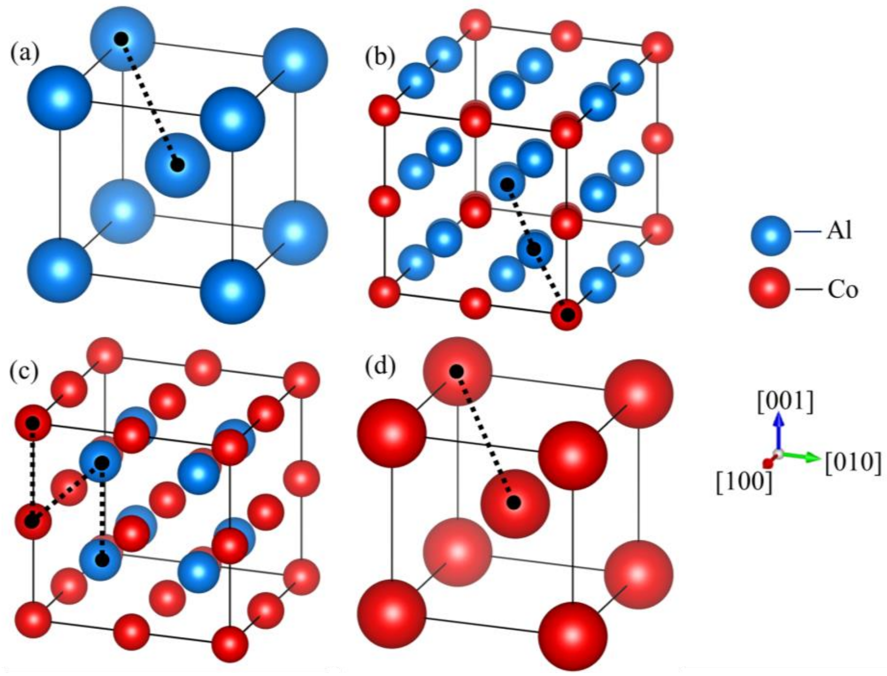

Figure 5.8: Crystal structures of ordered bcc Co-Al configurations. (a) Al. (b) Al_2Co. (c) AlCo. (d) Co. The NN bonds in each crystal structure are indicated by red lines.

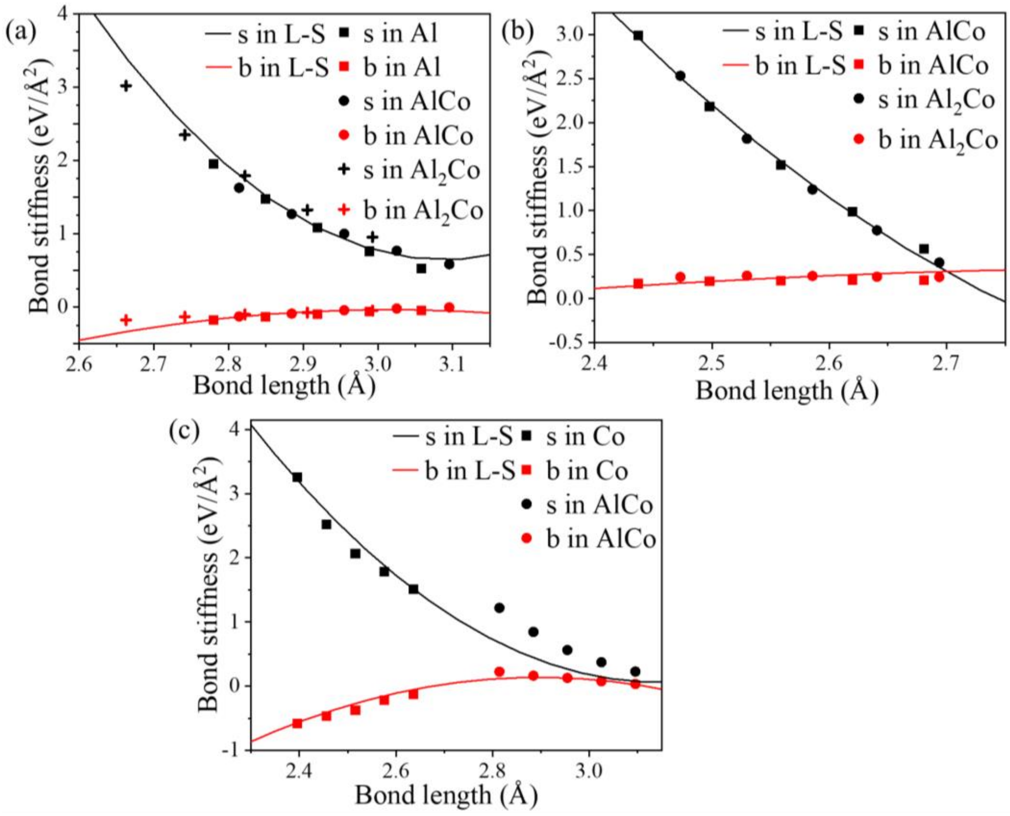

Figure 5.9: Bond length vs. bond stiffness relationships in the bcc lattice. (a) Al-Al bond. (b) Al-Co bond. (c) Co-Co bond. The symbols stand for the results obtained from ordered bcc Al-Co configurations by full phonon calculations according to eq. (2.11). The black and red curves stand for the fitted quadratic polynomials.

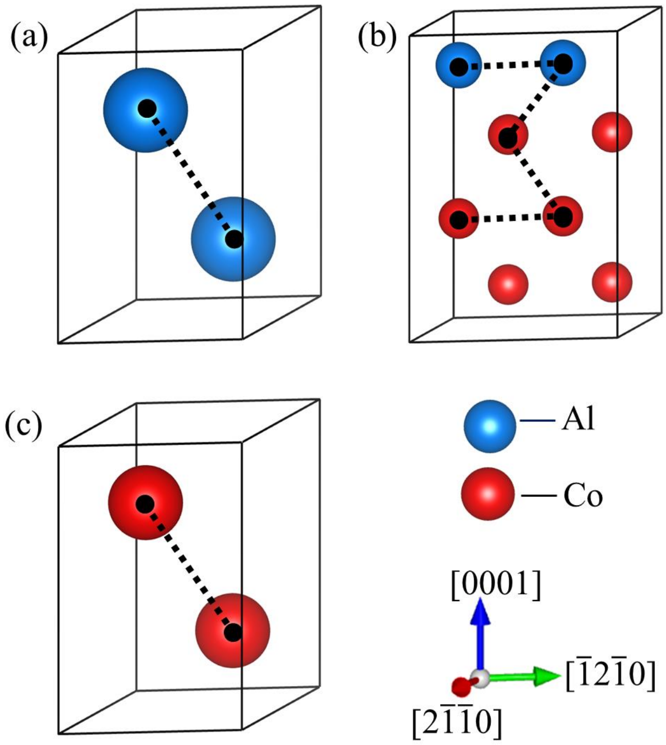

Figure 5.10: Crystal structures of ordered hcp Co-Al configurations. (a) Al. (b) $AlCo_3$. (c) Co. The NN bonds in each crystal structure are indicated by red lines.

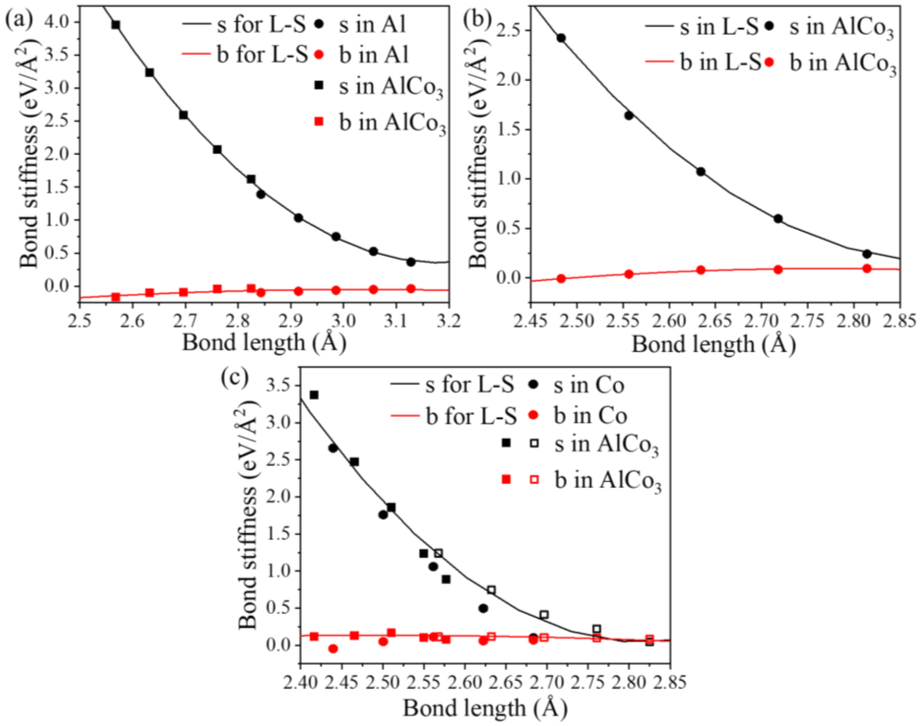

Figure 5.11: Bond length vs. bond stiffness relationships in the hcp lattice. (a) Al-Al bond. (b) Al-Co bond. (c) Co-Co bond. The symbols stand for the results obtained from ordered hcp Al-Co configurations by full phonon calculations according to eq. (2.11). The black and red curves stand for the fitted quadratic polynomials.

5.3.3. **Formation enthalpy including vibrational entropic contributions**

The L-S relationships were used to predict the force constant matrix of each configuration, and as a result, the corresponding vibrational free energy was obtained through eqs. (2.9) and (2.10). The accuracy of the L-S relationships was evaluated by comparing with the results obtained from full phonon calculations of certain phases. The phonon DOS of fcc Al, bcc AlCo, bcc $AlCo_2$, fcc $AlCo_3$, hcp Co and fcc Co predicted by the L-S relationships are plotted as black lines in Figure 5.12, and those obtained from full phonon calculations are plotted as red lines, together with the vibrational free energies F_{vib} as a function of temperature. The phonon DOS and vibrational free energies predicted by the L-S relationships are consistent with those obtained from full phonon calculations. It should be noted that the L-S relationships for complex phases Al_9Co_2, $Al_{13}Co_4$, Al_3Co and Al_5Co_2 are not calculated. Their phonon DOS and vibrational free energy as a function of temperature were determined only from full phonon calculations, and they are plotted in Figure 5.13.

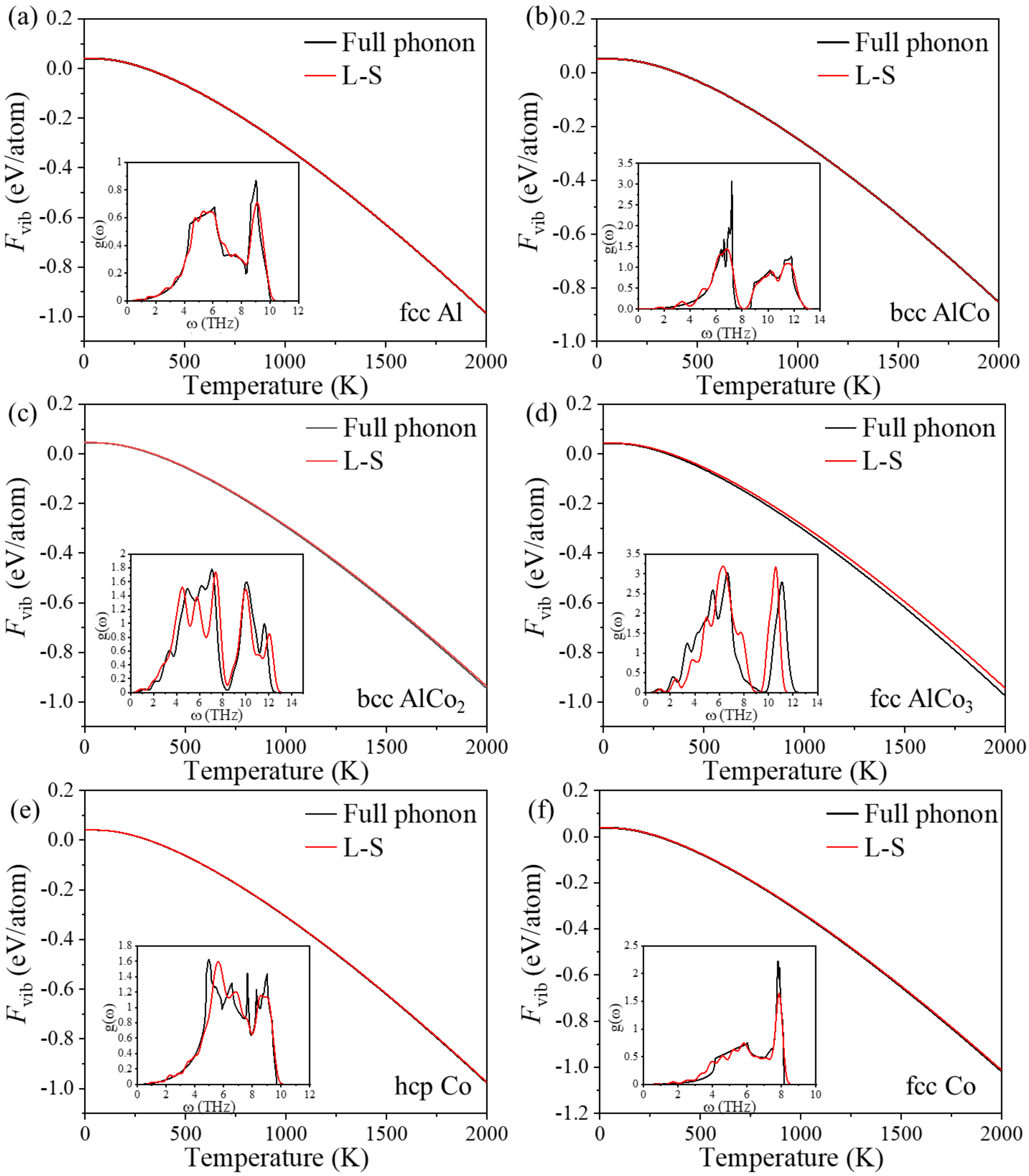

Figure 5.12: Phonon DOS and vibrational free energies of different phases in Co-Al system predicted from the L-S relationships (black lines) and from full phonon calculations (red lines). (a) fcc Al. (b) bcc AlCo. (c) bcc $AlCo_2$. (d) fcc $AlCo_3$. (e) hcp Co. (f) fcc Co. Phonon DOS are inserted in each figure.

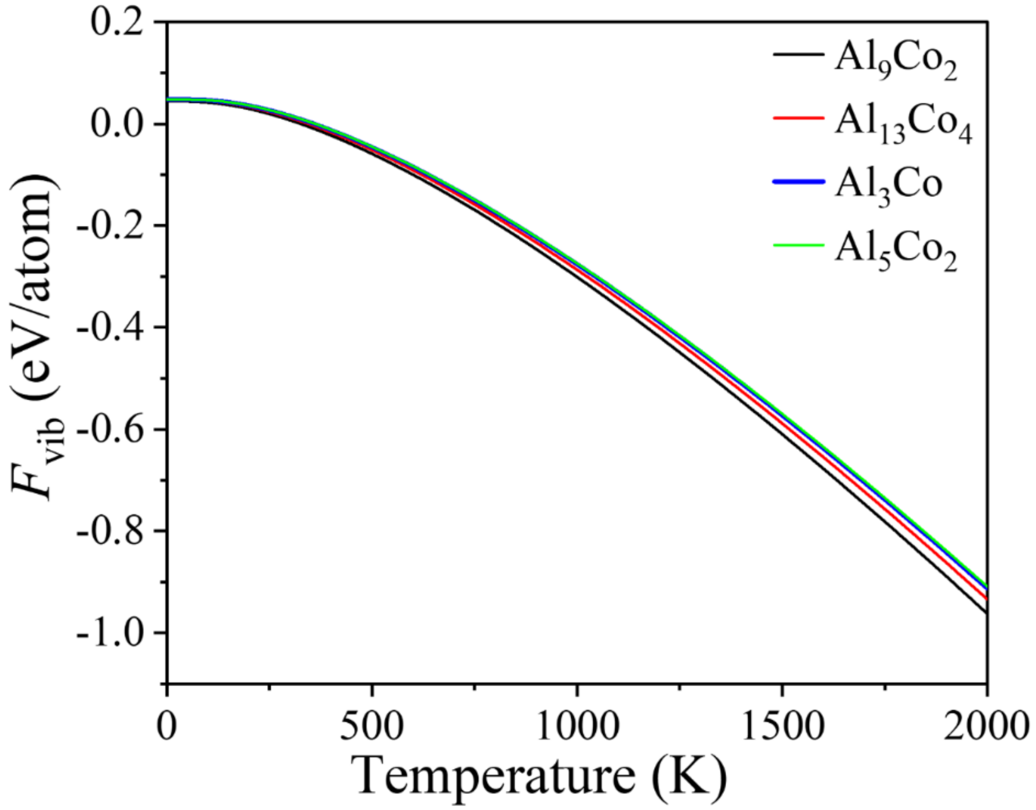

Figure 5.13: Vibrational free energies of Al_9Co_2, $Al13_3Co_4$, Al_3Co and Al_5Co_2 obtained from full phonon calculations.

The clusters for each lattice obtained in CE only including configurational occupation were maintained and the temperature-dependent ECIs including the vibrational entropy were fitted following the procedure indicated above using eq. (2.24). They are listed in Table C5, Table C6 and Table C7 in the Annex C. The values of mixing enthalpy including the vibrational entropy, H_{vib}, predicted by the CE and those obtained from the L-S relationships are compared in Figure C1, Figure C2 and Figure C3 in the Annex C for bcc, fcc and hcp lattices, respectively, at different temperatures, showing good agreement with each other. The cross-validation scores for bcc, fcc and hcp lattices at 400 K are 0.00373 eV/atom, 0.00284 eV/atom and 0.00206 eV/atom, respectively, while they are 0.014 eV/atom, 0.0108 eV/atom and 0.0079 eV/atom at 1600 K.

The formation enthalpies including both the configurational occupation and the vibrational entropic contribution, $H_f^{conf+vib}$, at different temperatures (400 K, 800 K, 1200 K and 1600 K) of all configurations were obtained through eq. (13) and are plotted in Figure 5.14. The convex hulls at different temperatures provide information about the stability change of each configuration due to lattice vibration. The phases on the convex hulls at 400 K (Figure 5.14(a) are the same as those at 0 K (Figure 5.13). However, $Al_{13}Co_4$ and Al_3Co (marked by purple and orange symbols) appear on the convex hull at 600 K and 1200 K respectively (Figure 5.14(b) and Figure 5.14(c)), which means they are stabilized at high temperature due to lattice vibrations. Instead, Al_3Co and Al_5Co_2 are no longer located on the convex hull at 1600 K (Figure 5.14(d)). The hcp Co on the convex hull is also replaced by fcc Co at 1200 K. Other phases including Al, Al_9Co_2 and AlCo are still on the convex hull.

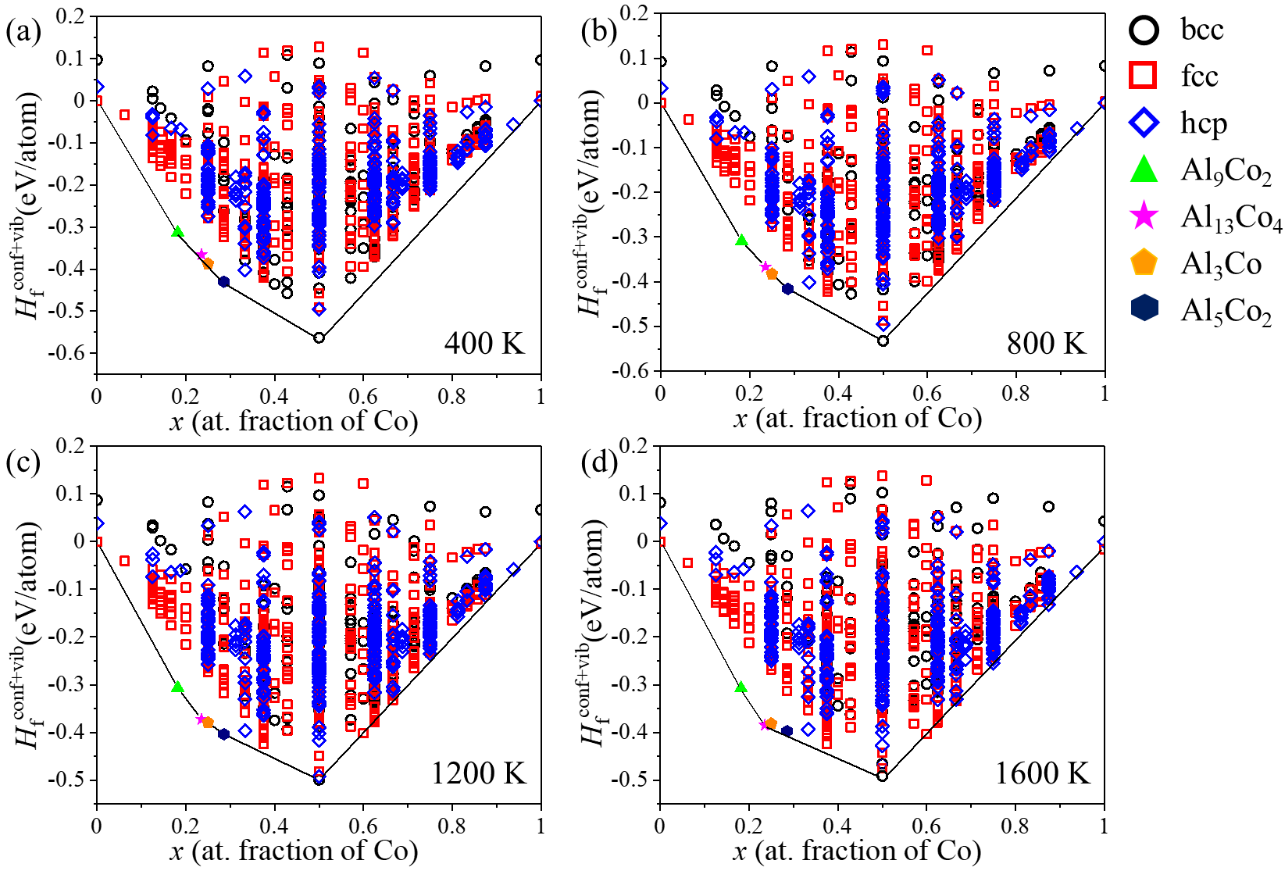

Figure 5.14: Formation enthalpies including the configurational occupation and the vibrational entropic contribution of all configurations at different temperatures. (a) 400 K. (b) 800 K. (c) 1200 K. (d) 1600 K. The red symbols stand for the fcc configurations, the black symbols for the bcc configurations, and the blue symbols for the hcp configurations. The green, purple, orange and dark blue symbols stand for Al_9Co_2, $Al_{13}Co_4$, Al_3Co and Al_5Co_2, respectively.

5.3.4. **Magnetic free energy**

The coupling constants of Co-Co pairs in fcc, bcc and hcp lattices were calculated based on the Heisenberg Hamiltonian following eq. (2.12). They are listed in Table 5.3, and compared with data available in [255]. The magnetic specific heat C_{mag} of each configuration at different temperatures was determined from MC simulations of the Heisenberg Hamiltonian, which were performed using the VAMPIRE package [244]. They are plotted in Figure 5.15(a), Figure 5.15(c) and Figure 5.15(e) for bcc, fcc and hcp Co.

The magnetic specific heat C_{mag} of each configuration was used to calculate the magnetic entropy S_{mag} and magnetic free energy F_{mag} through eqs. (2.13) and (2.14). The Curie temperature T_C of pure Co was determined from the peak value of C_{mag}. They are 1400 K, 1460 K and 1550 K for bcc Co, fcc Co, and hcp Co, respectively, which are close to the data reported in the literature, i.e. 1420 K [255], 1396 K [256], and 1679 K [69]. The F_{mag} of bcc Co, fcc Co, and hcp Co calculated by eq. (2.13) are plotted in Figure 5.15(b), Figure 5.15(d) and Figure 5.15(f).

Table 5.3: Calculated coupling constants J of nearest-neighbor Co-Co pairs in fcc, bcc and hcp lattices.

Lattice	J (eV/pair)	
	This work	Reference
fcc	0.012241	0.01382 [255]
bcc	0.019136	0.01848 [255]
hcp	0.015941	0.01466 [255]

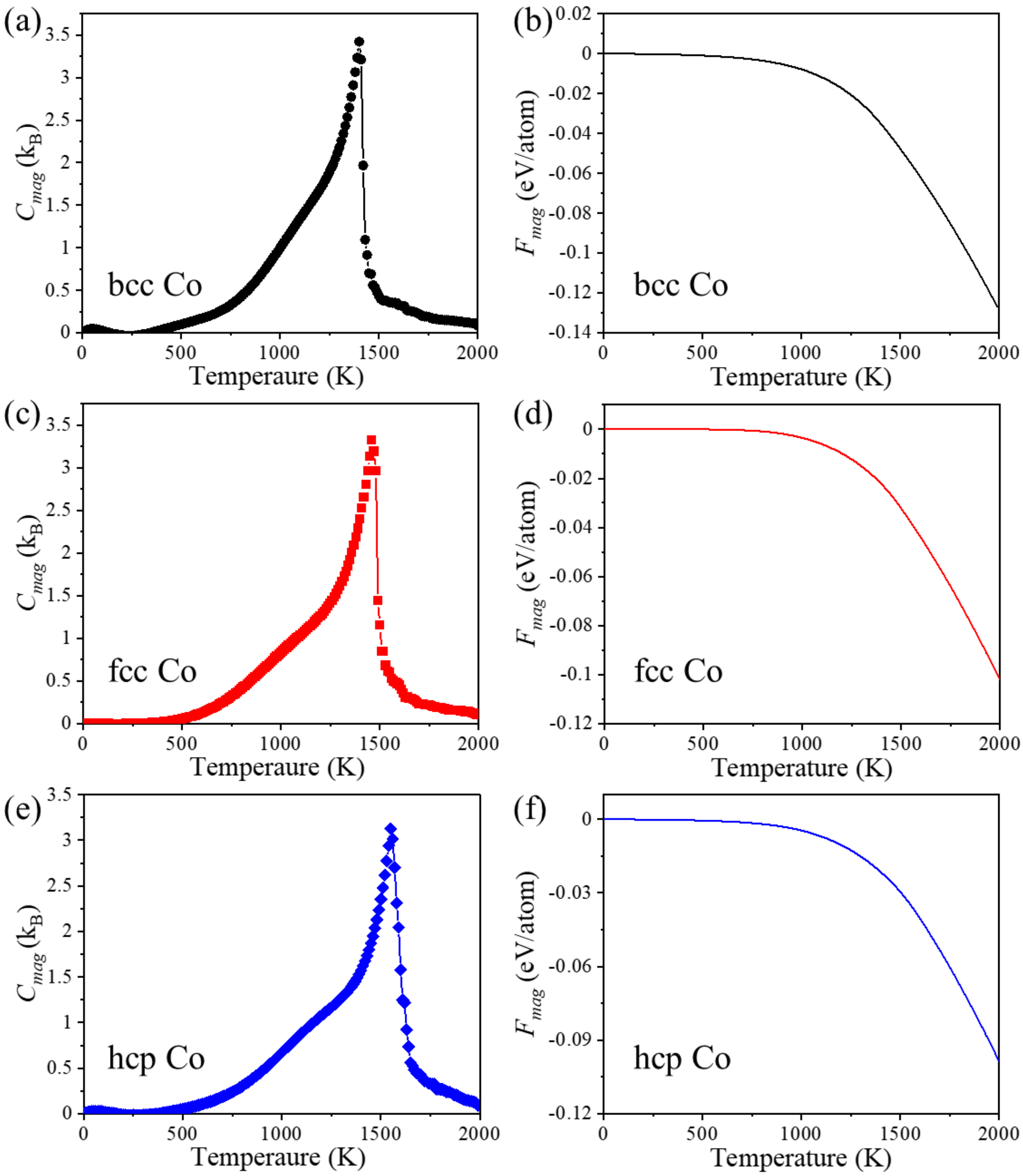

Figure 5.15: Magnetic specific heat C_{mag} and magnetic free energy F_{mag} of pure Co from MC simulation. (a), (b) bcc Co. (c), (d) fcc Co. (e), (f) hcp Co.

5.3.5. **Formation enthalpy including vibrational and magnetic entropy**

Another temperature-dependent CE including the contribution of the configurational occupation as well as the vibrational and magnetic entropic contributions was fitted for each lattice using the same clusters and the same strategy indicated above. The corresponding ECIs are listed in Table C8, Table C9 and Table C10 in the Annex C. The corresponding mixing enthalpies, H_{mag}, predicted by the CE and those obtained from eq. (2.25) are compared in Figure C4, Figure C5 and Figure C6 in the Annex C for bcc, fcc and hcp lattices, respectively, at different temperatures. They are in good agreement and the cross-validation scores of bcc, fcc and hcp lattices at 400 K are 0.00041 eV/atom, 0.00049 eV/atom and 0.0005 eV/atom, respectively, while they are 0.00718 eV/atom, 0.0113 eV/atom and 0.00871 eV/atom at 1600 K.

The formation enthalpies including the contribution of the configurational occupation as well as the vibrational and magnetic entropy, $H_f^{conf+vib+mag}$, at different temperatures (400 K, 800 K, 1200 K and 1600 K) of all configurations were obtained through eq. (5.8) and are plotted in Figure 5.16. The ground states located on the convex hull at different temperatures are the same as those in Figure 5.14 at each temperature.

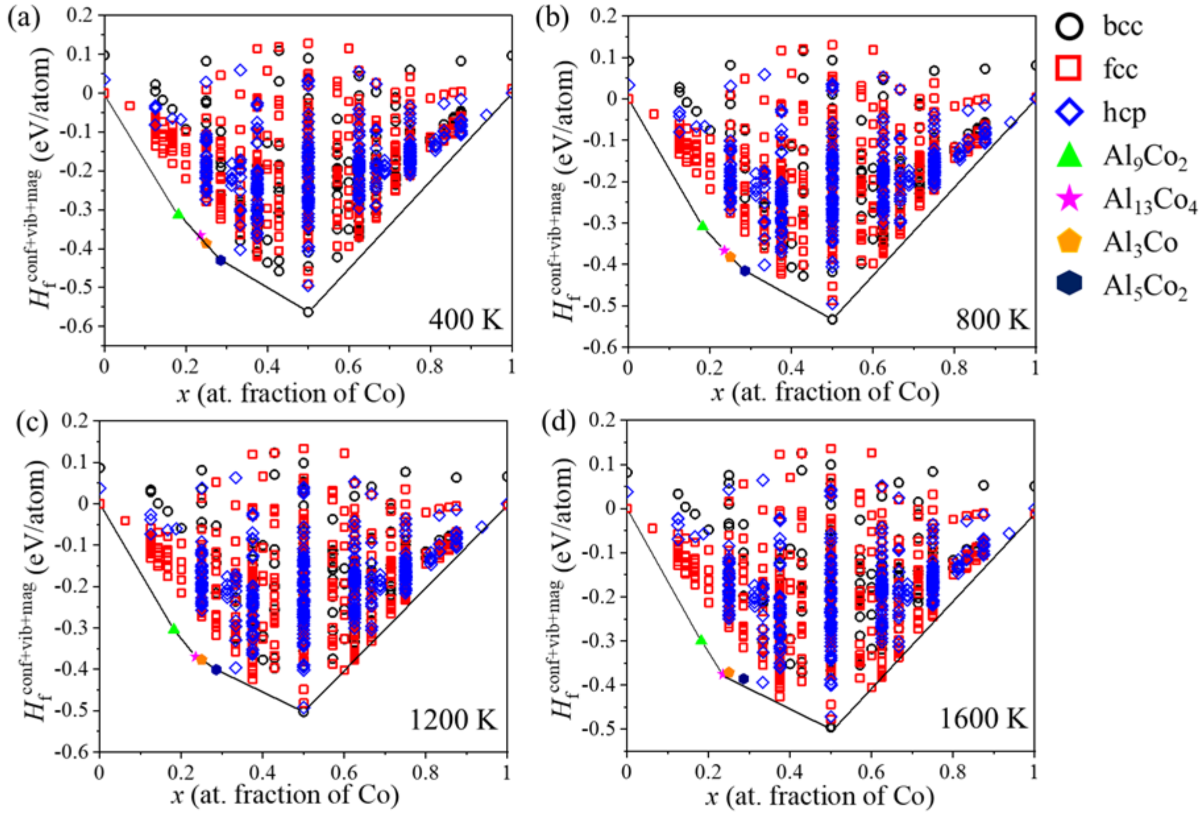

Figure 5.16: Formation enthalpies including the configurational occupation and the vibrational and magnetic entropic contributions of all configurations at different temperatures. (a) 400 K. (b) 800 K. (c) 1200 K. (d) 1600 K. The red symbols stand for the fcc configurations, the black symbols for the bcc configurations, and the blue symbols for the hcp configurations. The green, purple, orange and dark blue symbols stand for Al_9Co_2, $Al_{13}Co_4$, Al_3Co and Al_5Co_2, respectively.

5.4. Phase diagram construction

5.4.1. Al-Al_9Co_2 phase boundary

The Gibbs free energy of fcc Al solid solution was obtained from MC simulations, while the formation enthalpy of Al_9Co_2 obtained from eq. (2.25) at different temperatures was used as its Gibbs free energy. Both free energies are plotted in Figure 5.17 at different temperatures. The dash line in Figure 5.17(a) shows the common tangent at 900 K, from which the composition of each phase at this temperature is determined. The corresponding two-phase region between Al and Al_9Co_2 is plotted in Figure 5.17(b) as a dashed line and the whole Al-Al_9Co_2 phase boundary was obtained following this procedure and is plotted in Figure 5.17(b). The melting point of Al is 933 K [257], so the Al-Al_9Co_2 two-phase region is determined below this temperature.

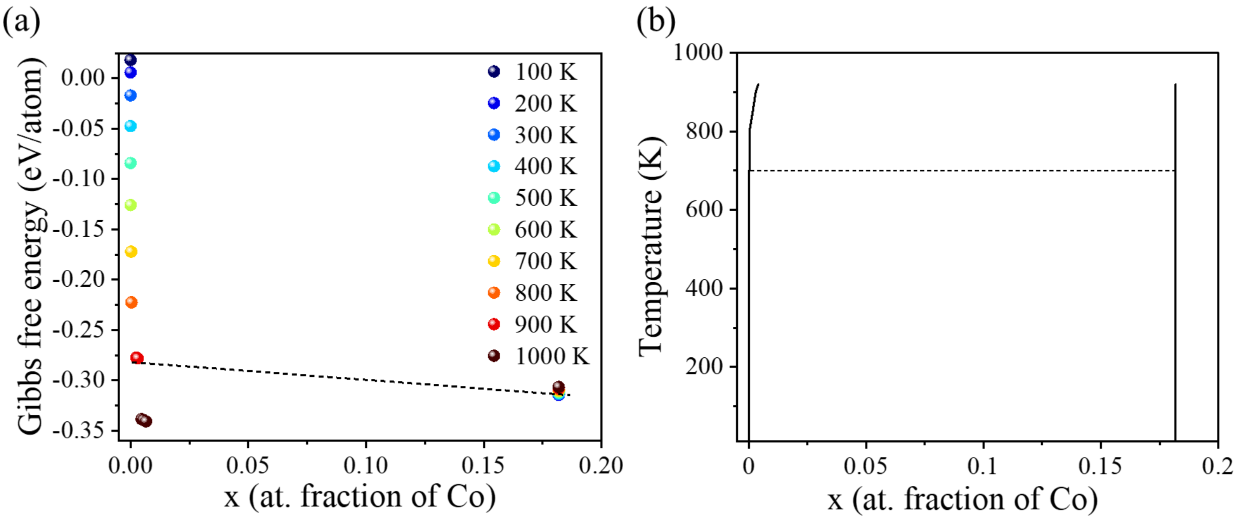

Figure 5.17: (a) Gibbs free energies of Al and Al_9Co_2 at different temperatures. (b) Al-Al_9Co_2 phase boundary.

5.4.2. Al_9Co_2-$Al_{13}Co_4$, $Al_{13}Co_4$-Al_3Co and Al_3Co-Al_5Co_2 phase boundaries

All other stables phases in the Al-rich part of the phase diagram have complex crystal structures. Their Gibbs free energy at different temperatures only include the vibrational and magnetic entropic contributions and they are shown in Figure 5.18(a) and (b). From Figure 5.18(a), $Al_{13}Co_4$ is unstable below 700 K (Figure 5.18(a)) and the Al_9Co_2-$Al_{13}Co_4$ phase boundary above 700 K was determined and shown in Figure 5.18(c). Similar to $Al_{13}Co_4$, Al_3Co is metastable below 690 K, so the $Al_{13}Co_4$-Al_3Co phase boundary above 690 K was determined. Al_5Co_2 (adjacent to Al_3Co) is stable only below 1410 K, so the Al_9Co_2-Al_5Co_2 phase boundary below

690 K and the Al_3Co-Al_5Co_2 phase boundary between 690 K and 1410 K were determined. The Al_9Co_2-$Al_{13}Co_4$-Al_3Co-Al_5Co_2 phase boundaries are plotted in Figure 5.18(c) as a function of temperature

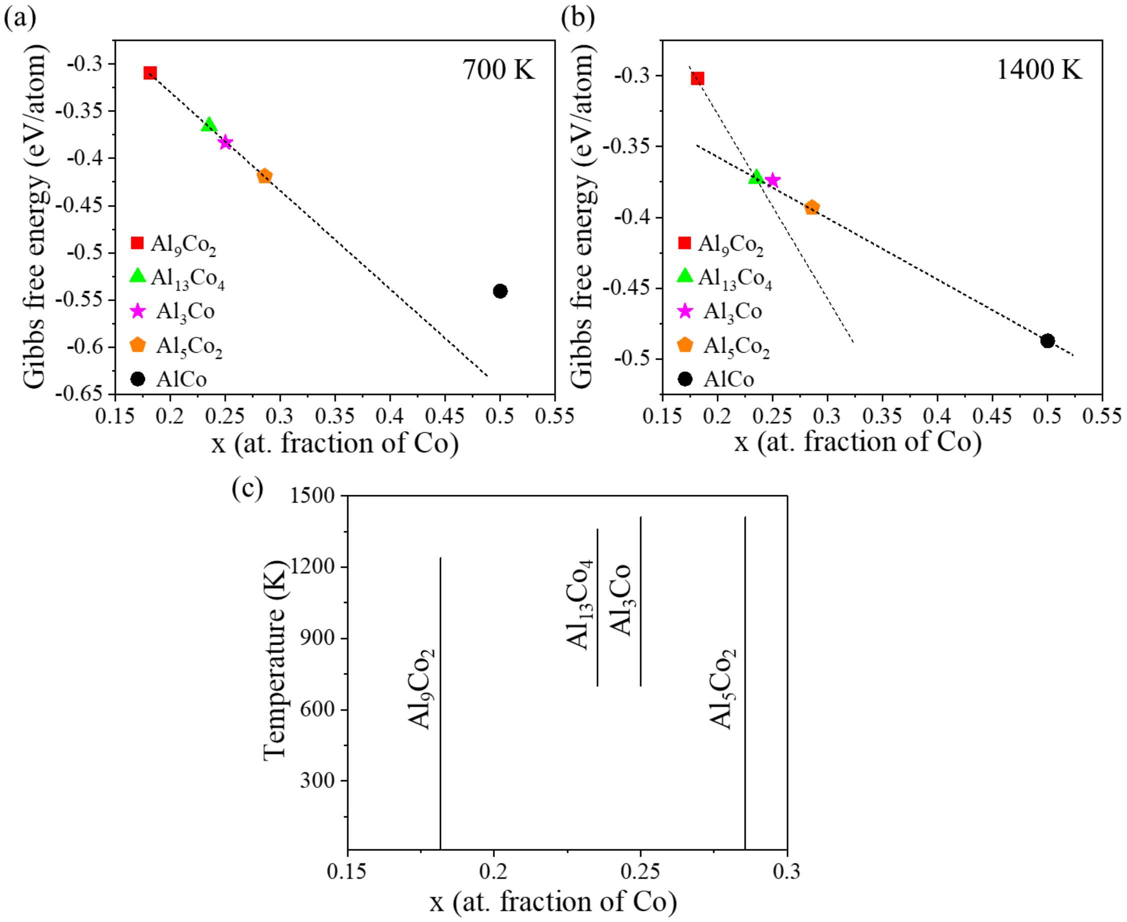

Figure 5.18: Gibbs free energies of Al_9Co_2, $Al_{13}Co_4$, Al_3Co, Al_5Co_2 and AlCo at 700 K (a) and 1400 (b). (c) Al_9Co_2-$Al_{13}Co_4$-Al_3Co-Al_5Co_2 phase boundary.

5.4.3. Al_5Co_2-AlCo phase boundary

The other adjacent stable phase to Al_5Co_2 is AlCo, with a bcc lattice. The Gibbs free energies of Al_5Co_2 and AlCo are plotted in Figure 5.19(a) as a function of temperature. The dash line in Figure 5.19(a) shows the common tangent between their Gibbs free energy at 1200 K, from which the composition of each phase at this temperature is determined and shown by a dashed line in Figure 5.19(b). The Al_5Co_2-AlCo two-phase region was obtained following this procedure at different temperatures and is plotted in Figure 5.19(b). There is no common tangent between them above 1410 K, which means that they become solid solutions.

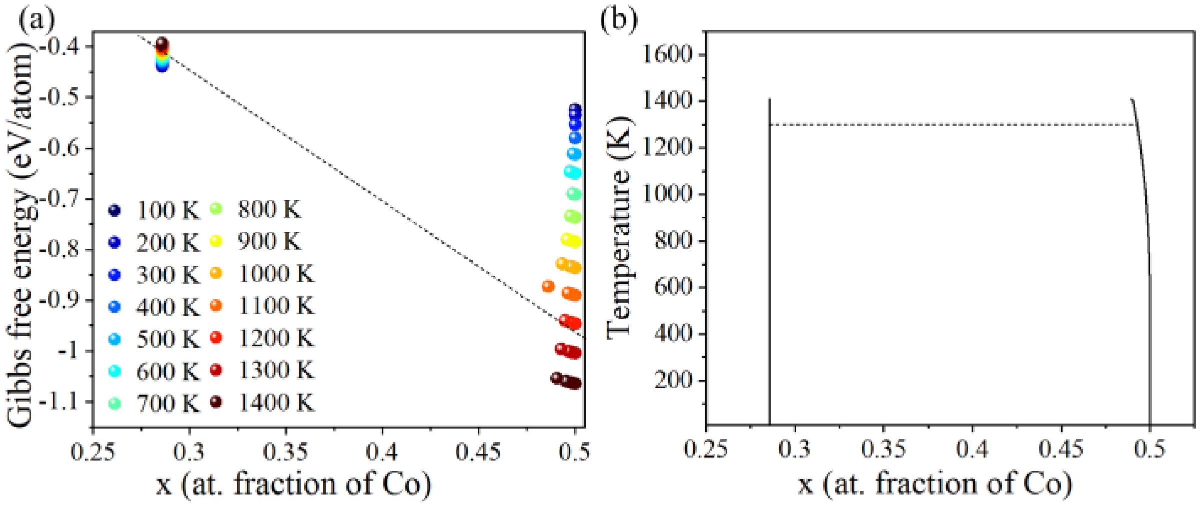

Figure 5.19: (a) Gibbs free energies of Al_5Co_2 and AlCo at different temperatures. (b) Al_5Co_2-AlCo phase boundary.

5.4.4. AlCo-Co phase boundary

The AlCo-Co phase boundary was determined by the common tangent of their Gibbs free energies. The Gibbs free energies of hcp Co and fcc Co at different temperatures are firstly compared in Figure 5.20(a), where the solid line represents the Gibbs free energy of hcp Co and the dashed line represents that of fcc Co. The Gibbs free energy of hcp Co is lower than that of fcc Co below 1000 K, which means AlCo is in equilibrium with hcp Co below this temperature but with fcc Co above 1000 K.

The Gibbs free energies between AlCo and hcp Co below 1000 K are shown in Figure 5.20(b). The dash line in Figure 5.20(b) shows the common tangent at 700 K, from which the composition of each phase is determined. This strategy was used to obtain the two-phase region between AlCo and hcp Co at different temperatures, which is depicted by the solid line in Figure 5.20(d). The Gibbs free energies between AlCo and fcc Co above 1000 K are shown in Figure 5.20(c), from which the composition of each phase is determined. Then the two-phase region between AlCo and fcc Co was obtained as a function of temperature and is depicted by the dashed line in Figure 5.20(d). AlCo and fcc Co become solid solution above 1650 K.

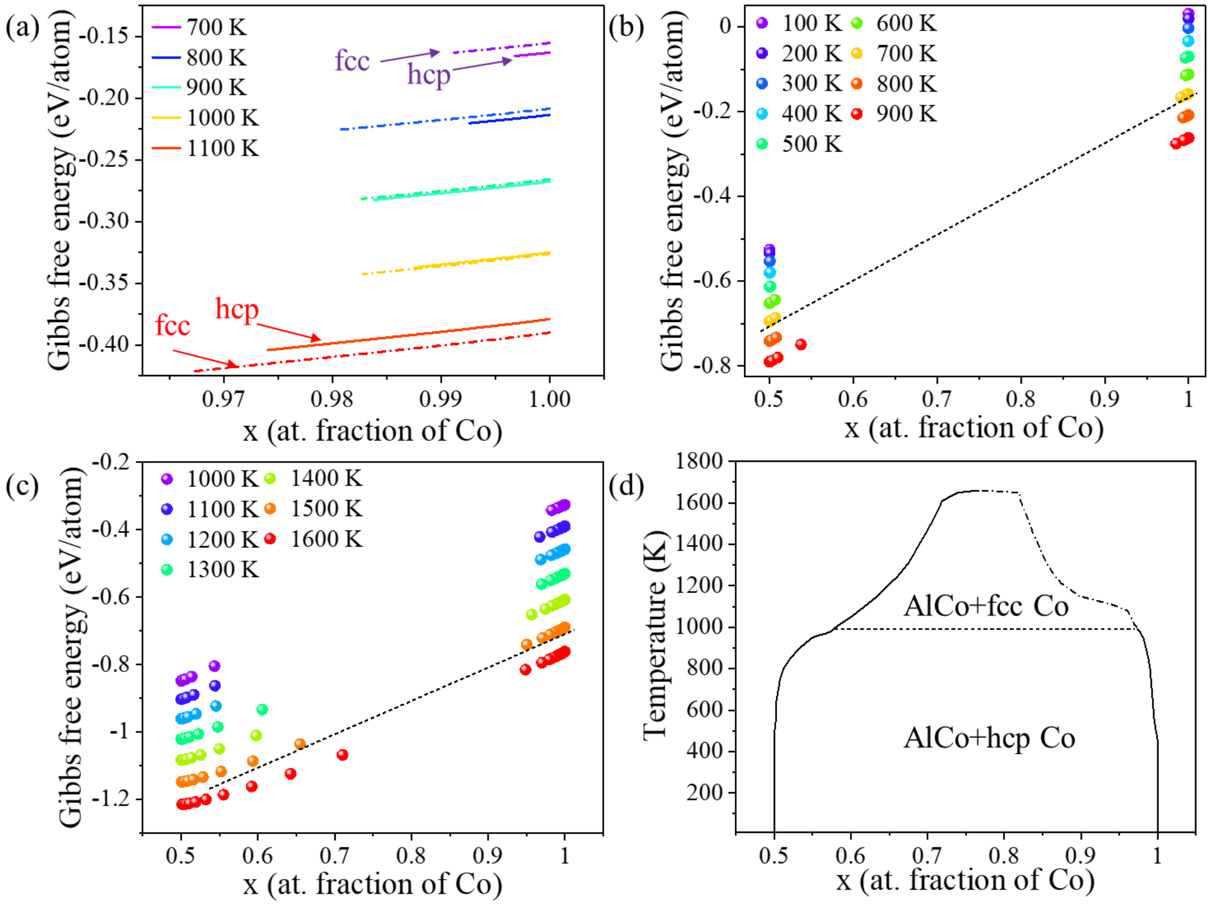

Figure 5.20: (a) Gibbs free energies of hcp (solid line) and fcc (dashed line) Co at different temperatures. (b) Gibbs free energies of AlCo and hcp Co below 1000 K. (c) Gibbs free energies of AlCo and fcc Co above 1000 K. (d) AlCo and hcp Co and fcc Co phase boundary.

5.4.5. AlCo-bcc Co metastable phase boundary

Even though the bcc Co is less stable than fcc Co or hcp Co at all temperatures, it has been reported that the metastable bcc Co and AlCo can coexist in Al-Co binary alloy at 515~600 °C but it will transform into the hcp Co as a result of aging [128]. This metastable two-phase region was also observed in Al-Co-Fe alloys above 800 °C. Kamiya et al. [258] ascribed the reason for the formation of the bcc Co to chemical and magnetic ordering. Both bcc Co and AlCo share the same bcc lattice, and their phase boundary was obtained by the intersection of their grand potentials obtained at increasing and decreasing Δμ. Their grand potentials at 650 K are plotted as a function of $\Delta\mu$ in Figure 5.21(a). The black curve corresponds to AlCo by increasing $\Delta\mu$, while the red one is obtained from bcc Co by decreasing $\Delta\mu$. $\emptyset_{\mathrm{AlCo}} < \emptyset_{Co}$ on the left of the intersection, indicating that AlCo is more stable. $\emptyset_{\mathrm{AlCo}} > \emptyset_{Co}$ on the right and bcc Co is more stable in this region. The intersection is mapped onto the conjugated composition of AlCo and bcc Co, which is shown in Figure 5.21(b). The composition of AlCo and bcc Co at 600 K was determined and is shown by the dashed line in Figure 5.21(c). This procedure was repeated at different temperatures and the whole phase boundary was built. Above 930 K, the grand potentials for AlCo and bcc Co overlap, indicating that they become a solid solution.

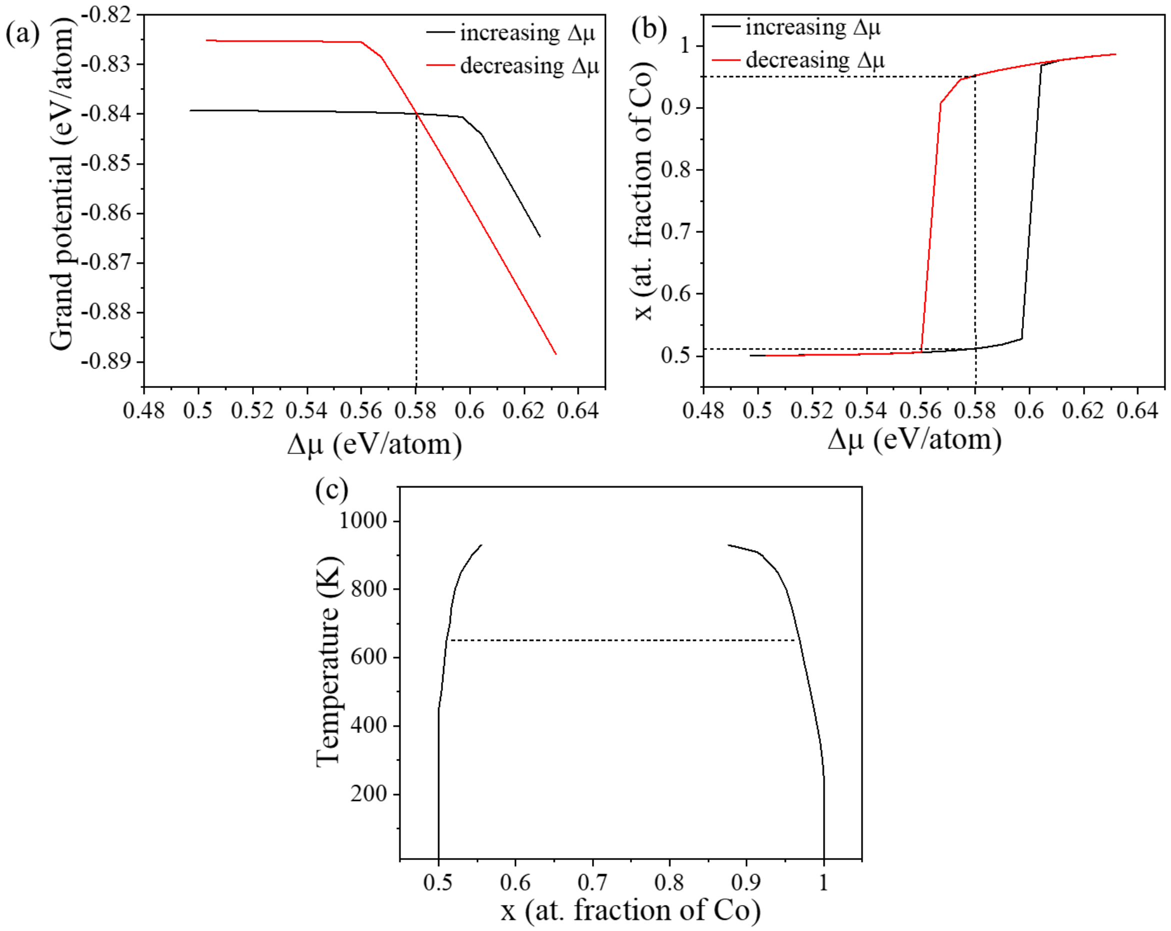

Figure 5.21: (a) Grand potentials of bcc AlCo and bcc Co as a function of chemical potential $\Delta\mu$ at 650 K. (b) Conjugated composition as a function of chemical potential at 650 K. (c) Metastable phase boundary between AlCo and bcc Co.

5.4.6. **Magnetic phase transition**

The C_{mag} of the solid solutions with different Co contents as a function of temperature are plotted in Figure 5.22(a). C_{mag} of each solid solution has a clear peak at certain temperature, which corresponds to the T_C at the given content. It is obvious that T_C moves to higher values as Co content increases. The phase boundary between the ferro-magnetic (FM) and para-magnetic (PM) states is represented by T_C, which is plotted in the Figure 5.22(b), together with the experimental results [259] and those calculated using Calphad [260]. It is shown that the experimental results and Calphad results are consistent, while our results exhibit a T_C difference with maximum of about 200 K, which may be caused because magnetic interactions between next-nearest neighbor atoms was not taken into account in our work [261]. From the experimental viewpoint, T_C is typically determined from the magnetic susceptibility or the hysteresis loop [262]. However, several factors may contribute to uncertainties in the experimental determination of T_C, including the inhomogeneity of the sample, uneven distribution of local magnetic moments [263], and drastic fluctuations in magnetic behavior near the T_C [264]. Additionally, the magnitude and direction of the external magnetic field may influence the magnetic response of materials [265], further affecting the experimental accuracy of the Curie temperature determination. It should be also noted that the good agreement of Calphad predictions with the experimental values maybe partially attributed to the fitting strategy [266]. This strategy is highly dependent on the reliability of the physical models and accurate experimental measurements. Given the very limited number of discrete experimental data as shown in Figure 5.22(b), the differences between our results and the experimental data show the need of more experiments to assess the accuracy of our predictions.

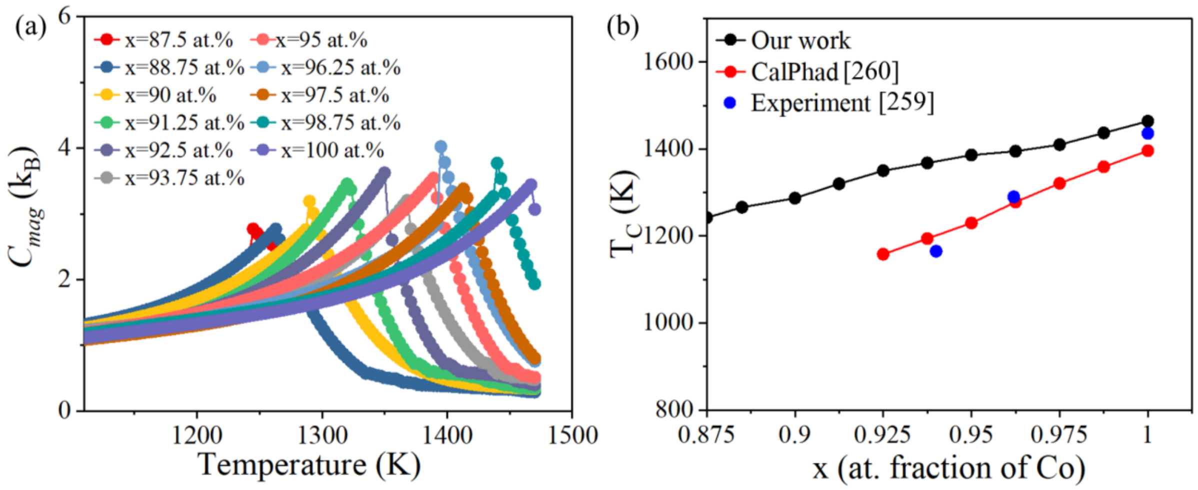

Figure 5.22: Magnetic specific heat and Curie temperature with different compositions. (a) Magnetic specific heat, C_{mag}, of hcp Co solid solutions with different compositions as a function of temperature. (b) Curie temperature as a function of Co content.

5.5. Discussion

5.5.1. Comparison with the experimental phase diagram

The solid region of the Co-Al phase diagram was built by integrating the phase boundaries between adjacent phases and is plotted in Figure 5.23 with the red lines. The thin dashed black lines stand for the experimental phase diagram while the thick dashed black lines stand for the experimental liquidus and solidus curves, that cannot be captured with our strategy [267]. Overall, the calculated phase diagram is in excellent agreement with the experimental one, demonstrating the capabilities of the methodology used in this paper to determine the thermodynamic properties of unknow phases, including the contributions from configuration, lattice vibration and magnetism. The calculated Al-Al_9Co_2 two-phase region is superposed to the experimental ones up to 930 K. The predicted maximum solubility of Co in α-Al is 3.76 at.% at 930 K while that obtained from the experimental phase diagram is 3.2% [268]. The Al_9Co_2-$Al_{13}Co_4$ two-phase region exists in the range between 700 K and 1240 K, while $Al_{13}Co_4$-Al_3Co two-phase region exists at temperatures higher than 1350 K. It should be noted that the line compounds $Al_{13}Co_4$ and Al_3Co in the experimental phase diagram are present at room temperature, while they exist only at high temperature in the calculated one. This difference reflects a limitation of the experimental technique, where the compounds are created by melting at high temperature and progressively cooled down. These complex compounds are formed at high temperature, and they will not disappear at room temperature (even though they are metastable) because of the sluggish kinetics. Moreover, Fleischer et al. [254] studied the stability of the $Al_{13}Co_4$ and Al_3Co using experiments and first-principles calculations. They found that the enthalpies of $Al_{13}Co_4$ and Al_3Co are higher than those of the Al_5Co_2-Al_9Co_2 tie-line according to first-principles calculations, but they appeared at high temperature in the experiments. This behavior can be rationalized by our results that the lattice vibrations play a crucial role in the high-temperature stability of $Al_{13}Co_4$ and Al_3Co.

The Al_5Co_2-AlCo two phase region shows that they can coexist at 1410 K. The minimum composition of Co in AlCo is 49.01 at.% at 1410 K, which is slightly higher than the one reported experimentally (48.2 at.%) . In the Co-rich part, the predicted transition temperature from hcp to fcc Co is 1000 K, which is higher than the experimental value of 700 K, but lower than the previously reported theoretical value 1274 K [269]. This discrepancy may mainly come from other contributions to the free energy (such as electronic excitations) that were not considered in our analysis. The phase boundary between AlCo and the metastable bcc Co was also determined in our work, and it was found that they can coexist below 930 K. Overall, the AlCo-Co phase boundary basically coincides with the experimental phase diagram. Moreover, the Curie temperature, which is difficult to obtain through experiments, can be obtained by MC simulations.

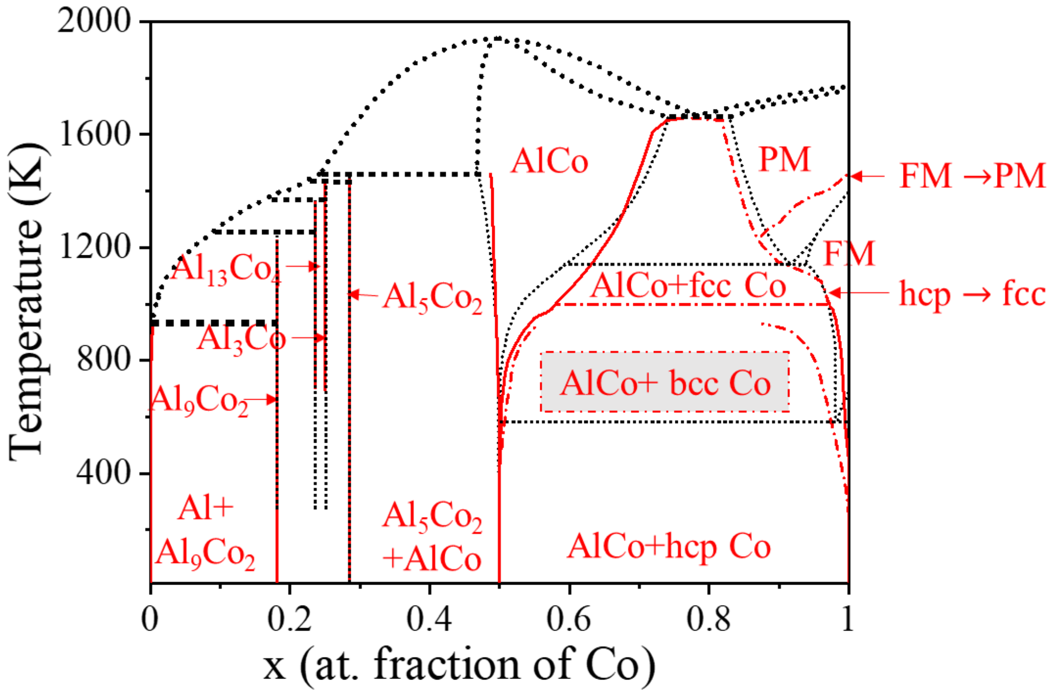

Figure 5.23: Comparison of the experimental Co-Al phase diagram [267] (dashed black lines) with those obtained from first-principles calculations (red lines). The thick black dashed lines stand for the liquidus and solidus curves.

5.5.2. **Influence of vibrational and magnetic contributions**

Another version of the Co-Al phase diagram was obtained following the same methodology but neglecting the effect of magnetic contribution is neglected. The corresponding phase boundaries between each two adjacent phases are depicted in Figure C7 to Figure C8 in the Annex C. The whole phase diagram is plotted in Figure 5.24(a). It is obvious that neglecting magnetic contribution leads to few changes, that are only relevant in the Co-rich region of the phase diagram.

Similarly, the Co-Al phase diagram only considering the configurational contribution is obtained following the same methodology by neglecting both magnetic and vibrational effects. The corresponding phase boundaries between each two adjacent phases are depicted in Figure C9 to Figure C12 in the Annex C. The whole phase diagram is plotted in Figure 5.24(b) with the blue lines. It is very similar to the one in Figure 5.23 at low temperatures, but there are large discrepancies at higher temperatures. Al_3Co_4 and Al_3Co phases do not appear in the phase diagram and the phase transition from hcp→ fcc Co is not detected. Figure 5.24(a) and Figure 5.24(b) indicate that the effect of magnetic entropy is lower than that of vibrational entropy.

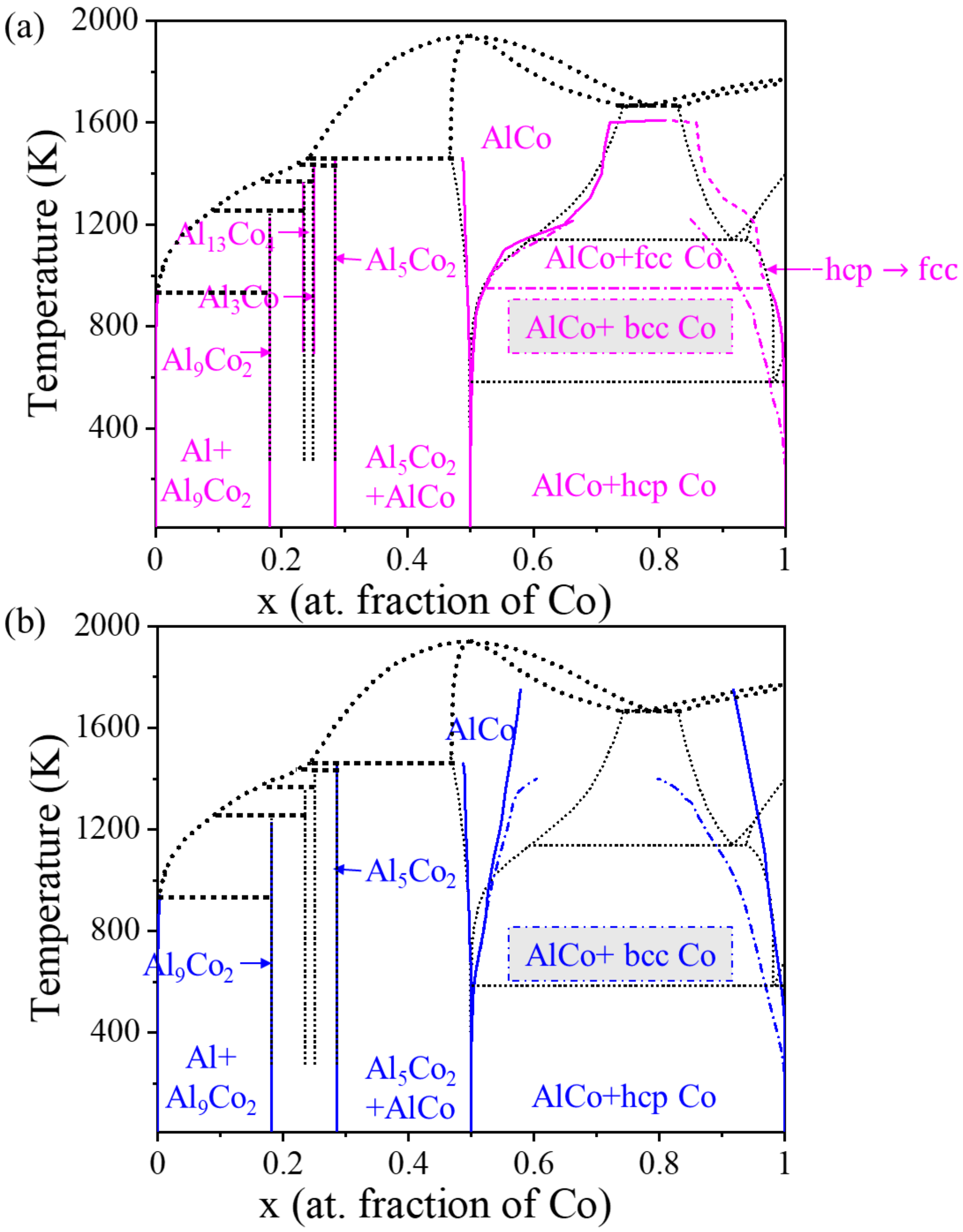

Figure 5.24: (a) Comparison of the experimental Co-Al phase diagram [267] (dashed black lines) with that calculated phase diagram including only configurational and vibrational entropic contributions (purple lines). (b) Idem compared with the calculated phase diagram including only configurational entropic contributions (blue lines). The thick black dashed lines stand for the liquidus and solidus curves.

5.5.3. **Conclusions**

The phase diagram of the Co-Al system was predicted by means of first principles simulations and statistical mechanics. The phases on the Al-rich part - with the exception of Al - can be treated as line compounds, the Gibbs free energies of these phases were determined by formation enthalpy at 0 K and vibrational free energy at different temperatures. While the phases on the Al-rich part configurations can be treated as configurations existing on fcc, bcc or hcp lattices, with the atomic sites accommodating Al and Co atoms. The temperature-dependent mixing enthalpies of the configurations in each lattice were approximated by the cluster expansion formalism, including the effect of vibrational entropy which was calculated from the corresponding length-stiffness relationships and of magnetic entropy which was calculated from the Heisenberg model MC simulation. The thermodynamic grand potential of each phase and the Gibbs free energy were calculated from MC simulations and used to predict the phase diagram.

Five ground state phases were found at 0 K, namely Al, Al_9Co_2, Al_5Co_2, AlCo, and hcp Co. Among them, Al_9Co_2 and Al_5Co_2were line compounds. Two high temperature phases, $Al_{13}Co_4$ and Al_3Co, appeared on the convex hull after considering the vibrational entropic effect, and Co transformed from hcp to fcc crystal structure. Magnetic entropic contribution to free energy is smaller than vibrational entropy because the transition temperature of Co from hcp to fcc is only slightly changed. The predicted phase diagram was in excellent agreement with the current experimentally accepted Co-Al phase diagram. It not only provided accurate predictions of the two-phase boundaries, critical equilibrium temperatures and solubility of the phases, also predicted the Curie temperature of fcc solid solution with different Co composition and provided the PM-FM phase boundaries. In addition, the prediction of a metastable two-phase (AlCo-bcc Co) region fills the gap in the current Co-Al phase diagram.

Predictions of the phase diagram were carried out by neglecting the effect of magnetic and of vibrational entropy. It was found that neglecting magnetic contribution only leads to few changes, that are only relevant in the Co-rich region of the phase diagram. While vibrational entropy is necessary to predict accurately the phase boundaries and the critical equilibrium temperatures for high temperature phases ($Al_{13}Co_4$ and Al_3Co) and AlCo-Co two phase region.

Data availability

The computational data generated in this chapter can be found at https://zenodo.org/doi/10.5281/zenodo.12509680.

6. Conclusions and Future work

6.1. Conclusions

The main conclusions of the results presented in this thesis are the following:

• It has been demonstrated that the solid-state region of the phase diagrams of binary metallic alloys can be accurately predicted through the combination of first-principles calculations with statistical mechanics principles.

• First principles calculations provide information about the stable phases at 0 K while different statistical and quantum mechanics strategies are used to include the entropic contributions to the free energy at finite temperatures. In particular, the cluster expansion methodology together with MC simulations can be used to predict the configurational entropic contribution. Similarly, the bond length *vs* bond stiffness relationships for each type of bond in each lattice provides an accurate and computationally efficient route to determine the vibrational entropic contribution. Finally, the Heisenberg model was used to obtain the magnetic contribution to the free energy. To this end, a Heisenberg Hamiltonian reflecting the magnetic interactions among atoms is obtained from first principles calculations and the magnetic specific heat of each phase at different temperature is determined by means of MC simulations based on the Heisenberg Hamiltonian. The Curie temperature is given by the peak value of the magnetic specific heat, while the magnetic entropy is obtained by integrating the magnetic specific heat with respect to the temperature.

• The information of first principles calculations is useful to find the stable phases at low temperatures but it may lead to significant errors at temperatures above 300K and it cannot capture the presence of metastable phases as well as many complex phase transformations. Vibrational entropic contributions are necessary to obtain accurate predictions of the phase diagrams at higher temperatures. Moreover, if one or both phases are magnetic, the contributions of magnetic enthalpy and entropy should be included. The latter is critical to predict accurately magnetic phase transitions.

6.2. Future work

• The methodology presented in this thesis is restricted to the solid-state region of the phase diagram. An obvious development is to combine this methodology with the information available in by Calphad databases for the free energies in the liquid region of the phase diagram to predict the whole phase diagram including the solidus and liquidus lines as well as the liquid-to-solid phase transitions (e.g. eutectic).

- The Calphad methodology uses thermodynamic databases in combination with different approximations to calculate the phase diagram. Incorporating the accurate thermodynamic information obtained with the methodology developed in this thesis into Calphad databases may lead to improvements in Calphad predictions.

- It is currently recognized that multi-principal elements alloys offer a huge potential for many engineering applications. The experimental exploration of the phase diagrams of these alloys is extremely costly because of the large number of potential compositions. This fact also limits the application of the Calphad methodology, whose thermodynamic databases are usually obtained from experiments. Moreover, the accuracy of the Calphad predictions for binary and ternary systems is often the result of the fitting strategy but this success is not guaranteed in the case of extrapolations to more complex alloys. Within this scenario, the accurate thermodynamic properties that can be obtained for binary -and even ternary- systems using the methodology presented in this thesis may be used as input to predict the phase diagrams of multi-principal element alloys in combination with the Calphad methodology.

Bibliography

[1] A.D. Pelton, Thermodynamics and Phase Diagrams of Materials, in: Phase Transformations in Materials, John Wiley & Sons, Ltd, 2001: pp. 1-80. https://doi.org/10.1002/352760264X.ch1.

[2] Y.A. Chang, S. Chen, F. Zhang, X. Yan, F. Xie, R. Schmid-Fetzer, W.A. Oates, Phase diagram calculation: past, present and future, Progress in Materials Science 49 (2004) 313-345. https://doi.org/10.1016/S0079-6425(03)00025-2.

[3] P. Hu, P. Hu, T.D. Vu, M. Li, S. Wang, Y. Ke, X. Zeng, L. Mai, Y. Long, Vanadium Oxide: Phase Diagrams, Structures, Synthesis, and Applications, Chem. Rev. 123 (2023) 4353-4415. https://doi.org/10.1021/acs.chemrev.2c00546.

[4] A.M. Holder, S. Siol, P.F. Ndione, H. Peng, A.M. Deml, B.E. Matthews, L.T. Schelhas, M.F. Toney, R.G. Gordon, W. Tumas, J.D. Perkins, D.S. Ginley, B.P. Gorman, J. Tate, A. Zakutayev, S. Lany, Novel phase diagram behavior and materials design in heterostructural semiconductor alloys, Science Advances 3 (2017) e1700270. https://doi.org/10.1126/sciadv.1700270.

[5] G.B. Olson, Preface to the viewpoint set on: The Materials Genome, Scripta Materialia 70 (2014) 1-2. https://doi.org/10.1016/j.scriptamat.2013.09.013.

[6] W. Yi Wang, J. Li, W. Liu, Z.-K. Liu, Integrated computational materials engineering for advanced materials: A brief review, Computational Materials Science 158 (2019) 42-48. https://doi.org/10.1016/j.commatsci.2018.11.001.

[7] L. Kaufman, J. Ågren, CALPHAD, first and second generation - Birth of the materials genome, Scripta Materialia 70 (2014) 3-6. https://doi.org/10.1016/j.scriptamat.2012.12.003.

[8] Z.-K. Liu, Ocean of Data: Integrating First-Principles Calculations and CALPHAD Modeling with Machine Learning, J. Phase Equilib. Diffus. 39 (2018) 635-649. https://doi.org/10.1007/s11669-018-0654-z.

[9] M.H. Chiu, E.J. Prenner, Differential scanning calorimetry: An invaluable tool for a detailed thermodynamic characterization of macromolecules and their interactions, J Pharm Bioallied Sci 3 (2011) 39-59. https://doi.org/10.4103/0975-7406.76463.

[10] P. Gill, T.T. Moghadam, B. Ranjbar, Differential Scanning Calorimetry Techniques: Applications in Biology and Nanoscience, J Biomol Tech 21 (2010) 167-193.

[11] S. Gibout, E. Franquet, D. Haillot, J.-P. Bédécarrats, J.-P. Dumas, Challenges of the Usual Graphical Methods Used to Characterize Phase Change Materials by Differential

Scanning Calorimetry, Applied Sciences 8 (2018) 66. https://doi.org/10.3390/app8010066.

[12] Introduction to Thermal Analysis, n.d. https://link.springer.com/book/10.1007/0-306-48404-8 (accessed April 23, 2024).

[13] Handbook of Thermal Analysis and Calorimetry: Recent Advances, Techniques and Applications, Elsevier, 2018.

[14] K. Harris, Powder Diffraction Crystallography of Molecular Solids, Topics in Current Chemistry 315 (2011) 133-77. https://doi.org/10.1007/128_2011_251.

[15] P. Kalita, P. Specht, S. Root, N. Sinclair, A. Schuman, M. White, A.L. Cornelius, J. Smith, S. Sinogeikin, Direct Observations of a Dynamically Driven Phase Transition with in situ X-Ray Diffraction in a Simple Ionic Crystal, Phys Rev Lett 119 (2017) 255701. https://doi.org/10.1103/PhysRevLett.119.255701.

[16] N. Bensebaa, N. Loudjani, S. Alleg, L. Dekhil, J.J. Suñol, M. Al Sae, M. Bououdina, XRD analysis and magnetic properties of nanocrystalline Ni20Co80 alloys, Journal of Magnetism and Magnetic Materials 349 (2014) 51-56. https://doi.org/10.1016/j.jmmm.2013.08.045.

[17] K. Han, I. Ohnuma, K. Okuda, R. Kainuma, Experimental determination of phase diagram in the Zn-Fe binary system, Journal of Alloys and Compounds 737 (2018) 490-504. https://doi.org/10.1016/j.jallcom.2017.11.320.

[18] M. Yasseri, A. Sankhla, H. Kamila, R. Orenstein, D.Y.N. Truong, N. Farahi, J. de Boor, E. Mueller, Solid solution formation in Mg_2(Si,Sn) and shape of the miscibility gap, Acta Materialia 185 (2020) 80-88. https://doi.org/10.1016/j.actamat.2019.11.054.

[19] R. Tamim, K. Mahdouk, S. Otmani, K. Achgar, Thermodynamic description of the aluminum-rhenium system, J Therm Anal Calorim 139 (2020) 953-961. https://doi.org/10.1007/s10973-019-08538-5.

[20] C. Nataraj, E.J.L. Borda, A. van de Walle, A. Samanta, A systematic analysis of phase stability in refractory high entropy alloys utilizing linear and non-linear cluster expansion models, Acta Materialia 220 (2021) 117269. https://doi.org/10.1016/j.actamat.2021.117269.

[21] Y.Z. Zhan, Y. Du, Y.H. Zhuang, Chapter 4 - Determination of phase diagrams using equilibrated alloys, in: J.-C. Zhao (Ed.), Methods for Phase Diagram Determination, Elsevier Science Ltd, Oxford, 2007: pp. 108-150. https://doi.org/10.1016/B978-008044629-5/50004-5.

[22] N. Saunders, A.P. Miodownik, CALPHAD (calculation of phase diagrams): a comprehensive guide, Elsevier, 1998.

[23] B. Sundman, Q. Chen, Y. Du, A Review of Calphad Modeling of Ordered Phases, J. Phase Equilib. Diffus. 39 (2018) 678-693. https://doi.org/10.1007/s11669-018-0671-y.

[24] Q. Luo, C. Zhai, D. Sun, W. Chen, Q. Li, Interpolation and extrapolation with the CALPHAD method, Journal of Materials Science & Technology 35 (2019) 2115-2120. https://doi.org/10.1016/j.jmst.2019.05.016.

[25] U.R. Kattner, The need for reliable data in computational thermodynamics, High Temp High Press 49 (2020) https://doi.org/10.32908/hthp.v49.853.

[26] G. Xu, L. Zhang, L. Liu, Y. Du, F. Zhang, K. Xu, S. Liu, M. Tan, Z. Jin, Thermodynamic database of multi-component Mg alloys and its application to solidification and heat treatment, Journal of Magnesium and Alloys 4 (2016) 249-264. https://doi.org/10.1016/j.jma.2016.11.004.

[27] C. Zhang, M.C. Gao, CALPHAD Modeling of High-Entropy Alloys, in: M.C. Gao, J.-W. Yeh, P.K. Liaw, Y. Zhang (Eds.), High-Entropy Alloys: Fundamentals and Applications, Springer International Publishing, Cham, 2016: pp. 399-444. https://doi.org/10.1007/978-3-319-27013-5_12.

[28] M.C. Gao, C. Zhang, P. Gao, F. Zhang, L.Z. Ouyang, M. Widom, J.A. Hawk, Thermodynamics of concentrated solid solution alloys, Current Opinion in Solid State and Materials Science 21 (2017) 238-251. https://doi.org/10.1016/j.cossms.2017.08.001.

[29] F. Zhang, C. Zhang, S.L. Chen, J. Zhu, W.S. Cao, U.R. Kattner, An understanding of high entropy alloys from phase diagram calculations, Calphad 45 (2014) 1-10. https://doi.org/10.1016/j.calphad.2013.10.006.

[30] A. Kroupa, Modelling of phase diagrams and thermodynamic properties using *Calphad* method - Development of thermodynamic databases, Computational Materials Science 66 (2013) 3-13. https://doi.org/10.1016/j.commatsci.2012.02.003.

[31] H.-L. Chen, H. Mao, Q. Chen, Database development and Calphad calculations for high entropy alloys: Challenges, strategies, and tips, Materials Chemistry and Physics 210 (2018) 279-290. https://doi.org/10.1016/j.matchemphys.2017.07.082.

[32] O.N. Senkov, J.D. Miller, D.B. Miracle, C. Woodward, Accelerated exploration of multi-principal element alloys for structural applications, Calphad 50 (2015) 32-48. https://doi.org/10.1016/j.calphad.2015.04.009.

[33] C. Zhang, Y. Yang, The CALPHAD approach for HEAs: Challenges and opportunities, MRS Bulletin 47 (2022) 158-167. https://doi.org/10.1557/s43577-022-00284-8.

[34] P. Feng, L. Hao, W. Xiong, Calphad modeling and prediction of magnetic phase diagram for the Fe-Cr-Ni system, Ingenium: Undergraduate Research at the Swanson School of Engineering (2021).

[35] L. Wang, M. h. Kaye, Non-Equilibrium structural factors in experimental U-Pd phase diagram determinations and thermodynamic evaluations, Canadian Metallurgical Quarterly (n.d.) 1-13. https://doi.org/10.1080/00084433.2024.2306007.

[36] K. Sato, H. Katayama-Yoshida, First principles materials design for semiconductor spintronics, Semicond. Sci. Technol. 17 (2002) 367. https://doi.org/10.1088/0268-1242/17/4/309.

[37] B. Liu, J. Zhao, Y. Liu, J. Xi, Q. Li, H. Xiang, Y. Zhou, Application of high-throughput first-principles calculations in ceramic innovation, Journal of Materials Science & Technology 88 (2021) 143-157. https://doi.org/10.1016/j.jmst.2021.01.071.

[38] C. Ravi, H.K. Sahu, M.C. Valsakumar, A. van de Walle, Cluster expansion Monte Carlo study of phase stability of vanadium nitrides, Phys. Rev. B 81 (2010) 104111. https://doi.org/10.1103/PhysRevB.81.104111.

[39] S. Liu, E. Martínez, J. LLorca, Prediction of the Al-rich part of the Al-Cu phase diagram using cluster expansion and statistical mechanics, Acta Materialia 195 (2020) 317-326. https://doi.org/10.1016/j.actamat.2020.05.018.

[40] D. Cheng, K. Wang, B.-C. Zhou, Crystal structure and stability of phases in Mg-Zn alloys: A comprehensive first-principles study, Acta Materialia 242 (2023) 118443. https://doi.org/10.1016/j.actamat.2022.118443.

[41] M. Widom, W.P. Huhn, S. Maiti, W. Steurer, Hybrid Monte Carlo/Molecular Dynamics Simulation of a Refractory Metal High Entropy Alloy, Metall Mater Trans A 45 (2014) 196-200. https://doi.org/10.1007/s11661-013-2000-8.

[42] J.M. Sanchez, Cluster expansion and the configurational theory of alloys, Phys. Rev. B 81 (2010) 224202. https://doi.org/10.1103/PhysRevB.81.224202.

[43] D. Wen, M.S. Titus, First-principles study of Suzuki segregation at stacking faults in disordered face-centered cubic Co-Ni alloys, Acta Materialia 221 (2021) 117358. https://doi.org/10.1016/j.actamat.2021.117358.

[44] S. Zhu, J. Shittu, A. Perron, C. Nataraj, J. Berry, J.T. McKeown, A. van de Walle, A. Samanta, Probing phase stability in CrMoNbV using cluster expansion method,

CALPHAD calculations and experiments, Acta Materialia 255 (2023) 119062. https://doi.org/10.1016/j.actamat.2023.119062.

[45] A.R. Natarajan, P. Dolin, A. Van der Ven, Crystallography, thermodynamics and phase transitions in refractory binary alloys, Acta Materialia 200 (2020) 171-186. https://doi.org/10.1016/j.actamat.2020.08.034.

[46] V. Ozoliņš, C. Wolverton, A. Zunger, First-principles theory of vibrational effects on the phase stability of Cu-Au compounds and alloys, Phys. Rev. B 58 (1998) R5897-R5900. https://doi.org/10.1103/PhysRevB.58.R5897.

[47] K. Li, C.-C. Fu, Ground-state properties and lattice-vibration effects of disordered Fe-Ni systems for phase stability predictions, Phys. Rev. Mater. 4 (2020) 023606. https://doi.org/10.1103/PhysRevMaterials.4.023606.

[48] J.M. Sanchez, J.P. Stark, V.L. Moruzzi, First-principles calculation of the Ag-Cu phase diagram, Phys. Rev. B 44 (1991) 5411-5418. https://doi.org/10.1103/PhysRevB.44.5411.

[49] L. Monacelli, R. Bianco, M. Cherubini, M. Calandra, I. Errea, F. Mauri, The stochastic self-consistent harmonic approximation: calculating vibrational properties of materials with full quantum and anharmonic effects, J. Phys.: Condens. Matter 33 (2021) 363001. https://doi.org/10.1088/1361-648X/ac066b.

[50] A. Togo, I. Tanaka, First principles phonon calculations in materials science, Scripta Materialia 108 (2015) 1-5. https://doi.org/10.1016/j.scriptamat.2015.07.021.

[51] T. Kamencek, S. Wieser, H. Kojima, N. Bedoya-Martínez, J.P. Dürholt, R. Schmid, E. Zojer, Evaluating Computational Shortcuts in Supercell-Based Phonon Calculations of Molecular Crystals: The Instructive Case of Naphthalene, J. Chem. Theory Comput. 16 (2020) 2716-2735. https://doi.org/10.1021/acs.jctc.0c00119.

[52] F. Geng, J.R. Boes, J.R. Kitchin, First-principles study of the Cu-Pd phase diagram, Calphad 56 (2017) 224-229. https://doi.org/10.1016/j.calphad.2017.01.009.

[53] H. Tao Xue, F.L. Tang, X. Kang Li, F. Cheng Wan, W. Jiang Lu, Z. Yuan Rui, Y. Dong Feng, Phase equilibrium of a $CuInSe_2$-$CuInS_2$ pseudobinary system studied by combined first-principles calculations and cluster expansion Monte Carlo simulations, Materials Science in Semiconductor Processing 25 (2014) 251-257. https://doi.org/10.1016/j.mssp.2013.12.021.

[54] A. Woźniakowski, J. Deniszczyk, Title: Phase diagram calculations for the ZnSe-BeSe system by first-principles base thermodynamic Monte Carlo integration, (n.d.).

[55] A. van de Walle, G. Ceder, The effect of lattice vibrations on substitutional alloy thermodynamics, Rev. Mod. Phys. 74 (2002) 11-45. https://doi.org/10.1103/RevModPhys.74.11.

[56] B. Fultz, Vibrational thermodynamics of materials, Progress in Materials Science 55 (2010) 247-352.

[57] W. Shao, S. Liu, J. LLorca, First principles prediction of the Al-Li phase diagram including configurational and vibrational entropic contributions, 2022. https://doi.org/10.48550/arXiv.2211.03664.

[58] H.I. Soezen, T. Hickel, J. Neugebauer, Impact of magnetism on the phase stability of rare-earth based hard magnetic materials, Calphad 68 (2020) 101731.

[59] H. Ohtani, M. Yamano, M. Hasebe, Thermodynamic analysis of the Co-Al-C and Ni-Al-C systems by incorporating ab initio energetic calculations into the CALPHAD approach, Calphad 28 (2004) 177-190.

[60] I. Ohnuma, H. Enoki, O. Ikeda, R. Kainuma, H. Ohtani, B. Sundman, K. Ishida, Phase equilibria in the Fe-Co binary system, Acta Materialia 50 (2002) 379-393. https://doi.org/10.1016/S1359-6454(01)00337-8.

[61] W. Xiong, Thermodynamic and Kinetic Investigation of the Fe-Cr-Ni System Driven by Engineering Applications, (2012). https://urn.kb.se/resolve?urn=urn:nbn:se:kth:diva-96707 (accessed April 3, 2024).

[62] A. Jacob, E. Povoden-Karadeniz, P. Retzl, E. Kozeschnik, Reassessment of low-temperature Gibbs energies of BCC and FCC in steel for T_0-temperature evaluation, Calphad 81 (2023) 102531. https://doi.org/10.1016/j.calphad.2023.102531.

[63] X. Yuan, L. Zhang, Y. Du, W. Xiong, Y. Tang, A. Wang, S. Liu, A new approach to establish both stable and metastable phase equilibria for fcc ordered/disordered phase transition: application to the Al-Ni and Ni-Si systems, Materials Chemistry and Physics 135 (2012) 94-105. https://doi.org/10.1016/j.matchemphys.2012.04.028.

[64] Y. Zhang, B. Wang, Y. Guo, Q. Li, J. Wang, A universal framework for metropolis Monte Carlo simulation of magnetic Curie temperature, Computational Materials Science 197 (2021) 110638. https://doi.org/10.1016/j.commatsci.2021.110638.

[65] V.-T. Tran, C.-C. Fu, A. Schneider, Effective interaction model for coupled magnetism and phase stability in bcc Fe-Co systems, Computational Materials Science 183 (2020) 109906.

[66] A.V. Ruban, V.I. Razumovskiy, First-principles based thermodynamic model of phase equilibria in bcc Fe-Cr alloys, Phys. Rev. B 86 (2012) 174111. https://doi.org/10.1103/PhysRevB.86.174111.

[67] H. Ben Hamed, M. Hoffmann, W.A. Adeagbo, A. Ernst, W. Hergert, T. Hynninen, K. Kokko, P. Paturi, First-principles investigations of the magnetic phase diagram of $Gd_{1-x}Ca_xMnO_3$, Phys. Rev. B 99 (2019) 144428. https://doi.org/10.1103/PhysRevB.99.144428.

[68] R. Troć, Z. Gajek, A. Pikul, H. Misiorek, E. Colineau, F. Wastin, Phenomenological crystal-field model of the magnetic and thermal properties of the Kondo-like system UCu_2Si_2, Physical Review B 88 (2013). https://doi.org/10.1103/PhysRevB.88.024416.

[69] M. Pajda, J. Kudrnovský, I. Turek, V. Drchal, P. Bruno, *Ab initio* calculations of exchange interactions, spin-wave stiffness constants, and Curie temperatures of Fe, Co, and Ni, Phys. Rev. B 64 (2001) 174402. https://doi.org/10.1103/PhysRevB.64.174402.

[70] M. Matyunina, M. Zagrebin, V. Sokolovskiy, V. Buchelnikov, Ab initio study of magnetic and structural properties of Fe-Ga alloys, in: EPJ Web of Conferences, EDP Sciences, 2018: p. 04013.

[71] A. Kashyap, R. Skomski, R.F. Sabiryanov, S.S. Jaswal, D.J. Sellmyer, Exchange interactions and Curie temperature of Y-Co compounds, IEEE Transactions on Magnetics 39 (2003) 2908-2910. https://doi.org/10.1109/TMAG.2003.815744.

[72] I. Turek, J. Rusz, M. Diviš, Electronic structure and volume magnetostriction of rare-earth metals and compounds, Journal of Magnetism and Magnetic Materials 290 (2005) 357-363.

[73] J.C. Williams, E.A. Starke, Progress in structural materials for aerospace systems1, Acta Materialia 51 (2003) 5775-5799. https://doi.org/10.1016/j.actamat.2003.08.023.

[74] E. Kaya, M.R. Sheikhi, S. Gürgen, M.C. Kuşhan, Aluminum-Lithium Alloys in Aircraft Structures, in: M.C. Kuşhan, S. Gürgen, M.A. Sofuoğlu (Eds.), Materials, Structures and Manufacturing for Aircraft, Springer International Publishing, Cham, 2022: pp. 1-25. https://doi.org/10.1007/978-3-030-91873-6_1.

[75] H. M, L. Swadzba, B. Mendala, Advanced materials and protective coatings in aero-engines application, Journal of Achievements in Materials and Manufacturing Engineering 24 (2007).

[76] N. Prasad, P. Rao, Low cycle fatigue resistance of Al-Li alloys, Materials Science and Technology 16 (2000) 408-426. https://doi.org/10.1179/026708300101508009.

[77] A. Abd El-Aty, Y. Xu, X. Guo, S.-H. Zhang, Y. Ma, D. Chen, Strengthening mechanisms, deformation behavior, and anisotropic mechanical properties of Al-Li alloys: A review, Journal of Advanced Research 10 (2018) 49-67. https://doi.org/10.1016/j.jare.2017.12.004.

[78] E.A. Hajjioui, K. Bouchaâla, M. Faqir, E. Essadiqi, A review of manufacturing processes, mechanical properties and precipitations for aluminum lithium alloys used in aeronautic applications, Heliyon 9 (2023). https://doi.org/10.1016/j.heliyon.2022.e12565.

[79] R.K. Gupta, N. Nayan, G. Nagasireesha, S.C. Sharma, Development and characterization of Al-Li alloys, Materials Science and Engineering: A 420 (2006) 228-234. https://doi.org/10.1016/j.msea.2006.01.045.

[80] R.J. Rioja, J. Liu, The Evolution of Al-Li Base Products for Aerospace and Space Applications, Metall Mater Trans A 43 (2012) 3325-3337. https://doi.org/10.1007/s11661-012-1155-z.

[81] R. Wanhill, G.H. Bray, Aerostructural Design and Its Application to Aluminum-Lithium Alloys, in: 2014: pp. 27-58. https://doi.org/10.1016/B978-0-12-401698-9.00002-1.

[82] T. Dursun, C. Soutis, Recent developments in advanced aircraft aluminium alloys, Materials & Design (1980-2015) 56 (2014) 862-871. https://doi.org/10.1016/j.matdes.2013.12.002.

[83] A.A. El-Aty, Y. Xu, S. Zhang, Y. Ma, D. Chen, Experimental investigation of tensile properties and anisotropy of 1420, 8090 and 2060 Al-Li alloys sheet undergoing different strain rates and fibre orientation: a comparative study, Procedia Engineering 207 (2017) 13-18. https://doi.org/10.1016/j.proeng.2017.10.730.

[84] A.J. Ardell, The Equilibrium α (Al-Li Solid Solution) and Metastable δ′ (Al_3Li) Phase Boundaries in Aluminum-Lithium Alloys, J. Phase Equilib. Diffus. 44 (2023) 255-268. https://doi.org/10.1007/s11669-023-01039-x.

[85] I. Ansara, N. Dupin, H.L. Lukas, B. Sundman, Thermodynamic assessment of the Al-Ni system, Journal of Alloys and Compounds 247 (1997) 20-30. https://doi.org/10.1016/S0925-8388(96)02652-7.

[86] P. Neibecker, M. Leitner, M. Kushaim, T. Boll, D. Anjum, T. Al-Kassab, F. Haider, L12 ordering and δ′ precipitation in Al-Cu-Li, Sci Rep 7 (2017) 3254. https://doi.org/10.1038/s41598-017-03203-z.

[87] C. Sigli, J.M. Sanchez, Calculation of phase equilibrium in Al-Li alloys, Acta Metallurgica 34 (1986) 1021-1028. https://doi.org/10.1016/0001-6160(86)90211-7.

[88] M. Sluiter, D. de Fontaine, X.Q. Guo, R. Podloucky, A.J. Freeman, First-principles calculation of phase equilibria in the aluminum lithium system, Phys. Rev. B 42 (1990) 10460-10476. https://doi.org/10.1103/PhysRevB.42.10460.

[89] S. Liu, G. Esteban-Manzanares, J. LLorca, First Principles Prediction of the Al-Li Phase Diagram, Metall Mater Trans A 52 (2021) 4675-4690. https://doi.org/10.1007/s11661-021-06419-x.

[90] E. Siswanto, D.B. Darmadi, A.S. Widodo, M. Talice, Enhancement of combustion performances and reduction of combustible species emission using an additional of combustion-reaction of engine, Case Studies in Thermal Engineering 49 (2023) 103328. https://doi.org/10.1016/j.csite.2023.103328.

[91] H. Dong, T. Xu, T. Ning, M. Liu, D. Wu, H. Ma, Z. Feng, B. Narayanaswamy, R. Su, T. Wang, Atomic simulations on the deformation mechanisms in nano-crystalline Ni-Al series Ni-based superalloy based on grain size, strain rate and temperature, Journal of Materials Research and Technology 23 (2023) 77-89. https://doi.org/10.1016/j.jmrt.2022.12.183.

[92] A. Korashy, H. Attia, V. Thomson, S. Oskooei, Characterization of fretting wear of cobalt-based superalloys at high temperature for aero-engine combustor components, Wear 330 (2015) 327-337.

[93] R. Wu, Y. Zhao, Q. Yin, J. Wang, X. Ai, Z. Wen, Atomistic simulation studies of Ni-based superalloys, Journal of Alloys and Compounds 855 (2021) 157355. https://doi.org/10.1016/j.jallcom.2020.157355.

[94] G.R. Thellaputta, P.S. Chandra, C.S.P. Rao, Machinability of Nickel Based Superalloys: A Review, Materials Today: Proceedings 4 (2017) 3712-3721. https://doi.org/10.1016/j.matpr.2017.02.266.

[95] X. Ye, D. Zhou, B. Yang, F. Wang, J. Liu, Y. Li, Effect of cobalt on γ′ coarsening behavior of Ni-base powder metallurgy superalloy, Journal of Alloys and Compounds 921 (2022) 166057. https://doi.org/10.1016/j.jallcom.2022.166057.

[96] M. Dodaran, A.H. Ettefagh, S.M. Guo, M.M. Khonsari, W.J. Meng, N. Shamsaei, S. Shao, Effect of alloying elements on the γ’ antiphase boundary energy in Ni-base superalloys, Intermetallics 117 (2020) 106670. https://doi.org/10.1016/j.intermet.2019.106670.

[97] A. Biswas, S.K. Roy, K.R. Gurumurthy, N. Prabhu, S. Banerjee, A study of self-propagating high-temperature synthesis of NiAl in thermal explosion mode, Acta Materialia 50 (2002) 757-773. https://doi.org/10.1016/S1359-6454(01)00387-1.

[98] S. Neumeier, J. Ang, R.A. Hobbs, C. Rae, H. Stone, Lattice Misfit of High Refractory Ruthenium Containing Nickel-Base Superalloys, Advanced Materials Research 278 (2011) 60-65. https://doi.org/10.4028/www.scientific.net/AMR.278.60.

[99] P. Tsakiropoulos, Alloys for application at ultra-high temperatures: Nb-silicide *in situ* composites, Progress in Materials Science 123 (2022) 100714. https://doi.org/10.1016/j.pmatsci.2020.100714.

[100] Q. Feng, T.K. Nandy, S. Tin, T.M. Pollock, Solidification of high-refractory ruthenium-containing superalloys, Acta Materialia 51 (2003) 269-284. https://doi.org/10.1016/S1359-6454(02)00397-X.

[101] R.A. Hobbs, L. Zhang, C. Rae, S. Tin, Mechanisms of Topologically Close-Packed Phase Suppression in an Experimental Ruthenium-Bearing Single-Crystal Nickel-Base Superalloy at 1100 °C, Metallurgical and Materials Transactions A 39 (2008) 1014-1025. https://doi.org/10.1007/s11661-008-9490-9.

[102] W. Guo, H. Zhao, Y. Ru, Y. Pei, J. Wang, Q. Liu, X. Li, H. Wang, S. Zhang, S. Gong, S. Li, Topologically Closed Packed Phase and Its Interaction with Dislocation Movement in Ni-Based Superalloy during High-Temperature Creep, Crystals 12 (2022) 1446. https://doi.org/10.3390/cryst12101446.

[103] P. Zhao, G. Xie, C. Chen, X. Wang, P. Zeng, F. Wang, J. Zhang, K. Du, Interplay of chemistry and deformation-induced defects on facilitating topologically-close-packed phase precipitation in nickel-base superalloys, Acta Materialia 236 (2022) 118109. https://doi.org/10.1016/j.actamat.2022.118109.

[104] S.V. Raju, B.K. Godwal, J. Yan, R. Jeanloz, S.K. Saxena, Yield strength of Ni-Al-Cr superalloy under pressure, Journal of Alloys and Compounds 657 (2016) 889-892. https://doi.org/10.1016/j.jallcom.2015.10.092.

[105] C. Sigli, J.M. Sanchez, Theoretical description of phase equilibrium in binary alloys, Acta Metallurgica 33 (1985) 1097-1104. https://doi.org/10.1016/0001-6160(85)90203-2.

[106] A. Pasturel, C. Colinet, A.T. Paxton, M. van Schilfgaarde, First-principles determination of the Ni-Al phase diagram, J. Phys.: Condens. Matter 4 (1992) 945. https://doi.org/10.1088/0953-8984/4/4/005.

[107] J.G. Goiri, A. Van der Ven, Phase and structural stability in Ni-Al systems from first principles, Phys. Rev. B 94 (2016) 094111. https://doi.org/10.1103/PhysRevB.94.094111.

[108] C.F. Li, Y.P. Ren, G.W. Qin, Experimental Confirmation of Ni_5Al_3 Phase in Ni-Al Binary System by Diffusion Couple Technique, Advanced Materials Research 299-300 (2011) 224-227. https://doi.org/10.4028/www.scientific.net/AMR.299-300.224.

[109] N.V. Kataeva, S.V. Kositsyn, A.I. Valiullin, Formation of Ni_2Al and Ni_5Al_3 superstructures and reversibility of martensitic transformation in NiAl-based β-alloys, Materials Science and Engineering: A 438-440 (2006) 312-314. https://doi.org/10.1016/j.msea.2006.02.081.

[110] T. Chráska, J. Lašek, P. Chráska, Resistometric investigation of phase transformations in NiAl alloys, Materials Science and Engineering: A 244 (1998) 263-272. https://doi.org/10.1016/S0921-5093(97)00647-3.

[111] D. Coutsouradis, A. Davin, M. Lamberigts, Cobalt-based superalloys for applications in gas turbines, Materials Science and Engineering 88 (1987) 11-19. https://doi.org/10.1016/0025-5416(87)90061-9.

[112] T. Pollock, J. Dibbern, M. Tsunekane, J. Zhu, A. Suzuki, New Co-based γ-γ′ High-temperature alloys, JOM 62 (2010) 58-63. https://doi.org/10.1007/s11837-010-0013-y.

[113] W.W. Xu, S.L. Shang, C.P. Wang, T.Q. Gang, Y.F. Huang, L.J. Chen, X.J. Liu, Z.K. Liu, Accelerating exploitation of Co-Al-based superalloys from theoretical study, Materials & Design 142 (2018) 139-148. https://doi.org/10.1016/j.matdes.2018.01.013.

[114] A. Suzuki, H. Inui, T.M. Pollock, L12-Strengthened Cobalt-Base Superalloys, Annual Review of Materials Research 45 (2015) 345-368. https://doi.org/10.1146/annurev-matsci-070214-021043.

[115] S. Neumeier, L.P. Freund, M. Göken, Novel wrought γ/γ′ cobalt base superalloys with high strength and improved oxidation resistance, Scripta Materialia 109 (2015). https://doi.org/10.1016/j.scriptamat.2015.07.030.

[116] X. Zhang, H. Shang, Q. Gao, Q. Ma, H. Zhang, H. Li, L. Sun, Coarsening Evolution of γ′ Phase and Failure Mechanism of Co-Ni-Al-Ti-Based Superalloys During Isothermal Aging, Front. Mater. 9 (2022). https://doi.org/10.3389/fmats.2022.863305.

[117] A.F. Dinler, Synthesis and structural characterization of Co-Al based superalloys, Master Thesis, Middle East Technical University, 2019. https://open.metu.edu.tr/handle/11511/43460 (accessed April 16, 2024).

[118] J. Sato, T. Omori, K. Oikawa, I. Ohnuma, R. Kainuma, K. Ishida, Cobalt-Base High-Temperature Alloys, Science 312 (2006) 90-91. https://doi.org/10.1126/science.1121738.

[119] A. Suzuki, G.C. DeNolf, T.M. Pollock, Flow stress anomalies in γ/γ′ two-phase Co-Al-W-base alloys, Scripta Materialia 56 (2007) 385-388. https://doi.org/10.1016/j.scriptamat.2006.10.039.

[120] A. Bauer, S. Neumeier, F. Pyczak, M. Göken, Creep Strength and Microstructure of Polycrystalline γ' - Strengthened Cobalt-base Superalloys, in: Superalloys 2012 (Twelfth International Symposium), John Wiley & Sons, Inc., 2012: pp. 695-703. https://doi.org/10.1002/9781118516430.ch77.

[121] L. Shi, J.J. Yu, C.Y. Cui, X.F. Sun, Temperature dependence of deformation behavior in a Co-Al-W-base single crystal superalloy, Materials Science and Engineering: A 620 (2015) 36-43. https://doi.org/10.1016/j.msea.2014.09.074.

[122] S.K. Makineni, B. Nithin, K. Chattopadhyay, A new tungsten-free γ-γ’ Co-Al-Mo-Nb-based superalloy, Scripta Materialia 98 (2015) 36-39. https://doi.org/10.1016/j.scriptamat.2014.11.009.

[123] Y. Chen, C. Wang, J. Ruan, T. Omori, R. Kainuma, K. Ishida, X. Liu, High-strength Co-Al-V-base superalloys strengthened by γ′-Co_3(Al,V) with high solvus temperature, Acta Materialia 170 (2019) 62-74. https://doi.org/10.1016/j.actamat.2019.03.013.

[124] Y. Chen, C. Wang, J. Ruan, S. Yang, T. Omori, R. Kainuma, K. Ishida, J. Han, Y. Lu, X. Liu, Development of low-density γ/γ′ Co-Al-Ta-based superalloys with high solvus temperature, Acta Materialia 188 (2020) 652-664. https://doi.org/10.1016/j.actamat.2020.02.049.

[125] M.A. Shevchenko, V.V. Berezutskii, M.I. Ivanov, V.G. Kudin, V.S. Sudavtsova, Thermodynamic properties of alloys of the Al-Co and Al-Co-Sc systems, Russ. J. Phys. Chem. 88 (2014) 729-734. https://doi.org/10.1134/S003602441405029X.

[126] M. Ostrowska, G. Cacciamani, Critical evaluation and thermodynamic modeling of the Al-Co-Fe system, Journal of Alloys and Compounds 794 (2019) 553-568. https://doi.org/10.1016/j.jallcom.2019.04.170.

[127] T. Kozakai, T. Shikama, T. Koyama, M. Doi, Metastable Two-Phase Field(A2+B2) in Co-Al-Fe and Co-Al Alloy Systems, Materials Science Forum 449-452 (2004) 61-64. https://doi.org/10.4028/www.scientific.net/MSF.449-452.61.

[128] K. Niitsu, T. Omori, M. Nagasako, K. Oikawa, R. Kainuma, K. Ishida, Phase transformations in the B2 phase of Co-rich Co-Al binary alloys, Journal of Alloys and Compounds 509 (2011) 2697-2702.

[129] F.W. Gayle, J.B. Vander Sande, A.J. McAlister, The Al-Li (Aluminum-Lithium) system, Bulletin of Alloy Phase Diagrams 5 (1984) 19-20. https://doi.org/10.1007/BF02868711.

[130] H. Azza, N. Selhaoui, S. Kardellass, A. Iddaoudi, L. Bouirden, Thermodynamic description of the Aluminum-Lithium phase diagram, J. Mater. Environ. Sci. 6 (2015) 3501-3510.

[131] G.Y. Guo, Y.K. Wang, L.-S. Hsu, First-principles and experimental studies of the electronic structures and magnetism in and Ni_3In, Journal of Magnetism and Magnetic Materials 239 (2002) 91-93. https://doi.org/10.1016/S0304-8853(01)00564-9.

[132] M. Fedorov, J.S. Wróbel, A. Fernández-Caballero, K.J. Kurzydłowski, D. Nguyen-Manh, Phase stability and magnetic properties in fcc Fe-Cr-Mn-Ni alloys from first-principles modeling, Phys. Rev. B 101 (2020) 174416. https://doi.org/10.1103/PhysRevB.101.174416.

[133] D. Ma, B. Grabowski, F. Körmann, J. Neugebauer, D. Raabe, Ab initio thermodynamics of the CoCrFeMnNi high entropy alloy: Importance of entropy contributions beyond the configurational one, Acta Materialia 100 (2015) 90-97. https://doi.org/10.1016/j.actamat.2015.08.050.

[134] H. Zhao, Y. Yang, X. Shu, Y. Wang, Q. Ran, Adsorption of organic molecules on mineral surfaces studied by first-principle calculations: A review, Advances in Colloid and Interface Science 256 (2018) 230-241. https://doi.org/10.1016/j.cis.2018.04.003.

[135] S.P. Karna, Y. Zhang, M. Samoc, P.N. Prasad, B.A. Reinhardt, A.G. Dillard, Nonlinear optical properties of novel thiophene derivatives: Experimental and ab initio time-dependent coupled perturbed Hartree-Fock studies, The Journal of Chemical Physics 99 (1993) 9984-9993. https://doi.org/10.1063/1.465398.

[136] P. Blanchard, E. Brüning, Density Functional Theory of Atoms and Molecules, in: P. Blanchard, E. Brüning (Eds.), Mathematical Methods in Physics: Distributions, Hilbert Space Operators, Variational Methods, and Applications in Quantum Physics, Springer International Publishing, Cham, 2015: pp. 563-573. https://doi.org/10.1007/978-3-319-14045-2_37.

[137] P. Hohenberg, W. Kohn, Inhomogeneous Electron Gas, Phys. Rev. 136 (1964) B864-B871. https://doi.org/10.1103/PhysRev.136.B864.

[138] A. Klein, R.M. Dreizler, Variational principle for the ground-state energy as a functional of the one-particle density matrix: Beyond Hartree-Fock theory, Phys. Rev. A 57 (1998) 2485-2495. https://doi.org/10.1103/PhysRevA.57.2485.

[139] B.M. Deb, P.K. Chattaraj, Density-functional and hydrodynamical approach to ion-atom collisions through a new generalized nonlinear Schrödinger equation, Phys. Rev. A 39 (1989) 1696-1713. https://doi.org/10.1103/PhysRevA.39.1696.

[140] R.T. Pack, J.O. Hirschfelder, Energy Corrections to the Born-Oppenheimer Approximation. The Best Adiabatic Approximation, The Journal of Chemical Physics 52 (1970) 521-534. https://doi.org/10.1063/1.1673017.

[141] J.H. McGuire, L. Weaver, Independent electron approximation for atomic scattering by heavy particles, Phys. Rev. A 16 (1977) 41-47. https://doi.org/10.1103/PhysRevA.16.41.

[142] D.M. Ceperley, B.J. Alder, Ground State of the Electron Gas by a Stochastic Method, Phys. Rev. Lett. 45 (1980) 566-569. https://doi.org/10.1103/PhysRevLett.45.566.

[143] J.P. Perdew, Y. Wang, Accurate and simple analytic representation of the electron-gas correlation energy, Phys. Rev. B 45 (1992) 13244-13249. https://doi.org/10.1103/PhysRevB.45.13244.

[144] J.P. Perdew, K. Burke, M. Ernzerhof, Generalized Gradient Approximation Made Simple, Phys. Rev. Lett. 77 (1996) 3865-3868. https://doi.org/10.1103/PhysRevLett.77.3865.

[145] J.P. Perdew, A. Zunger, Self-interaction correction to density-functional approximations for many-electron systems, Phys. Rev. B 23 (1981) 5048-5079. https://doi.org/10.1103/PhysRevB.23.5048.

[146] G. Kresse, D. Joubert, From ultrasoft pseudopotentials to the projector augmented-wave method, Phys. Rev. B 59 (1999) 1758-1775. https://doi.org/10.1103/PhysRevB.59.1758.

[147] Z.-K. Liu, First-Principles Calculations and CALPHAD Modeling of Thermodynamics, J. Phase Equilib. Diffus. 30 (2009) 517-534. https://doi.org/10.1007/s11669-009-9570-6.

[148] J. Paier, R. Hirschl, M. Marsman, G. Kresse, The Perdew-Burke-Ernzerhof exchange-correlation functional applied to the G2-1 test set using a plane-wave basis set, J. Chem. Phys. 122 (2005) 234102. https://doi.org/10.1063/1.1926272.

[149] S. Scandolo, P. Giannozzi, C. Cavazzoni, S. de Gironcoli, A. Pasquarello, S. Baroni, First-principles codes for computational crystallography in the Quantum-ESPRESSO package, Zeitschrift Für Kristallographie - Crystalline Materials 220 (2005) 574.

[150] W.E. Pickett, Pseudopotential methods in condensed matter applications, Computer Physics Reports 9 (1989) 115-197. https://doi.org/10.1016/0167-7977(89)90002-6.

[151] H. Xing, P. Hu, S. Li, Y. Zuo, J. Han, X. Hua, K. Wang, F. Yang, P. Feng, T. Chang, Adsorption and diffusion of oxygen on metal surfaces studied by first-principle study: A

review, Journal of Materials Science & Technology 62 (2021) 180-194. https://doi.org/10.1016/j.jmst.2020.04.063.

[152] A.J.E. Foreman, W.M. Lomer, Lattice Vibrations and Harmonic Forces in Solids, Proc. Phys. Soc. B 70 (1957) 1143. https://doi.org/10.1088/0370-1301/70/12/305.

[153] D. Alfè, PHON: A program to calculate phonons using the small displacement method, Computer Physics Communications 180 (2009) 2622-2633. https://doi.org/10.1016/j.cpc.2009.03.010.

[154] J.M. Ziman, Electrons and Phonons: The Theory of Transport Phenomena in Solids, OUP Oxford, 2001.

[155] Y. Wang, S. Shang, Z.-K. Liu, L.-Q. Chen, Mixed-space approach for calculation of vibration-induced dipole-dipole interactions, Phys. Rev. B 85 (2012) 224303. https://doi.org/10.1103/PhysRevB.85.224303.

[156] S. Wei, M.Y. Chou, Ab initio calculation of force constants and full phonon dispersions, Physical Review Letters 69 (1992) 2799-2802. https://doi.org/10.1103/PhysRevLett.69.2799.

[157] A. van de Walle, G. Ceder, U. Waghmare, First-Principles Computation of the Vibrational Entropy of Ordered and Disordered Ni3Al, Physical Review Letters 80 (1998). https://doi.org/10.1103/PhysRevLett.80.4911.

[158] A. van de Walle, M. Asta, G. Ceder, The alloy theoretic automated toolkit: A user guide, Calphad 26 (2002) 539-553. https://doi.org/10.1016/S0364-5916(02)80006-2.

[159] J.Z. Liu, G. Ghosh, A. van de Walle, M. Asta, Transferable force-constant modeling of vibrational thermodynamic properties in fcc-based Al-TM (TM=Ti, Zr, Hf) alloys, Phys. Rev. B 75 (2007) 104117. https://doi.org/10.1103/PhysRevB.75.104117.

[160] B. Dutta, S. Ghosh, Phonon spectra of Pd_xFe_{1-x} alloys with transferable force constants, J. Phys.: Condens. Matter 21 (2009) 395401. https://doi.org/10.1088/0953-8984/21/39/395401.

[161] S.N. Datta, S. Hansda, Relationship between coupling constants in Heisenberg exchange Hamiltonian and Ising model, Chemical Physics Letters 621 (2015) 102-108. https://doi.org/10.1016/j.cplett.2015.01.001.

[162] C. Takahashi, M. Ogura, H. Akai, First-principles calculation of the Curie temperature Slater-Pauling curve, J. Phys.: Condens. Matter 19 (2007) 365233. https://doi.org/10.1088/0953-8984/19/36/365233.

[163] A. Loudaini, M. Aggour, L. Bahmad, O. Mounkachi, Magnetic properties, magnetocaloric effect and cooling performance of $AlFe_2B_2$compound: Ab initio, Monte Carlo and numerical modeling study, Materials Science and Engineering: B 264 (2021) 114935. https://doi.org/10.1016/j.mseb.2020.114935.

[164] R.F.L. Evans, W.J. Fan, P. Chureemart, T.A. Ostler, M.O.A. Ellis, R.W. Chantrell, Atomistic spin model simulations of magnetic nanomaterials, J. Phys.: Condens. Matter 26 (2014) 103202. https://doi.org/10.1088/0953-8984/26/10/103202.

[165] W. Nursiyanto, L. Rohman, M. N., E. Purwandari, The effect of Cobalt content on magnetic properties of CoFe alloys, Spektra: Jurnal Fisika Dan Aplikasinya 5 (2020) 87-96. https://doi.org/10.21009/SPEKTRA.052.01.

[166] L. Rohman, A. Arkundato, Y.T. Mulyani, D. Djuhana, Magnetic susceptibility and curie temperature of $Co_{1-x}Fe_x$ alloy nanocube and nanosphere using micromagnetic simulation, J. Phys.: Conf. Ser. 1825 (2021) 012003. https://doi.org/10.1088/1742-6596/1825/1/012003.

[167] Y.Q. Sun, C. Cole, M. Spiryagin, Monitoring vertical wheel-rail contact forces based on freight wagon inverse modelling, Advances in Mechanical Engineering 7 (2015) 1687814015585431. https://doi.org/10.1177/1687814015585431.

[168] S.K. Kolli, A.R. Natarajan, J.C. Thomas, T.M. Pollock, A. Van der Ven, Discovering hierarchies among intermetallic crystal structures, Phys. Rev. Mater. 4 (2020) 113604. https://doi.org/10.1103/PhysRevMaterials.4.113604.

[169] A.A. Emery, C. Wolverton, High-throughput DFT calculations of formation energy, stability and oxygen vacancy formation energy of ABO_3 perovskites, Sci Data 4 (2017) 170153. https://doi.org/10.1038/sdata.2017.153.

[170] G. Ghosh, A. van de Walle, M. Asta, First-principles calculations of the structural and thermodynamic properties of bcc, fcc and hcp solid solutions in the Al-TM (TM = Ti, Zr and Hf) systems: A comparison of cluster expansion and supercell methods, Acta Materialia 56 (2008) 3202-3221. https://doi.org/10.1016/j.actamat.2008.03.006.

[171] M. Chakraborty, J. Spitaler, P. Puschnig, C. Ambrosch-Draxl, ATAT@WIEN2k: An interface for cluster expansion based on the linearized augmented planewave method, Computer Physics Communications 181 (2010) 913-920. https://doi.org/10.1016/j.cpc.2010.01.003.

[172] A. van de Walle, M. Asta, Self-driven lattice-model Monte Carlo simulations of alloy thermodynamic properties and phase diagrams, Modelling Simul. Mater. Sci. Eng. 10 (2002) 521-538. https://doi.org/10.1088/0965-0393/10/5/304.

[173] H. De Raedt, A. Lagendijk, Monte Carlo simulation of quantum statistical lattice models, Physics Reports 127 (1985) 233-307. https://doi.org/10.1016/0370-1573(85)90044-4.

[174] G. Bhanot, The Metropolis algorithm, Rep. Prog. Phys. 51 (1988) 429. https://doi.org/10.1088/0034-4885/51/3/003.

[175] T. Mulla, S. Moeini, K. Ioannidou, R.J.-M. Pellenq, F.-J. Ulm, Phase diagram of brittle fracture in the semi-grand-canonical ensemble, Phys. Rev. E 103 (2021) 013003. https://doi.org/10.1103/PhysRevE.103.013003.

[176] G. Ceder, A derivation of the Ising model for the computation of phase diagrams, Computational Materials Science 1 (1993) 144-150. https://doi.org/10.1016/0927-0256(93)90005-8.

[177] S. Vafaei, B. Tomberli, C.G. Gray, McMillan-Mayer Theory of Solutions Revisited: Simplifications and Extensions, The Journal of Chemical Physics 141 (2014) 154501. https://doi.org/10.1063/1.4897980.

[178] A.I. Rusanov, A.K. Shchekin, D.V. Tatyanenko, Grand potential in thermodynamics of solid bodies and surfaces, J. Chem. Phys. 131 (2009) 161104. https://doi.org/10.1063/1.3254324.

[179] R.R. Boyer, J.D. Cotton, M. Mohaghegh, R.E. Schafrik, Materials considerations for aerospace applications, MRS Bulletin 40 (2015) 1055-1066. https://doi.org/10.1557/mrs.2015.278.

[180] T.S. Srivatsan, E.J. Lavernia, N. Eswara Prasad, V.V. Kutumbarao, Chapter 10 - Quasi-Static Strength, Deformation, and Fracture Behavior of Aluminum-Lithium Alloys, in: N. Eswara Prasad, A.A. Gokhale, R.J.H. Wanhill (Eds.), Aluminum-Lithium Alloys, Butterworth-Heinemann, Boston, 2014: pp. 305-339. https://doi.org/10.1016/B978-0-12-401698-9.00010-0.

[181] H. Ovri, E.T. Lilleodden, New insights into plastic instability in precipitation strengthened Al-Li alloys, Acta Materialia 89 (2015) 88-97. https://doi.org/10.1016/j.actamat.2015.01.065.

[182] H.-J. Kim, M. Niinomi, The role of microstructures on the strengthening mechanisms of a thermomechanically processed 2091 Al-Li alloy, Materials Science and Engineering: A 284 (2000) 14-24. https://doi.org/10.1016/S0921-5093(00)00802-9.

[183] N.E. Prasad, T.R. Ramachandran, Aluminum-Lithium Alloys: Chapter 3. Phase Diagrams and Phase Reactions in Al-Li Alloys, Butterworth-Heinemann, 2013.

[184] S.C. Jha, T.H. Sanders, M.A. Dayananda, Grain boundary precipitate free zones in Al-Li alloys, Acta Metallurgica 35 (1987) 473-482. https://doi.org/10.1016/0001-6160(87)90253-7.

[185] D. Venables, L. Christodoulou, J.R. Pickens, On the $\sigma' \rightarrow \sigma$ transformation in Al-Li alloys, Scripta Metallurgica 17 (1983) 1263-1268. https://doi.org/10.1016/0036-9748(83)90296-X.

[186] H. Peng, J.P. Perdew, Rehabilitation of the Perdew-Burke-Ernzerhof generalized gradient approximation for layered materials, Phys. Rev. B 95 (2017) 081105. https://doi.org/10.1103/PhysRevB.95.081105.

[187] H. Liu, I. Papadimitriou, F.X. Lin, J. LLorca, Precipitation during high temperature aging of Al−Cu alloys: A multiscale analysis based on first principles calculations, Acta Materialia 167 (2019) 121-135. https://doi.org/10.1016/j.actamat.2019.01.024.

[188] B. Montanari, N.M. Harrison, Lattice dynamics of TiO_2 rutile: influence of gradient corrections in density functional calculations, Chemical Physics Letters 364 (2002) 528-534. https://doi.org/10.1016/S0009-2614(02)01401-X.

[189] D. Lee, G. Sim, K. Zhao, J.J. Vlassak, Kinetic Role of Carbon in Solid-State Synthesis of Zirconium Diboride using Nanolaminates: Nanocalorimetry Experiments and First-Principles Calculations, Nano Lett. 15 (2015) 8266-8270. https://doi.org/10.1021/acs.nanolett.5b03829.

[190] K. Wang, D. Cheng, C.-L. Fu, B.-C. Zhou, First-principles investigation of the phase stability and early stages of precipitation in Mg-Sn alloys, Phys. Rev. Mater. 4 (2020) 013606. https://doi.org/10.1103/PhysRevMaterials.4.013606.

[191] K. Ueno, Y. Shibuta, Semi-grand canonical Monte Carlo simulation for derivation of thermodynamic properties of binary alloy, IOP Conf. Ser.: Mater. Sci. Eng. 529 (2019) 012037. https://doi.org/10.1088/1757-899X/529/1/012037.

[192] R. Novakovic, M. Mohr, D. Giuranno, E. Ricci, J. Brillo, R. Wunderlich, I. Egry, Y. Plevachuk, H.-J. Fecht, Surface Properties of Liquid Al-Ni Alloys: Experiments Vs Theory, Microgravity Sci. Technol. 32 (2020) 1049-1064. https://doi.org/10.1007/s12217-020-09832-w.

[193] Effect of phase composition and microstructure on the corrosion resistance of Ni-Al intermetallic compounds, Journal of Alloys and Compounds 695 (2017) 2424-2433. https://doi.org/10.1016/j.jallcom.2016.11.138.

[194] J. LLorca, P. Poza, Fracture toughness of Al/SiC composites in the temperature range [minus]136 C to 190 C, Scripta Metallurgica et Materialia; (United States) 29:2 (1993). https://doi.org/10.1016/0956-716X(93)90319-N.

[195] A. Martín, M.A. Martínez, J. Llorca, Wear of SiC-reinforced Al-matrix composites in the temperature range 20-200°C, Wear 193 (1996) 169-179. https://doi.org/10.1016/0043-1648(95)06704-3.

[196] A.A.S. Akl, M. Elhadi, Estimation of crystallite size, lattice parameter, internal strain and crystal impurification of nanocrystalline $al_3ni_{20}b_x$ alloy by williamson-hall method, Journal of Ovonic Research 16(5) (2020) 323-335.

[197] A.-P. Tsai, A. Inoue, T. Masumoto, Ductile Al-Ni-Zr amorphous alloys with high mechanical strength, J Mater Sci Lett 7 (1988) 805-807. https://doi.org/10.1007/BF00723766.

[198] M.I. Flores-Zamora, C.A. Martínez-Pérez, M. García-Guaderrama, I. Estrada-Guel, F. Espinosa-Maga, Comparative study of Al-Ni-Mo alloys obtained by mechanical alloying in different ball mills, Reviews on Advanced Materials Science 18(3) (2008) 301-304.

[199] C.T. Liu, V.K. Sikka, Nickel Aluminides for Structural Use, JOM 38 (1986) 19-21. https://doi.org/10.1007/BF03257837.

[200] M.L. Bakker, D.J. Young, M.S. Wainwright, Selective leaching of $NiAl_3$ and Ni_2Al_3 intermetallics to form Raney nickels, J Mater Sci 23 (1988) 3921-3926. https://doi.org/10.1007/BF01106814.

[201] Y.-J. Lee, Y.-S. Lee, J.Y. Cha, Y.S. Jo, H. Jeong, H. Sohn, C.W. Yoon, Y. Kim, K.-B. Kim, S.W. Nam, Development of porous nickel catalysts by low-temperature Ni-Al chemical alloying and post selective Al leaching, and their application for ammonia decomposition, International Journal of Hydrogen Energy 45 (2020) 19181-19191. https://doi.org/10.1016/j.ijhydene.2020.05.025.

[202] W.R. Osório, L.C. Peixoto, M.V. Canté, A. Garcia, Electrochemical corrosion characterization of Al-Ni alloys in a dilute sodium chloride solution, Electrochimica Acta 55 (2010) 4078-4085. https://doi.org/10.1016/j.electacta.2010.02.029.

[203] K. Hilpert, D. Kobertz, V. Venugopal, M. Miller, H. Gerads, F.J. Bremer, H. Nickel, Phase Diagram Studies on the Al- Ni System, Zeitschrift Für Naturforschung A 42 (1987) 1327-1332. https://doi.org/10.1515/zna-1987-1117.

[204] Y. Du, N. Clavaguera, Thermodynamic assessment of the Al-Ni system, Journal of Alloys and Compounds 237 (1996) 20-32. https://doi.org/10.1016/0925-8388(95)02085-3.

[205] W. Huang, Y.A. Chang, A thermodynamic analysis of the Ni-Al system, Intermetallics 6 (1998) 487-498. https://doi.org/10.1016/S0966-9795(97)00099-X.

[206] W. Yang, P. Wang, X. Huang, S. Zhang, Thermodynamic analysis of the Al-Ni system, Intermetallics 149 (2022) 107647. https://doi.org/10.1016/j.intermet.2022.107647.

[207] S. Tsuji, Numerical modeling of multiphase diffusion in the process of homogenizing in binary alloys, Metallurgical and Materials Transactions A 32 (2001) 681-690.

[208] I.M. Robertson, C.M. Wayman, Ni_5Al_3 and the nickel-aluminum binary phase diagram, Metallography 17 (1984) 43-55. https://doi.org/10.1016/0026-0800(84)90004-1.

[209] D. Schryvers, L. Toth, Y. Ma, L. Tanner, Nucleation and Growth of the Ni_5Al_3 Phase in Ni-Al Austenite and Martensite, J. Phys. IV France 05 (1995) C2-299-C2-304. https://doi.org/10.1051/jp4:1995246.

[210] P.S. Khadkikar, K. Vedula, An investigation of the Ni_5Al_3 phase, Journal of Materials Research 2 (1987) 163-167. https://doi.org/10.1557/JMR.1987.0163.

[211] D. Schryvers, Y. Ma, The growth of Ni_5Al_3 in $L1_0$ martensite studied by in situ transmission electron microscopy and high resolution electron microscopy, Journal of Alloys and Compounds 221 (1995) 227-234. https://doi.org/10.1016/0925-8388(94)01467-1.

[212] C.F. Li, Y.P. Ren, G.W. Qin, Experimental Confirmation of Ni_5Al_3 Phase in Ni-Al Binary System by Diffusion Couple Technique, AMR 299-300 (2011) 224-227. https://doi.org/10.4028/www.scientific.net/AMR.299-300.224.

[213] K. Bochenek, M. Basista, Advances in processing of NiAl intermetallic alloys and composites for high temperature aerospace applications, Progress in Aerospace Sciences 79 (2015) 136-146. https://doi.org/10.1016/j.paerosci.2015.09.003.

[214] J.H. Yang, C.M. Wayman, On the formation mechanism of Ni_5Al_3 in NiAl-base alloys: Part I. Microstructures, Intermetallics 2 (1994) 111-119. https://doi.org/10.1016/0966-9795(94)90005-1.

[215] E.J. Wu, G. Ceder, A. van de Walle, Using bond-length-dependent transferable force constants to predict vibrational entropies in Au-Cu, Au-Pd, and Cu-Pd alloys, Phys. Rev. B 67 (2003) 134103. https://doi.org/10.1103/PhysRevB.67.134103.

[216] S.B. Maisel, T.C. Kerscher, S. Müller, No miscibility gap in Pt-Rh binary alloys: A first-principles study, Acta Materialia 60 (2012) 1093-1098. https://doi.org/10.1016/j.actamat.2011.10.020.

[217] A. van de Walle, Multicomponent multisublattice alloys, nonconfigurational entropy and other additions to the Alloy Theoretic Automated Toolkit, Calphad 33 (2009) 266-278. https://doi.org/10.1016/j.calphad.2008.12.005.

[218] S. Liu, J. Wróbel, J. Llorca, First principles analysis of the Al-rich corner of Al-Li-Cu phase diagram, 2022.

[219] M. Ellner, S. Kek, B. Predel, Ni_3Al_4 - A phase with ordered vacancies isotypic to Ni3Ga4, Journal of the Less Common Metals 154 (1989) 207-215. https://doi.org/10.1016/0022-5088(89)90185-9.

[220] P. Delavignette, H. Richel, S. Amelinckx, The ordering of vacancies in $Ni_{1-x}Al$, Physica Status Solidi (a) 13 (1972) 545-555. https://doi.org/10.1002/pssa.2210130225.

[221] T.V. Panova, V.C. Kovivchak, V.I. Blinov, X-ray diffraction analysis of double-layer systems irradiated by a high-power ion beam, J. Surf. Investig. 2 (2008) 652-656. https://doi.org/10.1134/S1027451008040290.

[222] M. Yu. Lavrentiev, J. S. Wróbel, D. Nguyen-Manh, S. L. Dudarev, M. G. Ganchenkova, Magnetic cluster expansion model for random and ordered magnetic face-centered cubic Fe-Ni-Cr alloys, Journal of Applied Physics 120 (2016) 043902., https://doi.org/10.1063/1.4958981.

[223] D. Schryvers, L. Toth, Y. Ma, L. Tanner, Nucleation and Growth of the Ni_5Al_3 Phase in Ni-Al Austenite and Martensite, J. Phys. IV France 05 (1995) C2-304. https://doi.org/10.1051/jp4:1995246.

[224] M. Yang, Z. Zhang, Z. Han, J. Du, J. Huang, The formation of Ni_5Al_3 phase and its effect on the mechanical properties of In783 alloy, Intermetallics 126 (2020) 106930. https://doi.org/10.1016/j.intermet.2020.106930.

[225] P.L. Potapov, V.A. Udovenko, S.Y. Song, S.D. Prokoshkin, X-ray study of phase transformations in martensitic Ni-Al alloys, Metall Mater Trans A 28 (1997) 1133-1142. https://doi.org/10.1007/s11661-997-0279-z.

[226] P.L. Potapov, S.Y. Song, V.A. Udovenko, K.K. Jee, Effect of L1o → Ni_5Al_3 Reordering on Properties of Martensitic Ni-Al Alloys, J. Phys. IV France 07 (1997) C5-250. https://doi.org/10.1051/jp4:1997538.

[227] B.P. Burton, A. van de Walle, First-principles phase diagram calculations for the system NaCl-KCl: The role of excess vibrational entropy, Chemical Geology 225 (2006) 222-229. https://doi.org/10.1016/j.chemgeo.2005.08.016.

[228] X. Chong, J.P.S. Palma, Y. Wang, S.-L. Shang, F. Drymiotis, V.A. Ravi, K.E. Star, J.-P. Fleurial, Z.-K. Liu, Thermodynamic properties of the Yb-Sb system predicted from first-principles calculations, Acta Materialia 217 (2021) 117169. https://doi.org/10.1016/j.actamat.2021.117169.

[229] T. Davey, N.-D. Tran, A. Saengdeejing, Y. Chen, First-principles-only CALPHAD phase diagram of the solid aluminium-nickel (Al-Ni) system, Calphad 71 (2020) 102008. https://doi.org/10.1016/j.calphad.2020.102008.

[230] J.H. Yang, C.M. Wayman, On the formation mechanism of Ni5Al3 in NiAl-base alloys: Part II. Kinetics, Intermetallics 2 (1994) 121-126. https://doi.org/10.1016/0966-9795(94)90006-X.

[231] X. Wang, Z. Chen, D. Dong, D. Zhu, H. Wang, Z. Wei, Study on the Phase Selection and Debye Temperature of Hyper-Peritectic Al-Ni Alloy under High Pressure, Metals 11 (2021) 84. https://doi.org/10.3390/met11010084.

[232] A. Aguayo, I. Mazin, D. Singh, Why Ni_3Al is an Itinerant Ferromagnet but Ni_3Ga is Not, Phys. Rev. Lett. 92 (2004) 147201. https://doi.org/10.1103/PhysRevLett.92.147201.

[233] L. Ortenzi, I.I. Mazin, P. Blaha, L. Boeri, Accounting for spin fluctuations beyond local spin density approximation in the density functional theory, Phys. Rev. B 86 (2012) 064437. https://doi.org/10.1103/PhysRevB.86.064437.

[234] J. Kudrnovský, V. Drchal, P. Bruno, Magnetic properties of fcc Ni-based transition metal alloys, Phys. Rev. B 77 (2008) 224422. https://doi.org/10.1103/PhysRevB.77.224422.

[235] A. Nowotnik, K. Kubiak, J. Sieniawski, P. Rokicki, P. Pędrak, G. Mrówka-Nowotnik, Development of Nickel Based Superalloys for Advanced Turbine Engines, Materials Science Forum 783-786 (2014) 2491-2496. https://doi.org/10.4028/www.scientific.net/MSF.783-786.2491.

[236] P. Zhou, Y. Wang, Q. Liu, Y. Qiao, S. Chen, Hot Corrosion Behavior of Co-Al-W Superalloys with Si Additions, Coatings 13 (2023) 1031. https://doi.org/10.3390/coatings13061031.

[237] H. Chang, G. Xu, X.-G. Lu, L. Zhou, K. Ishida, Y. Cui, Experimental and phenomenological investigations of diffusion in Co-Al-W alloys, Scripta Materialia 106 (2015) 13-16. https://doi.org/10.1016/j.scriptamat.2015.03.021.

[238] Y. Jia, Z. Wang, Q. Wu, F. He, J. Li, J. Wang, Enhancing the yield strength of Ni-Co-Cr-Fe-Al as-cast hypoeutectic high-entropy alloys by introducing γ′ precipitation, Materials Science and Engineering: A 858 (2022) 144190. https://doi.org/10.1016/j.msea.2022.144190.

[239] B. Liao, X. Ouyang, H. Li, F. Yin, Z. Li, B. Yin, J. Hu, W. Zhang, Experimental investigation and thermodynamic calculation of the Co-Al-Mo ternary system, Journal of Alloys and Compounds 945 (2023) 169114. https://doi.org/10.1016/j.jallcom.2023.169114.

[240] P. Giannozzi, S. Baroni, N. Bonini, M. Calandra, R. Car, C. Cavazzoni, D. Ceresoli, G.L. Chiarotti, M. Cococcioni, I. Dabo, A.D. Corso, S. de Gironcoli, S. Fabris, G. Fratesi, R. Gebauer, U. Gerstmann, C. Gougoussis, A. Kokalj, M. Lazzeri, L. Martin-Samos, N. Marzari, F. Mauri, R. Mazzarello, S. Paolini, A. Pasquarello, L. Paulatto, C. Sbraccia, S. Scandolo, G. Sclauzero, A.P. Seitsonen, A. Smogunov, P. Umari, R.M. Wentzcovitch, QUANTUM ESPRESSO: a modular and open-source software project for quantum simulations of materials, J. Phys.: Condens. Matter 21 (2009) 395502. https://doi.org/10.1088/0953-8984/21/39/395502.

[241] R.A. Evarestov, V.P. Smirnov, Modification of the Monkhorst-Pack special points meshes in the Brillouin zone for density functional theory and Hartree-Fock calculations, Phys. Rev. B 70 (2004) 233101. https://doi.org/10.1103/PhysRevB.70.233101.

[242] H. Giefers, E.A. Tanis, S.P. Rudin, C. Greeff, X. Ke, C. Chen, M.F. Nicol, M. Pravica, W. Pravica, J. Zhao, A. Alatas, M. Lerche, W. Sturhahn, E. Alp, Phonon Density of States of Metallic Sn at High Pressure, Phys. Rev. Lett. 98 (2007) 245502. https://doi.org/10.1103/PhysRevLett.98.245502.

[243] A. van de Walle, P. Tiwary, M. de Jong, D.L. Olmsted, M. Asta, A. Dick, D. Shin, Y. Wang, L.-Q. Chen, Z.-K. Liu, Efficient stochastic generation of special quasirandom structures, Calphad 42 (2013) 13-18. https://doi.org/10.1016/j.calphad.2013.06.006.

[244] D.R. Evans, richard-evans/vampire, (2024). https://github.com/richard-evans/vampire (accessed January 18, 2024).

[245] K. Wang, D. Cheng, B.-C. Zhou, Generalization of the mixed-space cluster expansion method for arbitrary lattices, Npj Comput Mater 9 (2023) 1-11. https://doi.org/10.1038/s41524-023-01029-0.

[246] A. Díaz-Ortiz, R. Drautz, M. Fähnle, H. Dosch, J.M. Sanchez, Structure and magnetism in bcc-based iron-cobalt alloys, Phys. Rev. B 73 (2006) 224208. https://doi.org/10.1103/PhysRevB.73.224208.

[247] F. Dietermann, L.M. Sandratskii, M. Fähnle, On the energetics of transversal and longitudinal fluctuations of atomic magnetic moments, Journal of Magnetism and Magnetic Materials 324 (2012) 2693-2695. https://doi.org/10.1016/j.jmmm.2012.04.041.

[248] G.-Y. Guo, H. Wang, Gradient-Corrected Density Functional Calculation of Elastic Constants of Fe, Co and Ni in bcc, fcc and hcp Structures, Chinese Journal of Physics - CHIN J PHYS 38 (2000).

[249] C.H. Hu, X.Z. Li, Crystal structure of the HT-Al_3Co phase, Journal of Alloys and Compounds 473 (2009) L25-L27. https://doi.org/10.1016/j.jallcom.2008.06.023.

[250] P. Priputen, M. Kusý, M. Drienovský, D. Janičkovič, R. Čička, I. Černičková, J. Janovec, Experimental reinvestigation of Al-Co phase diagram in vicinity of $Al_{13}Co_4$ family of phases, Journal of Alloys and Compounds 647 (2015) 486-497. https://doi.org/10.1016/j.jallcom.2015.05.248.

[251] B. Grushko, R. Wittenberg, K. Bickmann, C. Freiburg, The constitution of aluminum-cobalt alloys between Al_5Co_2 and Al_9Co_2, Journal of Alloys and Compounds 233 (1996) 279-287. https://doi.org/10.1016/0925-8388(95)02045-4.

[252] W. Shao, J.M. Guevara-Vela, A. Fernández-Caballero, S. Liu, J. LLorca, Accurate prediction of the solid-state region of the Ni-Al phase diagram including configurational and vibrational entropy and magnetic effects, Acta Materialia 253 (2023) 118962. https://doi.org/10.1016/j.actamat.2023.118962.

[253] P. Šulhánek, M. Drienovský, I. Černičková, L. Ďuriška, R. Skaudžius, Ž. Gerhátová, M. Palcut, Oxidation of Al-Co Alloys at High Temperatures, Materials 13 (2020) 3152. https://doi.org/10.3390/ma13143152.

[254] F. Fleischer, T. Weber, D.Y. Jung, W. Steurer, o′-$Al_{13}Co_4$, a new quasicrystal approximant, Journal of Alloys and Compounds 500 (2010) 153-160. https://doi.org/10.1016/j.jallcom.2010.03.188.

[255] M. Ležaić, Ph. Mavropoulos, S. Blügel, First-principles prediction of high Curie temperature for ferromagnetic bcc-Co and bcc-FeCo alloys and its relevance to tunneling

magnetoresistance, Applied Physics Letters 90 (2007) 082504. https://doi.org/10.1063/1.2710181.

[256] A. Fernández Guillermet, Critical evaluation of the thermodynamic properties of cobalt, Int J Thermophys 8 (1987) 481-510. https://doi.org/10.1007/BF00567107.

[257] B. Zhang, H. Liao, C. Coddet, Effects of processing parameters on properties of selective laser melting Mg-9%Al powder mixture, Materials & Design 34 (2012) 753-758. https://doi.org/10.1016/j.matdes.2011.06.061.

[258] N. Kamiya, T. Sakai, R. Kainuma, I. Ohnuma, K. Ishida, Phase separation of BCC phase in the Co-rich portion of Co-Fe-Al system, Intermetallics 12 (2004) 417-423. https://doi.org/10.1016/j.intermet.2003.12.005.

[259] J. Wang, Y. Zhang, W. Zheng, X.-G. Lu, Thermodynamic and diffusion kinetic studies of the Co-Al-Fe system, J Mater Sci 57 (2022) 7343-7366. https://doi.org/10.1007/s10853-022-07109-8.

[260] F. Stein, C. He, N. Dupin, Melting behaviour and homogeneity range of B_2 CoAl and updated thermodynamic description of the Al-Co system, Intermetallics 39 (2013) 58-68. https://doi.org/10.1016/j.intermet.2013.03.011.

[261] J.M. MacLaren, T.C. Schulthess, W.H. Butler, R. Sutton, M. McHenry, Electronic structure, exchange interactions, and Curie temperature of FeCo, Journal of Applied Physics 85 (1999) 4833-4835. https://doi.org/10.1063/1.370036.

[262] R. Egli, Magnetic susceptibility measurements as a function of temeperature and freqeuncy I: Inversion theory, Geophysical Journal International 177 (2009) 395-420. https://doi.org/10.1111/j.1365-246X.2009.04081.x.

[263] M. Matsumoto, H. Akai, Calculating Curie temperatures for rare-earth permanent magnets: Ab initio inspection of localized magnetic moments in 3d-electron ferromagnetism, Phys. Rev. B 101 (2020) 144402. https://doi.org/10.1103/PhysRevB.101.144402.

[264] M.V. Mansilla, J. Gómez, E.S. Leva, F.C. Gamarra, A.A. Barahona, A. Butera, Thickness and temperature dependence of the dynamic magnetic behavior in disordered FePt films, Journal of Magnetism and Magnetic Materials 321 (2009) 2941-2945.

[265] C. Glorieux, J. Thoen, G. Bednarz, M.A. White, D.J.W. Geldart, Photoacoustic investigation of the temperature and magnetic-field dependence of the specific-heat capacity and thermal conductivity near the Curie point of gadolinium, Phys. Rev. B 52 (1995) 12770-12778. https://doi.org/10.1103/PhysRevB.52.12770.

[266] A.J. McAlister, The Al-Co (Aluminum-Cobalt) system, Bulletin of Alloy Phase Diagrams 10 (1989) 646-650. https://doi.org/10.1007/BF02877635.

[267] A.K. Sfikas, S. Gonzalez, A.G. Lekatou, S. Kamnis, A.E. Karantzalis, A Critical Review on Al-Co Alloys: Fabrication Routes, Microstructural Evolution and Properties, Metals 12 (2022) 1092. https://doi.org/10.3390/met12071092.

[268] S.G. Men’shikova, I.G. Shirinkina, I.G. Brodova, V.I. Lad’yanov, A.A. Suslov, Structure of Thin Ribbons from an Al - Co Alloy Under Rapid Cooling, Met Sci Heat Treat 58 (2016) 393-399. https://doi.org/10.1007/s11041-016-0023-7.

[269] R. Lizárraga, F. Pan, L. Bergqvist, E. Holmström, Z. Gercsi, L. Vitos, First Principles Theory of the hcp-fcc Phase Transition in Cobalt, Sci Rep 7 (2017) 3778. https://doi.org/10.1038/s41598-017-03877-5.

Annex A. Al-Li phase diagram

A.1. Effective cluster interaction parameters of the Al-Li system

All the ECIs including configurational, lattice vibrational effects in the bcc and fcc Al-Li system at different temperatures are listed in Tables A1-A4, which were used as input for the MC simulations to obtain the thermodynamic information of each phase in the Al-Li phase diagram.

Table A1: ECIs for fcc lattice in the Al-Li system at 0 K

cluster	labels	multiplicity	coordinates	Cluster diameter	ECI (eV/atom)
empty	1	1			-0.053444
point	1	1	1, 1, 1		-0.037194
pair	1	6	1, 1, 1 0.5, 1, 1.5	2.839478	0.0119263
	2	3	1, 1, 1 0, 1, 1	4.015628	-0.000911667
	3	12	1, 1, 1 0, 1.5, 1.5	4.918120	0.00218533
	4	6	1, 1, 1 0, 1, 2	5.678956	0.003422
	5	12	1, 1, 1 -0.5, 1, 1.5	6.349265	-0.00188567
triplet	1	8	1, 1, 1 0.5, 1, 1.5 1, 1.5, 1.5	2.839478	-2.325e-05
	2	12	1, 1, 1 0.5, 1, 1.5 0, 1, 1	4.015628	0.00256133
	3	24	1, 1, 1 1, 1.5, 1.5 0, 1.5, 1.5	4.918120	0.00022425

4	24	1, 1, 1 0.5, 1, 1.5 0, 1.5, 1.5	4.918120	-0.000949917
5	24	1, 1, 1 0.5, 0.5, 1 0, 1.5, 1.5	4.918120	-0.0002015
6	24	1, 1, 1 1, 1, 2 0, 1.5, 1.5	4.918120	6e-06
7	8	1, 1, 1 0.5, 2, 0.5 0, 1.5, 1.5	4.918120	0.0007125
8	48	1, 1, 1 1, 1.5, 1.5 0, 1, 2	5.678956	0.000828708
9	6	1, 1, 1 0.5, 1, 1.5 0, 1, 2	5.678956	-0.00139467
10	12	1, 1, 1 0, 1, 1 0, 1, 2	5.678956	-0.000433833
11	24	1, 1, 1 0.5, 2, 1.5 0, 1, 2	5.678956	-0.0003745
12	8	1, 1, 1 0, 2, 1 0, 1, 2	5.678956	0.00118725

Table A2: ECIs for fcc lattice in the Al-Li system at finite temperatures.

cluster	labels	ECI (eV/atom)				
		200 K	400 K	600 K	800 K	1000 K
empty	1	-0.073514	-0.137534	-0.227284	-0.334264	-0.423134
point	1	-0.035064	-0.030984	-0.026704	-0.022374	-0.019104
pair	1	0.011763	0.0113263	0.0108513	0.0103647	0.00999633
	2	-0.001005	-0.00117833	-0.00136167	-0.00155167	-0.00169167
	3	0.00215033	0.00208367	0.00201367	0.00194283	0.0018895
	4	0.003407	0.00338367	0.003362	0.00334033	0.00332367
	5	-0.00188067	-0.00187233	-0.001864	-0.0018565	-0.00184983
triplet	1	3.18E-05	0.00013925	0.000253	0.00036925	0.00045675
	2	0.002498	0.002358	0.00220717	0.00205383	0.001938
	3	0.00023883	0.00027425	0.000313	0.00035217	0.00038217
	4	-0.00100908	-0.00111742	-0.00123075	-0.00134533	-0.001432
	5	-0.000184	-0.00015483	-0.00012442	-9.40E-05	-7.07E-05
	6	-1.53E-05	-5.82E-05	-0.000104	-0.00015067	-0.00018567
	7	0.00073125	0.00075	0.00076625	0.0007825	0.000795
	8	0.00083871	0.00085683	0.00087579	0.00089517	0.00090975
	9	-0.00145633	-0.001578	-0.00170633	-0.00183633	-0.00193467
	10	-0.00045217	-0.00047383	-0.00049467	-0.0005155	-0.00053133
	11	-0.00039283	-0.00043117	-0.00047283	-0.00051367	-0.00054533
	12	0.001201	0.0012285	0.00125725	0.00128725	0.00130975

Table A3**:** ECIs for bcc lattice in the Al-Li system at 0 K.

cluster	labels	multiplicity	coordinates	Cluster diameter	ECI (eV/atom)
empty	1	1			-0.078929
point	1	1	1.22474, 0, 0		-0.036415
pair	1	4	1.22474, 0, 0	2.96771	0.0300775

			1.63299, 0.57735, 1		
	2	3	$\frac{1.22474, 0, 0}{0.40825, 0.57735, 1}$	3.42682	0.031184367
	3	6	$\frac{1.22474, 0, 0}{1.22474, -1.73205, -1}$	4.84625	0.008431
	4	12	$\frac{1.22474, 0, 0}{1.63299, -1.15470, -2}$	5.68273	0.0110165
	5	4	$\frac{1.22474, 0, 0}{0.40825, -1.15470, -2}$	5.93542	0.0110165
	6	3	$\frac{1.22474, 0, 0}{-0.40825, 1.15470, 2}$	6.85363	0.00492333
	7	12	$\frac{1.22474, 0, 0}{0.81650, -2.30940, -2}$	7.46857	0.000735
	8	12	$\frac{1.22474, 0, 0}{2.04124, -2.30940, -2}$	7.66260	0.00106317
	9	12	$\frac{1.22474, 0, 0}{1.22475, -1.73205, -3}$	8.39395	-0.0015835
	10	4	$\frac{1.22474, 0, 0}{0, -1.73205, -3}$	8.90313	-0.0006245
	11	12	$\frac{1.22474, 0, 0}{2.44949, -1.73205, -3}$	8.90313	-0.000127
	12	6	$\frac{1.22474, 0, 0}{1.22475, -3.46410, -2}$	9.69250	-0.00199033
	13	24	$\frac{1.22474, 0, 0}{1.63299, -2.88675, -3}$	10.13666	-0.00251167
	14	12	$\frac{1.22474, 0, 0}{0.40825, -2.88675, -3}$	10.28045	-0.00272667
	15	3	$\frac{1.22474, 0, 0}{-1.22475, 1.73205, 3}$	10.28045	-0.00321267

	16	12	1.22474, 0, 0 2.85774, -2.88675, -3	10.83655	-0.00273
	17	12	1.22474, 0, 0 0.81650, -2.30940, -4	11.23557	-0.00395683
	18	12	1.22474, 0, 0 2.04124, -2.30940, -4	11.36547	-0.0030385
	19	4	1.22474, 0, 0 -0.40825, -2.3094, -4	11.87084	-0.002398
	20	12	1.22474, 0, 0 0.81650, -4.04145, -3	12.23618	-0.000219833
	21	12	1.22474, 0, 0 3.26599, -2.3094, -4	12.23618	-0.0025276
triplet	1	12	1.22474, 0, 0 1.63299, 0.57735, 1 0.40825, 0.57735, 1	3.42682	0.00721517
	2	12	1.22474, 0, 0 0.81650, -0.57735, -1 1.22474, -1.73205, -1	4.84625	-0.000908833
	3	12	1.22474, 0, 0 2.04124, -0.57735, -1 1.22474, -1.73205, -1	4.84625	0.000403
	4	8	1.22474, 0, 0 1.22474, 0, -2 1.22474, -1.73205, -1	4.84625	-4.6e-05
	5	24	1.22474, 0, 0 0.81650, -0.57735, -1 1.63299, -1.15470, -2	5.68273	-0.000131417
	6	48	1.22474, 0, 0 1.63299, -0.57735, -1	5.68273	-8.2458e-05

			1.63299, -1.15470, -2		
	7	24	1.22474, 0, 0 0.40825, -0.57735, -1 1.63299, -1.1547, -2	5.68273	0.00109475
	8	12	1.22474, 0, 0 -0.40825, -0.57735, -1 1.63299, -1.1547, -2	5.68273	-0.0005405
	9	24	1.22474, 0, 0 2.85774, -0.57735, -1 1.63299, -1.1547, -2	5.68273	0.000612
	10	4	1.22474, 0, 0 0.8165, -0.57735, -1 0.40825, -1.1547, -2	5.93542	-0.001271
	11	24	1.22474, 0, 0 0, 0, 0 0.40825, -1.1547, -2	5.93542	0.000539083
	12	24	1.22474, 0, 0 2.04124, -0.57735, -1 0.40825, -1.1547, -2	5.93542	-0.00033775
	13	24	1.22474, 0, 0 2.44949, -1.73205, -1 0.40825, -1.1547, -2	5.93542	-0.00038075
	14	24	1.22474, 0, 0 1.63299, 0.57735, 1 -0.40825, -1.1547, -2	6.85363	0.00107258
	15	3	0.40825, 0, 0 1.63299, 0.57735, 1 -0.40825, -1.1547, -2	6.85363	0.00666567
	16	12	1.22474, 0, 0	6.85363	0.000590667

		1.22474, 1.73205, 1 -0.40825, -1.1547, -2		
17	12	1.22474, 0, 0 2.04124, 1.15470, 2 -0.40825, 1.15470, 2	6.85363	-0.00143033
18	24	1.22474, 0, 0 0.8165, -0.57735, -1 0.8165, -2.30940, -2	7.46857	0.000239667
19	24	1.22474, 0, 0 1.63299, -0.57735, -1 0.8165, -2.3094, -2	7.46857	0.000683
20	48	1.22474, 0, 0 2.04124, -0.57735, -1 0.8165, -2.3094, -2	7.46857	-0.00100321
21	12	1.22474, 0, 0 0.40825, -0.57735, -1 0.81650, -2.30940, -2	7.46857	-0.00112617
22	48	1.22474, 0, 0 1.22474, 0, -2 0.8165, -2.3094, -2	7.46857	-0.000205667
23	24	1.22474, 0, 0 2.85774, -1.1547, 0 0.8165, -2.3094, -2	7.46857	0.0007845
24	24	1.22474, 0, 0 0, 0, -2 0.8165, -2.3094, -2	7.46857	-0.000541583
25	48	1.22474, 0, 0 2.44949, 0, -2 0.8165, -2.3094, -2	7.46857	-0.000285417

	26	48	1.22474, 0, 0 0.8165, -0.57735, -1 2.04124, -2.3094, -2	7.66260	0.000495958
	27	48	1.22474, 0, 0 2.44949, 0, 0 2.04124, -2.3094, -2	7.66260	-0.00053225
	28	24	1.22474, 0, 0 2.04124, -0.57735, -1 2.04124, -2.3094, -2	7.66260	0.00033625
	29	24	1.22474, 0, 0 0.40825, -1.1547, 0 2.04124, -2.3094, -2	7.66260	-0.000473167
	30	48	1.22474, 0, 0 1.22474, 0, -2 2.04124, -2.3094, -2	7.66260	0.000558708
	31	24	1.22474, 0, 0 -0.40825, -0.57735, 1 2.04124, -2.3094, -2	7.66260	-0.000234
	32	12	1.22474, 0, 0 2.85774, 0.57735, -1 2.04124, -2.3094, -2	7.66260	-0.000888333
	33	48	1.22474, 0, 0 0, -1.73205, -1 2.04124, -2.3094, -2	7.66260	-0.0007825
	34	48	1.22474, 0, 0 0, 0, -2 2.04124, -2.3094, -2	7.66260	0.000349917
	35	12	1.22474, 0, 0 -0.40825, -2.30940, 0	7.66260	-0.000833667

			2.04124, -2.3094, -2		
	36	48	1.22474, 0, 0 -0.8165, -1.1547, -2 2.04124, -2.3094, -2	7.66260	-0.000103667
quadruplet	1	6	1.22474, 0, 0 0.8165, 1.1547, 0 1.63299, 0.57735, 1 0.40825, 0.57735, 1	3.42682	-0.003841
	2	6	1.22474, 0, 0 1.63299, -1.1547, 0 0.8165, -0.57735, -1 1.22474, -1.73205, -1	4.84625	-0.000515667
	3	24	1.22474, 0, 0 0.8165, -0.57735, -1 2.04124, -0.57735, -1 1.22474, -1.73205, -1	4.84625	-0.000759
	4	3	1.22474, 0, 0 0.40825, -1.1547, 0 2.04124, -0.57735, -1 1.22474, -1.73205, -1	4.84625	-0.000747
	5	8	1.22474, 0, 0 0.8165, -0.57735, -1 1.22474, 0, -2 1.22474, -1.73205, -1	4.84625	-0.00022375
	6	8	1.22474, 0, 0 2.04124, -0.57735, -1 1.22474, 0, -2 1.22474, -1.73205, -1	4.84625	0.00049725
	7	2	1.22474, 0, 0 -0.40825, -0.57735, -	4.84625	-0.001043

1
1.22474, 0, -2
1.22474, -1.73205, -1

Table A4: ECIs for bcc lattice in the Al-Li system at finite temperatures.

cluster	labels	ECI (eV/atom)				
		200 K	400 K	600 K	800 K	1000 K
empty	1	-0.095069	-0.152049	-0.234429	-0.333949	-0.446349
point	1	-0.036545	-0.036315	-0.036065	-0.035815	-0.035565
pair	1	0.02969	0.02851	0.0271675	0.02578	0.0243725
	2	0.0308443	0.029911	0.028861	0.0277743	0.0266743
	3	0.010618	0.0100047	0.00931633	0.00860633	0.00788967
	4	0.00816683	0.0075335	0.0068285	0.00610267	0.00536767
	5	0.010639	0.009769	0.008814	0.007834	0.0068415
	6	4.84E-03	0.00455	0.00420667	0.00385	0.00348667
	7	0.00057583	0.00025667	-8.58E-05	-0.000435	-0.0007867
	8	0.00100483	0.00088317	0.0007515	0.00061733	0.0004815
	9	-0.0016718	-0.0018152	-0.0019618	-0.0021093	-0.0022568
	10	-0.000682	-0.000727	-0.000757	-0.000782	-0.000807
	11	-7.12E-05	1.80E-05	0.00011133	0.00020467	0.00029883
	12	-0.002007	-0.001967	-0.001907	-0.0018403	-0.001772
	13	-0.0023917	-0.0021033	-0.0017833	-0.0014538	-0.0011204
	14	-0.0026433	-0.0024325	-0.0021958	-0.0019517	-0.0017042
	15	-0.003046	-0.0026993	-0.002326	-0.0019427	-0.0015593
	16	-0.0025742	-0.0022317	-0.001855	-0.0014683	-0.0010783
	17	-0.0038143	-0.0034952	-0.0031452	-0.002786	-0.0024227
	18	-0.0029327	-0.0026835	-0.0024085	-0.0021268	-0.001841
	19	-0.0022205	-0.0018455	-0.001438	-0.001023	-0.000603
	20	-0.0002557	-0.0003115	-0.000369	-0.0004265	-0.000484

	21	-0.0024318	-0.0022243	-0.0019977	-0.001766	-0.0015327
triplet	1	0.00686933	0.00622183	0.00555017	0.00487183	0.00419017
	2	-0.0009213	-0.000968	-0.0010255	-0.0010863	-0.0011488
	3	0.00027133	-1.70E-05	-0.000327	-0.0006437	-0.0009637
	4	-7.85E-05	-0.0001223	-0.0001635	-0.0002035	-0.0002448
	5	9.83E-06	0.00026942	0.00054025	0.00081442	0.00108983
	6	-0.000125	-0.0002252	-0.0003362	-0.0004502	-0.0005656
	7	0.00106892	0.00103892	0.00101225	0.00098683	0.00096142
	8	-0.0005288	-0.0005072	-0.000483	-0.000458	-0.000433
	9	0.00051658	0.00031658	0.00010325	-0.0001143	-0.000333
	10	-0.001346	-0.001611	-0.001921	-0.0022435	-0.0025735
	11	0.00049075	0.00036825	0.00023117	8.95E-05	-5.34E-05
	12	-0.0003161	-0.0002994	-0.0002886	-0.000279	-0.0002698
	13	-0.0003966	-0.0004258	-0.0004553	-0.0004849	-0.0005145
	14	0.00108092	0.00110217	0.00112717	0.00115258	0.00117842
	15	0.00729567	0.00857567	0.00994567	0.0113423	0.0127457
	16	0.00055067	0.00047233	0.0003915	0.00030983	0.00022817
	17	-0.0014287	-0.0014345	-0.0014428	-0.001452	-0.0014612
	18	0.00025008	0.000258	0.00026092	0.000263	0.00026425
	19	0.00071217	0.00079217	0.00088175	0.00097467	0.00106842
	20	-0.001004	-0.0010276	-0.0010595	-0.0010936	-0.0011288
	21	-0.0010553	-0.0008945	-0.0007178	-0.000537	-0.0003545
	22	-0.0001588	-5.46E-05	5.98E-05	0.00017704	0.00029558
	23	0.00082658	0.0009545	0.00110117	0.00125367	0.00140867
	24	-0.0005145	-0.0004416	-0.0003591	-0.0002737	-0.0001874
	25	-0.0002785	-0.0002671	-0.0002554	-0.0002438	-0.0002323
	26	0.00058763	0.00077804	0.000982	0.00118971	0.00139887
	27	-0.0005354	-0.0005641	-0.0006	-0.0006377	-0.0006764
	28	0.00044917	0.00066667	0.000895	0.00112667	0.00135958

	29	-0.0005036	-0.0005573	-0.0006119	-0.0006673	-0.0007228
	30	0.00055704	0.00057163	0.00059142	0.00061267	0.00063454
	31	-0.0002103	-0.0001407	-6.07E-05	2.27E-05	0.00010725
	32	-0.0010175	-0.0012975	-0.0016017	-0.0019125	-0.0022267
	33	-0.0008267	-0.0009033	-0.0009823	-0.0010619	-0.0011415
	34	0.00035575	0.00037971	0.00040846	0.00043867	0.0004695
	35	-0.0009303	-0.001147	-0.0013828	-0.0016237	-0.0018662
	36	-0.0001412	-0.0002233	-0.000312	-0.0004024	-0.0004937
quadruplet	1	-0.0037927	-0.003686	-0.0035727	-0.0034543	-0.0033377
	2	-0.000509	-0.000474	-0.0004323	-0.0003873	-0.0003423
	3	-0.0007586	-0.0007544	-0.0007486	-0.0007432	-0.0007369
	4	-0.000747	-0.000747	-0.0007437	-0.000737	-0.0007337
	5	-0.00024	-0.0002688	-0.0003	-0.0003325	-0.0003638
	6	0.0005185	0.00055475	0.000591	0.0006285	0.000666
	7	-0.000988	-0.000908	-0.000838	-0.000763	-0.000693

Annex B. Ni-Al phase diagram

B.1. Effective cluster interaction parameters of the Ni-Al system

All the ECIs including configurational, lattice vibrational effects in the bcc, fcc and bcc with vacancies of the Ni-Al system at different temperatures are listed in Tables B1-B6, which were used as input for the MC simulations to obtain the thermodynamic information of each phase in the Ni-Al phase diagram.

Table B1: ECIs of bcc lattices in the Al-Ni system at 0 K

Cluster	labels	Coordinates	Distance diameter (Å)	Multiplicity	ECI (eV/atom)
					0 K
empty	1			1	-0.536221
point	1	1, 1, 1		1	-0.106706
pair	1	1, 1, 1 0, 0, 2	2.501	4	0.068450
	2	1, 1, 1 1, 1, 3	2.8879	3	0.060560
	3	1, 1, 1 -1, -1, 1	4.08411	6	0.017292
	4	1, 1, 1 -2, 0, 0	4.78904	12	0.001389
	5	1, 1, 1 -1, -1, -1	5.0019	4	0.009526
	6	1, 1, 1 -3, 1, 1	5.7758	3	-0.015615
	7	1, 1, 1 -3, 1, 1	6.29404	12	-0.000058
	8	1, 1, 1 -2, -2, 0	6.45755	12	-0.007132
	9	1, 1, 1	7.07389	12	0.005085

		-3, 1, -1			
	10	1, 1, 1 3, 3, 5	7.50299	12	-0.002332
	11	1, 1, 1 0, 6, 2	7.50299	4	0.009660
	12	1, 1, 1 -3, -3, 1	8.16822	6	0.016470
triplet	1	1, 1, 1 0, 0, 2 1, 1, 3	2.8879	12	0.001522
	2	1, 1, 1 0, 0, 0 -1, -1, 1	4.08411	12	0.009249
	3	1, 1, 1 -1, 1, 1 -1, -1, 1	4.08411	12	-0.003006
	4	1, 1, 1 -1, 1, -1 -1, -1, 1	4.08411	8	-0.003303
	5	1, 1, 1 0, 0, 0 -2, 0, 0	4.78904	24	0.003971
	6	1, 1, 1 0, 0, 2 -2, 0, 0	4.78904	48	0.000168
	7	1, 1, 1 1, -1, 1 -2, 0, 0	4.78904	24	0.000654
	8	1, 1, 1	4.78904	12	0.002330

		1, -1, -1			
		-2, 0, 0			
	9	1, 1, 1	4.78904	24	-0.002955
		-1, 1, 3			
		-2, 0, 0			
	10	1, 1, 1	5.00199	4	-0.015857
		0, 0, 0			
		-1, -1, -1			
	11	1, 1, 1	5.00199	24	-0.002136
		0, 0, 2			
		-1, -1, -1			
	12	1, 1, 1	5.00199	24	0.002624
		-1, 1, 1			
		-1, -1, -1			
	13	1, 1, 1	5.00199	24	0.003667
		-2, 0, 2			
		-1, -1, -1			
	14	1, 1, 1	5.7758	24	-0.000098
		0, 0, 0			
		-3, 1, 1			
	15	1, 1, 1	5.7758	3	0.005902
		-1, 1, 1			
		-3, 1, 1			
	16	1, 1, 1	5.7758	12	-0.005653
		-1, -1, 1			
		-3, 1, 1			
	17	1, 1, 1	5.7758	12	-0.000309
		-1, -1, -1			
		-3, 1, 1			

quadruplet	1	1, 1, 1 0, 2, 2 0, 0, 2 1, 1, 3	2.8879	6	0.005362
	2	1, 1, 1 0, 0, 2 0, 0, 0 -1, -1, 1	4.08411	6	-0.019951
	3	1, 1, 1 0, 0, 0 -1, 1, 1 -1, -1, 1	4.08411	24	-0.001397
	4	1, 1, 1 1, -1, 1 -1, 1, 1 -1, -1, 1	4.08411	3	-0.012617
	5	1, 1, 1 0, 0, 0 -1, 1, -1 -1, -1, 1	4.08411	8	0.008030
	6	1, 1, 1 -1, 1, 1 -1, 1, -1 -1, -1, 1	4.08411	8	-0.005589
	7	1, 1, 1 1, -1, -1 -1, 1, -1 -1, -1, 1	4.08411	2	0.003141

Table B2: ECIs of fcc lattices in the Al-Ni system at 0 K

Cluster	labels	Coordinates	Distance (Å)	Multiplicity	ECI (eV/atom)	
					FM	NM
					0 K	0 K
empty	1			1	-0.38946	-0.41920
point	1	2, 2, 2		1	-0.09944	-0.13238
pair	1	2, 2, 2 1, 2, 3	2.83948	6	0.079566	0.078082
	2	2, 2, 2 0, 2, 2	4.01563	3	-0.00427	-0.00607
	3	2, 2, 2 0, 3, 3	4.91812	12	0.010493	0.009504
	4	2, 2, 2 0, 2, 4	5.67896	6	0.006547	0.006013
	5	2, 2, 2 -1, 2, 3	6.34927	12	-0.00063	1.8E-05
	6	2, 2, 2 0, 4, 4	6.95527	4	-0.00314	-0.00338
	7	2, 2, 2 -1, 3, 4	7.51255	24	0.000044	1.7E-05
	8	2, 2, 2 2, 2, 6	8.03126	3	-0.00238	-0.00182
	9	2, 2, 2 1, 1, 6	8.51843	12	-0.00237	-0.00216
	10	2, 2, 2 -1, -1, 2	8.51843	6	-0.00188	-0.00205
	11	2, 2, 2 0, 2, 6	8.97922	12	0.000567	0.000667
	12	2, 2, 2	9.41748	12	0.000637	0.000545

		-1, -1, 4				
	13	2, 2, 2 0, 0, 6	9.83624	12	0.001303	0.001387
	14	2, 2, 2 -2, -1, 3	10.23788	24	0.000784	0.000793
	15	2, 2, 2 -3, 1, 2	10.23788	12	-0.00121	-0.00102
	16	2, 2, 2 0, 7, 1	10.99725	24	-0.00158	-0.00152
	17	2, 2, 2 2, 6, 6	11.35791	6	-0.00058	-0.00057
	18	2, 2, 2 5, -1, 6	11.70747	12	-0.00010	-3.5E-05
	19	2, 2, 2 -3, 2, 5	11.70747	12	-0.00016	-7.3E-05
	20	2, 2, 2 -2, 4, 6	12.04688	12	-0.00110	-0.00098
	21	2, 2, 2 -4, 2, 2	12.04688	3	0.000499	0.000479
	22	2, 2, 2 -4, 1, 3	12.377	12	-0.00138	-0.00111
	23	2, 2, 2 4, -3, 5	12.377	24	-0.00044	-0.00018
	24	2, 2, 2 0, 2, 8	12.69853	12	-0.00047	-0.0005
	25	2, 2, 2 -3, 1, 6	13.01212	24	-0.00028	-0.00014
triplet	1	2, 2, 2 1, 2, 3	2.83948	8	0.010914	0.011659

	2, 3, 3				
2	2, 2, 2 1, 2, 3 0, 2, 2	4.01563	12	0.000661	0.000703
3	2, 2, 2 2, 3, 3 0, 3, 3	4.91812	24	0.001312	0.001398
4	2, 2, 2 1, 2, 3 0, 3, 3	4.91812	24	-0.00038	-0.00034
5	2, 2, 2 1, 1, 2 0, 3, 3	4.91812	24	0.001411	0.001226
6	2, 2, 2 2, 2, 4 0, 3, 3	4.91812	24	-0.00100	-0.00092
7	2, 2, 2 1, 4, 1 0, 3, 3	4.91812	8	-0.00047	-0.00068
8	2, 2, 2 2, 3, 3 0, 2, 4	5.67896	48	0.000910	0.000824
9	2, 2, 2 1, 2, 3 0, 2, 4	5.67896	6	-0.00591	-0.00623
10	2, 2, 2 0, 2, 2 0, 2, 4	5.67896	12	-0.00110	-0.00099
11	2, 2, 2	5.67896	12	0.000274	0.000137

	1, 4, 3 0, 2, 4				
12	2, 2, 2 0, 4, 2 0, 2, 4	5.67896	8	-0.00131	-0.00114
13	2, 2, 2 2, 3, 3 -1, 2, 3	6.34927	24	0.000867	0.00051
14	2, 2, 2 1, 2, 3 -1, 2, 3	6.34927	24	0.000553	0.000687
15	2, 2, 2 1, 3, 2 -1, 2, 3	6.34927	48	0.000187	0.000345
16	2, 2, 2 1, 2, 1 -1, 2, 3	6.34927	24	0.000081	0.000162
17	2, 2, 2 2, 2, 4 -1, 2, 3	6.34927	12	-0.00125	-0.00128
18	2, 2, 2 1, 1, 4 -1, 2, 3	6.34927	48	-0.00011	8.1E-05
19	2, 2, 2 1, 4, 3 -1, 2, 3	6.34927	48	-0.00008	0.000127
20	2, 2, 2 0, 2, 0 -1, 2, 3	6.34927	12	-0.00096	-0.00101

quadruplet	1	2, 2, 2 1, 3, 2 1, 2, 3 2, 3, 3	2.83948	2	0.006766	0.00668
	2	2, 2, 2 1, 3, 2 1, 2, 3 0, 2, 2	4.01563	12	0.000899	0.000928
	3	2, 2, 2 1, 2, 1 1, 2, 3 0, 2, 2	4.01563	3	-0.00721	-0.00715
	4	2, 2, 2 1, 2, 3 2, 3, 3 0, 3, 3	4.91812	48	-0.00084	-0.00088
	5	2, 2, 2 1, 1, 2 2, 3, 3 0, 3, 3	4.91812	48	-0.00110	-0.00119
	6	2, 2, 2 1, 3, 2 1, 2, 3 0, 3, 3	4.91812	12	-0.00503	-0.00489
	7	2, 2, 2 1, 1, 2 1, 2, 3 0, 3, 3	4.91812	24	-0.00059	-0.00031
	8	2, 2, 2	4.91812	48	0.000906	0.000781

	1, 2, 1 1, 2, 3 0, 3, 3				
9	2, 2, 2 1, 2, 1 1, 1, 2 0, 3, 3	4.91812	8	-0.00079	-0.00067
10	2, 2, 2 2, 3, 3 0, 2, 2 0, 3, 3	4.91812	6	0.002073	0.001989
11	2, 2, 2 2, 3, 3 2, 2, 4 0, 3, 3	4.91812	24	0.000167	0.000452
12	2, 2, 2 1, 2, 3 2, 2, 4 0, 3, 3	4.91812	24	0.001800	0.001821
13	2, 2, 2 1, 1, 2 2, 2, 4 0, 3, 3	4.91812	48	-0.00023	-0.00021
14	2, 2, 2 1, 3, 2 1, 4, 1 0, 3, 3	4.91812	8	0.001816	0.001926
15	2, 2, 2 2, 4, 2	4.91812	12	0.000292	0.000491

		1, 3, 4				
		0, 3, 3				
	16	2, 2, 2	4.91812	6	0.000884	0.000616
		2, 4, 2				
		0, 3, 1				
		0, 3, 3				
	17	2, 2, 2	5.67896	48	-0.00189	-0.00177
		1, 2, 3				
		2, 3, 3				
		0, 2, 4				
	18	2, 2, 2	5.67896	24	-0.00119	-0.00140
		1, 3, 2				
		2, 3, 3				
		0, 2, 4				
	19	2, 2, 2	5.67896	24	0.000493	0.000543
		2, 1, 3				
		2, 3, 3				
		0, 2, 4				
	20	2, 2, 2	5.67896	24	-0.00022	-0.00022
		1, 1, 2				
		2, 3, 3				
		0, 2, 4				
	21	2, 2, 2	5.67896	48	-0.00022	-0.00032
		2, 3, 3				
		0, 2, 2				
		0, 2, 4				
	22	2, 2, 2	5.67896	12	0.002555	0.002768
		1, 2, 3				
		0, 2, 2				

		0, 2, 4				
	23	2, 2, 2 1, 3, 2 0, 2, 2 0, 2, 4	5.67896	48	-0.00048	-0.00042
	24	2, 2, 2 2, 2, 4 0, 2, 2 0, 2, 4	5.67896	3	0.001308	0.001276
	25	2, 2, 2 2, 3, 3 0, 3, 3 0, 2, 4	5.67896	24	0.000130	0.000359
	26	2, 2, 2 1, 3, 2 0, 3, 3 0, 2, 4	5.67896	24	0.001853	0.002072
	27	2, 2, 2 2, 1, 3 0, 3, 3 0, 2, 4	5.67896	12	-0.00050	-0.00047
	28	2, 2, 2 1, 1, 2 0, 3, 3 0, 2, 4	5.67896	24	0.000629	0.000773
	29	2, 2, 2 1, 4, 3 0, 3, 3 0, 2, 4	5.67896	48	-0.00008	-0.00013

	30	2, 2, 2 1, 2, 3 1, 4, 3 0, 2, 4	5.67896	12	-0.00090	-0.00084
	31	2, 2, 2 0, 2, 2 1, 4, 3 0, 2, 4	5.67896	24	-0.00018	5.4E-05
	32	2, 2, 2 2, 3, 3 0, 4, 2 0, 2, 4	5.67896	24	-0.00010	-0.00028
	33	2, 2, 2 1, 2, 3 0, 4, 2 0, 2, 4	5.67896	24	0.000407	0.000425
	34	2, 2, 2 0, 2, 2 0, 4, 2 0, 2, 4	5.67896	8	0.000374	0.000582
	35	2, 2, 2 2, 4, 4 0, 4, 2 0, 2, 4	5.67896	2	0.001000	0.000764

Table B3**:** ECIs of bcc lattices with vacancies in the Al-Ni system at 0 K

Cluster	labels	Coordinates	Distance (Å)	Multiplicity	ECI (eV/atom)
empty	1			1	-0.149157

point	1	0.5, 0.5, 0.5		1	0.005375
pair	1	0.5, 0.5, 0.5 0.5, 1.5, 0.5	2.887902	3	0.045262
	2	0.5, 0.5, 0.5 1.5, 1.5, 0.5	4.084110	6	0.006392
	3	0.5, 0.5, 0.5 1.5, 1.5, -0.5	5.001993	4	0.004151
	4	0.5, 0.5, 0.5 0.5, 0.5, -1.5	5.775804	3	0.016621
	5	0.5, 0.5, 0.5 0.5, -0.5, -1.5	6.457545	12	-0.004274
	6	0.5, 0.5, 0.5 -0.5, 0.5, -1.5	7.073886	12	-0.000754
	7	0.5, 0.5, 0.5 0.5, -1.5, -1.5	8.16822	6	0.000821
	8	0.5, 0.5, 0.5 0.5, 0.5, -2.5	8.663706	3	-0.000021
	9	0.5, 0.5, 0.5 -0.5, -1.5, -1.5	8.663706	12	-0.000612
	10	0.5, 0.5, 0.5 0.5, -0.5, -2.5	9.132348	12	-0.002170
	11	0.5, 0.5, 0.5 -0.5, -2.5, 1.5	9.578087	12	0.000850
triplet	1	0.5, 0.5, 0.5 1.5, 0.5, 0.5 1.5, 1.5, 0.5	4.08411	12	-0.000699
	2	0.5, 0.5, 0.5 1.5, 0.5, 1.5 1.5, 1.5, 0.5	4.08411	12	0.001523

	3	0.5, 0.5, 0.5 1.5, 0.5, 0.5 1.5, 1.5, -0.5	5.001993	24	0.000153
	4	0.5, 0.5, 0.5 0.5, 0.5, -0.5 0.5, 0.5, -1.5	5.775804	3	-0.008709
	5	0.5, 0.5, 0.5 0.5, -0.5, -0.5 0.5, 0.5, -1.5	5.775804	12	0.000088
	6	0.5, 0.5, 0.5 1.5, 1.5, -0.5 0.5, 0.5, -1.5	5.775804	12	-0.000209
	7	0.5, 0.5, 0.5 0.5, 0.5, -0.5 0.5, -0.5, -1.5	6.457545	24	-0.000392
	8	0.5, 0.5, 0.5 0.5, -0.5, 0.5 0.5, -0.5, -1.5	6.457545	24	0.000421
	9	0.5, 0.5, 0.5 -0.5, 0.5, -0.5 0.5, -0.5, -1.5	6.457545	648	-0.000033
	10	0.5, 0.5, 0.5 0.5, 1.5, -0.5 0.5, -0.5, -1.5	6.457545	12	0.002070
	11	0.5, 0.5, 0.5 -0.5, -0.5, 0.5 0.5, -0.5, -1.5	6.457545	24	0.000314
	12	0.5, 0.5, 0.5 0.5, -1.5, 0.5	6.457545	12	0.000629

		0.5, -0.5, -1.5			
	13	0.5, 0.5, 0.5 0.5, 0.5, -0.5 -0.5, -0.5, -1.5	7.073886	24	-0.000692
	14	0.5, 0.5, 0.5 0.5, -0.5, 0.5 -0.5, -0.5, -1.5	7.073886	48	0.000202
	15	0.5, 0.5, 0.5 0.5, -0.5, -0.5 -0.5, -0.5, -1.5	7.073886	24	-0.001638
	16	0.5, 0.5, 0.5 1.5, 0.5, -0.5 -0.5, -0.5, -1.5	7.073886	24	0.001633
	17	0.5, 0.5, 0.5 -0.5, -0.5, 0.5 -0.5, -0.5, -1.5	7.073886	24	0.000168
	18	0.5, 0.5, 0.5 1.5, -0.5, -0.5 -0.5, -0.5, -1.5	7.073886	48	0.000024
	19	0.5, 0.5, 0.5 0.5, -1.5, 0.5 -0.5, -0.5, -1.5	7.073886	24	0.000261
	20	0.5, 0.5, 0.5 1.5, 0.5, -1.5 -0.5, -0.5, -1.5	7.073886	48	-0.000210
	21	0.5, 0.5, 0.5 1.5, -1.5, -0.5 -0.5, -0.5, -1.5	7.073886	8	-0.002428
quadruplet	1	0.5, 0.5, 0.5	4.08411	3	-0.001034

		0.5, 1.5, 0.5 1.5, 0.5, 0.5 1.5, 1.5, 0.5			
	2	0.5, 0.5, 0.5 1.5, 0.5, 0.5 1.5, 0.5, 1.5 1.5, 1.5, 0.5	4.08411	8	-0.001373
	3	0.5, 0.5, 0.5 0.5, 1.5, 1.5 1.5, 0.5, 1.5 1.5, 1.5, 0.5	4.08411	2	-0.000773
	4	0.5, 0.5, 0.5 0.5, 1.5, 0.5 1.5, 0.5, 0.5 1.5, 1.5, -0.5	5.001993	24	0.000080
	5	0.5, 0.5, 0.5 1.5, 0.5, 0.5 1.5, 1.5, 0.5 1.5, 1.5, -0.5	5.001993	24	0.000648
	6	0.5, 0.5, 0.5 0.5, 0.5, -0.5 1.5, 1.5, 0.5 1.5, 1.5, -0.5	5.001993	6	-0.000703
	7	0.5, 0.5, 0.5 0.5, 0.5, -0.5 0.5, -0.5, -0.5 0.5, 0.5, -1.5	5.775804	12	0.000899
	8	0.5, 0.5, 0.5 -0.5, 0.5, -0.5	5.775804	12	-0.000787

		0.5, -0.5, -0.5 0.5, 0.5, -1.5			
	9	0.5, 0.5, 0.5 0.5, 1.5, -0.5 0.5, -0.5, -0.5 0.5, 0.5, -1.5	5.775804	3	-0.000529
	10	0.5, 0.5, 0.5 0.5, 0.5, -0.5 1.5, 1.5, -0.5 0.5, 0.5, -1.5	5.775804	12	0.000168
	11	0.5, 0.5, 0.5 1.5, 0.5, -0.5 1.5, 1.5, -0.5 0.5, 0.5, -1.5	4.91812	24	-0.000543
	12	0.5, 0.5, 0.5 1.5, -0.5, -0.5 1.5, 1.5, -0.5 0.5, 0.5, -1.5	4.91812	6	0.000385

Table B4**:** ECIs of bcc lattices in the Al-Ni system at finite temperature

Cluster	labels	ECI (eV/atom)			
		500 K	1000 K	1500 K	2000 K
empty	1	-0.599631	-0.848741	-1.17171	-1.48857
point	1	-0.109656	-0.113366	-0.116976	-0.120056
pair	1	0.071645	0.0746575	0.077755	0.0804425
	2	0.0549667	0.05017	0.0451267	0.0407267
	3	0.0160103	0.014852	0.0136487	0.0126037
	4	0.00308733	0.00449567	0.00598733	0.0072915
	5	0.0095935	0.0095885	0.0095985	0.0096135

	6	-0.0139683	-0.0125317	-0.0110283	-0.00971833
	7	-0.00107883	-0.001918	-0.00280967	-0.00358883
	8	-0.00661533	-0.00619033	-0.0057395	-0.0053445
	9	0.00501167	0.00495	0.004885	0.00482833
	10	-0.00245117	-0.00258617	-0.0027195	-0.00283367
	11	0.0103725	0.0110025	0.01166	0.0122325
	12	0.0149667	0.01367	0.0123083	0.0111217
triplet	1	0.0042245	0.0066895	0.00924367	0.0114628
	2	0.009189	0.00912317	0.00905733	0.00900067
	3	-0.00233433	-0.00176267	-0.001161	-0.00063517
	4	-0.002303	-0.00136425	-0.0003968	0.000442
	5	0.00470142	0.00528308	0.005906	0.00645183
	6	-3.01E-05	-0.00023679	-0.0004449	-0.0006245
	7	-0.00135392	-0.00308892	-0.0049102	-0.00649725
	8	0.0028125	0.003285	0.00376667	0.00418417
	9	-0.0024525	-0.00198208	-0.0014975	-0.00107667
	10	-0.014882	-0.014122	-0.0133045	-0.012587
	11	-0.00137058	-0.0007135	-2.31E-05	0.00057942
	12	0.00142817	0.00038108	-0.0007143	-0.0016685
	13	0.002797	0.00206325	0.00128825	0.000612
	14	-0.00046717	-0.00080175	-0.0011493	-0.00145133
	15	0.0114853	0.0163587	0.021462	0.0259087
	16	-0.00586633	-0.00605967	-0.0062605	-0.00643467
	17	-0.00141567	-0.0023465	-0.0033298	-0.00418817
quadruplet	1	0.00498533	0.004622	0.00424867	0.003927
	2	-0.019406	-0.0189093	-0.018396	-0.0179493
	3	-0.00190825	-0.00235658	-0.0028258	-0.00323408
	4	-0.0136703	-0.014687	-0.0157303	-0.0166337
	5	0.00669625	0.00550875	0.00427125	0.00319375

	6	-0.004449	-0.003364	-0.0022503	-0.001284
	7	0.002821	0.002476	0.002131	0.001831

Table B5**:** ECIs of fcc lattices in the Al-Ni system at finite temperature

Cluster	labels	ECI (eV/atom)			
		FM		NM	
		1000 K	2000 K	1000 K	2000 K
empty	1	-0.711422	-1.39368	-0.742572	-1.42624
point	1	-0.09411	-0.08869	-0.125396	-0.118336
pair	1	0.0791243	0.0786893	0.0768387	0.075607
	2	-0.001462	0.00133133	-0.005898	-0.00571467
	3	0.00927133	0.008063	0.00891483	0.0083315
	4	0.00553533	0.004532	0.00604467	0.00607633
	5	-1.88E-05	0.0005945	0.00082467	0.00163217
	6	-0.0032665	-0.003394	-0.00408	-0.0047775
	7	-0.00021892	-0.00047808	-1.05E-05	-3.76E-05
	8	-0.00223333	-0.00208667	-0.00159433	-0.00136767
	9	-0.00190317	-0.00143317	-2.09E-03	-0.00201567
	10	-0.001769	-0.00166233	-0.00232433	-0.002601
	11	0.000187	-0.00018633	0.00092533	0.0011845
	12	0.000967	0.001292	0.00053417	0.00052167
	13	0.00198217	0.00265717	0.00155783	0.00172867
	14	0.000569	0.00035567	0.000753	0.00071258
	15	-0.00112567	-0.00103817	-0.00119467	-0.00136383
	16	-0.0017015	-0.0018165	-0.00152533	-0.00153242
	17	-0.00016833	0.000235	-0.00046067	-0.000354
	18	0.00011267	0.00032767	0.00023083	0.000495
	19	1.88E-05	0.0002005	-3.97E-05	-3.83E-06
	20	-0.00145567	-0.001809	-0.0010115	-0.00104483

	21	0.00107567	0.001649	0.00036233	0.000249
	22	-0.00106767	-0.00076267	-0.00105517	-0.00100517
	23	-0.00029525	-0.00015067	-6.00E-06	0.000169
	24	-0.00078467	-0.00109133	-0.00053717	-0.00057467
	25	-0.00032817	-0.00037775	-2.38E-05	9.45E-05
triplet	1	0.0105252	0.0101215	0.0111715	0.010669
	2	0.00073267	0.00080683	0.00086217	0.00102217
	3	0.0013445	0.00137408	0.00116883	0.00093842
	4	-0.00075775	-0.00113067	-0.00066625	-0.00099292
	5	0.00165933	0.00190517	0.00110142	0.00097642
	6	-0.00092033	-0.00083908	-0.00099525	-0.00106567
	7	-0.00058725	-0.00069975	-0.000592	-0.0004995
	8	0.00072938	0.00054938	0.00060192	0.00038067
	9	-0.00576733	-0.005614	-0.00573833	-0.00524333
	10	-0.00154683	-0.00198767	-0.0009655	-0.00093717
	11	0.000364	0.00045317	-4.47E-05	-0.00022633
	12	-0.001226	-0.001146	-0.0013335	-0.0015235
	13	0.00097408	0.00108033	0.00030667	0.00010333
	14	0.0005305	0.00050633	0.00087283	0.00105575
	15	0.00014908	0.00011158	0.00053479	0.00072417
	16	0.000211	0.00033933	0.00022492	0.00028742
	17	-0.00101483	-0.00078233	-0.00169167	-0.00210083
	18	-0.00015471	-0.00019742	8.77E-05	9.45E-05
	19	-0.00014283	-0.000207	0.00030763	0.00048804
	20	-0.000781	-0.00060183	-0.000847	-0.000687
quadruplet	1	0.006386	0.006021	0.006715	0.006755
	2	0.001144	0.00138733	1.23E-03	1.53E-03
	3	-0.007586	-0.007966	-0.00743133	-0.00771467
	4	-0.00073988	-0.00063717	-0.00096792	-0.00105479

	5	-0.00114671	-0.00118983	-0.00116742	-0.00114387
	6	-0.0048025	-0.00458167	-0.00466033	-0.00443033
	7	-0.00060192	-0.00061067	-0.00018733	-6.15E-05
	8	0.00106788	0.00122829	0.00086017	0.00093892
	9	-0.00064175	-0.00049925	-0.00077775	-0.0008815
	10	0.002913	0.00375133	0.00256233	0.00313567
	11	0.000132	9.62E-05	0.00040367	0.00035492
	12	0.0019175	0.00203417	0.00190808	0.00199475
	13	-9.94E-05	3.41E-05	-0.00033879	-0.00046254
	14	0.0015335	0.0012535	0.00221975	0.00251225
	15	0.00018283	7.53E-05	0.000436	0.0003835
	16	0.00159067	0.00229233	0.00059767	0.00058267
	17	-0.00192237	-0.00195717	-0.00171829	-0.00167162
	18	-0.00114925	-0.00111175	-0.001617	-0.00183658
	19	0.0002555	1.97E-05	0.00055967	0.00057633
	20	-0.00051717	-0.00081508	-0.00033958	-0.00046458
	21	-0.00040438	-0.00058646	-0.00036867	-0.00041992
	22	0.00196917	0.00138667	0.00260133	0.00243383
	23	-0.00036233	-0.00024608	-0.00042708	-0.00043833
	24	6.80E-05	-0.00116533	0.001076	0.00087267
	25	-3.33E-05	-0.000195	0.00030108	0.00024317
	26	0.001958	0.00206383	0.00219617	0.00232117
	27	-0.00060417	-0.0007125	-0.000388	-0.00030467
	28	0.00048983	0.00035233	0.00094467	0.00111467
	29	-4.96E-06	7.05E-05	-0.00017625	-0.00022708
	30	-0.0003735	0.000144	-0.00070267	-0.000571
	31	-0.00036525	-0.00054525	0.00011192	0.000169
	32	-0.00016433	-0.00023225	-0.00044875	-0.0006175
	33	0.00065158	0.00089408	0.00040375	0.00038292

	34	0.000524	0.000674	0.00083075	0.0010795
	35	0.00077	0.000545	0.000779	0.000794

Table B6**:** ECIs of bcc lattices with vacancies in the Al-Ni system at finite temperature

Cluster	labels	ECI (eV/atom)			
		500 K	1000 K	1500 K	2000 K
empty	1	-0.256817	-0.638617	-1.12058	-1.66806
point	1	0.022775	0.132375	0.275355	0.440235
pair	1	0.0440553	0.0428087	0.0414887	0.040142
	2	0.00626867	0.00639867	0.00661867	0.006892
	3	0.003296	0.002341	0.001361	0.000366
	4	0.016401	0.0162143	0.0160277	0.0158477
	5	-0.00416233	-4.04E-03	-0.003919	-0.00379233
	6	-0.00069733	-0.00057567	-0.000434	-0.00027567
	7	9.14E-04	0.00096767	0.001011	0.00104767
	8	8.57E-05	0.00015233	0.000199	0.00023233
	9	-0.00057033	-0.00048033	-0.000372	-0.000252
	10	-0.00209333	-0.00212667	-0.00219833	-0.00229667
	11	0.00094667	0.001085	0.00123667	0.0014
triplet	1	-0.000324	2.77E-05	0.00037767	0.00072433
	2	0.0025705	0.003488	0.004368	0.005223
	3	0.00018217	0.00023383	0.000293	0.000358
	4	-0.00918233	-0.009649	-0.0101357	-0.0106223
	5	-0.000532	-0.00123033	-0.00196367	-0.002722
	6	-0.00019233	-0.00020067	-0.000219	-0.000244
	7	-5.91E-04	-0.0007495	-0.00089617	-0.00103617

	8	6.30E-04	8.85E-04	0.00115933	0.001446
	9	8.03E-05	0.00026117	0.00046867	0.00069367
	10	0.002175	0.002315	0.00247	0.00263333
	11	0.00036817	0.00037817	0.000374	0.0003615
	12	0.00083233	0.00098233	0.00111567	0.00123733
	13	-0.00074283	-0.00090783	-0.00111367	-0.00134617
	14	0.00012908	4.33E-05	-4.76E-05	-0.00014175
	15	-0.00222133	-0.00280383	-0.0033955	-0.00399217
	16	0.001903	0.00222633	0.00257383	0.00293633
	17	0.00017717	0.00020467	0.00023967	0.000278
	18	-4.75E-06	-6.85E-05	-0.00014558	-0.00023142
	19	0.00055017	0.0008485	0.00115517	0.001466
	20	-0.00017083	-0.00012625	-8.00E-05	-3.29E-05
	21	-0.0024605	-0.002478	-0.0024905	-0.0025005
quadruplet	1	-0.00112067	-0.00134067	-0.00160733	-0.00190067
	2	-0.001313	-0.001253	-0.0011905	-0.001128
	3	-0.000873	-0.000723	-0.000493	-0.000203
	4	0.00014917	0.00015167	0.00013333	0.0001
	5	0.00068383	0.00072383	0.00076467	0.0008055
	6	-0.000403	-0.00017633	3.03E-05	0.00022033
	7	0.000959	0.00111733	0.001309	0.001524
	8	-0.000927	-0.00111033	-0.00131033	-0.00152367
	9	-0.00102233	-0.001649	-0.002329	-0.00304233
	10	0.000268	0.00042133	0.000598	0.00078633
	11	-0.0006055	-0.000683	-0.0007655	-0.00085133

12	0.00050167	0.00063167	0.00076833	0.00090833

B.2. Bond length vs. bond stiffness relationships in the Ni-Al system

The L-S relationships in Ni-Al system without magnetic effects are shown in Figure B1, and the vibrational free energies, F_{vib}, of NM-Ni and NM-$AlNi_3$ are shown in Figure B2, which are also compared with those of FM-Ni and FM-$AlNi_3$. The vibrational free energies of NM- and FM-Ni or NM- and FM-$AlNi_3$ overlap, which indicates that magnetism has no effect on vibrational free energy.

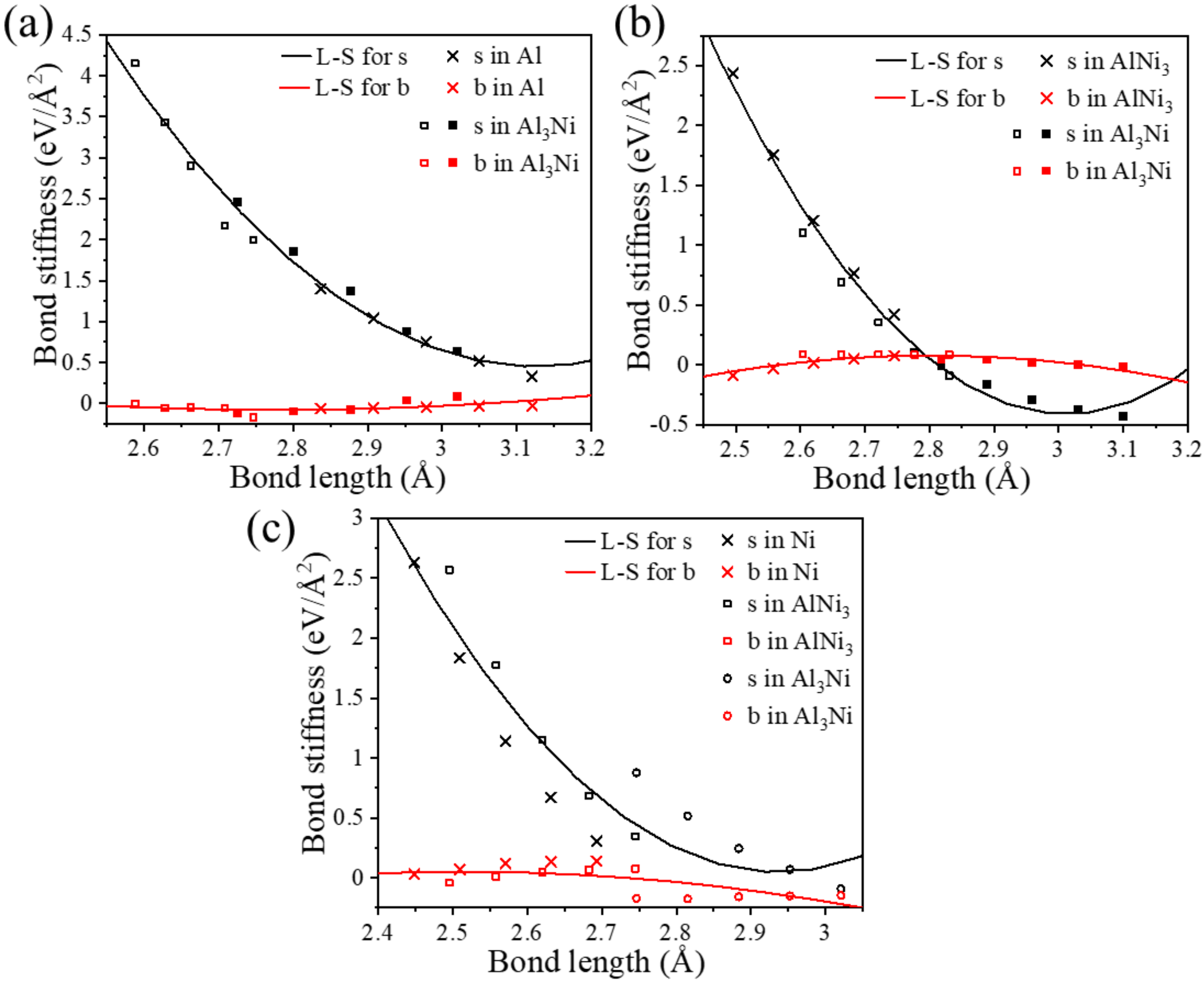

Figure B1: L-S relationship for three bond types in the fcc lattice without magnetism. (a) Al-Al bond. (b) Al-Ni bond. (c) Ni-Ni bond.

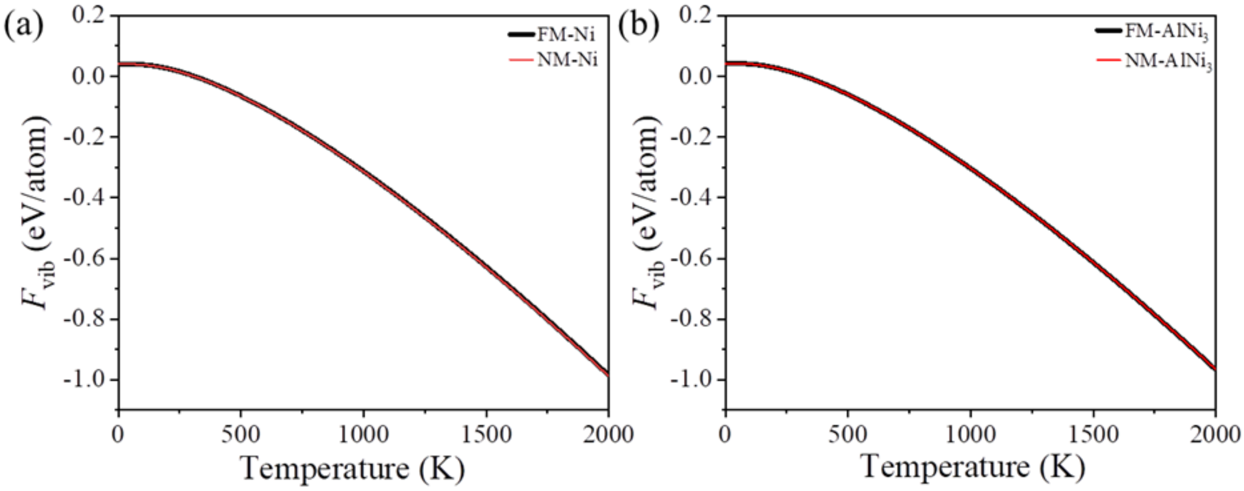

Figure B2: Vibrational free energies of ferromagnetic and non-magnetic (a) Ni and (b) $AlNi_3$.

B.3. Mixing enthalpies in the Ni-Al system

The mixing enthalpies, H_{mix}, contribution due to lattice vibration in Ni-Al system were calculate by eqs. (2.17), (2.18) and (2.20), which are also compared with H_{mix} fitted using CE, as shown in Figures B3-B5. The H_{mix} calculated using first-principles combined with L-S relationship and fitted using CE at each temperature for bcc, fcc and bcc with vacancies Ni-Al system are very close.

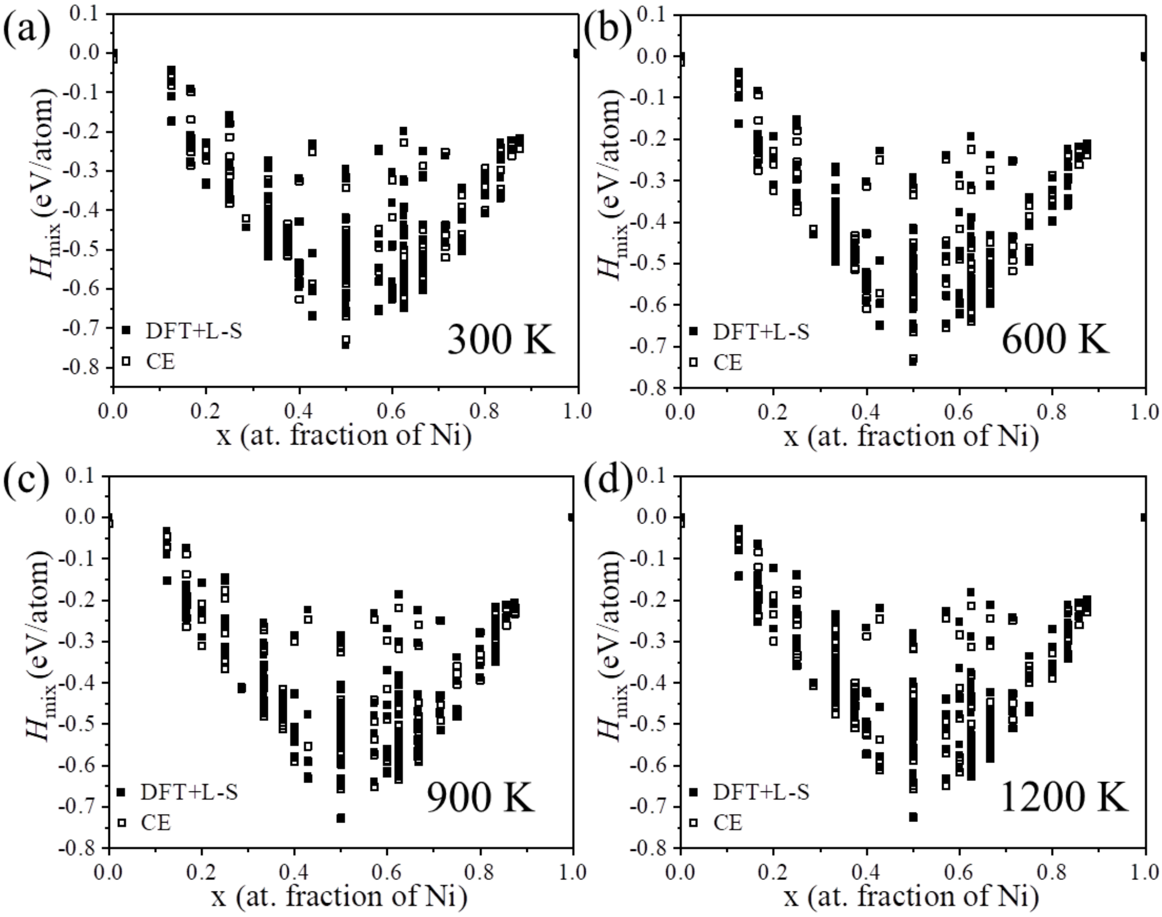

Figure B3**:** Mixing enthalpies for bcc lattices at different temperatures. (a) 300 K. (b) 600 K. (c) 900 K. (d) 1200 K.

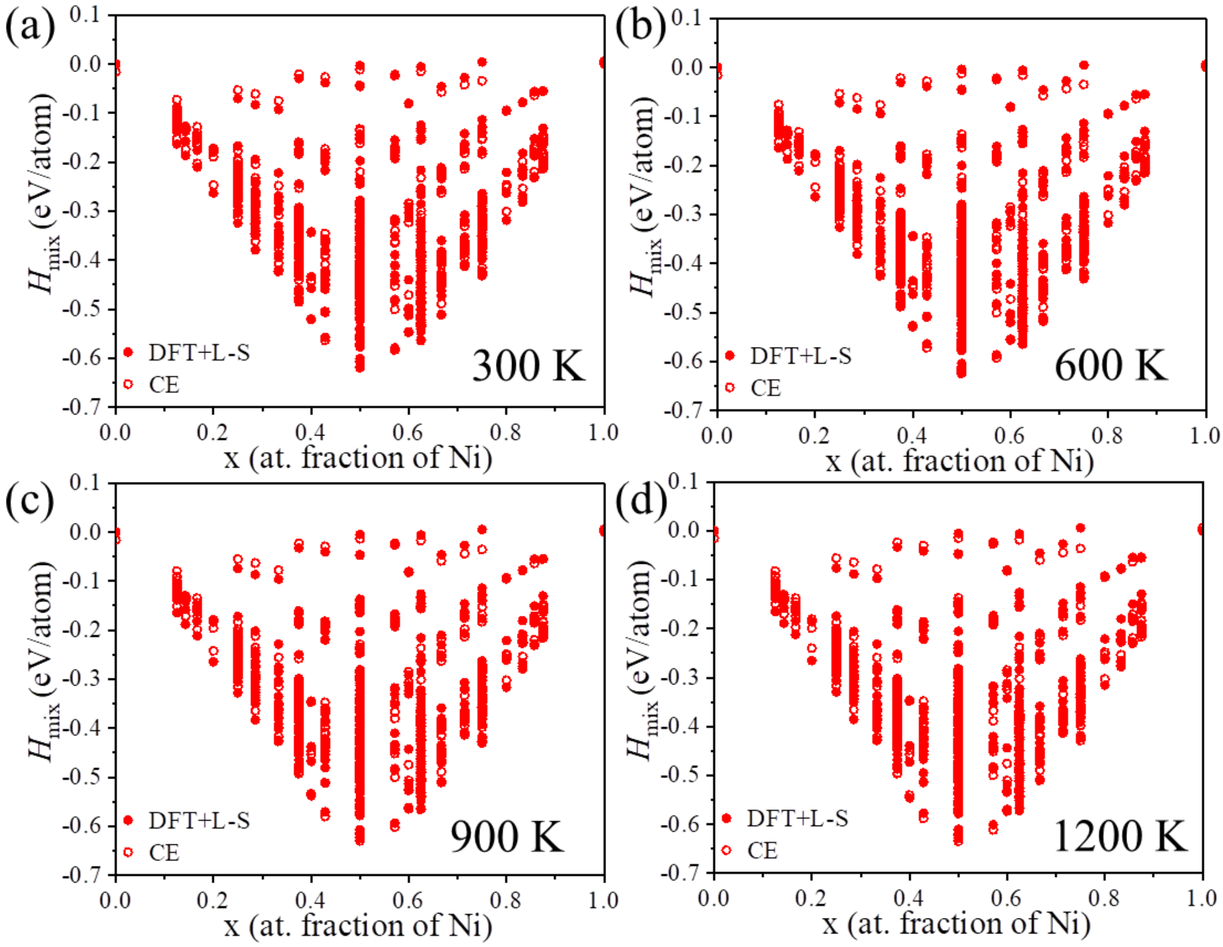

Figure B4**:** Mixing enthalpies for fcc lattices at different temperatures. (a) 300 K. (b) 600 K. (c) 900 K. (d) 1200 K.

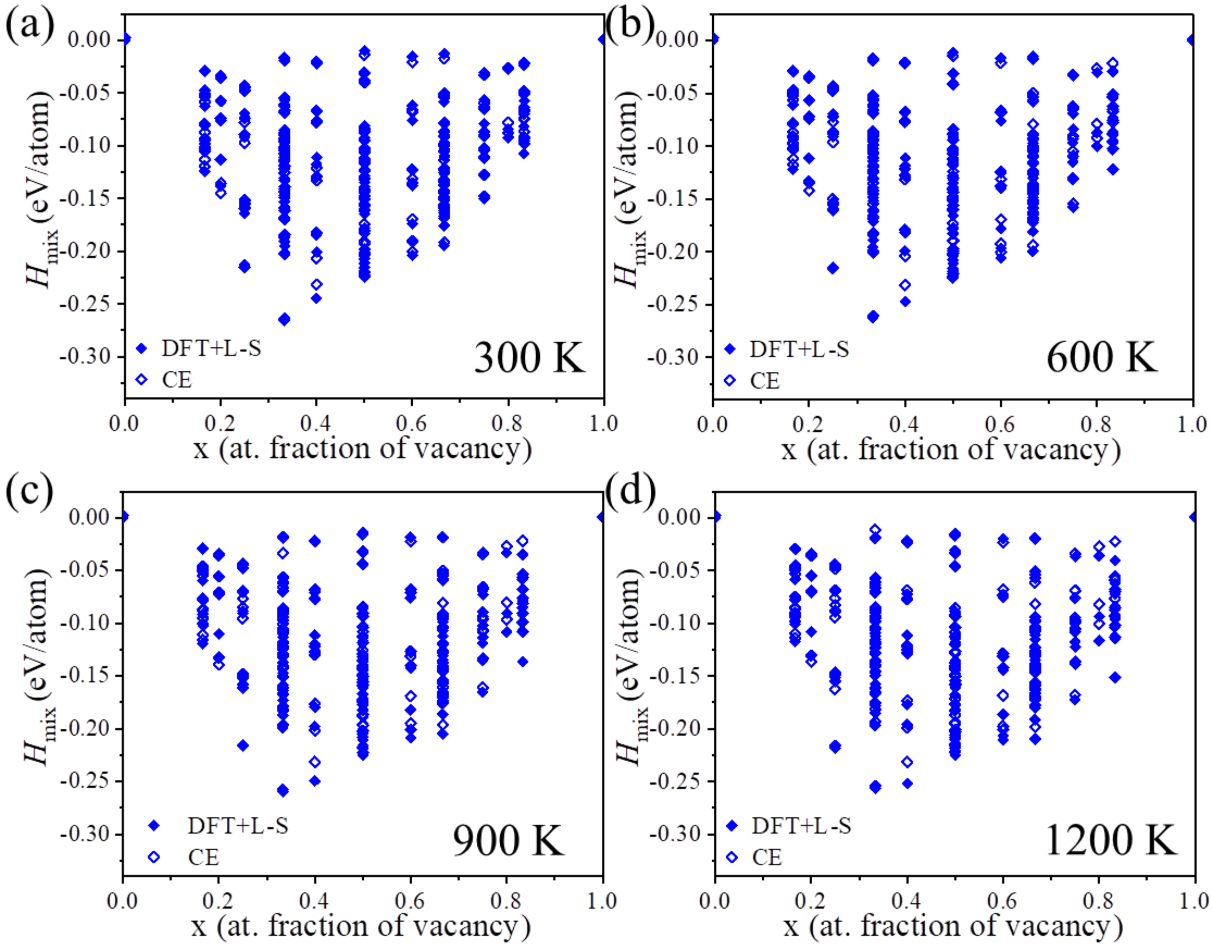

Figure B5**:** Mixing enthalpies for bcc lattices with vacancies at different temperatures. (a) 300 K. (b) 600 K. (c) 900 K. (d) 1200 K.

B.4. Gibbs free energies and phase boundaries in the Ni-Al system including configurational and vibrational entropy

The Gibbs free energies and phase boundaries including only configurational and vibrational entropy for Ni-Al system are shown in Figures B6-B11, which were integrated to obtain the whole Ni-Al phase diagram considering configurational and vibrational entropic effect.

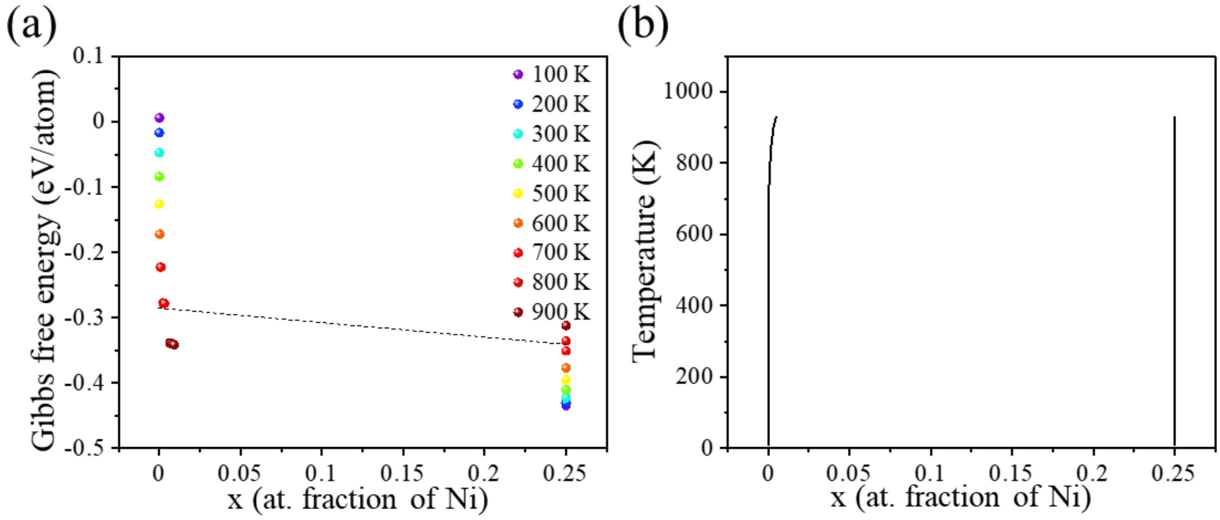

Figure B6**:** (a) Gibbs free energy of Al and Al_3Ni at different temperatures. (b) Phase boundary between Al and Al_3Ni.

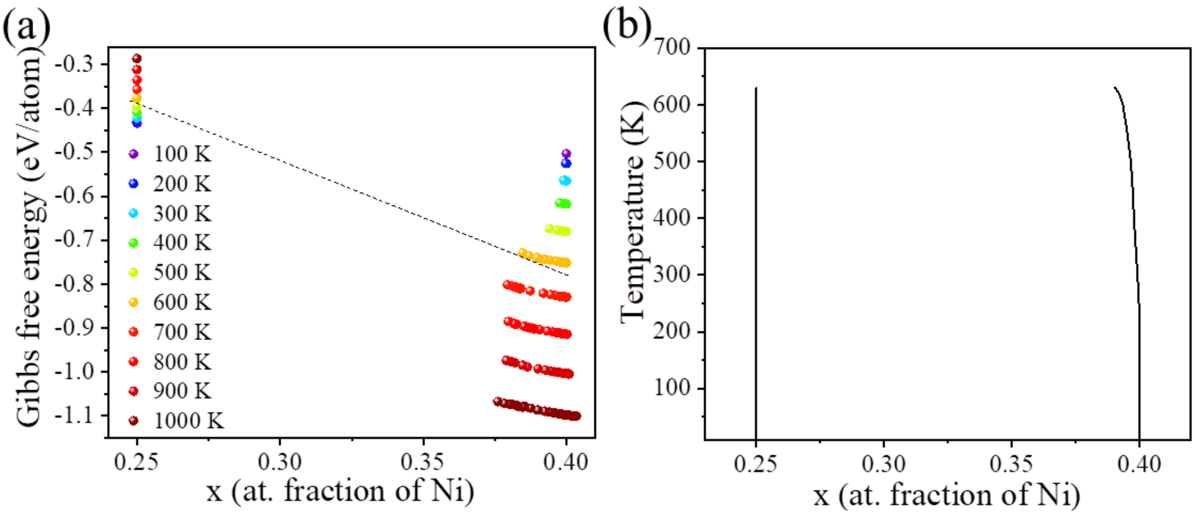

Figure B7**:** (a) Gibbs free energy of Al_3Ni and Al_3Ni_2 at different temperatures. (b) Phase boundary between Al_3Ni and Al_3Ni_2.

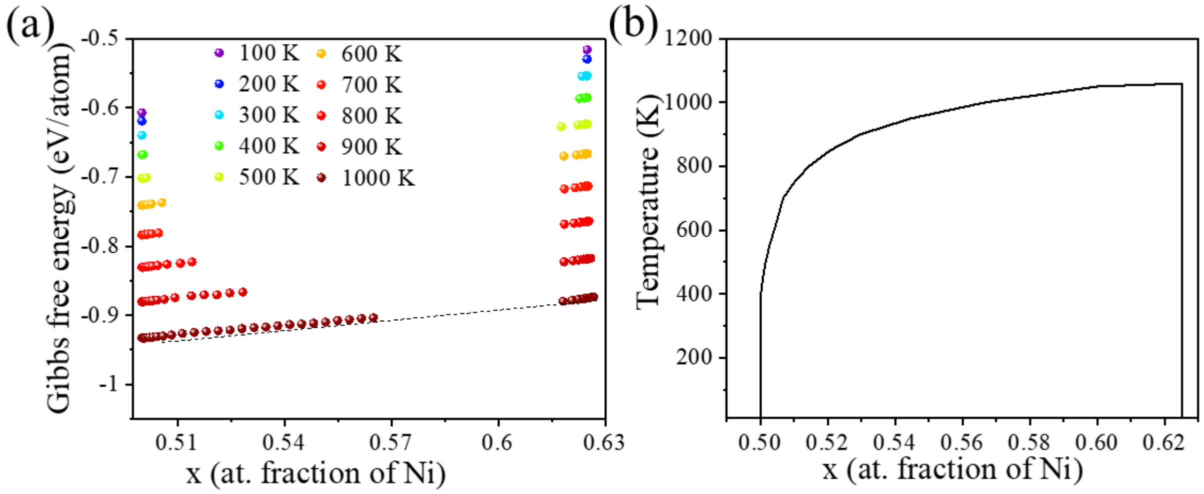

Figure B8**:** (a) Gibbs free energy of AlNi and Al_3Ni_5 at different temperatures. (b) Phase boundary between AlNi and Al_3Ni_5.

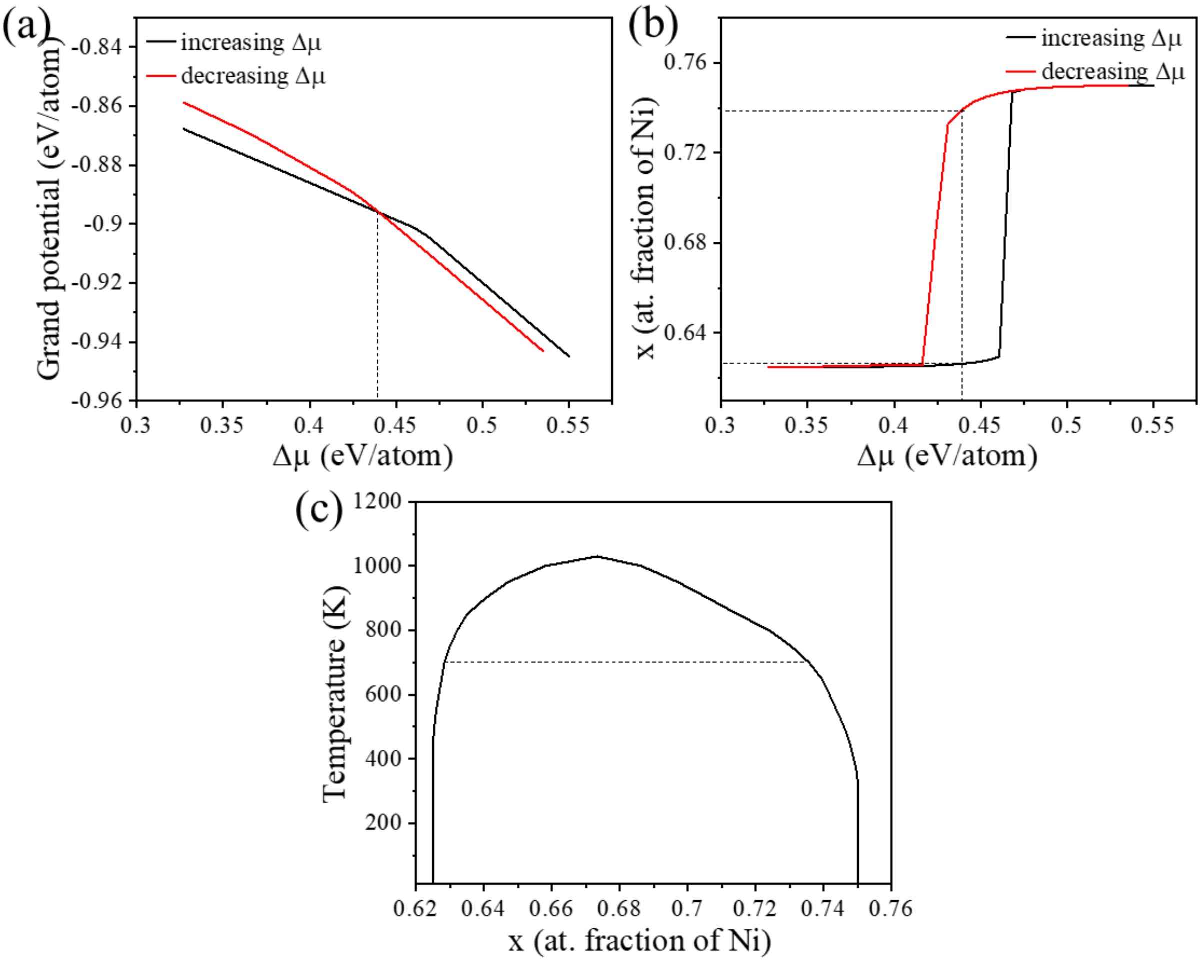

Figure B9**:** (a) Grand potentials of Al_3Ni_5 and $AlNi_3$ as a function of chemical potential at 700 K. (b) Composition of Ni as a function of chemical potential at 700 K. (c) Phase boundary between Al_3Ni_5 and $AlNi_3$.

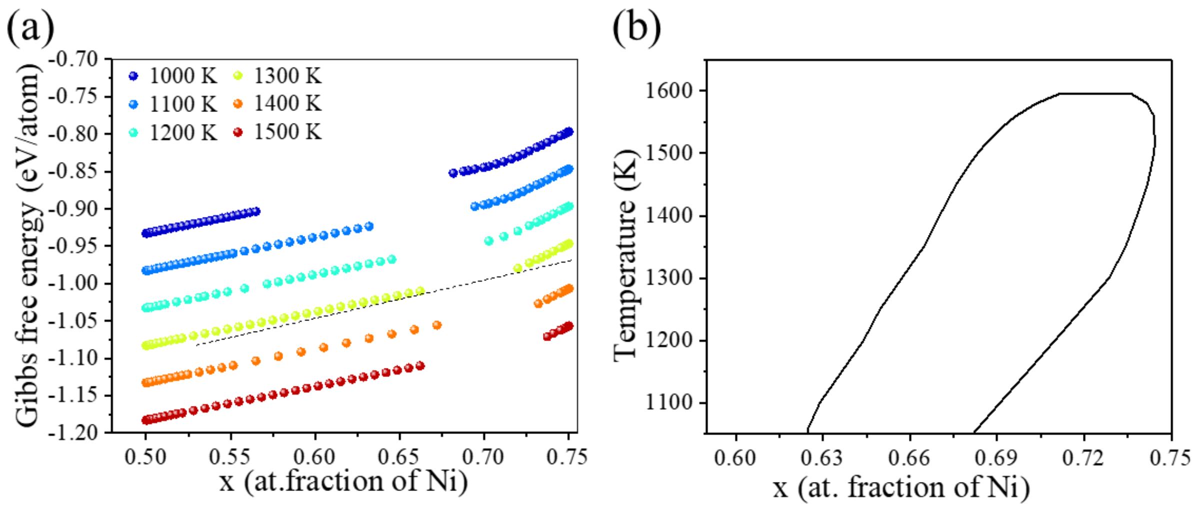

Figure B10**:** (a) Gibbs free energy of AlNi and $AlNi_3$ at temperature above 1030 K; (b) Phase boundary between AlNi and Al_3Ni_5.

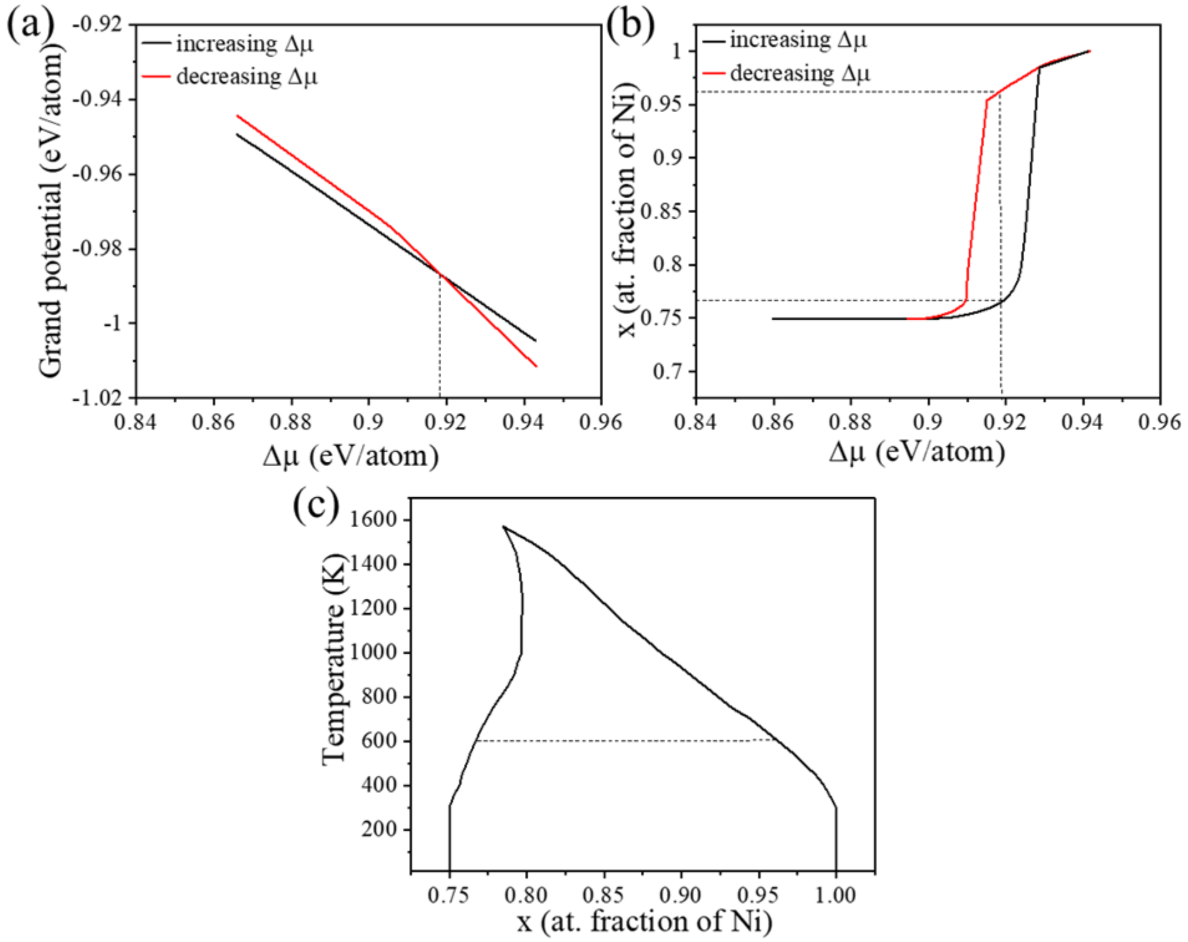

Figure B11**:** (a) Grand potentials of $AlNi_3$ and Ni as a function of chemical potential at 600 K. (b) Composition of Ni as a function of chemical potential at 600 K. (c) Phase boundary between $AlNi_3$ and Ni.

B.5. Gibbs free energies and phase boundaries in the Ni-Al system including configurational entropy

The Gibbs free energies and phase boundaries including only configurational entropy for Ni-Al system are shown in Figures B12-B19, which were integrated to obtain the whole Ni-Al phase diagram considering configurational entropic effect.

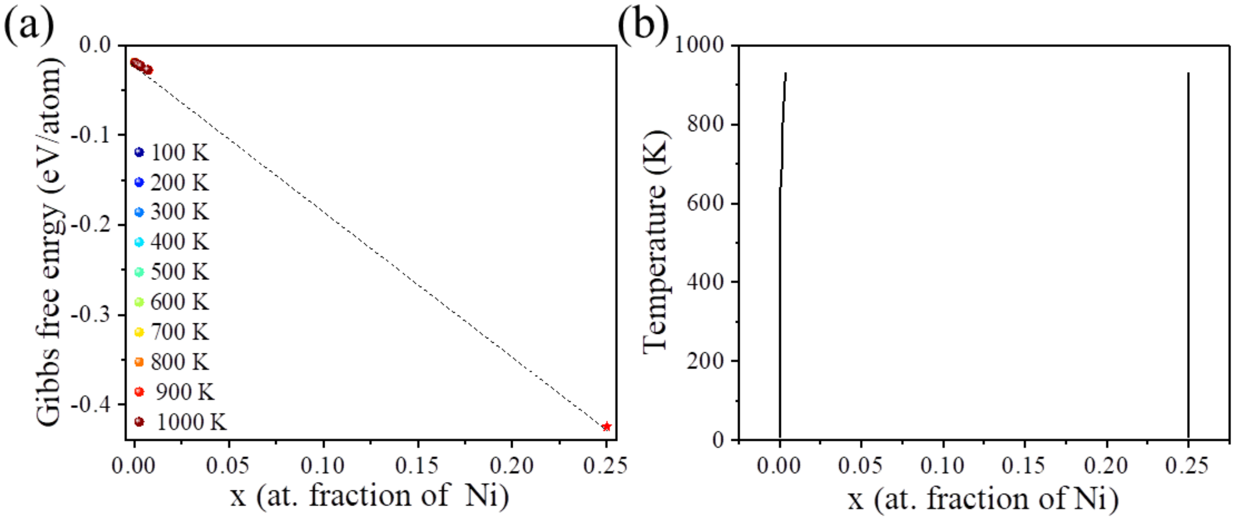

Figure B12**:** (a) Gibbs free energy of Al and Al_3Ni at different temperatures. (b) Phase boundary between Al and Al_3Ni.

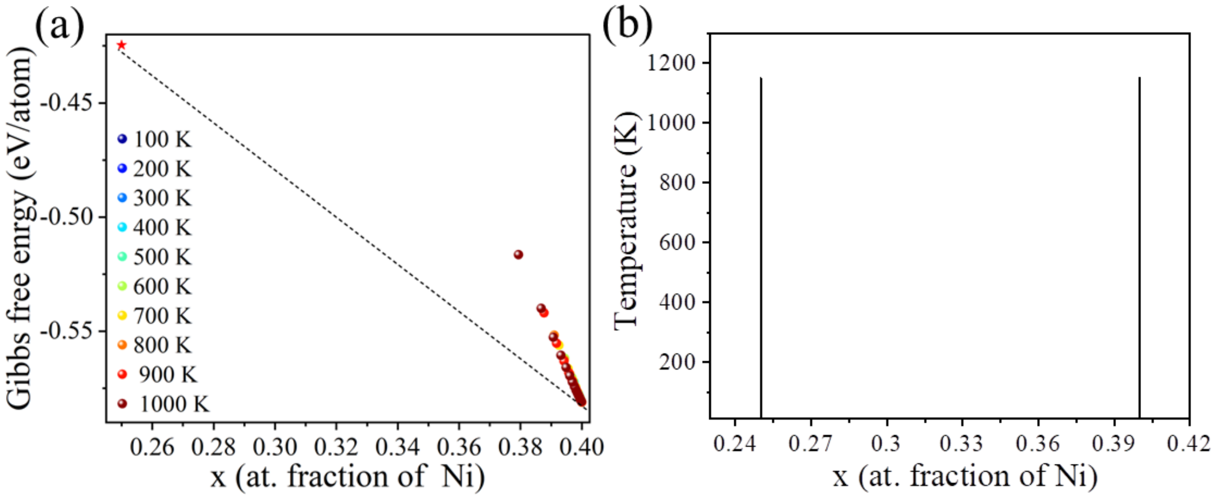

Figure B13**:** (a) Gibbs free energy of Al_3Ni and Al_3Ni_2 at different temperatures. (b) Phase boundary between Al_3Ni and Al_3Ni_2.

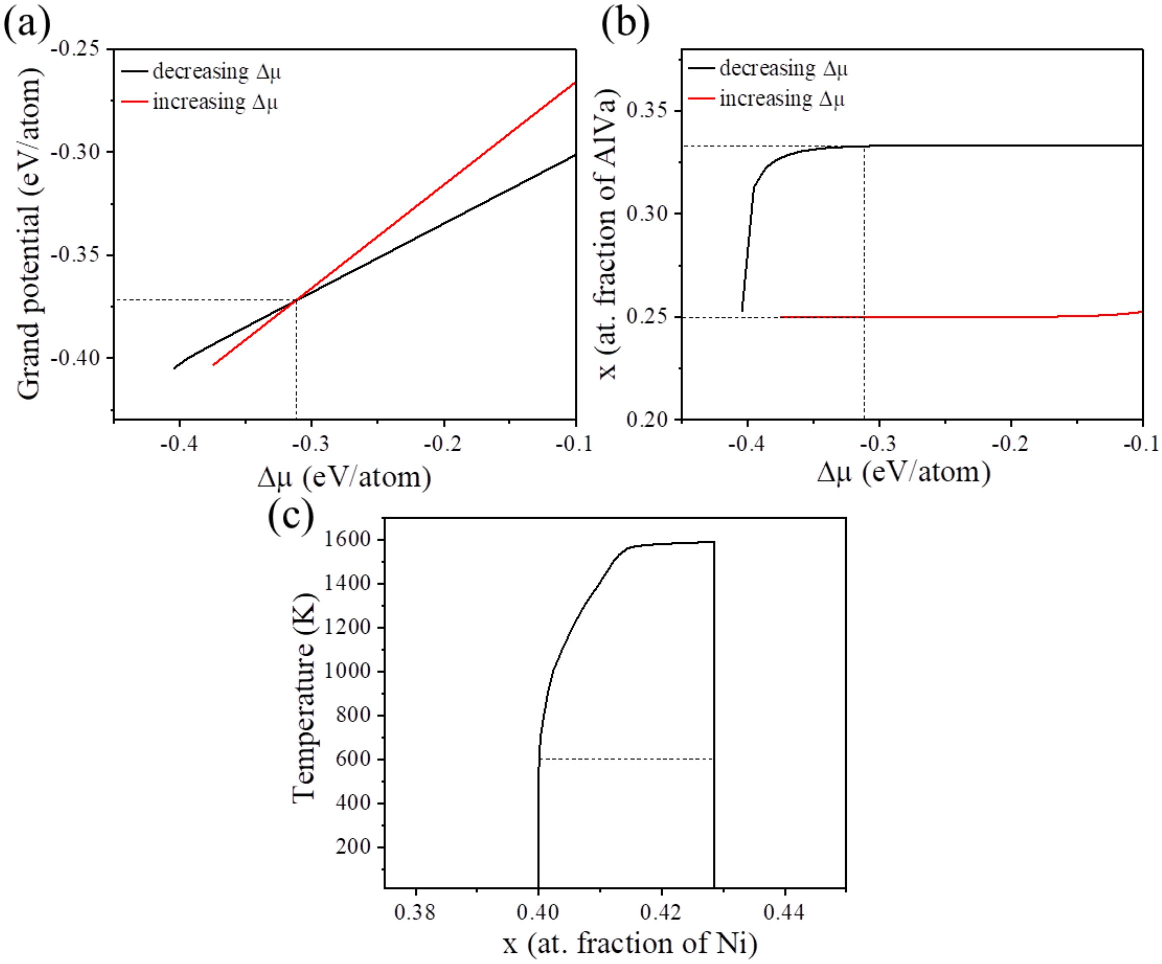

Figure B14**:** (a) Grand potentials of Al_3Ni_2 and Al_4Ni_3 as a function of chemical potential at 600 K. (b) Composition of AlVa as a function of chemical potential at 600 K. (c) Phase boundary between Al_3Ni_2 and Al_4Ni_3.

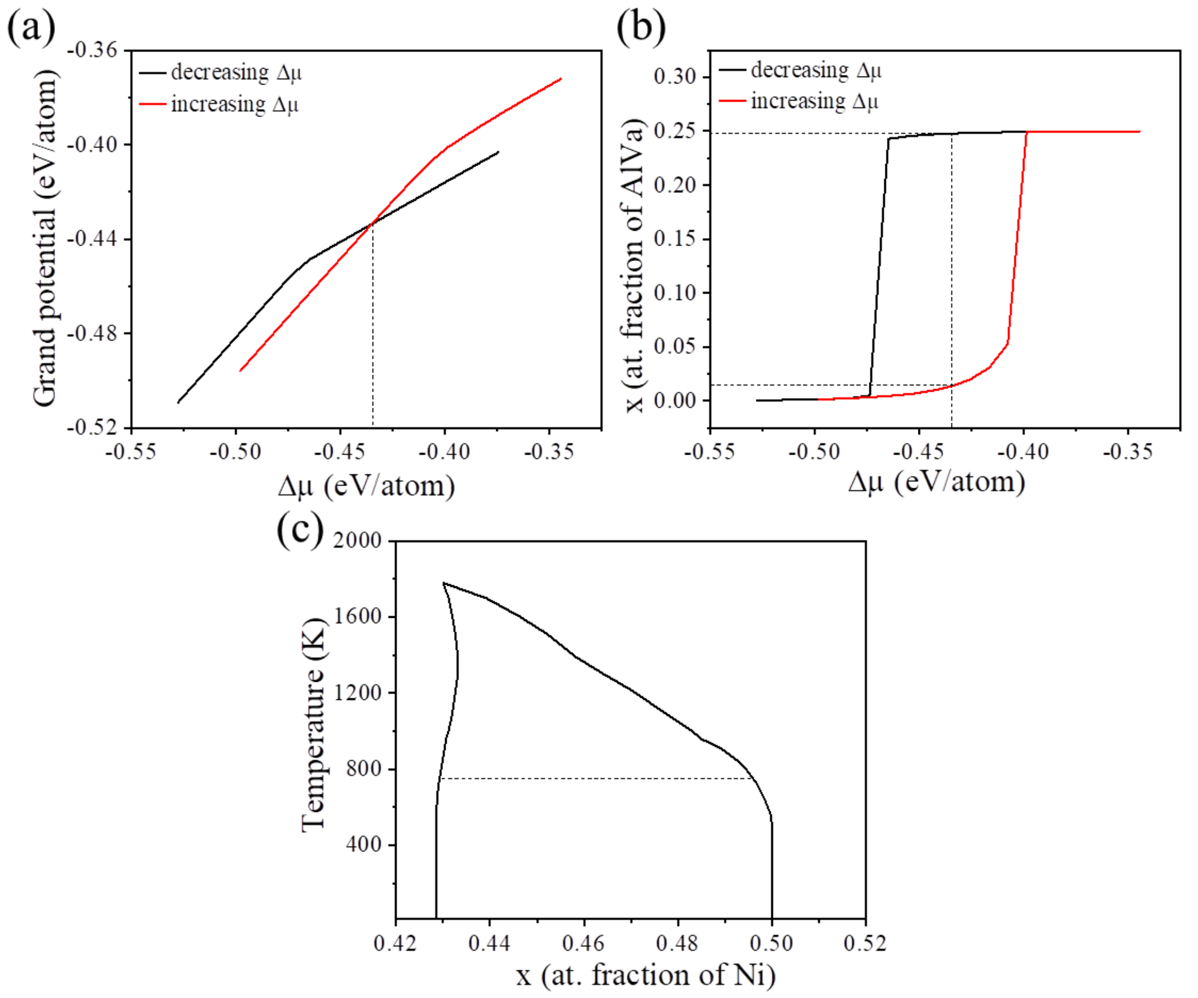

Figure B15**:** (a) Grand potentials of Al_4Ni_3 and AlNi as a function of chemical potential at 750 K. (b) Composition of AlVa as a function of chemical potential at as a function of $\Delta\mu$ at 750 K. (c) Phase boundary between Al_4Ni_3 and AlNi.

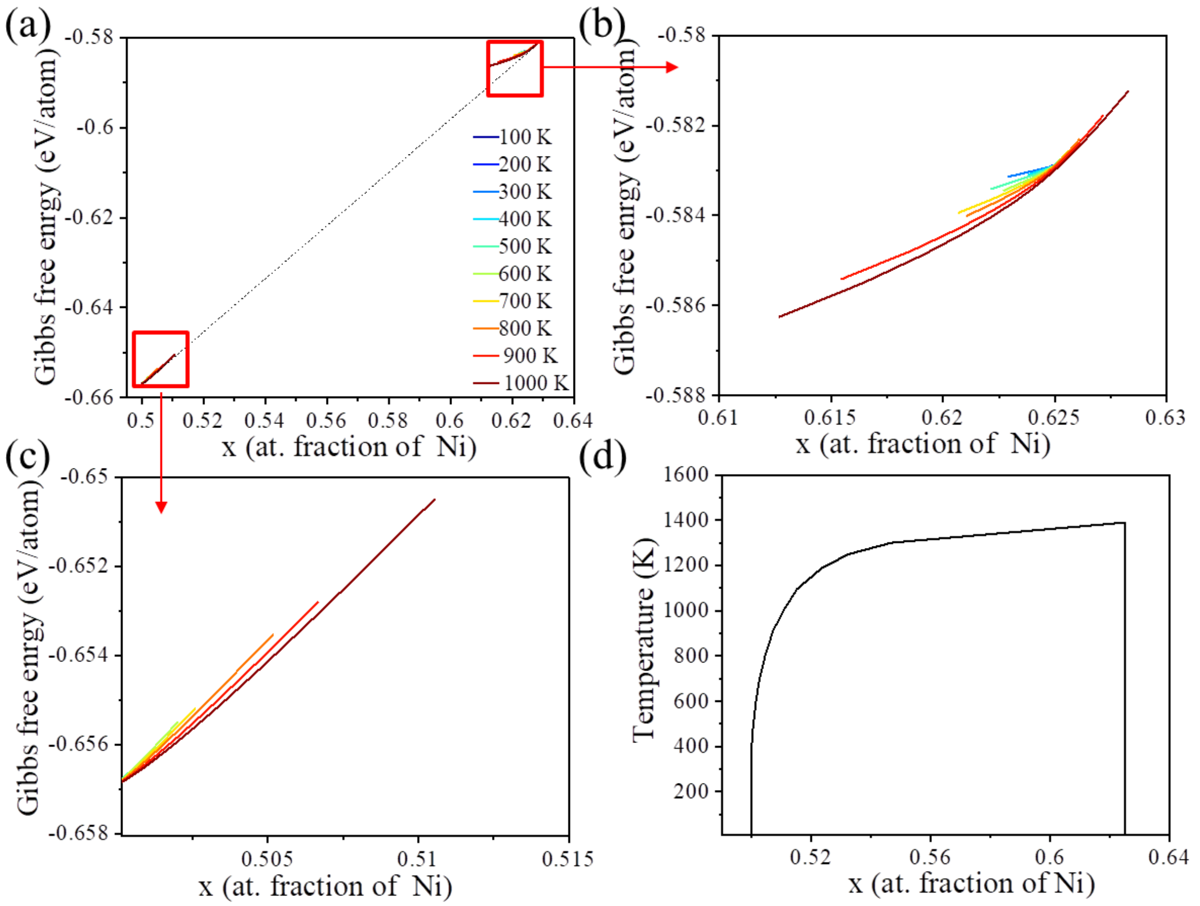

Figure B16**:** (a) Gibbs free energy of AlNi and Al_3Ni_5 at different temperatures. Gibbs free energy of AlNi (b) and Al_3Ni_5 (c). (d) Phase boundary between AlNi and Al_3Ni_5.

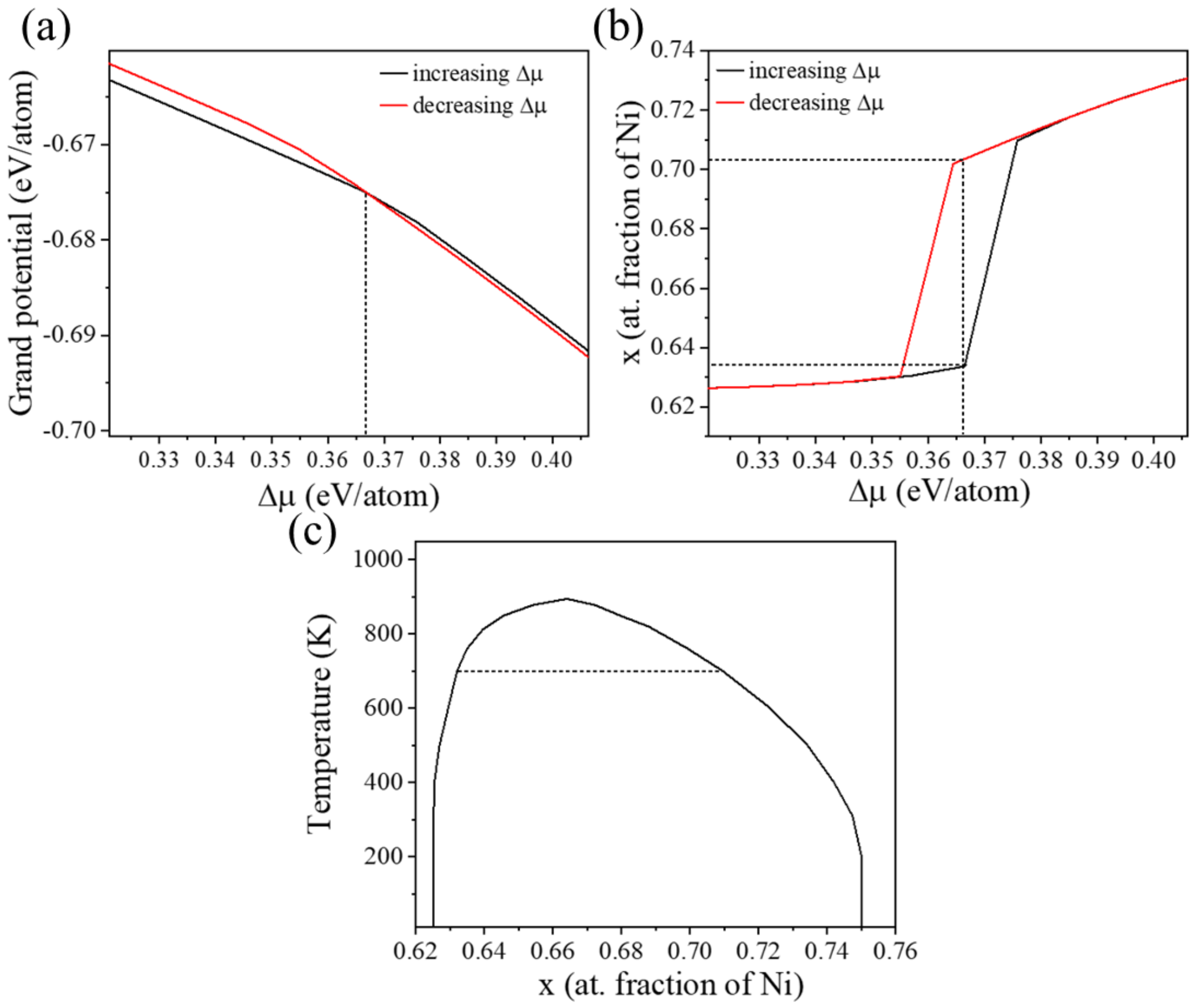

Figure B17**:** (a) Grand potentials of Al_3Ni_5 and $AlNi_3$ as a function of chemical potential at 700 K. (b) Composition of Ni as a function of chemical potential at 700 K. (c) Phase boundary between Al_3Ni_5 and $AlNi_3$.

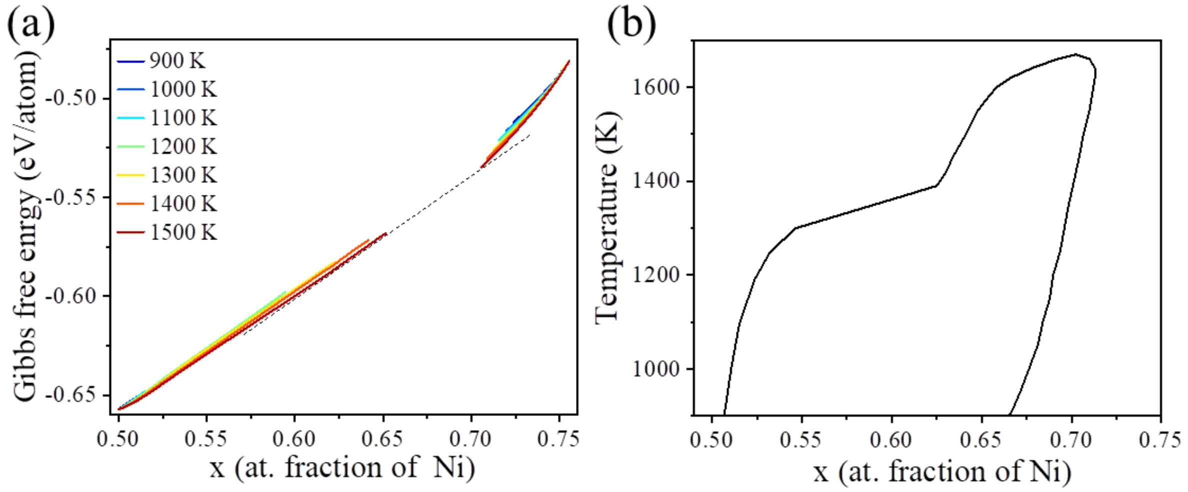

Figure B18**:** (a) Gibbs free energy of AlNi and $AlNi_3$ at temperature above 1030 K; (b) Phase boundary between AlNi and Al_3Ni_5.

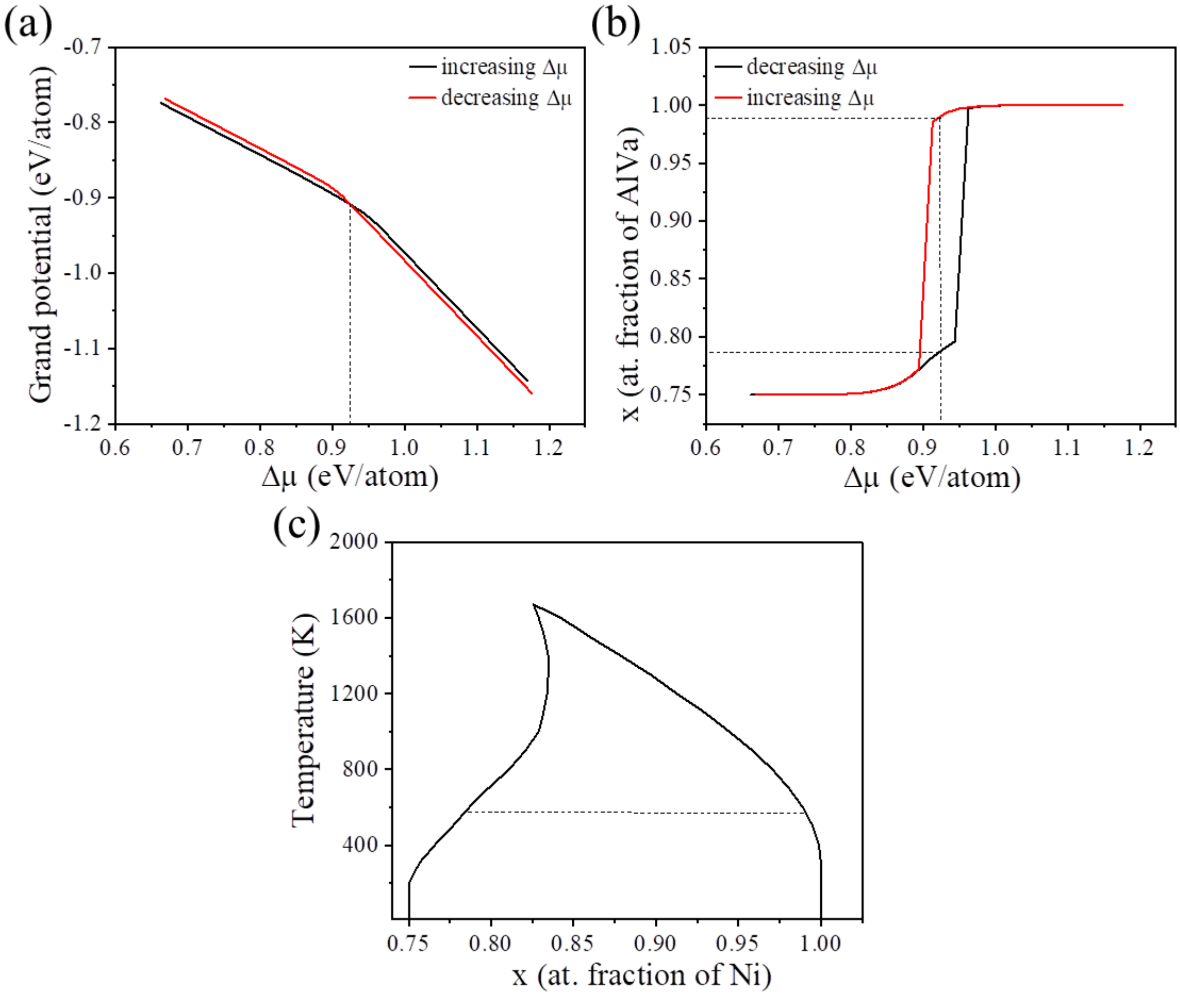

Figure B19**:** (a) Grand potentials of AlNi$_3$ and Ni as a function of chemical potential at 600 K. (b) Composition of Ni as a function of chemical potential at 600 K. (c) Phase boundary between AlNi$_3$ and Ni.

Annex C. Co-Al phase diagram

C.1. Cluster information of the SQS candidates

The cluster information of the SQS candidates and the ideal solid solution for each composition are listed in Table C1, and the correlation functions of the SQS candidates and the ideal solid solution are compared to determine whether the SQS can represent the ideal solid solution.

Table C1: Cluster number, correlation functions of the SQS candidates and the ideal solid solution for each composition

Labels	Correlation functions for each composition (at.%)							
	87.5		88.75		90		91.25	
	$\rho_\alpha(\sigma^{SQS})$	$\rho_\alpha(\sigma^{rnd})$	$\rho_\alpha(\sigma^{SQS})$	$\rho_\alpha(\sigma^{rnd})$	$\rho_\alpha(\sigma^{SQS})$	$\rho_\alpha(\sigma^{rnd})$	$\rho_\alpha(\sigma^{SQS})$	$\rho_\alpha(\sigma^{rnd})$
1	0.566667	0.5625	0.6	0.600625	0.633333	0.64	0.675	0.680625
2	0.566667	0.5625	0.6	0.600625	0.633333	0.64	0.683333	0.680625
3	0.566667	0.5625	0.6	0.600625	0.641667	0.64	0.679167	0.680625
4	0.55	0.5625	0.6	0.600625	0.633333	0.64	0.683333	0.680625
5	0.566667	0.5625	0.6	0.600625	0.641667	0.64	0.683333	0.680625
6	0.55	0.5625	0.6	0.600625	0.625	0.64	0.6875	0.680625
7	0.533333	0.5625	0.589583	0.600625	0.666667	0.64	0.704167	0.680625
8	0.566667	0.5625	0.6	0.600625	0.6	0.64	0.666667	0.680625
9	0.541667	0.5625	0.579167	0.600625	0.641667	0.64	0.679167	0.680625
10	0.55	0.5625	0.608333	0.600625	0.616667	0.64	0.675	0.680625
11	0.55	0.5625	0.591667	0.600625	0.65	0.64	0.691667	0.680625
12	0.425	0.421875	0.45	0.465484	0.5	0.512	0.55	0.561516
13	0.433333	0.421875	0.475	0.465484	0.483333	0.512	0.558333	0.561516
14	0.441667	0.421875	0.466667	0.465484	0.508333	0.512	0.55	0.561516
15	0.433333	0.421875	0.466667	0.465484	0.508333	0.512	0.554167	0.561516
16	0.441667	0.421875	0.470833	0.465484	0.508333	0.512	0.558333	0.561516
17	0.433333	0.421875	0.4625	0.465484	0.508333	0.512	0.5625	0.561516
18	0.425	0.421875	0.475	0.465484	0.5	0.512	0.5625	0.561516
19	0.433333	0.421875	0.475	0.465484	0.5	0.512	0.558333	0.561516
20	0.420833	0.421875	0.460417	0.465484	0.504167	0.512	0.558333	0.561516
21	0.416667	0.421875	0.466667	0.465484	0.5	0.512	0.566667	0.561516
22	0.4	0.421875	0.466667	0.465484	0.5	0.512	0.566667	0.561516
23	0.4	0.421875	0.475	0.465484	0.5	0.512	0.5625	0.561516
24	0.425	0.421875	0.458333	0.465484	0.508333	0.512	0.5625	0.561516
25	0.425	0.421875	0.4625	0.465484	0.5	0.512	0.558333	0.561516
26	0.433333	0.421875	0.454167	0.465484	0.516667	0.512	0.5625	0.561516
27	0.408333	0.421875	0.4625	0.465484	0.508333	0.512	0.558333	0.561516
28	0.416667	0.421875	0.475	0.465484	0.516667	0.512	0.575	0.561516
29	0.433333	0.421875	0.460417	0.465484	0.516667	0.512	0.558333	0.561516
30	0.420833	0.421875	0.458333	0.465484	0.5125	0.512	0.5625	0.561516
31	0.433333	0.421875	0.466667	0.465484	0.516667	0.512	0.575	0.561516

Correlation functions for each composition (at.%)											
92.5		93.75		95		96.25		97.5		98.75	
$\rho_\alpha(\sigma^{SQS})$	$\rho_\alpha(\sigma^{rnd})$	$\rho_\alpha(\sigma^{SQS})$	$\rho_\alpha(\sigma^{rnd})$	$\rho_\alpha(\sigma^{SQS})$	$\rho_\alpha(\sigma^{rnd})$	$\rho_\alpha(\sigma^{SQS})$	$\rho_\alpha(\sigma^{rnd})$	$\rho_\alpha(\sigma^{SQS})$	$\rho_\alpha(\sigma^{rnd})$	$\rho_\alpha(\sigma^{SQS})$	$\rho_\alpha(\sigma^{rnd})$
0.716667	0.7225	0.766667	0.765625	0.816667	0.81	0.858333	0.855625	0.9	0.9025	0.95	0.950625
0.733333	0.7225	0.766667	0.765625	0.8	0.81	0.85	0.855625	0.9	0.9025	0.95	0.950625
0.725	0.7225	0.766667	0.765625	0.808333	0.81	0.854167	0.855625	0.9	0.9025	0.95	0.950625
0.716667	0.7225	0.766667	0.765625	0.8	0.81	0.858333	0.855625	0.9	0.9025	0.95	0.950625
0.725	0.7225	0.766667	0.765625	0.816667	0.81	0.854167	0.855625	0.908333	0.9025	0.95	0.950625
0.725	0.7225	0.7625	0.765625	0.8	0.81	0.85	0.855625	0.9	0.9025	0.95	0.950625
0.7125	0.7225	0.76875	0.765625	0.808333	0.81	0.85625	0.855625	0.904167	0.9025	0.95	0.950625
0.7	0.7225	0.766667	0.765625	0.8	0.81	0.85	0.855625	0.9	0.9025	0.95	0.950625
0.708333	0.7225	0.758333	0.765625	0.808333	0.81	0.854167	0.855625	0.9	0.9025	0.95	0.950625
0.7	0.7225	0.766667	0.765625	0.8	0.81	0.858333	0.855625	0.9	0.9025	0.95	0.950625
0.708333	0.7225	0.766667	0.765625	0.816667	0.81	0.85	0.855625	0.9	0.9025	0.95	0.950625
0.6	0.614125	0.675	0.669922	0.75	0.729	0.8	0.791453	0.85	0.857375	0.925	0.926859
0.616667	0.614125	0.675	0.669922	0.733333	0.729	0.791667	0.791453	0.85	0.857375	0.925	0.926859
0.608333	0.614125	0.675	0.669922	0.741667	0.729	0.795833	0.791453	0.85	0.857375	0.925	0.926859
0.625	0.614125	0.670833	0.669922	0.725	0.729	0.7875	0.791453	0.85	0.857375	0.925	0.926859
0.608333	0.614125	0.675	0.669922	0.733333	0.729	0.791667	0.791453	0.85	0.857375	0.925	0.926859
0.625	0.614125	0.670833	0.669922	0.716667	0.729	0.783333	0.791453	0.85	0.857375	0.925	0.926859
0.625	0.614125	0.675	0.669922	0.725	0.729	0.7875	0.791453	0.85	0.857375	0.925	0.926859
0.6	0.614125	0.675	0.669922	0.733333	0.729	0.8	0.791453	0.85	0.857375	0.925	0.926859
0.608333	0.614125	0.672917	0.669922	0.725	0.729	0.795833	0.791453	0.85	0.857375	0.925	0.926859
0.633333	0.614125	0.675	0.669922	0.7	0.729	0.783333	0.791453	0.85	0.857375	0.925	0.926859
0.616667	0.614125	0.675	0.669922	0.716667	0.729	0.791667	0.791453	0.85	0.857375	0.925	0.926859
0.6	0.614125	0.675	0.669922	0.7	0.729	0.8	0.791453	0.85	0.857375	0.925	0.926859
0.608333	0.614125	0.670833	0.669922	0.733333	0.729	0.7875	0.791453	0.858333	0.857375	0.925	0.926859
0.616667	0.614125	0.66875	0.669922	0.733333	0.729	0.791667	0.791453	0.858333	0.857375	0.925	0.926859
0.616667	0.614125	0.670833	0.669922	0.75	0.729	0.791667	0.791453	0.866667	0.857375	0.925	0.926859
0.608333	0.614125	0.675	0.669922	0.733333	0.729	0.791667	0.791453	0.858333	0.857375	0.925	0.926859
0.633333	0.614125	0.675	0.669922	0.733333	0.729	0.783333	0.791453	0.866667	0.857375	0.925	0.926859
0.616667	0.614125	0.672917	0.669922	0.733333	0.729	0.7875	0.791453	0.858333	0.857375	0.925	0.926859
0.616667	0.614125	0.675	0.669922	0.725	0.729	0.791667	0.791453	0.858333	0.857375	0.925	0.926859
0.616667	0.614125	0.675	0.669922	0.733333	0.729	0.791667	0.791453	0.866667	0.857375	0.925	0.926859

C.2. Effective interaction coefficients of the Co-Al system

All the ECIs including configurational, lattice vibrational and magnetic excitation effects in the bcc, fcc and hcp Co-Al system at different temperatures are listed in Tables C2-C10, which were used as input for the MC simulations to obtain the thermodynamic information of each phase in the Co-Al phase diagram.

Table C2: ECIs for bcc lattice in the Co-Al system at 0 K

Cluster	labels	Coordinates	Distance diameter (Å)	Multiplicity	ECI (eV/atom)
empty	1			1	-0.282783
point	1	1, 1, 1		1	-0.025558
pair	1	1, 1, 1 1, 1, 0	2.756072	4	0.101317
	2	1, 1, 1 1, 0, 0	3.182437	3	-0.009005
	3	1, 1, 1 0, 0, -1	4.500646	6	0.002223
	4	1, 1, 1 -1, -1, 0	5.277475	12	-0.002635
	5	1, 1, 1 -1, -1, -1	5.512143	4	0.001909
	6	1, 1, 1 1, -1, -1	6.364875	3	0.003581
	7	1, 1, 1 -1, -1, -2	6.935962	12	-0.002248
	8	1, 1, 1 0, -1, -2	7.116146	12	-0.002089
	9	1, 1, 1 2, 2, -1	7.795348	12	-0.001598
triplet	1	1, 1, 1 0, 0, 0 1, 0, 0	3.182437	12	0.004658

	2	1, 1, 1 0, 0, 0 0, 0, -1	4.500646	12	-0.007664
	3	1, 1, 1 1, 0, 0 0, 0, -1	4.500646	12	0.000541
	4	1, 1, 1 0, -1, 0 0, 0, -1	4.500646	8	0.001310
	5	1, 1, 1 0, 0, 0 -1, -1, 0	5.277475	24	-0.000892
	6	1, 1, 1 1, 0, 1 -1, -1, 0	5.277475	48	0.000708
	7	1, 1, 1 1, 0, 0 -1, -1, 0	5.277475	24	0.001315
	8	1, 1, 1 0, 0, -1 -1, -1, 0	5.277475	12	0.001135
	9	1, 1, 1 1, 0, 2 -1, -1, 0	5.277475	24	0.000662
	10	1, 1, 1 0, 0, 0 -1, -1, -1	5.512143	4	-0.010557
	11	1, 1, 1 1, 1, 0 -1, -1, -1	5.512143	24	0.001288
	12	1, 1, 1 1, 0, 0	5.512143	24	0.001317

		-1, -1, -1			
	13	1, 1, 1 0, -1, 1 -1, -1, -1	5.512143	24	-0.000206
	14	1, 1, 1 0, 0, 0 1, -1, -1	6.364875	24	-0.000724
	15	1, 1, 1 1, 0, 0 1, -1, -1	6.364875	3	-0.005196
	16	1, 1, 1 0, 0, -1 1, -1, -1	6.364875	12	-0.000739
	17	1, 1, 1 -1, -1, -1 1, -1, -1	6.364875	12	-0.000510
quadruplet	1	1, 1, 1 1, 1, 0 0, 0, 0 1, 0, 0	3.182437	6	-0.001964

Table C3: ECIs for fcc lattice in the Co-Al system at 0 K

Cluster	labels	Coordinates	Distance diameter (Å)	Multiplicity	ECI (eV/atom)
empty	1			1	-0.238514
point	1	1, 1, 1		1	0.045221
pair	1	1, 1, 1 2, 1, 0	2.489760	6	0.070771
	2	1, 1, 1	3.521052	3	-0.015545

		2, 0, 0			
	3	1, 1, 1 2, 1, -1	4.312390	12	0.005996
	4	1, 1, 1 1, 1, -1	4.979519	6	0.002602
	5	1, 1, 1 2, 0, -1	5.567272	12	-0.001928
	6	1, 1, 1 2, 2, -2	6.098641	4	-0.007292
	7	1, 1, 1 2, 1, -2	6.587285	24	-0.003197
	8	1, 1, 1 3, -1, -1	7.042104	3	-0.002662
	9	1, 1, 1 3, 3, -2	7.469279	12	-0.003104
triplet	1	1, 1, 1 2, 1, 0 1, 1, 0	2.489760	8	0.004582
	2	1, 1, 1 1, 1, 0 2, 0, 0	3.521052	12	-0.000836
	3	1, 1, 1 1, 1, 0	4.312390	24	-0.002703

		2, 1, -1			
quadruplet	1	1, 1, 1 1, 2, 0 2, 1, 0 1, 1, 0	2.489760	2	0.005504
	2	1, 1, 1 2, 1, 0 1, 1, 0 2, 0, 0	3.521052	6	0.000321
	3	1, 1, 1 2, 0, 1 1, 1, 0 2, 0, 0	3.521052	3	-0.010883
	4	1, 1, 1 2, 1, 0 1, 1, 0 2, 1, -1	4.312390	12	-0.006074
	5	1, 1, 1 1, 2, 0 1, 1, 0 2, 1, -1	4.312390	48	-0.001891
	6	1, 1, 1 1, 0, 1	4.312390	24	-0.002746

		1, 1, 0 2, 1, -1			
	7	1, 1, 1 2, 0, 1 1, 1, 0 2, 1, -1	4.312390	48	0.001420
	8	1, 1, 1 1, 0, 1 1, 2, 0 2, 1, -1	4.312390	48	0.000531
	9	1, 1, 1 2, 0, 1 1, 0, 1 2, 1, -1	4.312390	8	-0.001694
	10	1, 1, 1 1, 2, 0 2, 0, 0 2, 1, -1	4.312390	6	0.000865
	11	1, 1, 1 1, 1, 0 0, 2, 0 2, 1, -1	4.312390	24	0.002520
	12	1, 1, 1	4.312390	24	0.000966

		1, 2, 0 0, 2, 0 2, 1, -1			
	13	1, 1, 1 1, 0, 1 0, 2, 0 2, 1, -1	4.312390	48	-0.001664
	14	1, 1, 1 2, 2, 0 1, 2, -1 2, 1, -1	4.312390	12	-0.001819
	15	1, 1, 1 0, 2, 0 1, 0, 0 2, 1, -1	4.312390	6	0.001977
	16	1, 1, 1 1, 1, 0 0, 1, 0 2, 1, -1	4.312390	8	0.001240
	17	1, 1, 1 2, 1, 0 1, 1, 0 1, 1, -1	4.979519	48	-0.000557

	18	1, 1, 1 1, 2, 0 2, 1, 0 1, 1, -1	4.979519	24	-0.001743
	19	1, 1, 1 1, 0, 1 2, 1, 0 1, 1, -1	4.979519	24	0.001116
	20	1, 1, 1 0, 1, 1 2, 1, 0 1, 1, -1	4.979519	24	-0.001059
	21	1, 1, 1 1, 1, 0 2, 0, 0 1, 1, -1	4.979519	12	0.000679
	22	1, 1, 1 2, 1, 0 2, 0, 0 1, 1, -1	4.979519	48	0.000538
	23	1, 1, 1 1, 2, 0 2, 0, 0	4.979519	48	-0.000766

		1, 1, -1			
	24	1, 1, 1 0, 2, 0 2, 0, 0 1, 1, -1	4.979519	3	0.006829
	25	1, 1, 1 2, 1, 0 2, 1, -1 1, 1, -1	4.979519	24	0.002608
	26	1, 1, 1 1, 2, 0 2, 1, -1 1, 1, -1	4.979519	24	-0.001290
	27	1, 1, 1 1, 0, 1 2, 1, -1 1, 1, -1	4.979519	24	0.001256
	28	1, 1, 1 0, 1, 1 2, 1, -1 1, 1, -1	4.979519	12	-0.001052
	29	1, 1, 1 2, 2, -1	4.979519	48	0.000600

		2, 1, -1 1, 1, -1			
	30	1, 1, 1 1, 1, 0 2, 2, -1 1, 1, -1	4.979519	12	0.000382
	31	1, 1, 1 2, 0, 0 2, 2, -1 1, 1, -1	4.979519	24	0.000262
	32	1, 1, 1 1, 1, 0 3, 1, -1 1, 1, -1	4.979519	24	0.000438
	33	1, 1, 1 1, 2, 0 3, 1, -1 1, 1, -1	4.979519	24	0.000446
	34	1, 1, 1 2, 0, 0 3, 1, -1 1, 1, -1	4.979519	8	-0.001104
	35	1, 1, 1	4.979519	2	-0.000298

		1, 3, -1 3, 1, -1 1, 1, -1			
	36	1, 1, 1 2, 1, 0 1, 1, 0 2, 0, -1	5.567272	48	0.001696
	37	1, 1, 1 1, 2, 0 1, 1, 0 2, 0, -1	5.567272	24	-0.000457
	38	1, 1, 1 2, 0, 1 1, 1, 0 2, 0, -1	5.567272	24	-0.001352
	39	1, 1, 1 1, 2, 0 2, 1, 0 2, 0, -1	5.567272	24	-0.000492
	40	1, 1, 1 2, 0, 1 2, 1, 0 2, 0, -1	5.567272	24	0.001271

	41	1, 1, 1 2, 0, 1 2, 1, 0 2, 0, -1	5.567272	48	-0.000226
	42	1, 1, 1 0, 1, 1 2, 1, 0 2, 0, -1	5.567272	48	0.000262
	43	1, 1, 1 2, 0, 1 1, 2, 0 2, 0, -1	5.567272	48	0.000019
	44	1, 1, 1 0, 1, 1 1, 2, 0 2, 0, -1	5.567272	24	-0.001209
	45	1, 1, 1 1, 1, 0 2, 0, 0 2, 0, -1	5.567272	12	-0.000676
	46	1, 1, 1 2, 1, 0 2, 0, 0	5.567272	48	0.000412

		2, 0, -1			
	47	1, 1, 1 1, 2, 0 2, 0, 0 2, 0, -1	5.567272	48	-0.000833
	48	1, 1, 1 2, 0, 1 2, 0, 0 2, 0, -1	5.567272	24	0.000041
	49	1, 1, 1 0, 2, 0 2, 0, 0 2, 0, -1	5.567272	24	0.000818
	50	1, 1, 1 1, 1, 0 0, 2, 0 2, 0, -1	5.567272	12	-0.000997
	51	1, 1, 1 2, 1, 0 0, 2, 0 2, 0, -1	5.567272	48	0.000386
	52	1, 1, 1 2, 0, 0	5.567272	24	0.000790

		0, 2, 0 2, 0, -1			

Table C4: ECIs for hcp lattice in the Co-Al system at 0 K

Cluster	labels	Coordinates	Distance (Å)	Multiplicity	ECI (eV/atom)
empty	1			1	-0.501017
point	1	0.333333, 0.666667, 0.25		2	0.082482
pair	1	0.333333, 0.666667, 0.25 0.666667, 1.333333, 0.75	2.480238	6	0.061135
	2	0.666667, 0.333333, 0.75 -0.333333, 0.333333, 0.75	2.500784	6	0.068470
	3	0.666667, 0.333333, 0.75 -0.666667, -0.333333, 0.25	3.522144	6	-0.018530
	4	0.666667, 0.333333, 0.75 0.666667, 0.333333, 1.75	4.033331	2	0.015087
	5	0.666667, 0.333333, 0.75 -0.666667, -1.333333, 1.25	4.319655	12	0.006492
	6	0.666667, 0.333333, 0.75 -1.333333, -0.666667, 0.75	4.331484	6	0.012884
	7	0.666667, 0.333333, 0.75 -0.333333, 0.333333, 1.75	4.745701	12	-0.002078
	8	0.666667, 0.333333, 0.75 2.666667, 0.333333, 0.75	5.001567	6	0.002415
	9	0.666667, 0.333333, 0.75 1.333333, -1.333333, 1.25	5.582764	12	-0.005499

	10	0.666667, 0.333333, 0.75 -1.333333, -0.666667, -0.25	5.918574	12	-0.006837
	11	0.333333, 0.666667, 0.25 1.666667, 3.333333, -0.25	6.117285	6	0.001080
	12	0.333333, 0.666667, 0.25 0.666667, 1.333333, -1.25	6.219895	6	-0.008827
	13	0.666667, 0.333333, 0.75 2.666667, 0.333333, 1.75	6.425219	12	-0.002729
	14	0.666667, 0.333333, 0.75 0.333333, -2.333333, 0.25	6.608713	12	-0.000381
	15	0.666667, 0.333333, 0.75 3.666667, 1.333333, 0.75	6.616452	12	-0.005605
triplet	1	0.666667, 0.333333, 0.75 0. 333333, 0.666667, 0.25 -0.333333, 0. 333333, 0.75	2.500784	12	0.001185
	2	0.666667, 0.333333, 0.75 -0. 333333, -0.666667, 0.75 -0.333333, 0. 333333, 0.75	2.500784	2	0.045942
	3	0.666667, 0.333333, 0.75 0.666667, 1. 333333, 0.75 -0.333333, 0. 333333, 0.75	2.500784	2	-0.047062
	4	0.666667, 0.333333, 0.75 0.333333, -0. 333333, 0.25 -0.666667, -0.333333, 0.25	3.522144	24	-0.003273

	5	0.666667, 0.333333, 0.75 0.333333, -0. 333333, 1.25 0.666667, 0.333333, 1.75	4.033331	6	-0.004713
	6	0.666667, 0.333333, 0.75 1.333333, -0. 333333, 1.25 0.666667, 0.333333, 1.75	4.033331	6	-0.002108
	7	0.666667, 0.333333, 0.75 0.333333, -0. 333333, 1.25 -0.666667, -1.333333, 1.25	4.319655	24	-0.002968
	8	0.666667, 0.333333, 0.75 -0.333333, 0. 333333, 0.75 -0.666667, -1.333333, 1.25	4.319655	12	0.004809
	9	0.666667, 0.333333, 0.75 0.666667, -0.666667, 0.75 -0.666667, -1.333333, 1.25	4.319655	24	0.000914
	10	0.666667, 0.333333, 0.75 0.666667, 0.333333, 1.75 -0.666667, -1.333333, 1.25	4.319655	12	-0.000530
	11	0.666667, 0.333333, 0.75 0.333333, -0.333333, 0.25 -1.333333, -0.666667, 0.75	4.331484	24	-0.002423
quadruplet	1	0.666667, 0.333333, 0.75 0.333333, 0.666667, 0.25 0.666667, 1.333333, 0.75	2.500784	4	0.005858

	-0.333333, 0.333333, 0.75			
2	0.666667, 0.333333, 0.75	3.522144	12	-0.000074
	0.333333, 0.666667, 0.25			
	0.333333, -0.333333, 0.25			
	-0.66667, -0.333333, 0.25			
3	0.666667, 0.333333, 0.75	3.522144	6	-0.006263
	0.333333, -0.333333, 0.25			
	-0.333333, 0.333333, 0.75			
	-0.666667, -0.333333, 0.25			
4	0.666667, 0.333333, 0.75	3.522144	12	0.007146
	0.333333, 0.666667, 0.25			
	-0.333333, 0.333333, 0.75			
	-0.666667, -0.333333, 0.25			
5	0.666667, 0.333333, 0.75	4.033331	6	-0.003323
	1.333333, 0.666667, 0.25			
	0.333333, -0.333333, 1.25			
	0.666667, 0.333333, 1.75			
6	0.666667, 0.333333, 0.75	4.033331	12	-0.003015
	0.333333, -0.333333, 1.25			
	1.333333, -0.333333, 0.75			
	0.666667, 0.333333, 1.75			
7	0.666667, 0.333333, 0.75	4.319655	24	-0.000981
	0.333333, -0.333333, 1.25			
	-0.333333, 0.333333, 0.75			

	-0.666667, -1.333333, 1.25			
8	0.666667, 0.333333, 0.75 -0.333333, -0.666667, 0.75 -0.333333, 0.333333, 0.75 -0.666667, -1.333333, 1.25	4.319655	12	-0.003227
9	0.666667, 0.333333, 0.75 0.333333, -0.333333, 1.25 -0.333333, -0.666667, 0.75 -0.666667, -1.333333, 1.25	4.319655	12	-0.009770
10	0.666667, 0.333333, 0.75 0.666667, -0.666667, 0.75 -0.333333, -0.666667, 0.75 -0.666667, -1.333333, 1.25	4.319655	24	0.000948
11	0.666667, 0.333333, 0.75 0.333333, -0.333333, 1.25 0.666667, -0.666667, 0.75 -0.666667, -1.333333, 1.25	4.319655	24	-0.000290
12	0.666667, 0.333333, 0.75 0.666667, -0.666667, 0.75 -0.666667, -0.333333, 1.25 -0.666667, -1.333333, 1.25	4.319655	6	0.001639
13	0.666667, 0.333333, 0.75	4.319655	12	0.002187

	0.333333, -0.333333, 1.25			
	-0.666667, 0.333333, 1.75			
	-0.666667, -1.333333, 1.25			
14	0.666667, 0.333333, 0.75	4.319655	12	0.002313
	-0.666667, -0.333333, 1.25			
	0.666667, 0.333333, 1.75			
	-0.666667, -1.333333, 1.25			
15	0.666667, 0.333333, 0.75	4.319655	6	-0.003150
	-0.333333, 0.333333, 0.75			
	-0.666667, -1.333333, 0.25			
	-0.666667, -1.333333, 1.25			
16	0.666667, 0.333333, 0.75	4.331484	12	0.000261
	0.333333, -0.333333, 1.25			
	0.333333, -0.333333, 0.25			
	-1.333333, -0.666667, 0.75			
17	0.666667, 0.333333, 0.75	4.331484	12	0.000628
	0.333333, 0.666667, 0.25			
	0.333333, -0.333333, 0.25			
	-1.333333, -0.666667, 0.75			
18	0.666667, 0.333333, 0.75	4.331484	24	0.001644
	0.333333, -0.333333, 0.25			
	-0.333333, 0.333333, 0.75			

		-1.333333, -0.666667, 0.75			
	19	0.666667, 0.333333, 0.75 0.333333, 0.666667, 0.25 -0.333333, 0.333333, 0.75 -1.333333, -0.666667, 0.75	4.331484	24	-0.000051
	20	0.666667, 0.333333, 0.75 -0.333333, -0.666667, 0.75 -0.333333, 0.333333, 0.75 -1.333333, -0.666667, 0.75	4.331484	6	-0.005959
	21	0.666667, 0.333333, 0.75 0.333333, -0.333333, 0.25 -0.666667, -0.333333, 0.25 -1.333333, -0.666667, 0.75	4.331484	24	0.000950
	22	0.666667, 0.333333, 0.75 -0.333333, 0.333333, 0.75 -0.66667, -0.333333, 0.25 -1.333333, -0.66667, 0.75	4.331484	24	0.000959
	23	0.666667, 0.333333, 0.75 -0.666667, -0.333333, 1.25 -0.666667, -0.333333, 0.25 -1.333333, -0.666667, 0.75	4.331484	6	-0.001796
	24	0.666667, 0.333333, 0.75 0.333333, -0.333333, 1.25	4.331484	24	-0.000130

	-0.666667, 1.333333, 1.25	
	-1.333333, -0.666667, 0.75	

Table C5: ECIs of bcc Co-Al including vibrational entropy at finite temperatures.

Cluster	labels	ECI (eV/atom)			
		500 K	1000 K	1500 K	2000 K
empty	1	-0.03859	-0.25828	-0.53675	-0.89879
point	1	-0.02669	-0.05237	-0.07774	-0.10634
pair	1	-0.003515	-0.00692	-0.0102775	-0.0140625
	2	0.000656667	0.00131667	0.00196	0.00268667
	3	-0.00166	-0.00319833	-0.00473167	-0.00646333
	4	-0.00073833	-0.00140167	-0.0020675	-0.00282083
	5	-0.0010975	-0.002155	-0.0032	-0.0043775
	6	-0.00135333	-0.00260667	-0.00385667	-0.00526667
	7	-0.0003225	-0.00064333	-0.00095833	-0.00131333
	8	0	7.50E-06	1.25E-05	1.75E-05
	9	-8.25E-05	-0.00017167	-0.0002575	-0.00035333
triplet	1	-6.25E-05	-0.00012667	-0.00018833	-0.00025833
	2	0.000648333	0.0012025	0.001765	0.00240417
	3	7.75E-05	0.000149167	0.00022	0.0003
	4	4.00E-05	8.25E-05	0.00012375	0.00016875
	5	0.00021125	0.000400417	0.000590417	0.000805417
	6	0.000108125	0.0002075	0.000306667	0.00041875
	7	-0.00014083	-0.00026125	-0.00038375	-0.0005225
	8	0.0002175	0.000448333	0.000671667	0.000921667
	9	-0.00043042	-0.00081667	-0.00120417	-0.00164333
	10	0.0001025	0.0002675	0.0004175	0.00058
	11	-0.00011958	-0.00023667	-0.00035208	-0.00048167

	12	0.000203333	0.000403333	0.000600417	0.000821667
	13	0.000230417	0.00044	0.00065	0.0008875
	14	0.000240833	0.000469583	0.00069625	0.000952083
	15	0.000143333	0.000173333	0.00023	0.000296667
	16	-0.00061333	-0.0011775	-0.00174083	-0.0023775
	17	-1.08E-05	-7.50E-06	-7.50E-06	-8.33E-06
quadruplet	1	3.67E-05	6.00E-05	8.50E-05	0.000115

Table C6: ECIs of fcc Co-Al including vibrational entropy at finite temperatures.

Cluster	labels	ECI (eV/atom)			
		500 K	1000 K	1500 K	2000 K
empty	1	-0.06137	-0.29321	-0.6001	-0.95835
point	1	-0.00129	-0.00202	-0.00292	-0.00387
pair	1	0.00028	0.000346667	0.000433333	0.000533333
	2	-0.00322	-0.00569333	-0.00835667	-0.01111
	3	-0.00015583	-0.00031167	-0.00047167	-0.000635
	4	-0.000265	-0.00052333	-0.00079167	-0.001065
	5	8.25E-05	0.000165833	0.000253333	0.0003425
	6	0.00048	0.00083	0.0012075	0.0015975
	7	0.00021125	0.000233333	0.000277083	0.000331667
	8	-0.00092667	-0.00143	-0.002	-0.00260333
	9	-0.00063583	-0.00081583	-0.00105417	-0.0013225
triplet	1	0.00012	3.75E-05	-1.75E-05	-6.25E-05
	2	3.75E-05	9.58E-05	1.56E-04	0.000215
	3	-3.25E-05	-9.58E-06	7.50E-06	2.17E-05
quadruplet	1	-0.001075	-0.001915	-0.00282	-0.003745
	2	-0.00048083	-0.000925	-0.00139083	-0.0018675
	3	0.000903333	0.00183667	0.00280667	0.00378667
	4	0.000118333	0.000249167	0.0003825	0.000516667

	5	5.21E-06	6.46E-06	8.13E-06	1.00E-05
	6	0.000122917	0.000213333	0.00031125	0.0004125
	7	0.000112292	0.000239167	0.00037	0.000502292
	8	-4.44E-05	-1.44E-05	8.54E-06	2.75E-05
	9	-0.0002725	-0.00059	-0.000915	-0.00124375
	10	-0.00038333	-0.00067833	-0.00099833	-0.00132833
	11	3.42E-05	4.21E-05	5.25E-05	6.46E-05
	12	0.00013625	0.000252083	0.000375	0.000501667
	13	-0.00015458	-0.00028958	-0.00043208	-0.00057792
	14	0.000420833	0.0007225	0.0010525	0.00139417
	15	-0.00038833	-0.00076667	-0.00116167	-0.001565
	16	0.00039375	0.0007475	0.00112	0.00150125
	17	0.000332083	0.000657708	0.000998542	0.00134542
	18	-0.00022542	-0.00040333	-0.00059333	-0.00078958
	19	0.00012625	0.00022375	0.000328333	0.00043625
	20	-9.00E-05	-0.00015583	-0.00022667	-0.00030042
	21	-1.75E-05	-2.50E-05	-3.25E-05	-4.08E-05
	22	-0.00034104	-0.00061938	-0.00091708	-0.00122333
	23	6.79E-05	6.79E-05	7.50E-05	8.58E-05
	24	0.00122	0.00225667	0.00335667	0.00449
	25	-0.00014208	-0.00023875	-0.000345	-0.00045583
	26	0.000320417	0.000554167	0.0008075	0.00107042
	27	0.000237917	0.000447083	0.00066875	0.000895833
	28	-0.00028333	-0.00053667	-0.00080417	-0.00107667
	29	-0.00010375	-0.00015458	-0.00021375	-0.00027688
	30	-0.00044083	-0.000785	-0.001155	-0.00153583
	31	0.000149583	0.000260833	0.00038125	0.000505833
	32	-8.33E-05	-3.46E-05	3.33E-06	3.46E-05
	33	1.29E-05	-8.13E-05	-1.68E-04	-0.00025083

	34	-3.00E-05	-4.88E-05	-6.88E-05	-8.88E-05
	35	3.00E-05	-0.00021	-4.40E-04	-0.000655
	36	0.0001375	0.000247292	0.000364167	0.000484583
	37	0.0001225	0.00027125	0.00042375	0.000576667
	38	-7.33E-05	-9.42E-05	-1.20E-04	-0.00014792
	39	5.00E-05	7.58E-05	1.06E-04	0.0001375
	40	-0.0002225	-0.00042292	-0.00063625	-0.00085458
	41	4.42E-05	1.25E-06	-3.40E-05	-6.48E-05
	42	3.02E-05	4.02E-05	5.29E-05	6.71E-05
	43	-0.00021417	-0.00038667	-0.00057104	-0.00076083
	44	3.33E-06	8.33E-05	1.59E-04	0.000232083
	45	0.000228333	0.000349167	0.000486667	0.0006325
	46	5.06E-05	6.29E-05	8.02E-05	0.0001
	47	-1.77E-05	-3.52E-05	-5.29E-05	-7.10E-05
	48	0.000117083	0.000143333	0.000180417	0.000223333
	49	4.00E-05	0.00013	2.17E-04	0.000302083
	50	6.67E-05	8.58E-05	1.11E-04	0.000139167
	51	1.69E-05	1.85E-05	2.13E-05	2.48E-05
	52	-8.00E-05	-0.00010833	-1.43E-04	-0.00018125

Table C7: ECIs of hcp Co-Al including vibrational entropy at finite temperatures.

Cluster	labels	ECI (eV/atom)			
		500 K	1000 K	1500 K	2000 K
empty	1	-0.11718	-0.59034	-1.19268	-1.92432
point	1	-0.00462	-0.00837	-0.01229	-0.01649
pair	1	0.000296667	0.00061	0.000916667	0.00124
	2	0.000186667	0.00037	0.000556667	0.00075
	3	-0.00022667	-0.00037667	-0.00054333	-0.00072333
	4	0.00013	0.00026	0.00039	0.00053

	5	8.17E-05	0.000165	0.000248333	0.000335
	6	-0.00033333	-0.00064333	-0.00096	-0.00129667
	7	0.000128333	0.000258333	0.000386667	0.000523333
	8	-6.00E-05	-0.00011667	-0.00017333	-0.00023667
	9	-0.00019333	-0.000365	-0.00054167	-0.00072833
	10	-9.67E-05	-0.00016333	-0.00023833	-0.00031667
	11	-0.00010333	-0.00020667	-0.00031	-0.00041667
	12	4.00E-05	9.67E-05	0.000153333	0.00021
	13	-0.0001	-0.00019333	-0.00028667	-0.00038667
	14	-2.67E-05	-4.50E-05	-6.50E-05	-8.83E-05
	15	7.00E-05	0.000146667	0.000221667	0.0003
triplet	1	0.00064	0.00120167	0.00177667	0.00239167
	2	-3.00E-05	-1.00E-05	0	1.00E-05
	3	0.00121	0.00222	0.00326	0.00438
	4	-3.92E-05	-7.75E-05	-0.00011667	-0.00015667
	5	-3.67E-05	-6.00E-05	-8.33E-05	-0.00011
	6	-0.00033667	-0.00067	-0.00100667	-0.00136
	7	-0.0003875	-0.000745	-0.0011075	-0.00149417
	8	0.00058	0.00111	0.00164833	0.00222167
	9	0.000136667	0.000254167	0.000375833	0.000505
	10	6.00E-05	0.000116667	0.000175	0.000236667
	11	0.000123333	0.00024	0.000356667	0.000481667
quadruplet	1	-0.000125	-0.00026	-0.00039	-0.00053
	2	8.33E-06	2.33E-05	3.50E-05	4.83E-05
	3	-0.00064	-0.00124333	-0.00185	-0.0025
	4	1.67E-05	2.83E-05	4.33E-05	5.67E-05
	5	0	1.00E-05	1.67E-05	2.67E-05
	6	0.000191667	0.000353333	0.00052	0.000698333
	7	5.25E-05	9.92E-05	0.0001475	0.000198333

	8	-9.33E-05	-0.00017167	-0.00025333	-0.00034
	9	-0.000345	-0.00067333	-0.00100333	-0.001355
	10	2.50E-05	5.08E-05	7.67E-05	0.000103333
	11	3.25E-05	6.92E-05	0.000105833	0.000143333
	12	0.000476667	0.000926667	0.00138	0.00186333
	13	-4.33E-05	-9.83E-05	-0.00015	-0.00020333
	14	-0.00021667	-0.000405	-0.00059833	-0.000805
	15	-0.00012333	-0.00021667	-0.00032	-0.00042667
	16	0.000105	0.000191667	0.000281667	0.000376667
	17	0.000188333	0.00037	0.000551667	0.000746667
	18	-8.92E-05	-0.00017333	-0.00025833	-0.00034833
	19	3.33E-05	6.50E-05	9.67E-05	0.00013
	20	-0.00023333	-0.00045333	-0.00067333	-0.00091
	21	1.50E-05	3.83E-05	6.00E-05	8.17E-05
	22	0.000185	0.000353333	0.000523333	0.000705833
	23	-2.33E-05	-3.67E-05	-5.33E-05	-7.33E-05
	24	-0.00016917	-0.00034	-0.00051	-0.00069

Table C8: ECIs of bcc Co-Al including vibrational and magnetic entropy at finite temperatures.

Cluster	labels	ECI (eV/atom)			
		500 K	1000 K	1500 K	2000 K
empty	1	-0.00138	-0.01421	-0.03884	-0.07483
point	1	0.00208	0.00168	-0.02088	-0.05018
pair	1	0.0003375	0.0011825	1.50E-05	-0.0020225
	2	0.00025	0.00265	0.00545667	0.00928
	3	7.83E-05	0.00134333	0.00253833	0.00435833
	4	-8.92E-05	-0.00024167	-0.00065417	-0.00120333
	5	-6.50E-05	0.0002	0.0004525	0.0006975
	6	-5.67E-05	-0.00051667	-0.00146667	-0.00264333

	7	-3.33E-05	-0.00013667	-0.00030333	-0.0007225
	8	-2.67E-05	-0.000175	-0.00043	-0.0009075
	9	-1.42E-05	-2.92E-05	-8.42E-05	-0.0002225
triplet	1	1.50E-05	0.000620833	0.000985	0.0015175
	2	7.83E-05	0.000458333	0.000956667	0.00145
	3	-0.00016	-0.00105417	-0.00204	-0.0036125
	4	-3.75E-05	-0.000155	-0.00024875	-0.00040875
	5	3.25E-05	0.000169583	0.000425	0.000746667
	6	-6.52E-05	-0.00019896	-0.00035229	-0.00062167
	7	1.79E-05	0.0001025	0.000370833	0.000738333
	8	5.17E-05	4.67E-05	-1.83E-05	-0.00013417
	9	0.000112917	0.000340833	0.00081375	0.00140583
	10	-3.25E-05	0.0002475	0.0009175	0.002025
	11	1.42E-05	6.29E-05	0.000137917	0.00015625
	12	-5.21E-05	-0.00019417	-0.00029417	-0.00042333
	13	-6.33E-05	-0.00029958	-0.00071958	-0.00135208
	14	-1.42E-05	1.00E-05	5.50E-05	3.88E-05
	15	0.000196667	0.00059	0.000793333	0.00102667
	16	-2.17E-05	-4.50E-05	0.0001475	0.0003475
	17	7.58E-05	0.000218333	0.000450833	0.000749167
quadruplet	1	-0.000105	-0.00078833	-0.00134167	-0.00249667

Table C9: ECIs of fcc Co-Al including vibrational and magnetic entropy at finite temperatures.

Cluster	labels	ECI (eV/atom)			
		500 K	1000 K	1500 K	2000 K
empty	1	-0.00237	-0.01848	-0.0478	-0.09758
point	1	0.00061	0.00994	-0.00227	-0.00177
pair	1	7.00E-05	0.00445333	0.008575	0.0174033
	2	0.00152	0.00324333	0.00738333	0.01121

	3	4.25E-05	0.000170833	0.00138417	0.00263833
	4	0.000726667	0.00217333	0.00350667	0.00471833
	5	-9.33E-05	-0.0012625	-0.00322333	-0.00699083
	6	-0.000155	-0.0005725	-0.0002375	-8.50E-05
	7	-5.00E-06	-4.83E-05	-0.00018333	-0.00053708
	8	-0.00027667	-0.00114333	-0.00310333	-0.00623333
	9	-0.00014	-0.000655	-0.00147	-0.00289417
triplet	1	-0.00017625	-0.00199625	-0.00402625	-0.00949625
	2	9.50E-05	0.000806667	0.00137167	0.00245833
	3	3.96E-05	-2.92E-06	0.000470833	0.0006275
quadruplet	1	-0.000755	-0.003535	-0.007955	-0.013475
	2	9.17E-06	0.000259167	0.00038	5.17E-05
	3	-0.00028	-0.00209667	-0.00281	-0.00319
	4	0.000303333	0.000768333	0.000525	-0.000135
	5	0.000162917	0.000892292	0.00176917	0.00322708
	6	-0.00028958	-0.00085458	-0.00132958	-0.00186792
	7	1.21E-05	-0.00013354	-0.00023896	-0.00056479
	8	-0.00021563	-0.00105729	-0.00269667	-0.00515937
	9	0.00065	0.0030975	0.006235	0.0111313
	10	0.000601667	0.00184333	0.00319333	0.00458667
	11	2.71E-05	-0.0001475	-0.00041333	-0.00077625
	12	-0.00055042	-0.00185042	-0.00347917	-0.00587542
	13	9.31E-05	0.00052875	0.00110854	0.00193938
	14	1.92E-05	0.0003975	0.00116	0.00247417
	15	0.000171667	0.000935	0.00286833	0.00612167
	16	-0.000555	-0.0026725	-0.0060575	-0.0111263
	17	-0.00010958	-0.00050021	-0.00105417	-0.00185229
	18	-5.42E-05	4.17E-06	0.000729583	0.00181042
	19	-1.96E-05	-0.00010667	-0.00046208	-0.00124208

20	4.79E-05	9.33E-05	0.000223333	0.00045125
21	-0.00011583	-0.00067667	-0.00131917	-0.00197417
22	6.15E-05	0.000202708	0.000319167	0.00041625
23	0.000225208	0.000854375	0.00159375	0.00269542
24	-0.00098667	-0.00327	-0.00624	-0.01117
25	0.000191667	0.000545833	0.00139708	0.00258125
26	-0.00039208	-0.00126833	-0.00279333	-0.00483333
27	-0.00026917	-0.00106	-0.00244208	-0.00443917
28	0.0001025	0.000385	0.0009975	0.00172667
29	7.17E-05	0.000237708	0.000567708	0.00101833
30	7.67E-05	-2.50E-05	1.00E-05	0.000296667
31	0.000124167	0.000499167	0.00106708	0.00190375
32	-4.17E-06	-8.88E-05	-3.96E-05	-8.46E-05
33	-4.71E-05	-5.71E-05	-0.00039083	-0.00078458
34	-2.50E-06	0.00010625	-8.00E-05	-0.0002375
35	0.00031	0.00102	0.00312	0.006555
36	0.000272917	0.00106604	0.00254792	0.00470667
37	-6.13E-05	-0.00014417	-0.00021	-0.00013125
38	-0.00037625	-0.00127917	-0.00257417	-0.0044425
39	-0.00011208	-0.00021875	1.83E-05	0.00034375
40	1.46E-05	-0.00011833	-0.00037875	-0.00070208
41	4.81E-05	0.000381458	0.000867292	0.00184979
42	0.000138125	0.000543542	0.000907917	0.00152458
43	-6.73E-05	-0.00029854	-0.00071583	-0.00133437
44	-0.00013458	-0.00026958	-0.00035458	-0.00056042
45	7.00E-05	0.000375833	0.001005	0.00265167
46	-0.00014417	-0.00064333	-0.00147417	-0.00283875
47	-1.98E-05	-0.00013688	-0.0002825	-0.00054313
48	0.0003075	0.00112167	0.00254958	0.00430417

	49	-6.71E-05	-0.00029667	-0.00027333	-0.00024583
	50	0.000379167	0.00131	0.0016275	0.00207583
	51	-1.06E-05	-9.54E-05	-1.67E-05	0.000160833
	52	-4.79E-05	-0.00014042	-0.00045125	-0.00103708

Table C10: ECIs of hcp Co-Al including vibrational and magnetic entropy at finite temperatures.

Cluster	labels	ECI (eV/atom)			
		500 K	1000 K	1500 K	2000 K
empty	1	-0.00306	-0.0318	-0.083	-0.16728
point	1	0.002	0.01455	-0.0088	-0.03501
pair	1	-0.00245	-0.00252333	-0.00598333	-0.0130967
	2	0.000776667	0.00680667	0.0127567	0.0188367
	3	0.00359	0.00320667	0.02132	0.0496067
	4	0.00032	0.00163	0.00309	0.00496
	5	-0.00107	-0.00216667	-0.0109517	-0.02366
	6	6.33E-05	-3.33E-06	-0.00137333	-0.00430333
	7	4.00E-05	-1.67E-06	0.000638333	0.000948333
	8	-0.00014333	-0.00052667	-0.00038	-0.00085333
	9	-0.00017667	-0.00085833	-0.00152167	-0.00250833
	10	1.00E-05	-5.67E-05	9.67E-05	0.000111667
	11	0.000496667	0.00136667	0.00311	0.00655667
	12	0.000126667	0.000206667	0.000353333	0.00100667
	13	-8.33E-05	-0.00033167	-0.00075833	-0.00156667
	14	3.83E-05	0.000208333	0.000836667	0.00106
	15	-5.83E-05	-0.00027833	-0.00066667	-0.00146667
triplet	1	0.00199	0.00303167	0.01117	0.0237317
	2	0.00169	-0.00259	0.00476	0.0193
	3	-0.00402	-0.01293	-0.02372	-0.04002
	4	-0.00170417	-0.00270167	-0.0149217	-0.0350267

	5	0.000116667	-0.00024333	-0.00013333	0.0007
	6	3.33E-05	-5.33E-05	-0.00050667	-0.00111667
	7	0.000925	0.00146167	0.00617083	0.0128375
	8	0.000758333	0.00191667	0.00538333	0.0107683
	9	-0.0004325	-0.00049417	0.00187333	0.005205
	10	-5.00E-06	0.000206667	0.00123	0.00189167
	11	-0.00016833	-0.00071167	-0.00014083	0.0003125
quadruplet	1	-0.00243	-0.003085	-0.02481	-0.056835
	2	0.000698333	8.00E-05	0.00670167	0.0168067
	3	0.00022	0.00117	0.00477667	0.0109467
	4	0.000163333	0.000751667	0.005885	0.0132167
	5	0.00026	0.000636667	0.00240333	0.005
	6	-1.67E-05	0.00018	8.33E-06	-0.00063
	7	-0.00026167	-0.00183333	-0.00417167	-0.00743583
	8	-0.00057667	0.000188333	-0.00080333	-0.00283
	9	-6.33E-05	-0.00012667	-0.00061	-0.001555
	10	0.00052	0.00150917	0.00256417	0.003845
	11	3.33E-06	0.000136667	-0.00031917	-0.000425
	12	-5.00E-05	6.67E-06	-0.00228	-0.00654667
	13	-6.67E-05	-0.00029333	-0.00096333	-0.001625
	14	-5.17E-05	-0.00021833	-0.00038167	-0.00036833
	15	-0.00010333	-0.00055333	-0.00148667	-0.00236667
	16	-3.50E-05	-0.000115	-0.00083	-0.00177833
	17	0.000125	0.000426667	0.000905	0.001665
	18	0.0003825	0.000974167	0.00131833	0.0023525
	19	-0.00037333	-0.00094083	-0.00159167	-0.00297417
	20	1.33E-05	0.00012	-0.00052333	-0.00115667
	21	8.17E-05	0.000324167	0.000271667	0.000770833
	22	1.67E-06	-4.58E-05	0.000606667	0.001445

	23	3.33E-06	0.000213333	0.000996667	0.00227333
	24	-3.83E-05	-6.17E-05	-0.0003375	-0.0011175

C.3. Mixing enthalpies of the Co-Al system including vibrational entropy

The mixing enthalpies, H_{vib}, contribution due to lattice vibrations in Co-Al system were calculated eq. (2.18), which are also compared with H_{vib} fitted using CE, as shown in Figures C1-C3.

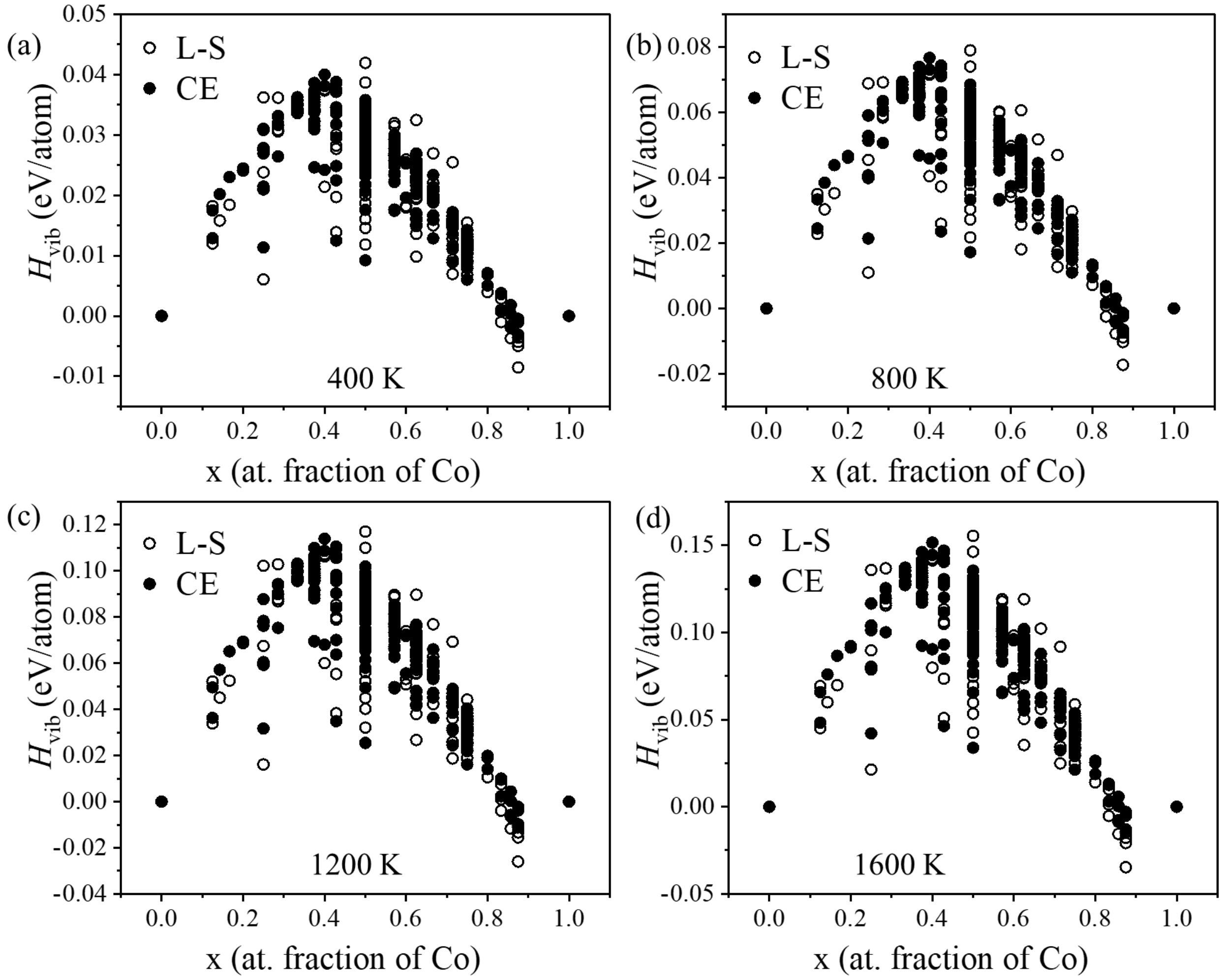

Figure C1: H_{vib} of bcc configurations in the Co-Al system predicted by the CE (solid symbols) and obtained from the L-S relationships (open symbols) at different temperatures. (a) 400 K. (b) 800 K. (c) 1200 K. (d) 1600 K.

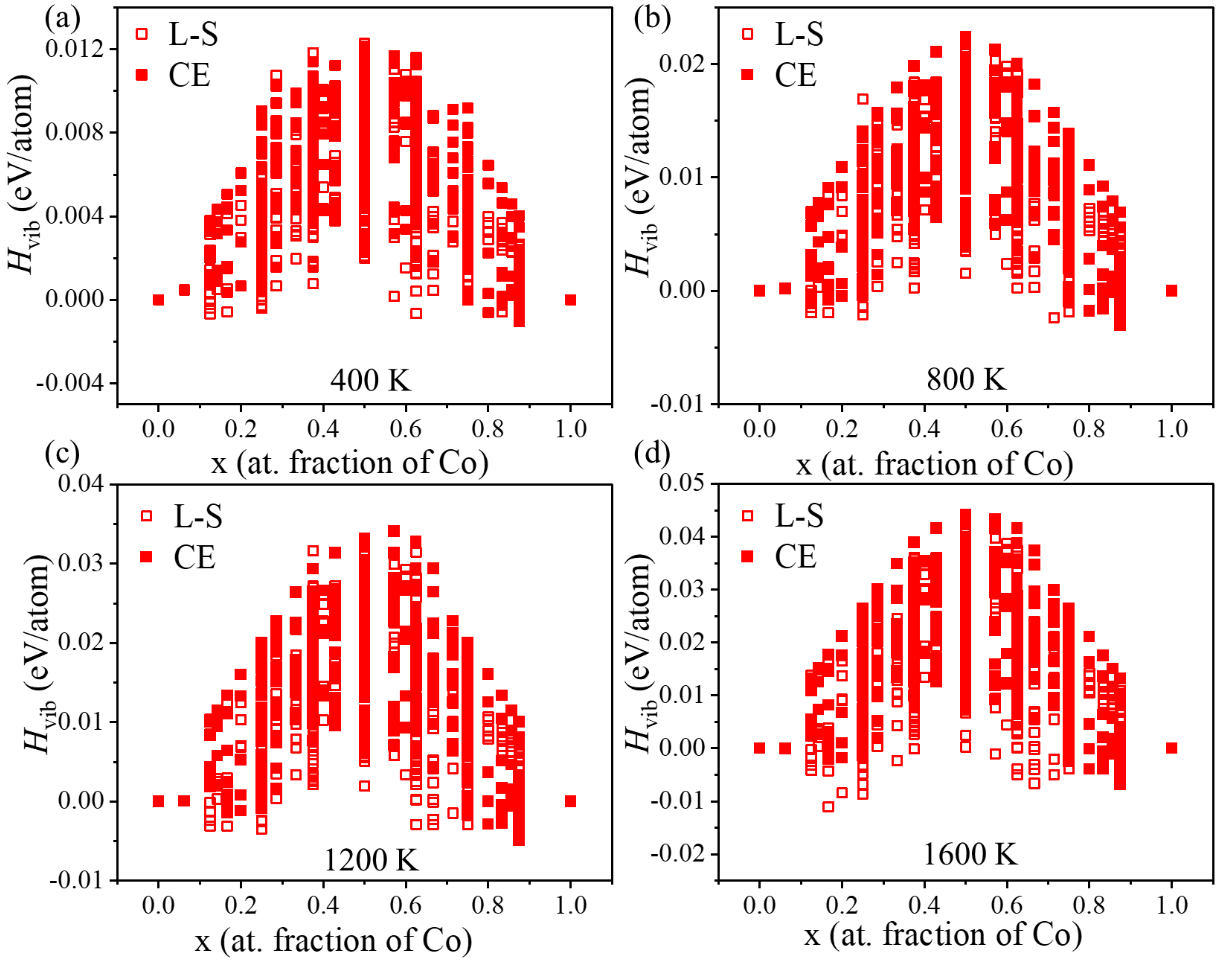

Figure C2: H_{vib} of fcc configurations in the Co-Al system predicted by the CE (solid symbols) and obtained from the L-S relationships (open symbols) at different temperatures. (a) 400 K. (b) 800 K. (c) 1200 K. (d) 1600 K.

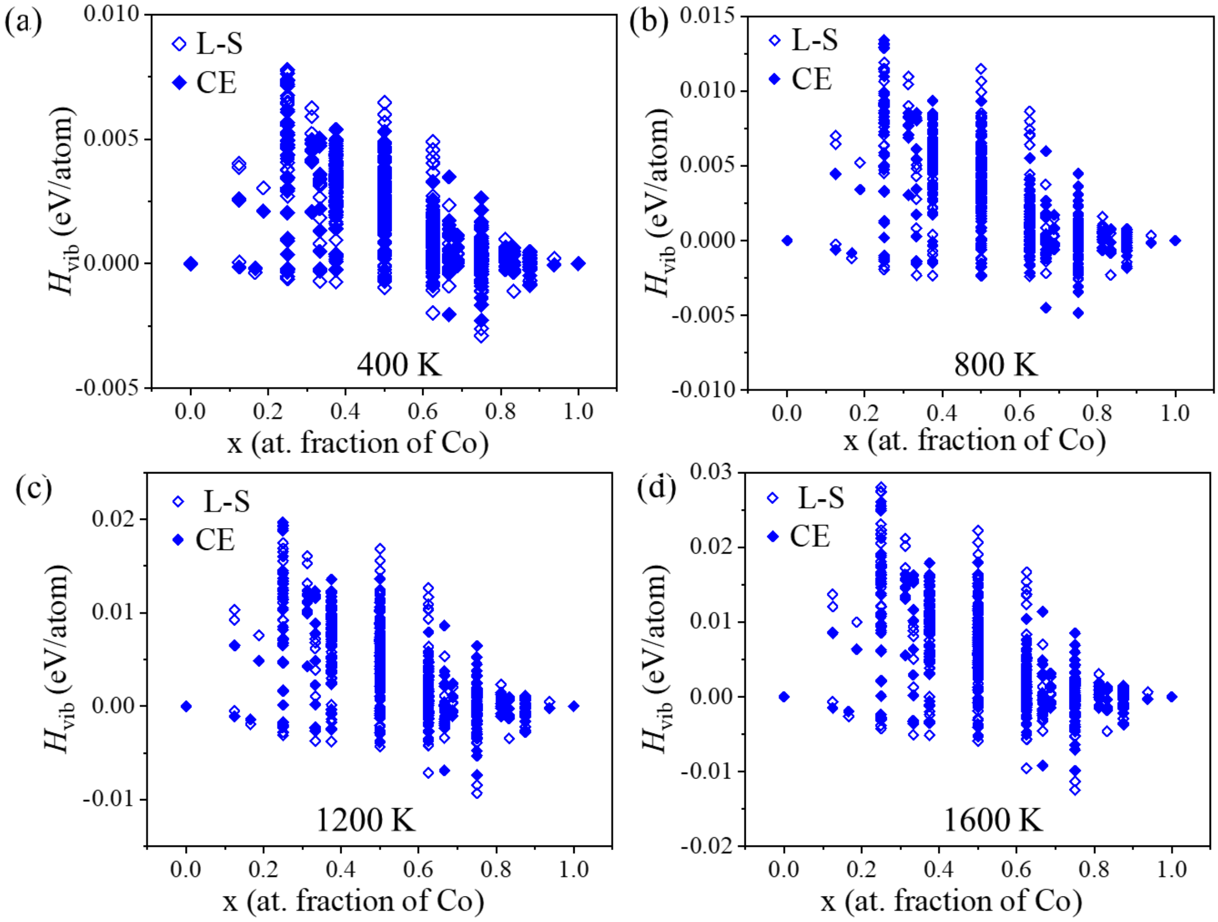

Figure C3: H_{vib} of hcp configurations in the Co-Al system predicted by the CE (solid symbols) and obtained from the L-S relationships (open symbols) at different temperatures. (a) 400 K. (b) 800 K. (c) 1200 K. (d) 1600 K.

C.4. Mixing enthalpies of the Co-Al system including magnetic entropy

The mixing enthalpies, H_{mag}, contribution due to magnetic excitation in Co-Al system were calculated eq. (2.19), which are also compared with H_{mag} fitted using CE, as shown in Figures C4-C6.

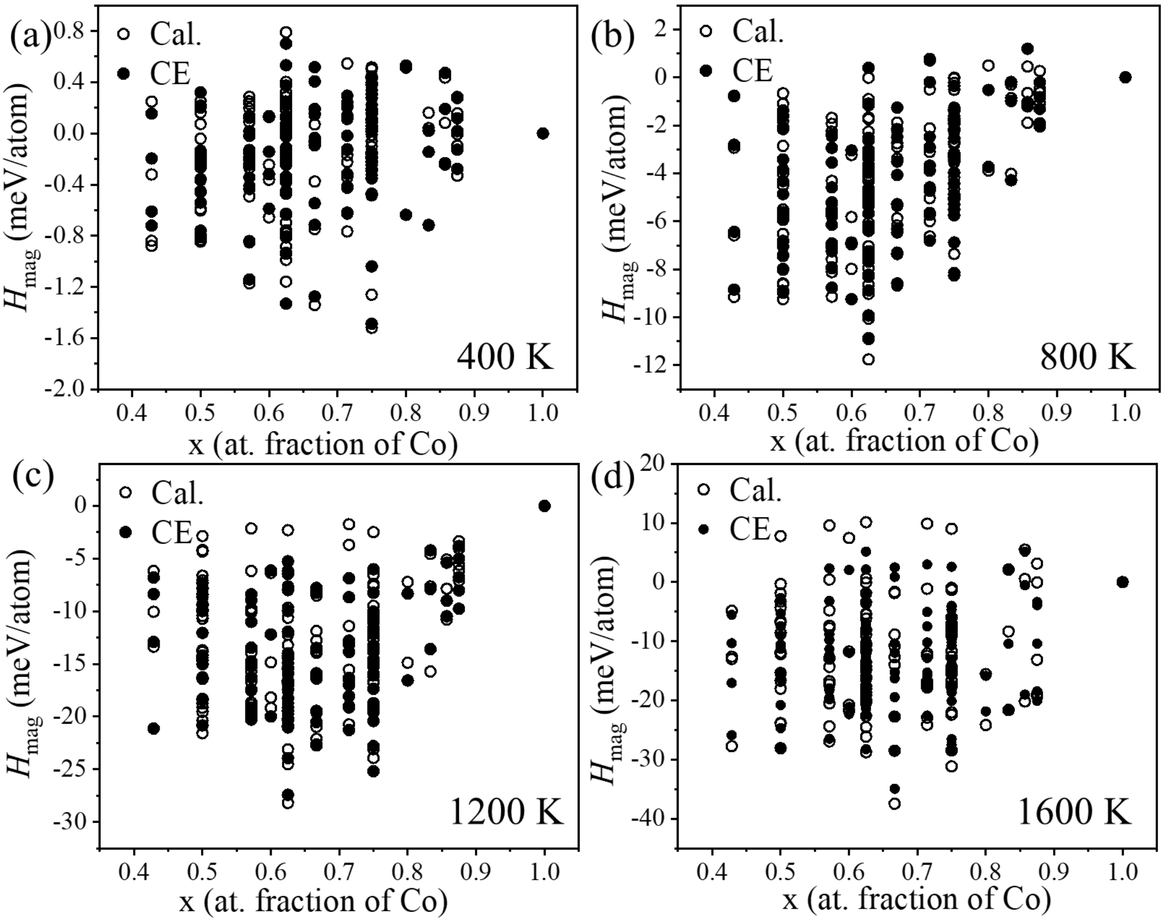

Figure C4: H_{mag} of bcc configurations at different temperatures. (a) 400 K. (b) 800 K. (c) 1200 K. (d) 1600 K. Solid symbols stand for the CE results and open symbols.

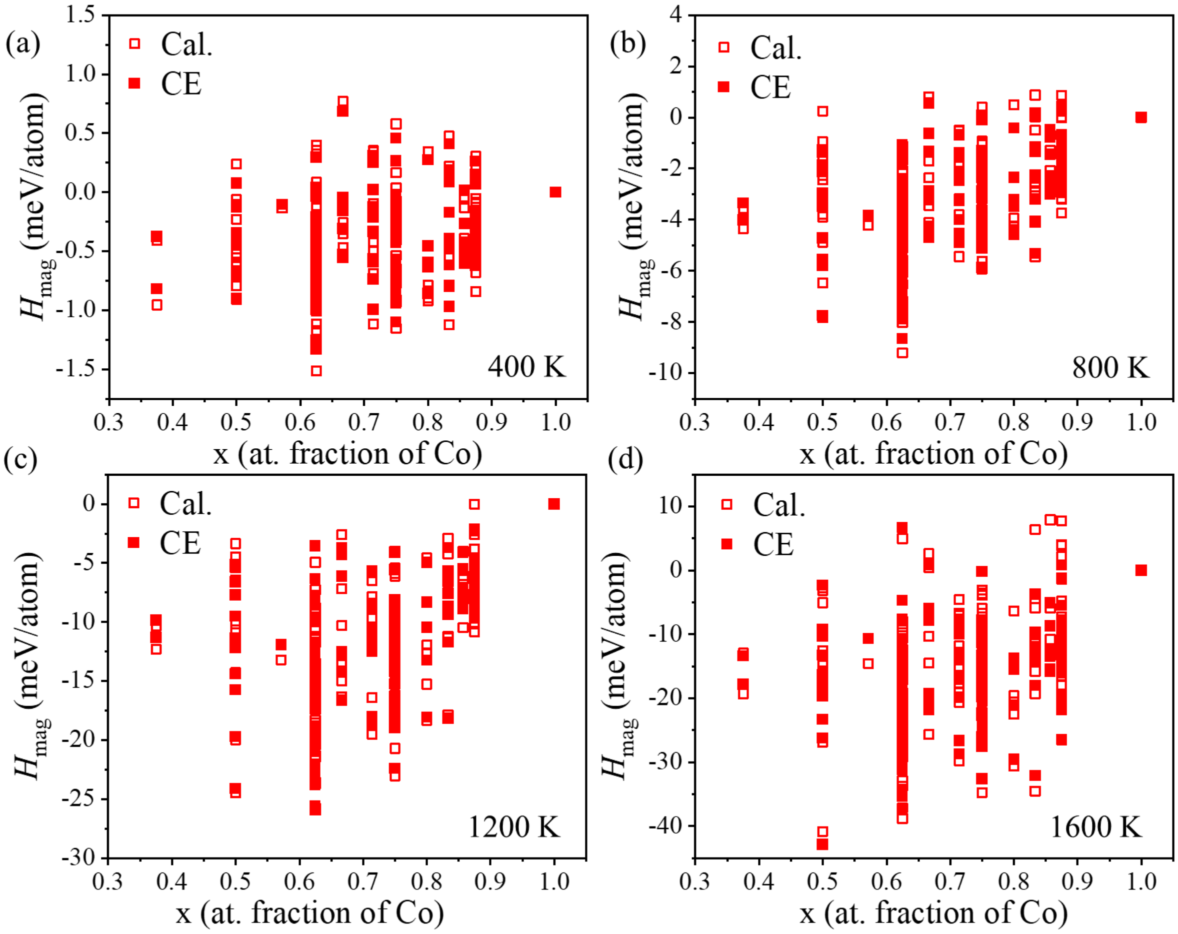

Figure C5**:** H_{mag} of fcc configurations at different temperatures. (a) 400 K. (b) 800 K. (c) 1200 K. (d) 1600 K. Solid symbols stand for the CE results and open symbols.

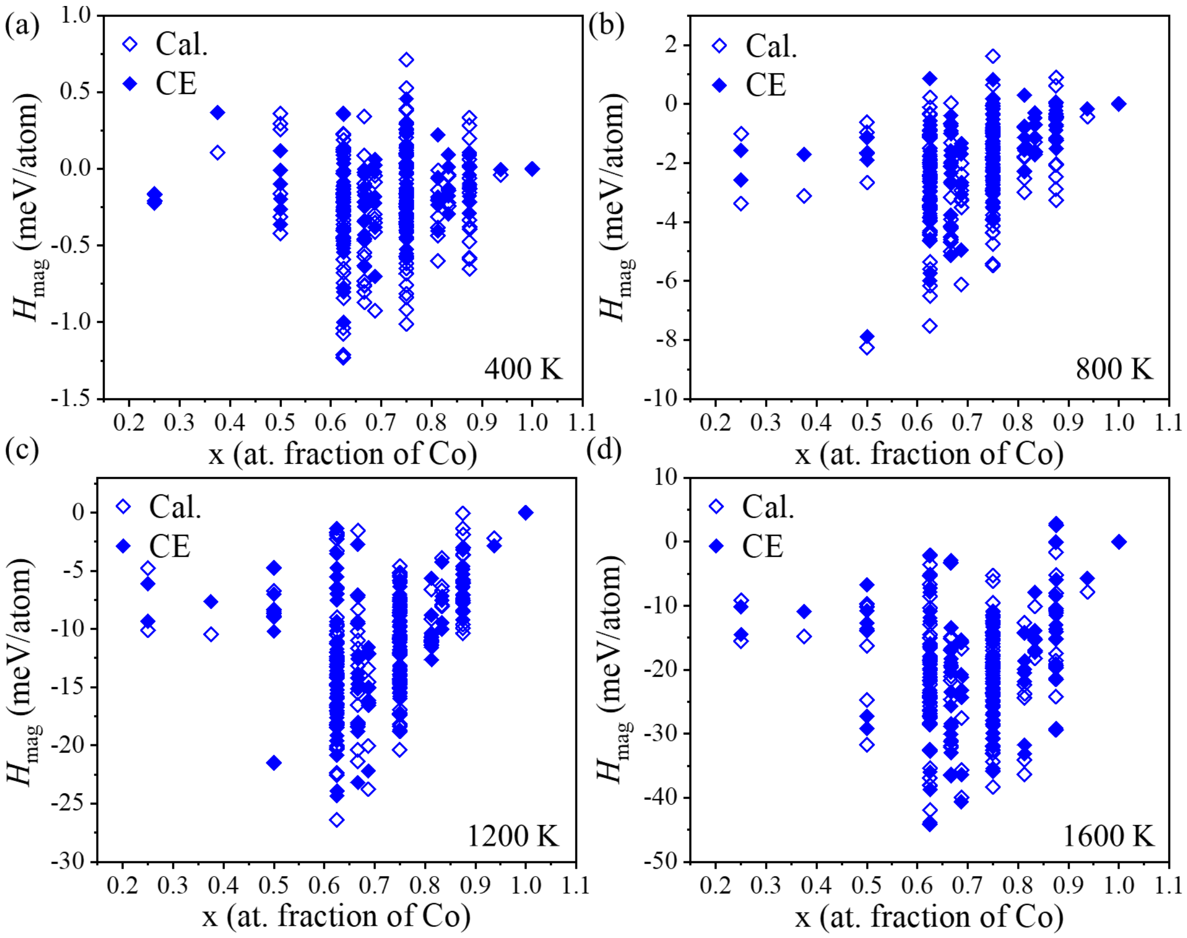

Figure C6**:** H_{mag} of hcp configurations at different temperatures. (a) 400 K. (b) 800 K. (c) 1200 K. (d) 1600 K. Solid symbols stand for the CE results and open symbols.

C.5. Gibbs free energies and phase boundaries in the Co-Al system including configurational and vibrational entropy

The Gibbs free energies and phase boundaries including configurational and vibrational entropy for Co-Al system are shown in Figures C7-C8, which were integrated to obtain the whole Co-Al phase diagram considering configurational and vibrational entropic effect.

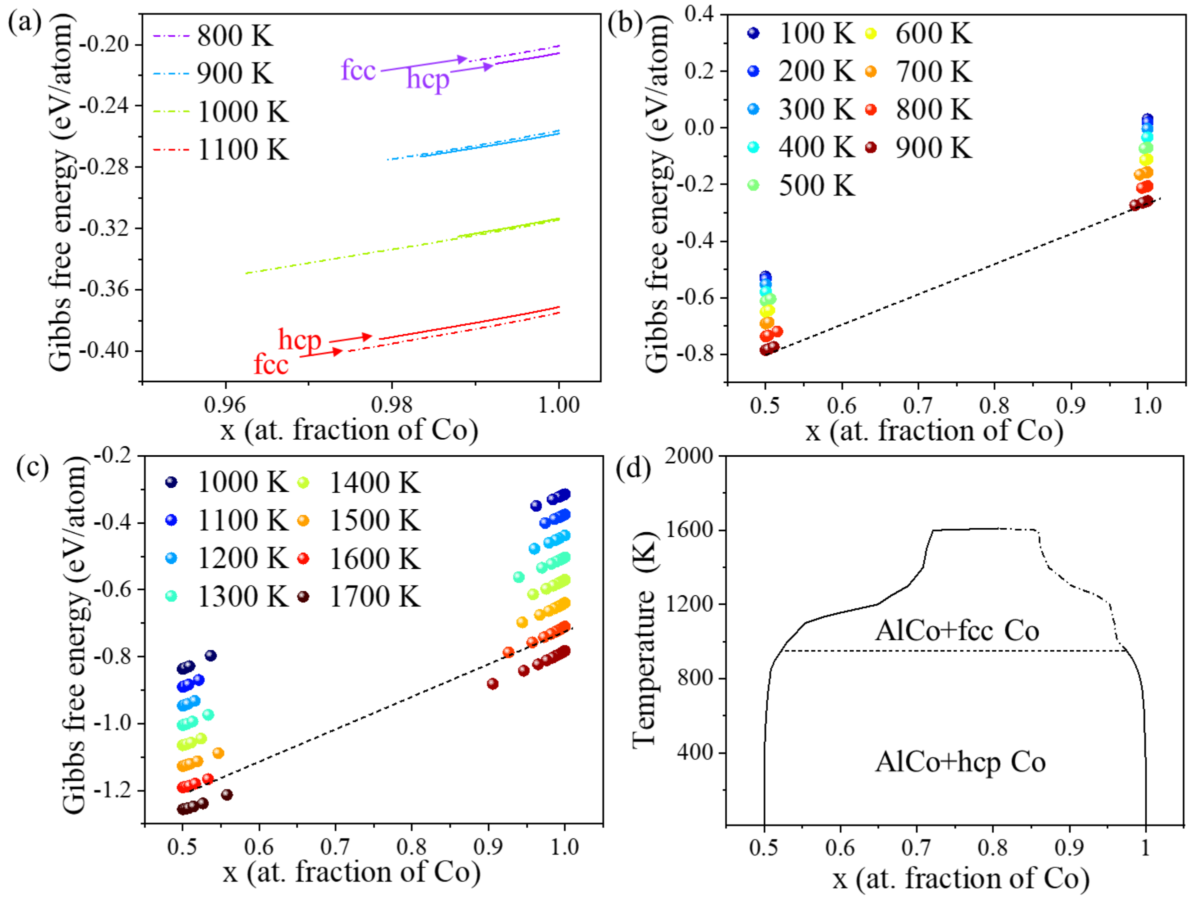

Figure C7: (a) Gibbs free energies of hcp (solid line) and fcc (dashed line) Co at different temperatures. (b) Gibbs free energies of AlCo and hcp Co below 900 K. (c) Gibbs free energies of AlCo and fcc Co above 1000 K. (d) AlCo and hcp Co and fcc Co phase boundary.

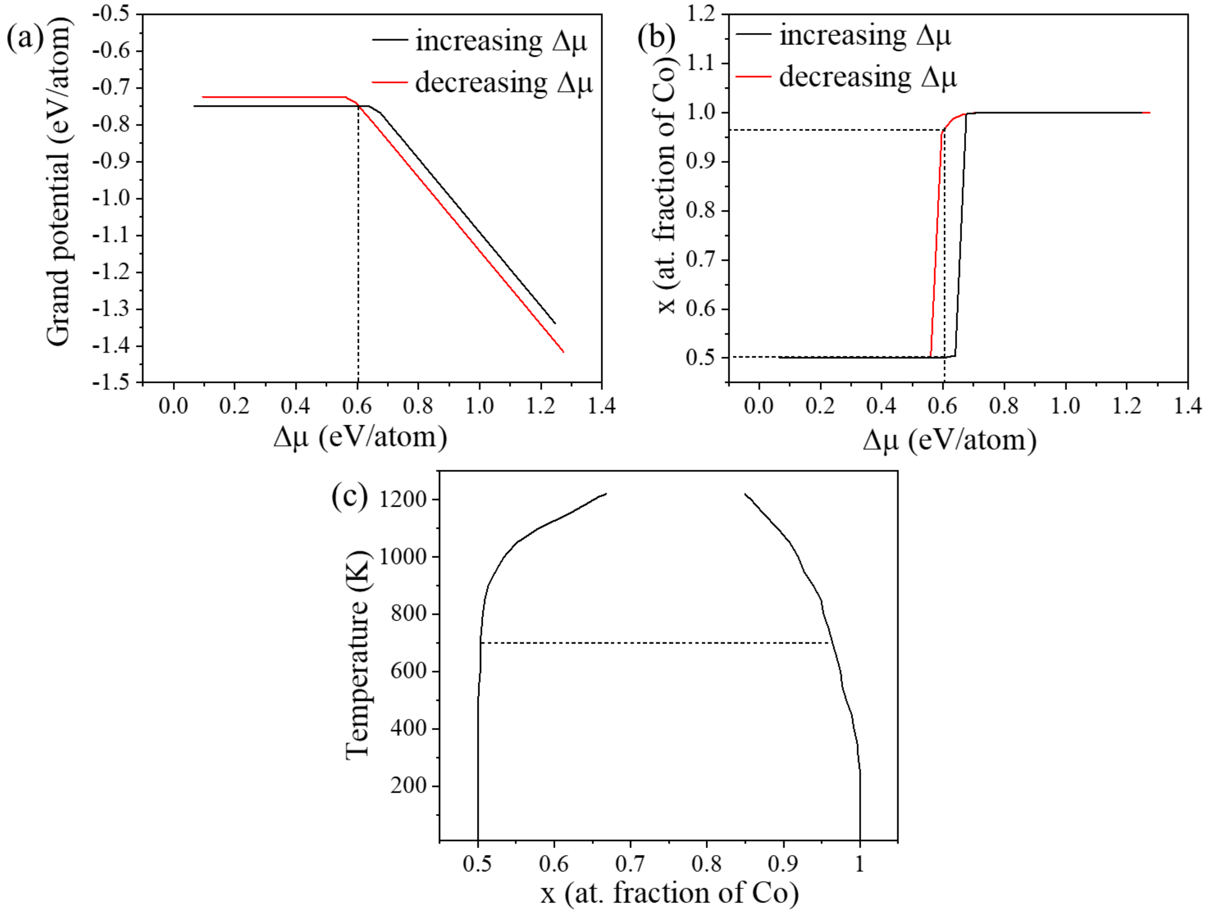

Figure C8: (a) Grand potentials of bcc AlCo and bcc Co as a function of chemical potential Δμ at 700 K. (b) Conjugated composition as a function of chemical potential at 700 K. (c) Metastable phase boundary between AlCo and bcc Co.

C.6. Gibbs free energies and phase boundaries in the Co-Al system including configurational entropy

The Gibbs free energies and phase boundaries including only configurational entropy for Co-Al system are shown in Figures C9-C12, which were integrated to obtain the whole Co-Al phase diagram considering configurational entropic effect.

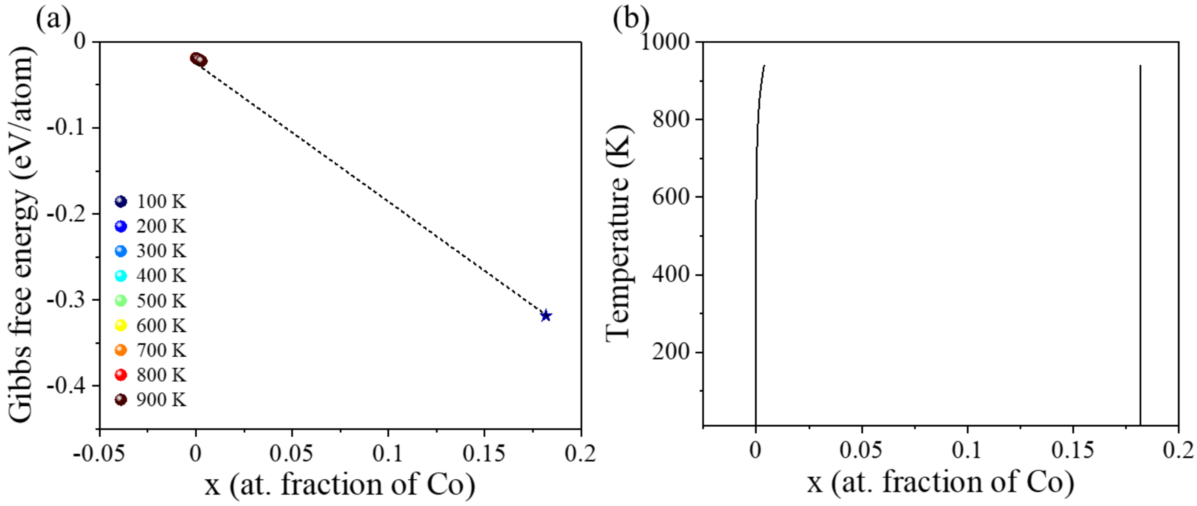

Figure C9: (a) Gibbs free energies of Al and Al_9Co_2 at different temperatures. (b) Al-Al_9Co_2 phase boundary

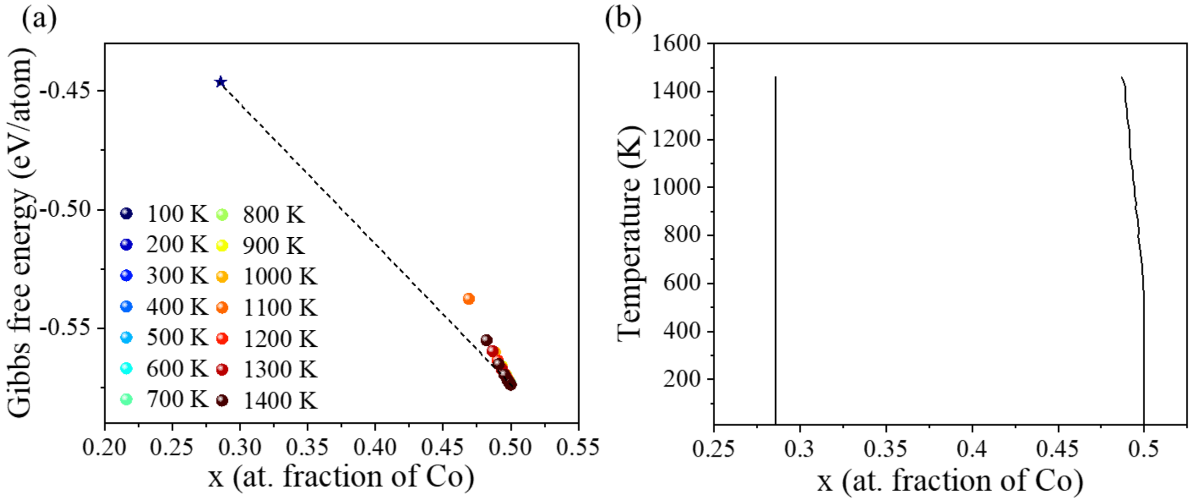

Figure C10: (a) Gibbs free energies of Al_5Co_2 and AlCo at different temperatures. (b) Al_5Co_2-AlCo phase boundary.

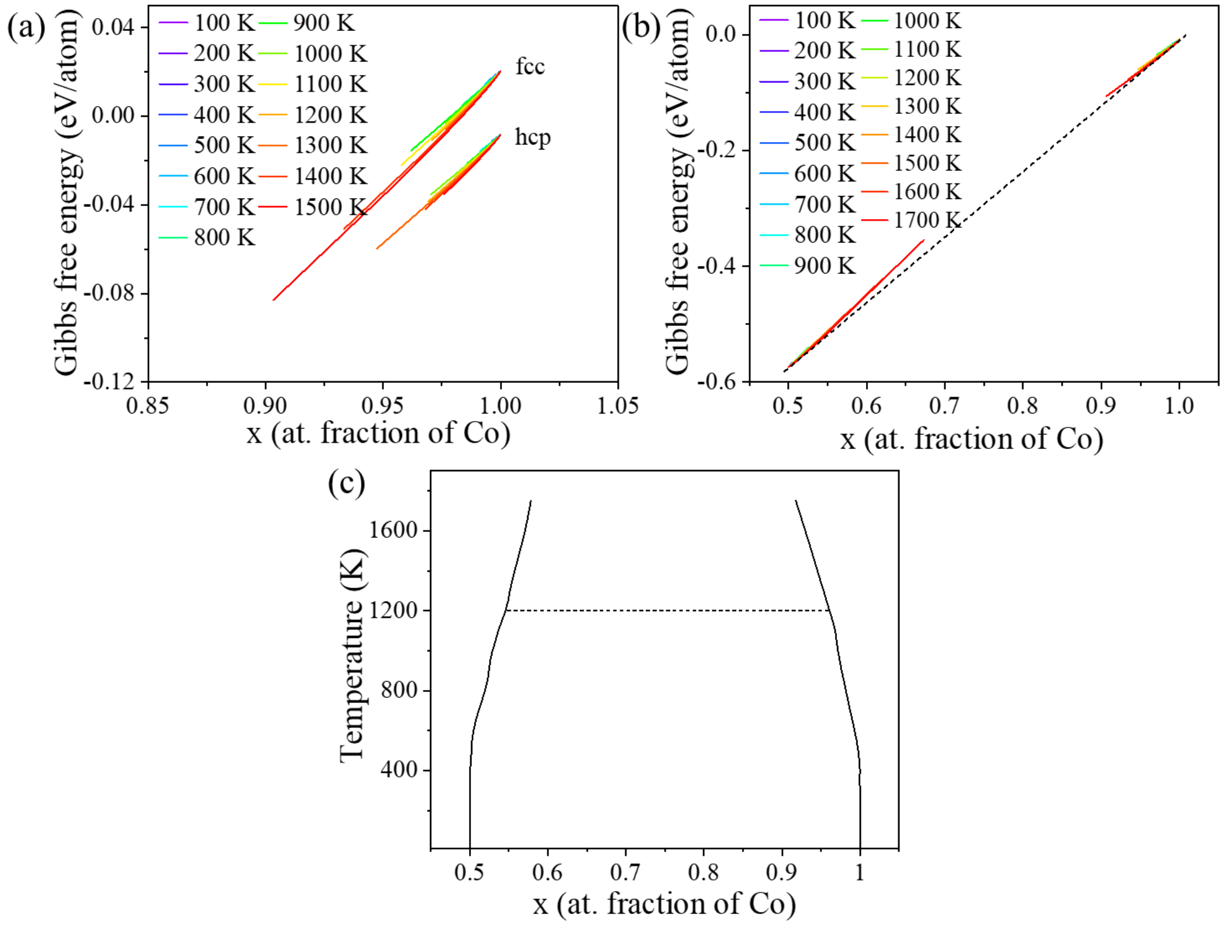

Figure C11: (a) Gibbs free energies of hcp and fcc Co at different temperatures. (b) Gibbs free energies of AlCo and hcp Co at different temperatures. (c) AlCo and hcp Co phase boundary.

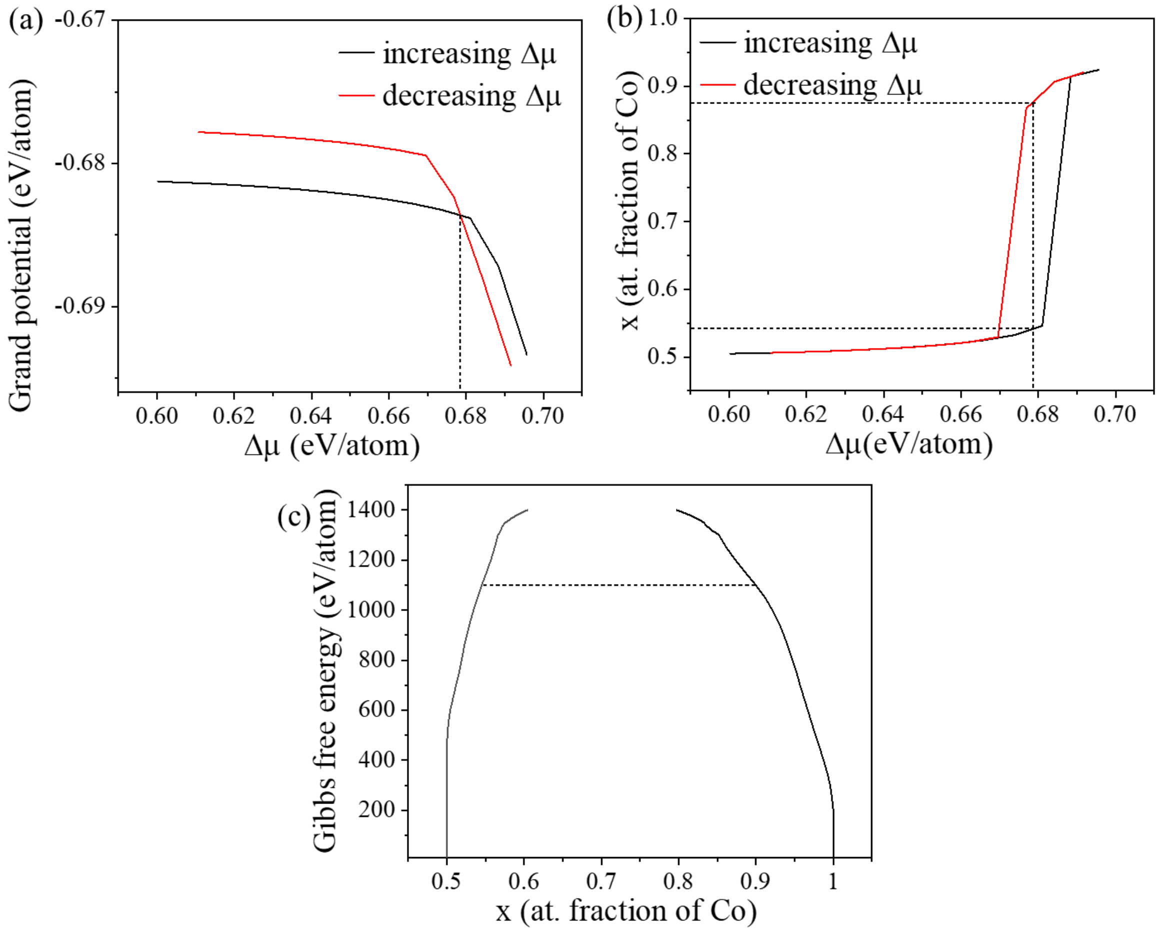

Figure C12: (a) Grand potentials of bcc AlCo and bcc Co as a function of chemical potential $\Delta\mu$ at 1100 K. (b) Conjugated composition as a function of chemical potential at 1100 K. (c) Metastable phase boundary between AlCo and bcc Co.